



**HAL**  
open science

# Contributions to numerical methods for coupled problems and incompressible flow

Miguel Angel Fernández

► **To cite this version:**

Miguel Angel Fernández. Contributions to numerical methods for coupled problems and incompressible flow. Numerical Analysis [math.NA]. Université Pierre et Marie Curie - Paris VI, 2010. tel-00854590

**HAL Id: tel-00854590**

**<https://theses.hal.science/tel-00854590>**

Submitted on 27 Aug 2013

**HAL** is a multi-disciplinary open access archive for the deposit and dissemination of scientific research documents, whether they are published or not. The documents may come from teaching and research institutions in France or abroad, or from public or private research centers.

L'archive ouverte pluridisciplinaire **HAL**, est destinée au dépôt et à la diffusion de documents scientifiques de niveau recherche, publiés ou non, émanant des établissements d'enseignement et de recherche français ou étrangers, des laboratoires publics ou privés.

UNIVERSITÉ PIERRE ET MARIE CURIE (PARIS VI)

Ensemble de travaux présentés pour obtenir

**L'HABILITATION À DIRIGER DES RECHERCHES**

Spécialité :

Mathématiques Appliquées et Applications des Mathématiques

par

**Miguel Ángel FERNÁNDEZ VARELA**

*Contributions aux méthodes numériques pour les  
problèmes couplés et les écoulements incompressibles*

Soutenue le 13 décembre 2010 devant le jury composé de

M. Roland BECKER	Rapporteur
M. Yves BOURGAULT	Rapporteur
M. Ramón CODINA	Rapporteur
M. Georges-Henri COTTET	
M. Jean-Frédéric GERBEAU	
M. Patrick LE TALLEC	
M. Yvon MADAY	
M. Bertrand MAURY	
M. Rolf STENBERG	Rapporteur



*À la mémoire de Felicitas,  
ma grand-mère maternelle.*



## Remerciements

Je voudrais tout d'abord remercier Roland Becker, Yves Bourgault, Ramón Codina et Rolf Stenberg d'avoir accepté la lourde tâche d'être rapporteurs. Je suis également très honoré que Georges-Henri Cottet, Yvon Maday et Bertrand Maury aient accepté de faire partie du jury.

J'exprime ma plus sincère gratitude à Patrick Le Tallec et à Alfio Quarteroni, pour leur contribution à ma trajectoire de chercheur. Ils ont su conforter ma vocation et m'ont soutenu à plusieurs reprises pendant ces années.

Le travail résumé dans ce mémoire est le fruit de nombreuses collaborations. C'est ainsi, avec très grand plaisir, que je remercie tous mes collaborateurs. Je tiens tout particulièrement à remercier Erik Burman, Jean-Frédéric Gerbeau et Marwan Moubachir, pour tous ces nombreux échanges passionnants et enrichissants sans lesquels ce manuscrit n'existerait pas.

Un grand merci à Dominique Chapelle et à Jean-Frédéric Gerbeau, pour leur soutien et ses précieux conseils.

Je souhaite exprimer ma gratitude envers l'Inria Paris-Rocquencourt, mon institut, et tous les membres du Bâtiment 16 qui m'ont permis d'avoir des conditions de travail plus qu'excellentes, avec une pensée tout particulière pour Marina Vidrascu.

Mes remerciements vont enfin à ma mère et à Elisa, mon épouse, pour tout leur soutien ou simplement pour leur présence.



# Contents

<b>Introduction</b> ( <i>in french</i> )	<b>9</b>
<b>Author's bibliography</b>	<b>17</b>
<b>1 Linear stability of fluid-structure interaction systems</b>	<b>21</b>
1.1 Motivations	21
1.2 Preliminaries	22
1.2.1 The coupled problem: ALE formalism	22
1.2.2 Coupling via transpiration: fixed domain approach	26
1.3 Linearization-transpiration framework	27
1.3.1 From ALE to transpiration ( <i>[10], [13], [40], [47, Chap. 2, 4]</i> )	28
1.3.2 Sensitivity analysis ( <i>[16], [24], [41], [47, Chap. 3]</i> )	30
1.4 Linear stability analysis	31
1.4.1 Spectral analysis ( <i>[13], [23], [47, Chap. 5]</i> )	32
1.4.2 Eigenvalues computation ( <i>[14], [47, Chap. 6, 7, 8]</i> )	38
<b>2 Algorithms for fluid-structure interaction</b>	<b>45</b>
2.1 Motivations	45
2.2 Implicit coupling ( <i>[43], [17], [33]</i> )	48
2.2.1 Variational setting	48
2.2.2 Partitioned solution methods	51
2.3 Semi-implicit coupling	55
2.3.1 Projection-based semi-implicit coupling ( <i>[11], [22]</i> )	56
2.4 Nitsche's based interface treatment	62
2.4.1 Stabilized explicit coupling ( <i>[7], [20]</i> )	62
2.4.2 Robin-based semi-implicit coupling ( <i>[1], [19]</i> )	70
2.5 Perspectives	74
<b>3 Numerical simulation of electrocardiograms</b>	<b>77</b>
3.1 Motivations	77
3.2 Mathematical modeling	79
3.3 Mathematical analysis ( <i>[3]</i> )	81
3.4 Meaningful ECG simulations ( <i>[2, 18]</i> )	83
3.5 Fully decoupled time marching schemes ( <i>[18]</i> )	87
3.5.1 Isolated bidomain model	87
3.5.2 Coupled heart-torso system	90
3.6 Perspectives	93

---

<b>4</b>	<b>Stabilized finite element methods for transient problems</b>	<b>95</b>
4.1	Motivations . . . . .	95
4.2	Preliminaries . . . . .	96
4.3	CIP stabilized FEM for the Oseen's equations ( <i>[8]</i> ) . . . . .	97
4.4	CIP stabilized FEM for the transient Navier-Stokes equations ( <i>[5]</i> ) . . . . .	102
4.5	Transient Stokes equations ( <i>[4]</i> ) . . . . .	105
4.6	Transient reaction-advection-diffusion equation ( <i>[6]</i> ) . . . . .	110
4.7	Perspectives . . . . .	114
	<b>Bibliography</b>	<b>117</b>

# Introduction *(in french)*

Ce mémoire résume mes principaux travaux de recherche menés à l'INRIA et à l'Université Paris IX, pendant mon doctorat (1998–2001), puis à l'École Polytechnique Fédérale de Lausanne, pendant mon séjour post-doctoral (2002–2004) et, depuis février 2004, à l'INRIA en tant que chercheur (CR). Ces travaux s'articulent, essentiellement, autour des deux thématiques suivantes :

- la modélisation et la simulation numériques de systèmes couplés (Chapitres 1–3) ;
- les méthodes d'éléments finis stabilisées pour des problèmes transitoires (Chapitre 4).

Les problèmes couplés considérés dans la première thématique sont issus, d'une part, de la modélisation de l'interaction fluide-structure et, d'autre part, de la modélisation de l'électrophysiologie cardiaque. Dans le cadre de l'interaction fluide-structure, deux types de problématiques ont été abordées : la stabilité linéaire (domaine fréquentiel) et la simulation numérique (domaine temporel).

Ce mémoire comporte ainsi quatre chapitres. Le premier, issu de la thèse, est consacré à l'étude de la stabilité linéaire de systèmes mécaniques en interaction fluide-structure. Leur analyse et simulation numériques sont l'objet du deuxième chapitre. Le troisième est consacré à la modélisation et la simulation numérique de l'électrocardiogramme. Enfin, le dernier chapitre traite du développement et de l'analyse de méthodes d'éléments finis stabilisées pour des problèmes transitoires.

Les divers travaux ne sont pas résumés de manière homogène : j'ai d'avantage détaillé ceux effectués après la thèse. Dans ce mémoire, un nombre entier entre crochets (p. ex., [17]) renvoie à la liste des publications auxquelles j'ai contribué (placées à la suite de cette introduction), tandis que les autres configurations (p. ex., [Zem09]) renvoient à la liste des références bibliographiques (placées en fin de document). Par souci de brièveté, les travaux correspondants aux références [9, 15, 12] n'ont pas été résumés dans ce mémoire.

## **Stabilité linéaire en interaction fluide-structure**

C'est au cours de ma thèse (voir [47]) que j'ai commencé à travailler sur les phénomènes d'interaction fluide structure. Ce travail a été réalisé dans le cadre d'un partenariat (ARC INRIA « Effets du vent sur les structures du génie civil ») entre l'INRIA (équipes MACS et CAIMAN), le Laboratoire Central des Ponts et Chaussées et le Centre Scientifique et Technique du Bâtiment. L'objectif de ce partenariat était le développement et l'analyse d'une série d'outils (« soufflerie numérique »), ayant vocation à être utilisés dans la conception et le dimensionnement des structures du génie civil (ponts suspendus, p. ex.), de façon complémentaire à la soufflerie expérimentale. Dans le cadre de cette ARC, mon travail de thèse avait comme objectif l'obtention et la justification de modèles simplifiés pour l'interaction fluide-structure, afin de développer un outil numérique pour la prédiction d'instabilités (flottement, flambage) d'une structure placée dans un écoulement, à un coût notablement réduit par rapport à celui d'une simulation du modèle complet (typiquement en formulation ALE).

De manière générale, les techniques numériques pour la détection des instabilités en interaction fluide-structure se répartissent en deux catégories bien différenciées. Dans la première, on peut situer les méthodes dites d'analyse instationnaire des phénomènes aéroélastiques (voir, p. ex., [PB01, FP04, BC07]). Il s'agit de résoudre le problème instationnaire couplé fluide-structure (objet du Chapitre 2 dans un autre contexte d'application), en prenant comme donnée initiale un mode structural associé à l'instabilité, ou à défaut, une combinaison des modes plus représentatifs du mouvement de la structure. Puis une analyse de l'amortissement du déplacement de la structure permettra de conclure sur la stabilité ou l'instabilité du système. Ces méthodes, pouvant devenir onéreuses en temps de calcul, permettent d'utiliser de codes de calcul fluide-structure évolués et précis (et ne se limitent pas au cadre de la stabilité linéaire). Ce type de méthodes n'a pas été abordé dans ma thèse, bien que les méthodes de transpiration que nous avons considéré puissent s'y appliquer (voir §1.2.2).

On peut classer, dans une deuxième catégorie, les méthodes de recherche de conditions d'instabilités. Il s'agit de déterminer pour une gamme précise de paramètres (vitesse de l'écoulement, géométrie, etc.) les conditions dans lesquelles le système est prédisposé à être instable. En se plaçant dans un cadre linéaire, le problème se réduit à la détermination des fréquences propres de vibration du système couplé autour d'une configuration d'équilibre donnée. L'étude de l'amortissement (partie réelle de la fréquence complexe) permet alors de conclure sur la stabilité ou l'instabilité de l'état d'équilibre en considération. Plus précisément, si l'amortissement est positif, les déformations de la structure seront amorties ; par contre si l'amortissement est négatif, les oscillations vont s'amplifier et le système devient instable. Le problème consiste alors en la détermination des fréquences de plus petite partie réelle.

Après un calcul préliminaire des modes de vibration de la structure d'intérêt, une première approche consiste à simplifier le problème couplé, en supposant que la réponse du fluide aux mouvements de la structure, peut être « condensée » à partir d'un développement caractérisé par des matrices de masse, d'amortissement et de rigidité dites *ajoutées* (voir, p. ex., [Ren98, PB01, WOO78, WOO78]). L'obtention de ces matrices ajoutées demande des calculs stationnaires et instationnaires non-linéaires associés aux déplacements modaux en question. La détermination des fréquences propres du système se réduit ainsi à la résolution d'un problème spectral matriciel quadratique, dont la taille est donnée par le nombre de modes structuraux fixés au départ.

Une deuxième approche plus générale (voir, p. ex., [Fan01]) consiste à condenser l'effet du fluide sans aucune hypothèse sur sa réponse. Ceci conduit, par contre, à un problème aux valeurs propres non-linéaire, qui est souvent résolu par une méthode de double balayage : le premier sur les modes pris en considération et le deuxième sur la vitesse aérodynamique. Cette méthode demande des résolutions aérodynamiques linéarisées associées à des mouvements sinusoïdaux de l'interface pour de nombreuses fréquences. Des méthodes d'interpolation linéaire ou de représentation par des fractions rationnelles de la réponse, permettent de réduire le nombre d'appels au solveur fluide linéarisé. Même si cette approche n'impose aucune expression particulière sur la réponse du fluide, elle demande la résolution d'un problème aux valeurs propres non-linéaire, dont les solutions obtenues par la méthode de double balayage ne correspondent pas forcément aux fréquences de plus petite partie réelle.

L'approche adoptée dans ma thèse rentre dans le cadre de la deuxième catégorie : il s'agit d'étudier la stabilité des états d'équilibre du système à partir de l'analyse des solutions harmoniques d'un problème linéaire, obtenu après une linéarisation spécifique autour de l'état d'équilibre du problème couplé complet fluide-structure. L'utilisation d'un modèle linéaire pour les analyses de stabilité en interaction fluide-structure ne constitue pas une « première ». Dans [HC93, CH00, LSHF01] une approche similaire a déjà été considérée pour des études de flottement des ailes d'avion. L'originalité de l'approche proposée réside dans la définition d'une nouvelle méthode de linéarisation permettant d'obtenir un modèle linéaire d'interaction fluide-structure de complexité

minimale, utilisant des techniques de type transpiration. Ces techniques de transpiration (voir [HC89, RH93, Deb96, Mor97, Ren98, MMS98, Med99, Fan01]), qui manquaient de justification théorique, ont été justifiées mathématiquement comme sous-produit de la nouvelle méthode de linéarisation. Ce travail est résumé dans §1.3. Enfin, dans §1.4, le problème spectral couplé, associé à l'étude des solutions harmoniques du problème linéaire, est analysé mathématiquement, et résolu numériquement avec une méthode spécifique de recherche des valeurs propres de partie réelle minimale.

### Méthodes numériques en interaction fluide-structure

La simulation numérique de l'interaction mécanique entre un fluide et une structure (CFSD) joue un rôle majeur dans pratiquement tous les domaines de l'ingénierie : de l'aéroélasticité à la biomécanique (voir, p. ex., [DGH82, MO95, Pip95, LTM01, MWR01, Tez01, GV03, WSKH04, BZ04, Hei04, COS05, FvdZG06, TS07, BC07, WRC<sup>+</sup>08, DSB<sup>+</sup>10]). Les travaux résumés dans le Chapitre 2 sont motivés par l'analyse et la simulation numériques de l'interaction (mécanique) entre la paroi des vaisseaux et le flux sanguin dans les grandes artères (voir, p. ex., [Nob01, GV03, WSKH04, LK06, FVCJ<sup>+</sup>06, YLY07, KNE<sup>+</sup>08, KGF<sup>+</sup>09, FPQ09]).

La simulation numérique de ces phénomènes d'interaction fluide-structure comporte de nombreuses difficultés. Parmi elles, le déplacement de la paroi ne peut pas être considéré comme infinitésimal (contrairement au cas du Chapitre 1). Des non-linéarités géométriques sont donc présentes dans la structure et dans le fluide qui doit être résolu dans un domaine en mouvement (typiquement avec un formalisme ALE). En outre, étant donné que les grandes artères ont des configurations élancées et que les densités du sang et de la paroi sont proches, la résolution du couplage doit être traitée soigneusement, afin d'éviter des instabilités numériques (liées aux effets de *masse-ajoutée* [CGN05]).

Dans les grandes (ou moyennes) artères, le sang est souvent modélisé comme un fluide homogène, visqueux, newtonien et incompressible (voir, p. ex., [Thi08, FPQ09]). Bien que la paroi de l'artère a un comportement visco-élastique (voir, p. ex., [Fun93]), nous limitons la présentation au cas d'un solide élastique non-linéaire, même si les algorithmes de couplage présentés dans le Chapitre 2 ne se limitent pas à ce comportement du solide. Comme modèle mathématique, nous considérons donc le système d'équations aux dérivées partielles comportant les équations de Navier-Stokes en domaine mobile, l'équation de l'élastodynamique non-linéaire et les conditions de couplage à l'interface suivantes :

- (i) continuité des déplacements (ou des vitesses) domaine fluide et structure ;
- (ii) continuité des vitesses fluide et structure ;
- (iii) équilibre des efforts fluide et structure.

Le Chapitre 2 traite de la discrétisation et de la résolution numérique de ce problème couplé. Nous renvoyons à [Mad09] pour une revue récente de l'analyse mathématique de problèmes de ce type.

Les discrétisations en temps de ce système couplé exploitent, de manière générale, la structure hétérogène du problème. Autrement dit, le fluide et la structure sont généralement discrétisés par des schémas différents, adaptés à leurs propriétés mathématiques. La discrétisation en temps des conditions (i)–(iii) définit ce qu'on appelle la procédure ou le schéma de couplage.

La procédure de couplage la plus élémentaire (peut-être la plus populaire dans la communauté aéroélastique) est basée sur le traitement explicite de (i) et (ii), ce qui donne le schéma présenté dans l'Algorithme 1. Dans la littérature aéroélastique, l'Algorithme 1 est connu sous l'appellation de schéma *décalé en série conventionnel* (voir, p. ex., [Pip97, LF98, PF03, FvdZG06]). Notons que

---

**Algorithm 1** Schéma de couplage explicite.

---

1. Calculer la nouvelle configuration du domaine fluide avec (i) ;
  2. Avancer en temps le fluide avec (ii) ;
  3. Avancer en temps la structure avec (iii) ;
  4. Passer au pas de temps suivant.
- 

l’Algorithme 1 est très séduisant en termes de coût de calcul, car il permet une résolution découplée du problème.

Les schémas de *couplage explicite (faible ou faiblement couplés)* sont ceux pour lesquels les conditions (ii) ou (iii) ne sont pas satisfaites exactement à chaque pas de temps. Une puissance parasite est donc générée à l’interface, qui doit être sous contrôle afin de garantir stabilité. L’Algorithme 1 est un schéma de couplage explicite, puisque la vitesse du fluide et celle du solide diffèrent à l’interface. Bien que les algorithmes de couplage explicite sont largement utilisés en aéroélasticité avec succès (voir, p. ex., [PB01, PF03, FP04, FvdZG06]), un certain nombre d’études numériques (voir, p. ex., [MWR99, LTM01, RB01, Nob01, GV03]) ont montré que l’Algorithme 1 est instable pour certaines valeurs des paramètres physiques. Typiquement, cela se produit lorsque les densités du fluide et du solide sont comparables ou lorsque le domaine de calcul a une forme élancée, indépendamment de la taille du pas de discrétisation en temps. Les écoulements sanguins sont un exemple bien connu d’une telle situation.

Des explications théoriques de ces phénomènes d’instabilité ont été proposées dans [CGN05] (voir aussi [FWR07]). En particulier, la condition d’instabilité suivante est établie dans [CGN05] pour un cas simplifié :

$$\frac{\rho^s \epsilon}{\rho^f \lambda_{\text{add}}} < 1, \quad (1)$$

où  $\epsilon > 0$  et  $\lambda_{\text{add}} > 0$  sont des grandeurs purement géométriques. La première est liée à l’épaisseur de la structure, alors que la dernière augmente avec la longueur du domaine (c’est la plus grande valeur propre de l’opérateur de masse-ajoutée). Notons que le membre de gauche de (1) est une grandeur purement physique, il mesure la « quantité » d’*effet de masse ajoutée* dans le système. En particulier, puisque (1) est indépendant de la taille du pas de temps, réduire le pas de temps n’élimine pas l’instabilité (comme mentionné ci-dessus).

Les schémas de *couplage implicite* sont ceux qui imposent les conditions de transmission (i)–(iii) exactement à chaque pas de temps. Les schémas qui satisfont (ii)–(iii) exactement sont appelés *fortement couplés*. Les schémas de couplage implicites sont donc fortement couplés. Ces schémas ont été, pendant des années, le seul moyen de contourner les instabilités numériques mentionnées ci-dessus. D’une certaine manière, ceci explique le fait que le développement de méthodes efficaces pour la résolution des systèmes couplés non-linéaires, résultant du couplage implicite, a été (et est encore) un domaine de recherche très actif.

Certaines de ces stratégies de couplage implicite sont décrites dans §2.2. Le reste du Chapitre 2 est consacré à la question suivante : comment éviter le couplage fort sans compromettre la stabilité ? Cette question est abordée de deux points de vue différents : via le couplage semi-implicite avec projection, dans §2.3, et par un traitement faible approprié des conditions d’interface au niveau discret, dans §2.4. Cette activité de recherche a été amorcée à l’École Polytechnique Fédérale de Lausanne et puis poursuivie à l’INRIA.

## Simulation numérique de l'électrocardiogramme

Comme les muscles squelettiques, le cœur est stimulé électriquement pour se contracter. L'électrocardiogramme (ECG) est un enregistrement non-invasif de routine de l'activité électrique du cœur. Il est obtenu à partir de mesures normalisées faites avec des électrodes placées sur la peau du patient (Figure 3.1 (gauche)) et présenté au médecin comme l'ECG à *12-dérivations* : c'est-à-dire, 12 graphiques de la différence de potentiel enregistrée en fonction du temps (Figure 3.1 (droite)). La Figure 3.2 illustre la connexion entre les déflexions de l'ECG et l'état électrique du myocarde (tissu cardiaque). L'onde P et le complexe QRS sont, respectivement, le résultat de la dépolarisation des oreillettes et des ventricules, tandis que l'onde T représente la repolarisation des ventricules (voir, p. ex., [MP95]).

L'ECG peut être considéré comme l'outil clinique le plus utilisé pour la détection et le diagnostic d'une vaste gamme de conditions cardiaques (voir, p. ex., [Aeh06, Gol06]). Malgré ceci, la signification clinique de certains ECG n'est pas encore complètement comprise. Des simulations numériques de l'ECG, reliant des modèles de l'activité électrique du cœur (dans des conditions normales ou pathologiques) au signal de l'ECG, peuvent être ainsi un outil précieux pour accroître ces connaissances. Un tel simulateur d'ECGs peut être également utile pour la construction d'une base de données virtuelle d'états pathologiques, afin de tester ou d'entraîner des dispositifs médicaux (voir [39]). De plus, la simulation numérique d'ECGs réalistes est une étape nécessaire en vue de l'objectif d'élaborer des modèles personnalisés à partir de données cliniques d'ECG.

Bien que de nombreux travaux aient été consacrés à la simulation numérique de l'électrophysiologie cardiaque (voir, p. ex., [Sac04, PBC05, SLC<sup>+</sup>06] et les références qui y sont citées), seul un petit nombre [Hui98, PDG03, LBG<sup>+</sup>03, KSW<sup>+</sup>07, TDP<sup>+</sup>04, PDV09] traitent de la simulation numérique de l'ECG avec des modèles de réaction-diffusion dans le cœur. Parmi eux, seulement [PDG03, PDV09] fournissent des simulations réalistes de l'ECG à 12 dérivations. Ces simulations reposent soit sur une approximation monodomaine, soit sur un découplage entre le cœur et le thorax et une représentation multi-dipôle de la source cardiaque (voir [LBG<sup>+</sup>03, Section 4.2.4] et [Gul88]).

Le Chapitre 3 traite de la simulation numérique de l'ECG en utilisant un modèle mathématique 3D complet, entièrement basé sur des équations aux dérivées partielles/ordinaires (EDP/EDO). Les principaux ingrédients de ce modèle sont bien connus : dynamique phénoménologique au niveau cellulaire, équation bidomaine (dans le cœur) et équation de Laplace généralisée (dans le thorax). Ces ingrédients sont présentés brièvement dans §3.2. L'existence de solution pour le problème couplé cœur-thorax est traitée dans §3.3. Cependant, pour obtenir des simulations réalistes de l'ECG, d'autres aspects essentiels à la modélisation doivent être élucidés (p. ex., les conditions de transmission cœur-thorax, l'hétérogénéité des cellules, la modélisation du Faisceau de His et l'anisotropie du myocarde), ces questions sont abordées dans §3.4. Enfin, quelques schémas de discrétisation en temps pour l'équation bidomaine et le système couplé cœur-thorax sont étudiés dans §3.5.

Les études présentées dans le Chapitre 3 ont été menées dans le cadre d'une Action d'Envergure Nationale de l'INRIA sur la simulation numérique du cœur (CardioSense3D<sup>1</sup>), que j'ai co-animée avec H. Delingette (INRIA) pendant la période 2005–2009. Ces études sont issues du séjour post-doctoral de M. Boulakia (Paris VI) et, tout particulièrement, de la thèse de N. Zemzemi [Zem09], que j'ai co-encadrés avec J.-F. Gerbeau (INRIA). Enfin, le travail résumé dans §3.4 est aussi le résultat d'une collaboration, amorcée par J.-F. Gerbeau, avec un clinicien (Dr. S. Cazeau, Hôpital Saint Joseph) et un industriel (ELA Medical).

---

<sup>1</sup><http://www-sop.inria.fr/CardioSense3D>

## Méthodes d'éléments finis stabilisés pour les problèmes transitoires

La motivation principale des études présentées dans le Chapitre 4 est la simulation numérique d'écoulements visqueux incompressibles (*cf.* Chapitres 1 et 2) décrits par les équations de Navier-Stokes instationnaires. Ces travaux sont issus d'une longue collaboration avec E. Burman (University of Sussex, UK). Ils ont été amorcés à l'École Polytechnique Fédérale de Lausanne et poursuivis à l'INRIA, grâce au programme de Professeurs Invités de l'UR de Paris-Rocquencourt et, depuis récemment, grâce au programme Franco-Britannique PHC Alliance (British Council et Ambassade de France à Londres).

Une approche naturelle pour l'approximation numérique de ces équations est la méthode *des lignes*, qui consiste à discrétiser d'abord en espace avec une méthode d'éléments finis et puis, en temps, avec un schéma  $\mathcal{A}$ -stable (voir, p. ex., [HR90]). Indépendamment de l'instationnarité et du traitement de la non-linéarité, il est bien connu que la méthode d'éléments finis Galerkin standard appliquée à ces équations perd de la stabilité dans les cas suivants :

- advection dominante;
- même approximation polynomiale pour la vitesse et la pression (ce qui est utile en pratique).

La premier cas donne lieu à des oscillations parasites dans la vitesse. Le deuxième enfreint la condition *inf-sup* discrète (voir, p. ex., [GR86]), ce qui mène à des instabilités dans la pression. Ces problèmes sont généralement traités par l'utilisation de méthodes d'éléments finis dites *stabilisées*, où l'on rajoute des termes (consistants) à la formulation de Galerkin permettant d'améliorer la stabilité, sans compromettre la précision.

Dans ce cadre, une approche très utilisée en pratique consiste à stabiliser simultanément la vitesse et la pression en combinant les méthodes Streamline-Upwind/Petrov-Galerkin (SUPG) [BH82] et Pressure-Stabilized/Petrov-Galerkin (PSPG) [HFB86]. La stabilité est améliorée en rajoutant des résidus locaux pondérés à la formulation de Galerkin. D'autres méthodes connexes, comportant des pondérations alternatives des résidus, sont la méthode Galerkin-Least-Square (GLS) [FF92] et la méthode Algebraic-Subgrid-Scale (ASGS) [Cod01, CPGB07]. Par leur structure, ces méthodes sont souvent appelées méthodes stabilisées *basées sur le résidu* (local). La méthode SUPG/PSPG doit son succès au traitement unifié des instabilités de la vitesse et de la pression. Cette méthode permet d'obtenir des estimations d'erreur *a priori*, uniformes par rapport à la viscosité (voir, p. ex., [HS90, TV96]), et a été utilisée intensivement en pratique avec de bons résultats.

Malgré cela, les méthodes stabilisées basées sur le résidu ont quelques inconvénients importants (voir [GLOS05, BBJL07]). Tout d'abord, la stabilisation introduit des termes non-symétriques artificiels et des couplages vitesse/pression non-physiques. Mais surtout, l'analyse de l'extension de ces méthodes au cas instationnaire (elles ont été initialement introduites pour des problèmes stationnaires) est un sujet controversé (à moins que l'on n'adopte des formulations espace-temps [HS90, Tez92]). De fait, la combinaison de ces méthodes avec des schémas en temps standards peut donner lieu à des instabilités pour des pas de temps petits (voir, p. ex., [BGS04, BGL07]). Dans [CPGB07], ces instabilités ont été corrigées dans la méthode ASGS en considérant des échelles de sous-maille dépendantes du temps.

Ces inconvénients ont motivé le développement de méthodes de stabilisation alternatives (non basées sur le résidu). Par exemple, la méthode des sous-échelles orthogonales (OSS) [CB97, Cod00], la méthode de viscosité de sous-maille [Gue99], la méthode de projection locale [BB01, BB06] et la méthode conforme de pénalisation intérieure (CIP) [BH04, BH06]. Le prix à payer pour l'utilisation de ces méthodes de stabilisation symétriques est une réduction de la structure creuse de la matrice *de raideur*, liée au calcul de projections ou à la présence de sauts de gradient dans l'opérateur de stabilisation.

L'extension de la méthode CIP au problème d'Oseen et aux équations de Navier-Stokes transitoires est traitée dans §4.3 et dans §4.4, respectivement. Des estimations d'erreur *a priori* (uniformes

---

par rapport à la viscosité) sont fournies pour des approximations vitesse/pression du même ordre. Une analyse d'erreur abstraite pour des méthodes de stabilisation symétriques est présentée, dans §4.5 pour les équations de Stokes transitoires et, dans §4.6 pour l'équation de réaction-advection-diffusion transitoire. Dans le cas de Stokes, nous montrons que l'instabilité des petits pas de temps peut être éliminée par un choix judicieux de l'approximation de la vitesse initiale. Enfin, dans le cas de l'équation de réaction-advection-diffusion, nous contournons le problème de la réduction de la structure creuse par un traitement explicite de la stabilisation (voir aussi [CB00]).



# Author's bibliography

## Papers in refereed journals

- [1] M. Astorino, F. Chouly, and M. A. Fernández. Robin based semi-implicit coupling in fluid-structure interaction: Stability analysis and numerics. *SIAM J. Sci. Comput.*, 31(6):4041–4065, 2009.
- [2] M. Boulakia, S. Cazeau, M.A. Fernández, J.-F. Gerbeau, and N. Zemzemi. Mathematical modeling of electrocardiograms: a numerical study. *Ann. Biomed. Eng.*, 38(3):1071–1097, 2010.
- [3] M. Boulakia, M.A. Fernández, J.-F. Gerbeau, and N. Zemzemi. A coupled system of PDEs and ODEs arising in electrocardiograms modeling. *Appl. Math. Res. Express. AMRX*, 2008(2):Art. ID abn002, 28, 2008.
- [4] E. Burman and M. A. Fernández. Galerkin finite element methods with symmetric pressure stabilization for the transient Stokes equations: stability and convergence analysis. *SIAM J. Numer. Anal.*, 47(1):409–439, 2008/09.
- [5] E. Burman and M.A. Fernández. Continuous interior penalty finite element method for the time-dependent Navier-Stokes equations: space discretization and convergence. *Numer. Math.*, 107(1):39–77, 2007.
- [6] E. Burman and M.A. Fernández. Finite element methods with symmetric stabilization for the transient convection-diffusion-reaction equation. *Comput. Methods Appl. Mech. Engrg.*, 198(33-36):2508–2519, 2009.
- [7] E. Burman and M.A. Fernández. Stabilization of explicit coupling in fluid-structure interaction involving fluid incompressibility. *Comput. Methods Appl. Mech. Engrg.*, 198(5-8):766–784, 2009.
- [8] E. Burman, M.A. Fernández, and P. Hansbo. Continuous interior penalty finite element method for Oseen's equations. *SIAM J. Numer. Anal.*, 44(3):1248–1274, 2006.
- [9] S. Deparis, M.A. Fernández, and L. Formaggia. Acceleration of a fixed point algorithm for fluid-structure interaction using transpiration conditions. *M2AN Math. Model. Numer. Anal.*, 37(4):601–616, 2003.
- [10] T. Fanion, M. A. Fernández, and P. Le Tallec. Deriving adequate formulations for fluid-structure interaction problems: from ALE to transpiration. *Rev. Européenne Élé. Finis*, 9(6-7):681–708, 2000.

- 
- [11] M.A. Fernández, J.-F. Gerbeau, and C. Grandmont. A projection semi-implicit scheme for the coupling of an elastic structure with an incompressible fluid. *Internat. J. Numer. Methods Engrg.*, 69(4):794–821, 2007.
- [12] M.A. Fernández, J.-F. Gerbeau, and V. Martin. Numerical simulation of blood flows through a porous interface. *M2AN Math. Model. Numer. Anal.*, 42(6):961–990, 2008.
- [13] M.A. Fernández and P. Le Tallec. Linear stability analysis in fluid-structure interaction with transpiration. I. Formulation and mathematical analysis. *Comput. Methods Appl. Mech. Engrg.*, 192(43):4805–4835, 2003.
- [14] M.A. Fernández and P. Le Tallec. Linear stability analysis in fluid-structure interaction with transpiration. II. Numerical analysis and applications. *Comput. Methods Appl. Mech. Engrg.*, 192(43):4837–4873, 2003.
- [15] M.A. Fernández, V. Milišić, and A. Quarteroni. Analysis of a geometrical multiscale blood flow model based on the coupling of ODEs and hyperbolic PDEs. *Multiscale Model. Simul.*, 4(1):215–236, 2005.
- [16] M.A. Fernández and M. Moubachir. Sensitivity analysis for an incompressible aeroelastic system. *Math. Models Methods Appl. Sci.*, 12(8):1109–1130, 2002.
- [17] M.A. Fernández and M. Moubachir. A Newton method using exact Jacobians for solving fluid-structure coupling. *Comp. & Struct.*, 83:127–142, 2005.
- [18] M.A. Fernández and N. Zemzemi. Decoupled time-marching schemes in computational cardiac electrophysiology and ECG numerical simulation. *Math. Biosci.*, 226(1):58–75, 2010.

### Refereed short papers (CRAS notes)

- [19] M. Astorino, F. Chouly, and M.A. Fernández. An added-mass free semi-implicit coupling scheme for fluid-structure interaction. *C. R. Math. Acad. Sci. Paris*, 347(1-2):99–104, 2009.
- [20] E. Burman and M.A. Fernández. Stabilized explicit coupling for fluid-structure interaction using Nitsche's method. *C. R. Math. Acad. Sci. Paris*, 345(8):467–472, 2007.
- [21] S. Deparis, M.A. Fernández, L. Formaggia, and F. Nobile. Modified fixed point algorithm in fluid-structure interaction. *C. R. Mecanique*, 331(8):525–530, 2003.
- [22] M.A. Fernández, J.-F. Gerbeau, and C. Grandmont. A projection algorithm for fluid-structure interaction problems with strong added-mass effect. *C. R. Math. Acad. Sci. Paris*, 342(4):279–284, 2006.
- [23] M.A. Fernández and P. Le Tallec. Un nouveau problème spectral en interaction fluide-structure avec transpiration. *C. R. Math. Acad. Sci. Paris*, 334(2):167–172, 2002.
- [24] M.A. Fernández and M. Moubachir. Étude de sensibilité d'un système mécanique en interaction fluide-structure. *C. R. Acad. Sci. Paris Sér. I Math.*, 333(5):487–492, 2001.
- [25] M.A. Fernández and M. Moubachir. An exact block-Newton algorithm for solving fluid-structure interaction problems. *C. R. Math. Acad. Sci. Paris*, 336(8):681–686, 2003.

## Technical reports

- [26] E. Burman, A. Ern, and M.A. Fernández. Explicit Runge-Kutta schemes and finite elements with symmetric stabilization for first-order linear PDE systems. Technical Report 409, ENPC CERMICS, May 2009. To appear in *SIAM J. Numer. Anal.*
- [27] E. Burman and M.A. Fernández. Analysis of the PSPG method for the transient Stokes' problem. Technical Report RR-7074, INRIA, October 2009. Submitted to *Comput. Methods Appl. Mech. Engrg.*
- [28] A. Caiazzo, M.A. Fernández, J.-F. Gerbeau, and V. Martin. Projection schemes for fluid flows through a porous interface. Technical Report RR-7225, INRIA, March 2010. Submitted to *SIAM J. Sci. Comput.*
- [29] M.A. Fernández. Incremental displacement-correction schemes for the explicit coupling of a thin structure with an incompressible fluid. Technical Report RR-7474, INRIA, December 2010. Submitted to *C. R. Math. Acad. Sci. Paris.*
- [30] M.A. Fernández, J.-F. Gerbeau, A. Gloria, and M. Vidrascu. A partitioned Newton method for the interaction of a fluid and a 3D shell structure. Technical Report RR-6623, INRIA, August 2008. To appear in *Eur. J. Comput. Mech.*

## Book chapters

- [31] T. Fanion, M.A. Fernández, and P. Le Tallec. Deriving adequate formulations for fluid-structure interaction problems: from ALE to transpiration. In *Fluid structure interaction*, Innovative Technology Series, pages 51–80. Kogan Page Science, 2003. Reprint of [10].
- [32] M.A. Fernández, L. Formaggia, J.-F. Gerbeau, and A. Quarteroni. The derivation of the equations for fluids and structures. In *Cardiovascular mathematics*, volume 1 of *MS&A. Model. Simul. Appl.*, pages 77–121. Springer, 2009.
- [33] M.A. Fernández and J.-F. Gerbeau. Algorithms for fluid-structure interaction problems. In *Cardiovascular mathematics*, volume 1 of *MS&A. Model. Simul. Appl.*, pages 307–346. Springer, 2009.

## Refereed conference proceedings

- [34] M. Boulakia, M.A. Fernández, J.-F. Gerbeau, and N. Zenzemi. Towards the numerical simulation of electrocardiograms. In F.B. Sachse and G. Seemann, editors, *Functional Imaging and Modeling of the Heart*, number 4466 in Lecture Notes in Computer Science, pages 240–249. Springer, 2007.
- [35] M. Boulakia, M.A. Fernández, J.-F. Gerbeau, and N. Zenzemi. Direct and inverse problems in electrocardiography. In Simos, T.E. and Psihoyios, G. and Tsitouras, C., editor, *Numerical analysis and applied mathematics*, volume 1048 of *AIP Conference Proceedings*, pages 113–117, 2008.
- [36] D. Chapelle, M.A. Fernández, J.-F. Gerbeau, P. Moireau, J. Sainte-Maire, and N. Zenzemi. Numerical simulation of the electromechanical activity of the heart. In N. Ayache, H. Delingette, and M. Sermesant, editors, *Functional Imaging and Modeling of the Heart*, volume 5528 of *Lecture Notes in Computer Science*, pages 357–365. Springer, 2009.

- [37] F. Chouly and M.A. Fernández. An enhanced Parareal algorithm for partitioned parabolic-hyperbolic coupling. In Simos, T.E. and Psihoyios, G. and Tsitouras, C., editor, *Numerical analysis and applied mathematics*, volume 1168 of *AIP Conference Proceedings*, pages 1517–1520, 2009.
- [38] S. Deparis, M.A. Fernández, L. Formaggia, and F. Nobile. Acceleration of a fixed point algorithm for fluid-structure interaction using transpiration conditions. In K.J. Bathe, editor, *Computational fluid and solid mechanics, Vol. 1, 2*. Elsevier, 2003.
- [39] G. Ebrard, M.A. Fernández, J.-F. Gerbeau, F. Rossi, and N. Zemzemi. From intracardiac electrograms to electrocardiograms. models and metamodels. In N. Ayache, H. Delingette, and M. Sermesant, editors, *Functional Imaging and Modeling of the Heart*, volume 5528 of *Lecture Notes in Computer Science*, pages 524–533. Springer, 2009.
- [40] M. A. Fernández and P. Le Tallec. From ALE to transpiration. In K.J. Bathe, editor, *Computational fluid and solid mechanics, Vol. 1, 2*, pages 1166–1169. Elsevier, 2001.
- [41] M. A. Fernández and M. Moubachir. Investigation of sensitivity analysis for fluid-structure interaction systems. In *Computational fluid and solid mechanics, Vol. 1, 2*, pages 1170–1173. Elsevier, 2001.
- [42] M.A. Fernández, J.-F. Gerbeau, A. Gloria, and M. Vidrascu. Domain decomposition based Newton methods for fluid-structure interaction problems. In *CANUM 2006—Congrès National d’Analyse Numérique*, volume 22 of *ESAIM Proc.*, pages 67–82. EDP Sci., 2008.
- [43] M.A. Fernández and M. Moubachir. An exact block-newton algorithm for the solution of implicit time discretized coupled systems involved in fluid-structure interaction problems. In K.J. Bathe, editor, *Computational fluid and solid mechanics, Vol. 1, 2*, pages 1337–1341. Elsevier, 2003.
- [44] M.A. Fernández, A. Moura, and C. Vergara. Defective boundary conditions applied to multiscale analysis of blood flow. In *CEMRACS 2004—mathematics and applications to biology and medicine*, volume 14 of *ESAIM Proc.*, pages 89–99. EDP Sci., 2005.

## Theses

- [45] M.A. Fernández. Verrouillage numérique des modèles non-linéaires de coques. Master’s thesis, Université Paris VI, France, 1998.
- [46] M.A. Fernández. Resolución numérica de modelos de elasticidad adaptativa en formación de huesos. Master’s thesis, Universidade de Santiago de Compostela, Spain, 1999.
- [47] M.A. Fernández. *Modèles simplifiés d’interaction fluide-structure*. PhD thesis, Université Paris IX, France, 2001. <http://tel.archives-ouvertes.fr/tel-00001954/en/>.

# Chapter 1

## Linear stability of fluid-structure interaction systems

This chapter provides a summary of my PhD thesis, prepared under the supervision of Prof. P. Le Tallec (École Polytechnique) at INRIA and Université Paris IX, during the period 1998–2001.

### 1.1 Motivations

This work was carried out in the framework of a Collaborative Research Initiative (ARC), funded by INRIA and entitled “wind effects on civil engineering structures”. The main objective of this ARC was to develop and analyze a series of numerical tools aimed at complementing wind tunnel studies in the design of civil engineering structures (*e.g.*, long span bridges). The ARC gathered researches from INRIA (MACS and CAIMAN teams), the Laboratoire Central des Ponts et Chaussées and the Centre Scientifique et Technique du Bâtiment.

One of the objectives of the PhD research was to derive and justify simplified models for fluid-structure interaction, with the aim of developing a numerical tool for the prediction of instabilities (*e.g.*, flutter) of a structure interacting with a fluid flow. The final goal being to provide reliable linear stability predictions at a reduced computational cost with respect to a direct fluid-structure simulation, typically involving moving-mesh (ALE) fluid computations. The research activity was split into two related areas:

1. the development of a linearization technique allowing to justify mathematically the transpiration interface conditions. The key point here was the parameterization of the sensitivity of the fluid state, which is an Eulerian quantity, with respect to the motion of the solid, which is a Lagrangian field. These results are summarized in §1.3;
2. the application of the developed linearization-transpiration philosophy to the linear stability analysis of fluid-structure interaction systems. The harmonic solutions of the obtained coupled linear problem, are solutions of a new spectral problem of minimal complexity, involving transpiration interface conditions. The spectrum was analyzed mathematically and approximated numerically using appropriate numerical tools. These contributions are presented in §1.4.

## 1.2 Preliminaries

This section contains introductory material. We first describe the main ingredients of the general model used to describe the interaction of a viscous incompressible Newtonian fluid with an elastic structure in large displacements (moving fluid-domain). Next, in §1.2.2, we present the main heuristic ideas of the transpiration framework (fixed fluid-domain), quite popular in the aeroelastic community.

### 1.2.1 The coupled problem: ALE formalism

The modeling of fluid-structure interaction systems under large displacements involves, in a general way, the coupling of two formulations: the solid classically treated in Lagrangian formulation, and the fluid described by an arbitrary Lagrangian-Eulerian (ALE) formulation (see, *e.g.*, [DGH82, NH92, MW01, LTM01] and [32]).

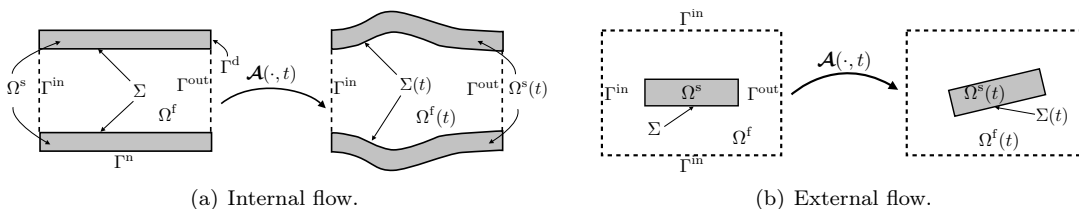


Figure 1.1: Geometrical fluid-structure configurations.

We consider a mechanical system occupying a moving domain  $\Omega(t)$ . It consists of a deformable structure  $\Omega^s(t)$  (*e.g.*, vessel wall, bridge deck, pipe-line) interacting with a fluid under motion (*e.g.*, blood, air, oil) in the complement  $\Omega^f(t)$  of  $\Omega^s(t)$  in  $\Omega(t)$ . We denote by  $\Sigma(t)$  the current configuration of the fluid-structure interface, that is,  $\Sigma(t) \stackrel{\text{def}}{=} \partial\Omega^f(t) \cap \partial\Omega^s(t)$  (see Figure 1.1). Let  $\Omega^f \cup \Omega^s$  be a reference configuration of the system (*e.g.*, the initial configuration). We denote by  $\Sigma \stackrel{\text{def}}{=} \partial\Omega^f \cap \partial\Omega^s$  the reference fluid-solid interface and  $\partial\Omega^f = \Gamma^{\text{in}} \cup \Gamma^{\text{out}} \cup \Sigma$ ,  $\partial\Omega^s = \Gamma^{\text{d}} \cup \Gamma^{\text{n}} \cup \Sigma$ , are given partitions of the fluid and solid boundaries respectively, see Figure 1.1. The fluid external boundaries  $\Gamma^{\text{in}}$  and  $\Gamma^{\text{out}}$  are supposed to be fixed. The corresponding outward normal vectors to the fluid and solid boundaries are denoted by  $\mathbf{n}$  and  $\mathbf{n}^s$ , respectively (the same notation is used for both the reference and the current configurations).

The problem consists in determining the time evolution of the configuration  $\Omega(t)$ , as well as the velocity and stress tensor within the fluid and the structure. The latter being governed by the classic conservation laws of the continuum mechanics, endowed with appropriate constitutive laws.

#### 1.2.1.1 Fluid equations: ALE formalism

The dynamics of the (moving) control volume  $\Omega^f(t)$  are parametrized in terms of a smooth injective map  $\mathcal{A} : \Omega^f \times \mathbb{R}^+ \rightarrow \mathbb{R}^d$ , the so-called ALE-map, such that

$$\Omega^f(t) = \mathcal{A}_t(\Omega^f),$$

with the notation  $\mathcal{A}_t \stackrel{\text{def}}{=} \mathcal{A}(\cdot, t)$ . The corresponding deformation gradient and Jacobian are denoted by  $\mathbf{F} \stackrel{\text{def}}{=} \nabla \mathcal{A}_t$  and  $J \stackrel{\text{def}}{=} \det \mathbf{F}$ , respectively. Moreover, we shall use the notation  $\mathbf{w} \stackrel{\text{def}}{=} \partial_t \mathcal{A}$  for the fluid domain velocity, and  $\mathbf{d}^f(\hat{\mathbf{x}}, t) \stackrel{\text{def}}{=} \mathcal{A}_t(\hat{\mathbf{x}}) - \hat{\mathbf{x}}$ ,  $\hat{\mathbf{x}} \in \Omega^f$ , for the fluid domain displacement.

**Remark 1.1** Thanks to the invertibility of  $\mathcal{A}_t$ , we can define all the physical quantities on the reference or on the current configuration, the choice being a matter of convenience. When the same field is evaluated in both the current and the reference configurations, we adopt the superscript  $\widehat{\phantom{x}}$  to indicate that it is defined in  $\Omega^f \times \mathbb{R}^+$  and we have the relations

$$\begin{aligned}\widehat{q}(\widehat{\mathbf{x}}, t) &\stackrel{\text{def}}{=} q(\mathcal{A}_t(\widehat{\mathbf{x}}), t) \quad \forall \widehat{\mathbf{x}} \in \Omega^f, \\ q(\mathbf{x}, t) &\stackrel{\text{def}}{=} \widehat{q}(\mathcal{A}_t^{-1}(\mathbf{x}), t) \quad \forall \mathbf{x} \in \Omega^f(t).\end{aligned}$$

In the rest of situations (i.e., a field is only used in one of the configurations), the superscript  $\widehat{\phantom{x}}$  is not used.

We assume the fluid to be homogeneous, Newtonian and incompressible. Its behavior is described in terms of its velocity  $\widehat{\mathbf{u}} : \Omega^f \times \mathbb{R}^+ \rightarrow \mathbb{R}^d$  and pressure  $\widehat{p} : \Omega^f \times \mathbb{R}^+ \rightarrow \mathbb{R}$  fields, which are governed by the following Navier-Stokes equations (written in ALE form):

$$\begin{cases} \rho^f \partial_t \mathbf{u}|_{\mathcal{A}} + \rho^f (\mathbf{u} - \mathbf{w}) \cdot \nabla \mathbf{u} - \text{div } \boldsymbol{\sigma}(\mathbf{u}, p) = \mathbf{0} & \text{in } \Omega^f(t), \\ \text{div } \mathbf{u} = 0 & \text{in } \Omega^f(t), \end{cases} \quad (1.2.1)$$

where  $\rho^f$  stands for the fluid density,  $\partial_t|_{\mathcal{A}} \mathbf{u}$  for the ALE time derivative and  $\boldsymbol{\sigma}(\mathbf{u}, p) \stackrel{\text{def}}{=} -p\mathbf{I} + 2\mu\boldsymbol{\epsilon}(\mathbf{u})$  for the fluid Cauchy stress tensor, with  $\mu$  the fluid dynamic viscosity and  $\boldsymbol{\epsilon}(\mathbf{u}) \stackrel{\text{def}}{=} \frac{1}{2}(\nabla \mathbf{u} + \nabla \mathbf{u}^T)$  the strain rate tensor.

System (1.2.1) has to be supplemented with boundary conditions, for instance,

$$\begin{cases} \mathbf{u} = \mathbf{u}_{\text{in}} & \text{on } \Gamma^{\text{in}}, \\ \boldsymbol{\sigma}(\mathbf{u}, p)\mathbf{n} = -p_{\text{out}}\mathbf{n} & \text{on } \Gamma^{\text{out}}, \end{cases}$$

and initial condition  $\mathbf{u}|_{t=0} = \mathbf{u}_0$ . Here,  $\mathbf{u}_{\text{in}}$ ,  $p_{\text{out}}$  and  $\mathbf{u}_0$  are given boundary and initial data. The conditions to be enforced on the fluid-structure interface  $\Sigma(t)$  are discussed in §1.2.1.3.

**Remark 1.2** Note that the importance of the presence of the ALE time-derivative  $\partial_t \mathbf{u}|_{\mathcal{A}}$  in (1.2.1) emerges in the context of the numerical discretisation (we recall that  $\widehat{\partial_t \mathbf{u}|_{\mathcal{A}}} \stackrel{\text{def}}{=} \partial_t \widehat{\mathbf{u}}$ ). Indeed, when computing numerically a solution in a moving domain we are usually interested in the time variation of quantities collocated at the nodes of a computational mesh (not at a particular fixed position), and the latter necessarily follows the evolution of the computational domain.

### 1.2.1.2 Solid equations

The dynamics of the structure are parametrized in terms of its motion  $\boldsymbol{\varphi} : \Omega^s \times \mathbb{R}^+ \rightarrow \mathbb{R}^d$ . That is, a smooth and injective mapping such that  $\Omega^s(t) = \boldsymbol{\varphi}_t(\Omega^s)$ . Moreover, for each  $\widehat{\mathbf{x}} \in \Omega^s$ ,  $\boldsymbol{\varphi}_t(\widehat{\mathbf{x}})$  gives the position at time  $t$  of the material point  $\widehat{\mathbf{x}}$  inside the solid domain. This corresponds to the classical Lagrangian flow. The solid displacement is then defined as  $\mathbf{d}(\widehat{\mathbf{x}}, t) \stackrel{\text{def}}{=} \boldsymbol{\varphi}_t(\widehat{\mathbf{x}}) - \widehat{\mathbf{x}}$ . Its evolution is generally governed by the non-linear elastodynamics equations (see also Remark 1.4 below)

$$\rho^s \partial_{tt} \mathbf{d} - \text{div } (\boldsymbol{\Pi}(\mathbf{d})) = \mathbf{0} \quad \text{in } \Omega^s, \quad (1.2.2)$$

where  $\rho^s$  represents the solid density and  $\boldsymbol{\Pi}(\mathbf{d})$  the first Piola-Kirchhoff stress tensor of the structure. The latter being related to  $\mathbf{d}$  through an appropriate constitutive law (see, e.g., [Gur81, Cia88, LT94]). For instance, for an hyper-elastic material, we have

$$\boldsymbol{\Pi}(\mathbf{d}) = \mathbf{F}^s \frac{\partial W}{\partial \mathbf{E}}(\mathbf{E}^s),$$

where  $\mathbf{F}^s \stackrel{\text{def}}{=} \nabla \boldsymbol{\varphi}_t$  stands for the gradient of deformation,  $\mathbf{E}^s \stackrel{\text{def}}{=} \frac{1}{2}((\mathbf{F}^s)^\top \mathbf{F}^s - \mathbf{I})$  for the Green-Lagrange strain tensor and  $W : \mathbb{R}^{d \times d} \rightarrow \mathbb{R}^+$  is a given density of elastic energy.

The solid equation (1.2.2) has to be supplemented also with boundary conditions, for instance,

$$\begin{cases} \mathbf{d} = \mathbf{0} & \text{on } \Gamma^d, \\ \boldsymbol{\Pi}(\mathbf{d})\mathbf{n}^s = \mathbf{0} & \text{on } \Gamma^n, \end{cases}$$

and initial conditions  $\mathbf{d}|_{t=0} = \mathbf{d}^0$ ,  $\partial_t \mathbf{d}|_{t=0} = \dot{\mathbf{d}}^0$ . The boundary conditions to be enforced on  $\Sigma$  are discussed in the next subsection.

### 1.2.1.3 Coupling conditions

In order to ensure a correct energy balance, both the kinematic and the kinetic continuity need to be enforced across the fluid-structure interface at all times (see, *e.g.*, [LTM01] and [32]). The equilibrium of stresses is given (in the reference configuration) by

$$\boldsymbol{\Pi}(\mathbf{d})\mathbf{n}^s = -J\widehat{\boldsymbol{\sigma}}(\mathbf{u}, p)\mathbf{F}^{-\top}\mathbf{n} \quad \text{on } \Sigma.$$

The continuity of the velocity is enforced by setting

$$\widehat{\mathbf{u}} = \partial_t \mathbf{d} \quad \text{on } \Sigma. \quad (1.2.3)$$

The fluid domain displacement is taken such that

$$\mathbf{d}^f = \mathbf{d} \quad \text{on } \Sigma, \quad (1.2.4)$$

that is, the fluid and solid domains remain stucked at all times. This last equality with (1.2.3) yields  $\mathbf{u} = \mathbf{w}$  on  $\Sigma(t)$ .

Note that, since we have assumed (for simplicity) that the inlet and outlet boundaries ( $\Gamma^{\text{in}}$ ,  $\Gamma^{\text{out}}$ ) remain fixed, we have

$$\mathbf{d}^f = \mathbf{0} \quad \text{on } \Gamma^{\text{in}} \cup \Gamma^{\text{out}}. \quad (1.2.5)$$

Therefore equations (1.2.4) and (1.2.5) constrain the value of  $\mathbf{d}^f$  on the whole boundary  $\partial\Omega^f$ . Inside  $\Omega^f$ , however, the displacement  $\mathbf{d}^f$  (and hence the map  $\mathcal{A}$ ) is arbitrary: it can be any reasonable extension of  $\mathbf{d}|_\Sigma$  over  $\Omega^f$  (subjected to (1.2.5)). In the sequel we will denote this operation by

$$\mathbf{d}^f = \text{Ext}(\mathbf{d}|_\Sigma). \quad (1.2.6)$$

For instance, the operator Ext can be given in terms of an harmonic extension, by solving:

$$\begin{cases} -\Delta \mathbf{d}^f = \mathbf{0} & \text{in } \Omega^f, \\ \mathbf{d}^f = \mathbf{0} & \text{on } \Gamma^{\text{in}} \cup \Gamma^{\text{out}}, \\ \mathbf{d}^f = \mathbf{d} & \text{on } \Sigma. \end{cases} \quad (1.2.7)$$

In summary, the interface coupling conditions are given by:

$$\begin{cases} \mathbf{d}^f = \text{Ext}(\mathbf{d}|_\Sigma), & \widehat{\mathbf{w}} = \partial_t \mathbf{d}^f & \text{in } \Omega^f, \\ & \widehat{\mathbf{u}} = \partial_t \mathbf{d} & \text{on } \Sigma, \\ \boldsymbol{\Pi}(\mathbf{d})\mathbf{n}^s = -J\widehat{\boldsymbol{\sigma}}(\mathbf{u}, p)\mathbf{F}^{-\top}\mathbf{n} & & \text{on } \Sigma. \end{cases} \quad (1.2.8)$$

**Remark 1.3** *The main ingredients of the ALE (arbitrary Lagrangian-Eulerian) formalism can be inferred from (1.2.8). Indeed, the conditions (1.2.8)<sub>1,2</sub> impose that the interface points must follow the same displacement as the fluid, thus the Lagrangian terminology. In contrast, the motion of the remaining points is not necessarily related to the fluid kinematics, so the Eulerian terminology.*

**Remark 1.4** *For the purpose of the spectral analysis presented in §1.4.1 and §1.4.2 we will also consider the (simplified) case in which the structural displacement is given in terms of a finite number of vibration modes  $\phi_i : \Omega^s \rightarrow \mathbb{R}^d$ ,  $1 \leq i \leq n^s$ , in such a way that*

$$\mathbf{d}(\hat{\mathbf{x}}, t) = \sum_{i=1}^{n^s} s_i(t) \phi_i(\hat{\mathbf{x}}), \quad \forall (\hat{\mathbf{x}}, t) \in \Omega^s \times \mathbb{R}^+,$$

with  $\mathbf{s}(t) = \{s_i(t)\}_{1 \leq i \leq n^s} \in \mathbb{R}^{n^s}$ . Hence,  $\mathbf{d} = \Phi \mathbf{s}$ , where  $\Phi = [\phi_1 | \phi_2 | \dots | \phi_{n^s}] \in \mathbb{R}^{d \times n^s}$  stands for the reduced modal basis matrix. In this way, the structural behavior is described by the projected equation

$$\mathbf{M} \ddot{\mathbf{s}} + \mathbf{K} \mathbf{s} = \int_{\Sigma} J \Phi^T \hat{\boldsymbol{\sigma}}(\mathbf{u}, p) \mathbf{F}^{-T} \mathbf{n},$$

where  $\mathbf{M}$ ,  $\mathbf{K}$  are given (possibly nonlinear) mass and stiffness operators.

#### 1.2.1.4 Energy balance

In summary, our fluid-structure system is governed by the following coupled problem: find the fluid domain displacement  $\mathbf{d}^f : \Omega^f \times \mathbb{R}^+ \rightarrow \mathbb{R}^d$ , the fluid velocity  $\hat{\mathbf{u}} : \Omega^f \times \mathbb{R}^+ \rightarrow \mathbb{R}^d$ , the fluid pressure  $\hat{p} : \Omega^f \times \mathbb{R}^+ \rightarrow \mathbb{R}$  and the structure displacement  $\mathbf{d} : \Omega^s \times \mathbb{R}^+ \rightarrow \mathbb{R}^d$  such that

$$\left\{ \begin{array}{l} \rho^f \partial_t \mathbf{u}|_{\mathcal{A}} + \rho^f (\mathbf{u} - \mathbf{w}) \cdot \nabla \mathbf{u} - \operatorname{div} \boldsymbol{\sigma}(\mathbf{u}, p) = \mathbf{0} \quad \text{in } \Omega^f(t), \\ \operatorname{div} \mathbf{u} = 0 \quad \text{in } \Omega^f(t), \\ \mathbf{u} = \mathbf{u}_{\text{in}} \quad \text{on } \Gamma^{\text{in}}, \\ \boldsymbol{\sigma}(\mathbf{u}, p) \mathbf{n} = -p_{\text{out}} \mathbf{n} \quad \text{on } \Gamma^{\text{out}}, \\ \rho^s \partial_{tt} \mathbf{d} - \operatorname{div} (\boldsymbol{\Pi}(\mathbf{d})) = \mathbf{0} \quad \text{in } \Omega^s, \\ \mathbf{d} = \mathbf{0} \quad \text{on } \Gamma^{\text{d}}, \\ \boldsymbol{\Pi}(\mathbf{d}) \mathbf{n}^s = \mathbf{0} \quad \text{on } \Gamma^{\text{n}}, \\ \mathbf{d}^f = \operatorname{Ext}(\mathbf{d}|_{\Sigma}), \quad \hat{\mathbf{w}} = \partial_t \mathbf{d}^f \quad \text{in } \Omega^f, \\ \hat{\mathbf{u}} = \partial_t \mathbf{d} \quad \text{on } \Sigma, \\ \boldsymbol{\Pi}(\mathbf{d}) \mathbf{n}^s = -J \hat{\boldsymbol{\sigma}}(\mathbf{u}, p) \mathbf{F}^{-T} \mathbf{n} \quad \text{on } \Sigma, \end{array} \right. \quad (1.2.9)$$

and satisfying the initial conditions  $\mathbf{u}|_{t=0} = \mathbf{u}_0$ ,  $\mathbf{d}|_{t=0} = \mathbf{d}^0$  and  $\partial_t \mathbf{d}|_{t=0} = \dot{\mathbf{d}}^0$ .

The next result (see, e.g., [Mou96] and [33] for a proof) shows that the coupled system (1.2.9) ensures a correct balance of the mechanical energy. As expected, dissipation only comes from the fluid viscous effects and the power exchanged by the fluid and the structure exactly balance at the interface. This balance is a direct consequence of the coupling conditions (1.2.8).

**Lemma 1.1** *Assume that the structure is hyper-elastic (with energy density function  $W$ ) and that*

the coupled fluid-structure system is isolated, i.e.,  $\mathbf{u} = \mathbf{0}$  on  $\Gamma^{\text{in}} \cup \Gamma^{\text{out}}$ . Let

$$E(t) \stackrel{\text{def}}{=} \underbrace{\int_{\Omega^f(t)} \frac{\rho^f}{2} |\mathbf{u}|^2 + \int_{\Omega^s} \frac{\rho^s}{2} |\dot{\mathbf{d}}|^2}_{\text{Kinetic energy}} + \underbrace{\int_{\Omega^s} W(\mathbf{E}^s(\mathbf{d}))}_{\text{Elastic potential energy}}$$

be the total mechanical energy of the fluid-structure system described by (1.2.9). Then, the following energy identity holds:

$$E(t) = E(0) - \underbrace{\int_0^t \int_{\Omega^f(t)} 2\mu |\boldsymbol{\epsilon}(\mathbf{u})|^2}_{\text{Viscous work}}.$$

### 1.2.2 Coupling via transpiration: fixed domain approach

The ALE formalism is particularly well adapted to the description of fluid flows with moving boundaries (from small to relatively large displacements, without topological changes) and owes its success to its inherent accurate description of interfaces. In the 90's (and late 80's), it was questioned whether the ALE formalism was strictly necessary within a small displacement framework (e.g., vibration or linear stability analysis). Note that, in practice, the ALE formalism requires updating the fluid mesh and its corresponding *grid velocity*  $\hat{\mathbf{w}}$  at each time level (see Chapter 2), and thus the flow solvers must be adapted accordingly.

In order to circumvent the ALE formalism, aeronautical engineers developed transpiration techniques (from an idea of Lighthill [Lig58, MGS95]) that bypass the use of moving grids via a modification of the interface conditions (see, e.g., [HC89, RH93, Deb96, Mor97, Ren98, MMS98, Med99, Fan01]). These formulations consider the fluid-structure interface as a (fixed) permeable surface, across which the fluid flows with a velocity (the so called *transpiration velocity*) given in terms of the interface velocity and displacement.

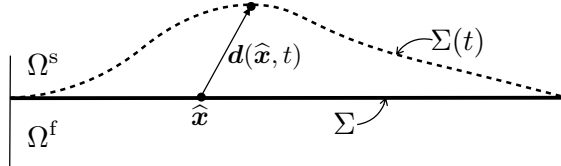


Figure 1.2: The fluid flows across the reference interface  $\Sigma$ .

The transpiration interface condition is typically derived, in an heuristic way, by performing a first order Taylor expansion of the fluid velocity around the reference fluid-structure interface  $\Sigma$ :

$$\hat{\mathbf{u}}(\hat{\mathbf{x}}, t) \stackrel{\text{def}}{=} \mathbf{u}(\hat{\mathbf{x}} + \mathbf{d}^f(\hat{\mathbf{x}}, t), t) \approx \mathbf{u}(\hat{\mathbf{x}}, t) + \mathbf{d}^f(\hat{\mathbf{x}}, t) \cdot \nabla \mathbf{u}(\hat{\mathbf{x}}, t) \quad \forall \hat{\mathbf{x}} \in \Sigma, \quad (1.2.10)$$

see Figure 1.2. Yet, from (1.2.8), we have  $\mathbf{d}^f = \mathbf{d}$  and  $\hat{\mathbf{u}} = \partial_t \mathbf{d}$  on  $\Sigma$ , so that (1.2.10) motivates the transpiration condition

$$\mathbf{u} = \partial_t \mathbf{d} - \mathbf{d} \cdot \nabla \mathbf{u} \quad \text{on } \Sigma. \quad (1.2.11)$$

By identifying  $\Omega^f(t)$  with  $\Omega^f$  condition (1.2.11) is finally applied to the fluid equations (1.2.1) written in the reference configuration  $\Omega^f$ . Hence, (1.2.6) is no longer needed.

The first order correction  $\mathbf{d} \cdot \nabla \mathbf{u}$  is often neglected in the applications (see, *e.g.*, [Deb96, Fan01, Med99]). In [HC89, Ren98], the implicit relation (1.2.11) is replaced by the (explicit) wall law

$$\mathbf{u} = \partial_t \mathbf{d} - \mathbf{d} \cdot \nabla \mathbf{u}_0 \quad \text{on } \Sigma, \quad (1.2.12)$$

where  $\mathbf{u}_0$  is the velocity field of a permanent flow without interface motion. Though heuristic, this simplification incorporates the superposition of the interface vibrations and a permanent flow, which are fundamental ingredients of the coupling.

Like for the velocity, the fluid stress at the interface must be expanded also around the fixed interface (see [Ren98]), yielding

$$\widehat{\boldsymbol{\sigma}}(\mathbf{u}, p) \approx \boldsymbol{\sigma}(\mathbf{u}, p) + \mathbf{d}^f \cdot \nabla \boldsymbol{\sigma}(\mathbf{u}, p) \quad \text{on } \Sigma. \quad (1.2.13)$$

On the other hand, a first order expansion of the Piola surface terms yields  $J\mathbf{F}^{-T} \mathbf{n} \approx \mathbf{n} + \boldsymbol{\eta}(\mathbf{d}^f)$ , where the first order surface normal rotation

$$\boldsymbol{\eta}(\mathbf{d}^f) \stackrel{\text{def}}{=} (\nabla \mathbf{d}^f)^T \mathbf{n} - (\text{div } \mathbf{d}^f) \mathbf{n}, \quad (1.2.14)$$

depends only on the trace  $\mathbf{d}^f|_\Sigma$  (see [Ren98]), so that  $\boldsymbol{\eta}(\mathbf{d}^f) = \boldsymbol{\eta}(\mathbf{d})$ . Thus, the kinetic coupling condition (1.2.8)<sub>3</sub> is replaced by

$$\boldsymbol{\Pi}(\mathbf{d}) \mathbf{n}^s = -\boldsymbol{\sigma}(\mathbf{u}, p) \mathbf{n} - \mathbf{d} \cdot \nabla \boldsymbol{\sigma}(\mathbf{u}, p) \mathbf{n} + \boldsymbol{\sigma}(\mathbf{u}, p) \boldsymbol{\eta}(\mathbf{d}) \quad \text{on } \Sigma. \quad (1.2.15)$$

As in (1.2.11), the first order term  $\mathbf{d} \cdot \nabla \boldsymbol{\sigma}(\mathbf{u}, p) \mathbf{n}$  in is often neglected in the applications [Fan01, Med99, FVCJ<sup>+</sup>06].

**Remark 1.5** *Note that the Taylor expansions (1.2.10) and (1.2.13) have only a sense in the particular case in which the fluid flow crosses the interface  $\Sigma$ , in other words, when the Eulerian fields  $(\mathbf{u}, p)$  are defined on  $\Sigma$  (see Figure 1.2). Moreover, in order to recover a fluid subproblem written in a fixed configuration, the transpiration framework requires the heuristic identification of  $\Omega^f(t)$  with  $\Omega^f$ , by neglecting the fluid domain displacement in (1.2.1).*

Although a number of studies (see, *e.g.*, [HC89, Deb96, Ren98, Med99, Fan01]) show that transpiration techniques give satisfactory results in the simulation of fluid-structure problems at moderate deformations, their heuristic foundation was subjected to debate (see Remark 1.5). These techniques are derived and mathematically justified in §1.3.1.

### 1.3 Linearization-transpiration framework

The transpiration framework can be mathematically derived through an appropriate asymptotic expansion, which reduces (1.2.9) to a linear coupled problem involving a fixed fluid domain with transpiration conditions. These results are summarized in the next subsection. We have also shown that the sensitivity of the coupled fluid-structure state, with respect to a given control parameter, can be determined via a generalization of the developed linearization-transpiration techniques. This is the topic of §1.3.2.

### 1.3.1 From ALE to transpiration ([10], [13], [40], [47, Chap. 2, 4])

Let  $(\mathbf{u}_0, p_0, \mathbf{d}_0^f = \mathbf{0}, \mathbf{d}_0 = \mathbf{0})$  be a steady equilibrium state of the fluid-structure system (1.2.9), given as the solution of:

$$\left\{ \begin{array}{ll} \rho^f \mathbf{u}_0 \cdot \nabla \mathbf{u}_0 - \operatorname{div} \boldsymbol{\sigma}(\mathbf{u}_0, p_0) = \mathbf{0} & \text{in } \Omega^f, \\ \operatorname{div} \mathbf{u}_0 = 0 & \text{in } \Omega^f, \\ \mathbf{u}_0 = \mathbf{u}_{\text{in}} & \text{on } \Gamma^{\text{in}}, \\ \boldsymbol{\sigma}(\mathbf{u}_0, p_0) \mathbf{n} = -p_{\text{out}} \mathbf{n} & \text{on } \Gamma^{\text{out}}, \\ \mathbf{u}_0 = \mathbf{0} & \text{on } \Sigma, \\ -\operatorname{div} \boldsymbol{\sigma}_0^s = \mathbf{0} & \text{in } \Omega^s, \\ \boldsymbol{\sigma}_0^s \mathbf{n}^s = \mathbf{0} & \text{on } \Gamma^n, \\ \boldsymbol{\sigma}_0^s \mathbf{n}^s = -\boldsymbol{\sigma}(\mathbf{u}_0, p_0) \mathbf{n} & \text{on } \Sigma, \end{array} \right. \quad (1.3.16)$$

where  $\boldsymbol{\sigma}_0^s$  stands for the structural residual stress which equilibrates the stress of the reference flow  $(\mathbf{u}_0, p_0)$  on the interface (*i.e.*, we assume that the reference configuration is at equilibrium). We now submit this steady state to a small perturbation  $(\delta \mathbf{u}^0, \delta \mathbf{d}^0, \delta \dot{\mathbf{d}}^0)$  which generates the perturbed coupled unsteady state  $(\hat{\mathbf{u}}, \hat{p}, \mathbf{d}^f, \mathbf{d})$  solving (1.2.9) with initial condition

$$(\mathbf{u}^0, \mathbf{d}^0, \dot{\mathbf{d}}^0) = (\mathbf{u}_0 + \delta \mathbf{u}^0, \delta \mathbf{d}^0, \delta \dot{\mathbf{d}}^0).$$

From (1.2.9), we can obtain a non-linear coupled problem governing the fluctuations

$$(\delta \mathbf{u}, \delta p, \delta \mathbf{d}^f, \delta \mathbf{d}) \stackrel{\text{def}}{=} (\hat{\mathbf{u}}, \hat{p}, \mathbf{d}^f, \mathbf{d}) - (\mathbf{u}_0, p_0, \mathbf{0}, \mathbf{0}). \quad (1.3.17)$$

Assuming that these generated fluctuations remain small for any time  $t > 0$ , we can neglect the higher order terms. Thus, we obtain a linearized problem driving, at first order, the fluctuations of the coupled system. Note that the complexity of the linearized problem strongly depends on the fluctuation definition. It is straightforward to verify (see [HC93, LF98, CH00, LSHF01] for instance) that taking (1.3.17) as the fluctuation definition, leads to a linearized problem where the fluid equations still depend on the fluid domain motion  $\delta \mathbf{d}^f$ . Hence, in this sense, its complexity is similar to the perturbed problem (1.2.9).

**Remark 1.6** *The fluctuation  $(\delta \mathbf{u}, \delta p, \delta \mathbf{d}^f, \delta \mathbf{d})$  provides the sensitivity of the coupled system, around the reference steady state, with respect to the perturbations  $(\delta \mathbf{u}^0, \delta \mathbf{d}^0, \delta \dot{\mathbf{d}}^0)$  in the initial data.*

Instead of (1.3.17), we introduced the following definition of the fluctuations:  $\delta \mathbf{d} \stackrel{\text{def}}{=} \mathbf{d}$ ,  $\delta \mathbf{d}^f \stackrel{\text{def}}{=} \mathbf{d}^f$  and

$$\begin{aligned} \delta \mathbf{u} &\stackrel{\text{def}}{=} \hat{\mathbf{u}} - (\mathbf{u}_0 + \delta \mathbf{d}^f \cdot \nabla \mathbf{u}_0) & \text{in } \Omega^f, \\ \delta p &\stackrel{\text{def}}{=} \hat{p} - (p_0 + \delta \mathbf{d}^f \cdot \nabla p_0) & \text{in } \Omega^f. \end{aligned} \quad (1.3.18)$$

Compared to (1.3.17) (as used in [LF98, LSHF01, HC93, CH00]), the new definition (1.3.18) takes into account the transport of the reference state  $(\mathbf{u}_0, p_0)$  at the new spatial point  $\hat{\mathbf{x}} + \delta \mathbf{d}^f(\hat{\mathbf{x}}, t)$ , due to the fluid domain motion. In other words, formally, we have

$$\delta \mathbf{u}(\hat{\mathbf{x}}, t) = \mathbf{u}(\hat{\mathbf{x}} + \delta \mathbf{d}^f(\hat{\mathbf{x}}, t), t) - \mathbf{u}_0(\hat{\mathbf{x}} + \delta \mathbf{d}^f(\hat{\mathbf{x}}, t))$$

and similarly for the pressure.

By inserting the fluctuations definition (1.3.18) into (1.2.9), and by neglecting the higher order terms, we have shown that  $(\delta \mathbf{u}, \delta p, \delta \mathbf{d})$  are governed (at first order) by the following linear coupled system:

$$\left\{ \begin{array}{l} \rho^f \partial_t \delta \mathbf{u} + \rho^f (\delta \mathbf{u} \cdot \nabla \mathbf{u}_0 + \mathbf{u}_0 \cdot \nabla \delta \mathbf{u}) - \mathbf{div} \boldsymbol{\sigma}(\delta \mathbf{u}, \delta p) = \mathbf{0} \quad \text{in } \Omega^f, \\ \mathbf{div} \delta \mathbf{u} = 0 \quad \text{in } \Omega^f, \\ \delta \mathbf{u} = \mathbf{0} \quad \text{on } \Gamma^{\text{in}}, \\ \boldsymbol{\sigma}(\delta \mathbf{u}, \delta p) \mathbf{n} = \mathbf{0} \quad \text{on } \Gamma^{\text{out}}, \\ \rho^s \partial_{tt} \delta \mathbf{d} - \mathbf{div} (\delta \mathbf{\Pi}(\delta \mathbf{d})) = \mathbf{0} \quad \text{in } \Omega^s, \\ \delta \mathbf{d} = \mathbf{0} \quad \text{on } \Gamma^{\text{d}}, \\ \delta \mathbf{\Pi}(\delta \mathbf{d}) \mathbf{n}^s = \mathbf{0} \quad \text{on } \Gamma^{\text{n}}, \\ \delta \mathbf{u} = \partial_t \delta \mathbf{d} - \delta \mathbf{d} \cdot \nabla \mathbf{u}_0 \quad \text{on } \Sigma, \\ \delta \mathbf{\Pi}(\delta \mathbf{d}) \mathbf{n}^s = -\boldsymbol{\sigma}(\delta \mathbf{u}, \delta p) \mathbf{n} - \delta \mathbf{d} \cdot \nabla \boldsymbol{\sigma}(\mathbf{u}_0, p_0) \mathbf{n} + \boldsymbol{\sigma}(\mathbf{u}_0, p_0) \boldsymbol{\eta}(\delta \mathbf{d}) \quad \text{on } \Sigma, \end{array} \right. \quad (1.3.19)$$

where  $\delta \mathbf{\Pi}(\delta \mathbf{d})$  represents the solid linearized stress tensor and  $\boldsymbol{\eta}(\delta \mathbf{d})$  is defined in (1.2.14).

Some observations are in order.

- The system (1.3.19) is written in the fixed reference configuration and the fluid equations are fully independent of the fluid domain displacement  $\delta \mathbf{d}^f$ . Hence, the fluid and solid fluctuations  $(\delta \mathbf{u}, \delta p, \delta \mathbf{d})$  can be computed irrespectively of  $\delta \mathbf{d}^f = \text{Ext}(\delta \mathbf{d}|_{\Sigma})$ , while keeping a fixed fluid domain. This is achieved by using non-standard coupling conditions on the fixed reference interface  $\Sigma$ .
- The kinematic continuity of the velocity is replaced by the transpiration condition

$$\delta \mathbf{u} = \partial_t \delta \mathbf{d} - \delta \mathbf{d} \cdot \nabla \mathbf{u}_0 \quad \text{on } \Sigma,$$

which is exactly (1.2.12). On the other hand, the kinetic continuity of stress becomes

$$\delta \mathbf{\Pi}(\delta \mathbf{d}) \mathbf{n}^s = -\boldsymbol{\sigma}(\delta \mathbf{u}, \delta p) \mathbf{n} - \delta \mathbf{d} \cdot \nabla \boldsymbol{\sigma}(\mathbf{u}_0, p_0) \mathbf{n} + \boldsymbol{\sigma}(\mathbf{u}_0, p_0) \boldsymbol{\eta}(\delta \mathbf{d}) \quad \text{on } \Sigma,$$

which contains two additional correction terms, as in (1.2.15).

- The proposed linearization procedure bypasses the heuristic arguments of §1.2.2 (see Remark 1.5) and, therefore, provides a mathematical justification of the transpiration based coupling.

The main ingredients in the derivation of the linear coupled problem (1.3.19) are the fluctuations definition (1.3.18) and the next result (see [10] and [47, Chapter 2] for a proof), which shows that the linear terms (from (1.3.18)) with volume dependencies on  $\delta \mathbf{d}^f$  vanish.

**Lemma 1.2** *Let us consider the flux notation*

$$\phi(\mathbf{u}, \boldsymbol{\sigma}) \stackrel{\text{def}}{=} \mathbf{I}_1(\rho^f \mathbf{u} \otimes \mathbf{u} - \boldsymbol{\sigma}) + \mathbf{I}_2 \otimes \mathbf{u}, \quad \mathbf{I}_1 \stackrel{\text{def}}{=} \begin{pmatrix} 1 & 0 & 0 \\ 0 & 1 & 0 \\ 0 & 0 & 1 \\ 0 & 0 & 0 \end{pmatrix}, \quad \mathbf{I}_2 \stackrel{\text{def}}{=} \begin{pmatrix} 0 \\ 0 \\ 0 \\ 1 \end{pmatrix}$$

and let  $(\mathbf{u}_0, \boldsymbol{\sigma}(\mathbf{u}_0, p_0)) \in \mathbf{C}^1(\overline{\Omega^f}) \times \mathbf{C}^1(\overline{\Omega^f})$  be a smooth solution of (1.3.16), that is,

$$\mathbf{div} \phi(\mathbf{u}_0, \boldsymbol{\sigma}(\mathbf{u}_0, p_0)) = \mathbf{0} \quad \text{in } \Omega^f.$$

Then, for each smooth displacement  $\delta \mathbf{d}^f \in C^1(\overline{\Omega^f})$  we have the first order perturbed equation

$$\operatorname{div} \left\{ \phi(\mathbf{u}_0, \boldsymbol{\sigma}(\mathbf{u}_0, p_0)) [(\operatorname{div} \delta \mathbf{d}^f) \mathbf{I} - (\nabla \delta \mathbf{d}^f)^\top] + \delta \mathbf{d}^f \cdot \nabla \phi(\mathbf{u}_0, \boldsymbol{\sigma}(\mathbf{u}_0, p_0)) \right\} = \mathbf{0} \quad \text{in } \Omega^f.$$

**Remark 1.7** *The above discussion has some connexions with the notions of Eulerian and material derivatives in PDE-constrained shape optimization (see, e.g., [SZ92, All07]). The fluid fluctuations  $(\delta \mathbf{u}, \delta p)$  given by (1.3.18) are related to the notion of Eulerian shape derivative of  $(\mathbf{u}_0, p_0)$  with respect to perturbations of the fluid domain, which is known to depend only on boundary perturbations (see [All07, §6.3.4]). On the contrary, the fluid fluctuations defined by (1.3.17) depend on the perturbation inside the domain and, therefore, are associated to a material derivative.*

The above presented linearization-transpiration techniques can be extended to the case of the linearization around an unsteady reference coupled state. This is the topic of the next subsection.

### 1.3.2 Sensitivity analysis ([16], [24], [41], [47, Chap. 3])

Instead of analyzing the fluctuations around a steady equilibrium, as considered above, we can face the stability of a fluid-structure system from a different point of view. That is, in terms of an inverse problem (see [Mou02, MZ06]), the control variable being the (possibly unsteady) inflow velocity  $\mathbf{u}_{\text{in}}$  in (1.2.9). For instance, we can think of the problem of recovering the smallest (critical) inflow velocities for which the induced structural vibrations reach a given critical level (that could damage the structure).

In order to characterize the sensitivity of the corresponding objective functional, with respect to the control variable  $\mathbf{u}_{\text{in}}$ , it is obvious that we need to characterize the sensitivity of the coupled fluid-structure state  $(\mathbf{u}, p, \mathbf{d}^f, \mathbf{d})$ , defined by (1.2.9), with respect to  $\mathbf{u}_{\text{in}}$ . The aim of the work summarized below was to show that this sensitivity can be derived through a generalization of the linearization-transpiration techniques described in §1.3.1. In other words, the linearization can be performed around an unsteady equilibrium state.

In order to ease the notation, we set  $\mathbf{g} \stackrel{\text{def}}{=} \mathbf{u}_{\text{in}}$ , the inflow velocity enforced on  $\Gamma^{\text{in}}$ . Let

$$\mathbf{d}^f : \Omega^f \times \mathbb{R}^+ \rightarrow \mathbb{R}^d, \quad \hat{\mathbf{u}} : \Omega^f \times \mathbb{R}^+ \rightarrow \mathbb{R}^d, \quad \hat{p} : \Omega^f \times \mathbb{R}^+ \rightarrow \mathbb{R}, \quad \mathbf{d} : \Omega^s \times \mathbb{R}^+ \rightarrow \mathbb{R}^d,$$

be a smooth state satisfying the coupled system (1.2.9) associated to the inlet boundary datum  $\mathbf{g} : \Gamma^{\text{in}} \times \mathbb{R}^+ \rightarrow \mathbb{R}^d$ . We showed that the state derivative with respect to  $\mathbf{g}$  in the perturbation direction  $\delta \mathbf{g} : \Gamma^{\text{in}} \times \mathbb{R}^+ \rightarrow \mathbb{R}^d$  can be computed as follows:

$$\begin{aligned} D_{\mathbf{g}} \mathbf{u} \delta \mathbf{g} &= \delta \mathbf{u} + \delta \mathbf{d}^f \cdot \nabla \mathbf{u} \quad \text{in } \Omega^f(t), \\ D_{\mathbf{g}} p \delta \mathbf{g} &= \delta p + \delta \mathbf{d}^f \cdot \nabla p \quad \text{in } \Omega^f(t), \\ D_{\mathbf{g}} \mathbf{d} \delta \mathbf{g} &= \delta \hat{\mathbf{d}} \quad \text{in } \Omega^s, \end{aligned} \tag{1.3.20}$$

where  $\delta \hat{\mathbf{d}} \stackrel{\text{def}}{=} D_{\mathbf{d}} \operatorname{Ext}(\mathbf{d}|_{\Sigma}) \delta \hat{\mathbf{d}}|_{\Sigma}$  and

$$\delta \hat{\mathbf{u}} : \Omega^f \times \mathbb{R}^+ \rightarrow \mathbb{R}^d, \quad \delta \hat{p} : \Omega^f \times \mathbb{R}^+ \rightarrow \mathbb{R}, \quad \delta \hat{\mathbf{d}} : \Omega^s \times \mathbb{R}^+ \rightarrow \mathbb{R}^d,$$

satisfy the following linear coupled system:

$$\left\{ \begin{array}{ll} \rho^f \partial_t \delta \mathbf{u}|_{\mathcal{A}} + \rho^f (\delta \mathbf{u} \cdot \nabla \mathbf{u} + (\mathbf{u} - \mathbf{w}) \cdot \nabla \delta \mathbf{u}) - \operatorname{div} \boldsymbol{\sigma}(\delta \mathbf{u}, \delta p) = \mathbf{0} & \text{in } \Omega^f(t), \\ \operatorname{div} \delta \mathbf{u} = 0 & \text{in } \Omega^f(t), \\ \delta \mathbf{u} = \delta \mathbf{g} & \text{on } \Gamma^{\text{in}}, \\ \boldsymbol{\sigma}(\delta \mathbf{u}, \delta p) \mathbf{n} = \mathbf{0} & \text{on } \Gamma^{\text{out}}, \end{array} \right. \quad (1.3.21)$$

$$\left\{ \begin{array}{ll} \rho^s \partial_{tt} \delta \hat{\mathbf{d}} - \operatorname{div} (\mathbf{F}^s \delta \Pi(\delta \hat{\mathbf{d}}) + (\nabla \delta \hat{\mathbf{d}}) \Pi(\mathbf{d})) = \mathbf{0} & \text{in } \Omega^s, \\ \delta \mathbf{d} = \mathbf{0} & \text{on } \Gamma^{\text{d}}, \\ (\mathbf{F}^s \delta \Pi(\delta \hat{\mathbf{d}}) + (\nabla \delta \hat{\mathbf{d}}) \Pi(\mathbf{d})) \mathbf{n}^s = \mathbf{0} & \text{on } \Gamma^{\text{n}}, \end{array} \right. \quad (1.3.22)$$

with the interface coupling conditions

$$\delta \mathbf{u} = \partial_t \delta \mathbf{d} - \delta \mathbf{d} \cdot \nabla \mathbf{u} \quad \text{on } \Sigma(t), \quad (1.3.23)$$

$$\begin{aligned} (\mathbf{F}^s \delta \Pi(\delta \hat{\mathbf{d}}) + (\nabla \delta \hat{\mathbf{d}}) \Pi(\mathbf{d})) \mathbf{n}^s &= -J(\hat{\boldsymbol{\sigma}}(\delta \mathbf{u}, \delta p) + \delta \hat{\mathbf{d}} \cdot \hat{\nabla} \boldsymbol{\sigma}(\mathbf{u}, p)) \mathbf{F}^{-\text{T}} \mathbf{n} \\ &+ J|\mathbf{F}^{-\text{T}} \mathbf{n}| \hat{\boldsymbol{\sigma}}(\mathbf{u}, p) \hat{\boldsymbol{\eta}}(\delta \mathbf{d}) \end{aligned} \quad \text{on } \Sigma, \quad (1.3.24)$$

the initial condition  $(\delta \hat{\mathbf{u}}, \delta \hat{\mathbf{d}}, \partial_t \delta \hat{\mathbf{d}})|_{t=0} = \mathbf{0}$  in  $\Omega^f \times \Omega^s \times \Omega^s$  and the notations

$$\begin{aligned} \boldsymbol{\eta}(\delta \mathbf{d}) &\stackrel{\text{def}}{=} (\nabla \delta \mathbf{d})^{\text{T}} \mathbf{n} - \operatorname{div}(\delta \mathbf{d}) \mathbf{n} \quad \text{on } \Sigma(t), \\ \delta \Pi(\delta \hat{\mathbf{d}}) &\stackrel{\text{def}}{=} D_{\mathbf{d}} \Pi(\mathbf{d}) \delta \hat{\mathbf{d}} \quad \text{in } \Omega^s. \end{aligned}$$

The derivation of the above results is a generalization of the ideas presented in §1.3.1 to the case of a linearization around the unsteady coupled stated  $(\mathbf{u}, p, \mathbf{d}^f, \mathbf{d})$  (see [16] for the details). Note that, although the fluid state derivatives in (1.3.20) depend on the fluid domain fluctuation  $\delta \hat{\mathbf{d}}^f$ , the (intrinsic) fluctuations  $(\delta \hat{\mathbf{u}}, \delta \hat{p}, \delta \hat{\mathbf{d}})$  can be computed, from (1.3.21)-(1.3.24), irrespectively of  $\delta \hat{\mathbf{d}}^f$  (as in §1.3.1). The coupling between the fluid  $(\delta \hat{\mathbf{u}}, \delta \hat{p})$  and solid  $\delta \hat{\mathbf{d}}$  fluctuations is enforced via transpiration conditions in the fluid (as in §1.3.1). However, in contrast to §1.3.1, here the fluid fluctuations  $(\delta \hat{\mathbf{u}}, \delta \hat{p})$  are computed in the moving (known) configuration  $\Omega^f(t)$ . This is a major difference with respect the linearized problem (1.3.19) which is written in the fixed fluid domain  $\Omega^f$ . Needless to say that, if we take  $\mathbf{d} = 0$  and  $(\mathbf{u}, p)$  steady in (1.3.21)-(1.3.24), we recover the linear transpiration-based coupled problem (1.3.19).

**Remark 1.8** *The adjoint counterpart of the above sensitivity analysis has been conducted in [MZ06, Chapter 8].*

## 1.4 Linear stability analysis

When a fluid-structure equilibrium is subjected to an initial small disturbance, the generated oscillations either decay or diverge, depending on whether the flow energy transmitted to the structure is less than or surpasses the energy dissipated by the damping of the system. If the fluid is at rest, any oscillation caused by the disturbance will be damped (for instance, by the viscosity of the fluid). When the velocity of the flow is augmented gradually the damping of the oscillations increases. However, with further increase in the flow velocity, a point is reached above which the system is no longer subject to damping. The oscillation just maintains its amplitude at the point where the damping vanishes. Above this point, any small disturbance generates oscillations of

large amplitude (that can damage the structure). This is a *flutter* instability and the point where the damping reduces to zero is called *flutter boundary*.

Flutter instabilities can take place in a number of civil engineering processes (see, *e.g.*, [CPTV94, CCC<sup>+</sup>04]): heat exchanger tubes in axial flow, flexible pipes with internal flow, wind effects on long span bridges, aircraft wings, and so forth. The analysis of flutter instabilities is a major concern in the design of civil engineering systems involving a fluid-structure coupling. Hence, a great number of experimental [ST71, WOOF78, WOOF80, SS96, Pai98] and numerical [HC93, Mor97, Ren98, CH00, PB01, LSHF01] works have been carried out on this subject. We refer to [BS91], for a presentation of one of the most-famous bridge flutter problems: the Tacoma Narrows bridge failure on November 7, 1940.

The aim of the work summarized in this section was to address the flutter problem of a coupled fluid-structure system involving an incompressible Newtonian fluid and an elastic structure, using a linear stability analysis framework. We must notice that the use of a linear model for flutter analysis was already addressed in the literature (see, *e.g.*, [HC93, CH00, LSHF01]). However, the originality of our approach lies in the linearization-transpiration formulation, described in §1.3.1, which provides a coupled eigenproblem of minimal complexity, involving transpiration interface conditions. The price to pay numerically is the accurate calculation of an equilibrium reference solution, which must be done once for all and on a rather fine mesh. The resulting unsteady or spectral problem is then simpler and, as shown by the mathematical analysis in §1.4.1, has a rather nice mathematical structure. A brief description of the numerical algorithm used for the approximation of the leftmost eigenvalues (critical dampings) and some numerical illustrations are given in §1.4.2.

### 1.4.1 Spectral analysis ([13], [23], [47, Chap. 5])

We consider the linear stability analysis of the steady reference state defined by (1.3.16). From the linear coupled problem (1.3.19) governing the fluctuations (at first order), the linear stability theory (see, *e.g.*, [Geo85]) assumes that each linear fluctuation  $(\delta \mathbf{u}, \delta p, \delta \mathbf{d})$  can be obtained by superposition of fluctuations of the type  $(\mathbf{u}(\hat{\mathbf{x}}), p(\hat{\mathbf{x}}), \mathbf{d}(\hat{\mathbf{x}}))e^{-\lambda t}$ , termed *normal modes*. By substituting this last expression in the linearized equations (1.3.19), we obtain that  $(\lambda; \mathbf{u}, p, \mathbf{d})$  is an eigenpair of the following spectral problem:

$$\left\{ \begin{array}{ll} \rho^f (\mathbf{u} \cdot \nabla \mathbf{u}_0 + \mathbf{u}_0 \cdot \nabla \mathbf{u}) - \operatorname{div} \boldsymbol{\sigma}(\mathbf{u}, p) = \lambda \rho^f \mathbf{u} & \text{in } \Omega^f, \\ \operatorname{div} \mathbf{u} = 0 & \text{in } \Omega^f, \\ \mathbf{u} = \mathbf{0} & \text{on } \Gamma^{\text{in}}, \\ \boldsymbol{\sigma}(\mathbf{u}, p) \mathbf{n} = \mathbf{0} & \text{on } \Gamma^{\text{out}}, \\ \rho^s \lambda^2 \mathbf{d} - \operatorname{div} (\delta \boldsymbol{\Pi}(\mathbf{d})) = \mathbf{0} & \text{in } \Omega^s, \\ \mathbf{d} = \mathbf{0} & \text{on } \Gamma^{\text{d}}, \\ \delta \boldsymbol{\Pi}(\mathbf{d}) \mathbf{n}^s = \mathbf{0} & \text{on } \Gamma^{\text{n}}, \\ \mathbf{u} = -\lambda \mathbf{d} - \mathbf{d} \cdot \nabla \mathbf{u}_0 & \text{on } \Sigma, \\ \delta \boldsymbol{\Pi}(\mathbf{d}) \mathbf{n}^s = -\boldsymbol{\sigma}(\mathbf{u}, p) \mathbf{n} - \mathbf{d} \cdot \nabla \boldsymbol{\sigma}(\mathbf{u}_0, p_0) \mathbf{n} + \boldsymbol{\sigma}(\mathbf{u}_0, p_0) \boldsymbol{\eta}(\mathbf{d}) & \text{on } \Sigma. \end{array} \right. \quad (1.4.25)$$

In linear stability theory, the permanent state defined by (1.3.16) is said linearly asymptotically stable, if all the eigenvalues of the spectral problem (1.4.25) have positive real parts. On the contrary, if there exists, at least, one eigenvalue with negative real part, the system is said asymptotically unstable.

In what follows, we assume that an homogenous Dirichlet boundary condition is imposed on whole external boundary  $\Gamma$  of  $\Omega^f$  (see Figure 1.3). That is, we take  $\Gamma^{\text{out}} = \emptyset$  in (1.4.25). In such

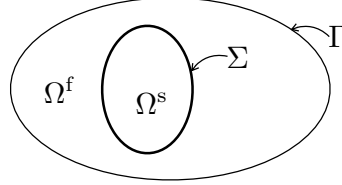


Figure 1.3: The computational domain,  $\Omega$ , defined by the system in its equilibrium configuration.

situations, the fluid pressure is defined up to a constant, which we fix by assuming  $p$  to be of zero average. We also assume a reduced behavior of the structure (see Remark 1.4) characterized by the mass and the stiffness matrices,  $\mathbf{M}$  and  $\mathbf{K}$  respectively, the mass matrix being supposed to be symmetric and positive definite. Moreover, the  $n^s$  modal shapes,  $\phi_i : \Omega^s \rightarrow \mathbb{R}^3$ , are assumed to be volume preserving, that is

$$\int_{\Sigma} \phi_i \cdot \mathbf{n} = 0 \quad (1.4.26)$$

for  $i = 1, \dots, n^s$ .

In this framework, the coupled spectral problem (1.4.25) reads: find  $\lambda \in \mathbb{C}$ ,  $\mathbf{u} : \Omega^f \rightarrow \mathbb{C}^d$ ,  $p : \Omega^f \rightarrow \mathbb{C}$  and  $\mathbf{s} \in \mathbb{C}^{n^s}$ , with  $\int_{\Omega^f} p = 0$  and  $(\mathbf{u}, p, \mathbf{s}) \neq \mathbf{0}$ , such that

$$\left\{ \begin{array}{l} \rho^f (\mathbf{u} \cdot \nabla \mathbf{u}_0 + \mathbf{u}_0 \cdot \nabla \mathbf{u}) - 2\mu \operatorname{div} \epsilon(\mathbf{u}) + \nabla p = \rho^f \lambda \mathbf{u} \quad \text{in } \Omega^f, \\ \operatorname{div} \mathbf{u} = 0 \quad \text{in } \Omega^f, \\ \mathbf{u} = \mathbf{0} \quad \text{on } \Gamma, \\ \mathbf{u} = -\lambda \Phi \mathbf{s} - (\Phi \mathbf{s}) \cdot \nabla \mathbf{u}_0 \quad \text{on } \Sigma, \\ \lambda^2 \mathbf{M} \mathbf{s} + (\mathbf{K} + \mathbf{B}_0) \mathbf{s} = - \int_{\Sigma} \Phi^T \boldsymbol{\sigma}(\mathbf{u}, p) \mathbf{n}, \end{array} \right. \quad (1.4.27)$$

where the *added stiffness*  $\mathbf{B}^0 \in \mathbb{R}^{n^s \times n^s}$ , is related to the sensitivity of the frozen interface stress vector to unit translation and rotation,

$$(\mathbf{B}_0)_{ij} = \int_{\Sigma} (\phi_j \cdot \nabla \boldsymbol{\sigma}(\mathbf{u}_0, p_0) \mathbf{n} - \boldsymbol{\sigma}(\mathbf{u}_0, p_0) \boldsymbol{\eta}(\phi_j)) \cdot \phi_i$$

for  $1 \leq i, j \leq n^s$ . We also assume that the reference flow  $(\mathbf{u}_0, p_0)$  is smooth enough, *e.g.*,  $\mathbf{u}_0 \in \mathcal{C}^2(\overline{\Omega^f})$  and  $p_0 \in C^1(\overline{\Omega^f})$ .

**Remark 1.9** Note that the volume preserving condition (1.4.26) is maintained after linear transport by the velocity field  $\mathbf{u}_0$  (see [13, Lemma 11]), that is,

$$\int_{\Sigma} \phi_i \cdot \nabla \mathbf{u}_0 \cdot \mathbf{n} = 0$$

for  $i = 1, \dots, n^s$ . Therefore, the transpiration condition in (1.4.27) is compatible with the divergence free constraint on  $\mathbf{u}$ .

In the particular case where the fluid is at rest (*i.e.*,  $(\mathbf{u}_0, p_0) = \mathbf{0}$ ) and the structure is rigid and elastically supported in translation ( $n^s = d$ ,  $\Phi = \mathbf{I}$ ,  $\mathbf{M} = m\mathbf{I}$ ,  $\mathbf{K} = k\mathbf{I}$ ,  $m, k > 0$ ) problem (1.4.27) becomes

$$\left\{ \begin{array}{l} -2\mu \operatorname{div} \epsilon(\mathbf{u}) + \nabla p = \rho^f \lambda \mathbf{u} \quad \text{in } \Omega^f, \\ \operatorname{div} \mathbf{u} = 0 \quad \text{in } \Omega^f, \\ \mathbf{u} = \mathbf{0} \quad \text{on } \Gamma, \\ \mathbf{u} = -\lambda \mathbf{s} \quad \text{on } \Sigma, \\ \lambda^2 m \mathbf{s} + k \mathbf{s} = - \int_{\Sigma} \boldsymbol{\sigma}(\mathbf{u}, p) \mathbf{n}, \end{array} \right. \quad (1.4.28)$$

which involves the Stokes equations. This kind of problem was proposed and analyzed in [CDP92], describing the vibration frequencies of a tube rack immersed in a viscous fluid at rest (see also [CPTV94]). Note that  $\mathbf{s}$  can be eliminated through (1.4.28)<sub>4</sub>, which yields a pure fluid problem with a non-local boundary condition on  $\Sigma$ . Numerical computations based on (1.4.28) have been reported in [CD95].

If we consider now the case in which the rigid structure is immersed in a permanent flow (*i.e.*,  $(\mathbf{u}_0, p_0) \neq \mathbf{0}$ ) and if we neglect  $\mathbf{B}^0$  and the gradient term  $\nabla \mathbf{u}_0$  in the transpiration condition, the quadratic eigenvalue problem (1.4.27) becomes

$$\left\{ \begin{array}{l} \rho^f (\mathbf{u} \cdot \nabla \mathbf{u}_0 + \mathbf{u}_0 \cdot \nabla \mathbf{u}) - 2\mu \operatorname{div} \epsilon(\mathbf{u}) + \nabla p = \rho^f \lambda \mathbf{u} \quad \text{in } \Omega^f, \\ \operatorname{div} \mathbf{u} = 0 \quad \text{in } \Omega^f, \\ \mathbf{u} = \mathbf{0} \quad \text{on } \Gamma, \\ \mathbf{u} = -\lambda \mathbf{s} \quad \text{on } \Sigma, \\ \lambda^2 m \mathbf{s} + k \mathbf{s} = - \int_{\Sigma} \boldsymbol{\sigma}(\mathbf{u}, p) \mathbf{n}. \end{array} \right.$$

This problem, involving the linearized Navier-Stokes equations, has been proposed without analysis in [PT93, CPTV94] generalizing (1.4.28) to the case of a tube rack placed in a cross-flow.

### Eigenfrequency characterization

The quadratic term in (1.4.27) can be linearized by introducing as new unknown the modal velocity  $\mathbf{z} = -\lambda \mathbf{s} \in \mathbb{C}^{n^s}$ . Hence (1.4.27) can be rewritten as: find  $\lambda \in \mathbb{C}$ ,  $\mathbf{u} : \Omega^f \rightarrow \mathbb{C}^d$ ,  $p : \Omega^f \rightarrow \mathbb{C}$  and  $\mathbf{s}, \mathbf{z} \in \mathbb{C}^{n^s}$ , with  $\int_{\Omega^f} p = 0$  and  $(\mathbf{u}, p, \mathbf{s}, \mathbf{z}) \neq \mathbf{0}$ , such that

$$\left\{ \begin{array}{l} \rho^f (\mathbf{u} \cdot \nabla \mathbf{u}_0 + \mathbf{u}_0 \cdot \nabla \mathbf{u}) - 2\mu \operatorname{div} \epsilon(\mathbf{u}) + \nabla p = \rho^f \lambda \mathbf{u} \quad \text{in } \Omega^f, \\ \operatorname{div} \mathbf{u} = 0 \quad \text{in } \Omega^f, \\ \mathbf{u} = \mathbf{0} \quad \text{on } \Gamma, \\ \mathbf{u} = \Phi \mathbf{z} - (\Phi \mathbf{s}) \cdot \nabla \mathbf{u}_0 \quad \text{on } \Sigma, \\ -\mathbf{z} = \lambda \mathbf{s}, \\ M^{-1} \left[ (\mathbf{K} + \mathbf{B}^0) \mathbf{s} + \int_{\Sigma} \Phi^T \boldsymbol{\sigma}(\mathbf{u}, p) \mathbf{n} \right] = \lambda \mathbf{z}. \end{array} \right. \quad (1.4.29)$$

The solutions of (1.4.29) can be characterized through the introduction of a linear operator

$$\mathcal{T} : (\mathbf{f}, \mathbf{h}, \mathbf{g}) \in \mathbf{L}^2(\Omega^f) \times \mathbb{C}^{n^s} \times \mathbb{C}^{n^s} \rightarrow \mathcal{T}(\mathbf{f}, \mathbf{g}, \mathbf{h}) = (\mathbf{u}, \mathbf{z}, \mathbf{s}) \in \mathbf{H}^1(\Omega^f) \times \mathbb{C}^{n^s} \times \mathbb{C}^{n^s},$$

where  $(\mathbf{u}, p, \mathbf{z}, \mathbf{s})$  is defined as the solution (for  $r > 0$  large enough) of the following coupled problem:

$$\left\{ \begin{array}{l} \rho^f (\mathbf{u} \cdot \nabla \mathbf{u}_0 + \mathbf{u}_0 \cdot \nabla \mathbf{u}) - 2\mu \operatorname{div} \boldsymbol{\epsilon}(\mathbf{u}) + \nabla p + r\rho^f \mathbf{u} = \rho^f \mathbf{f} \quad \text{in } \Omega^f, \\ \operatorname{div} \mathbf{u} = 0 \quad \text{in } \Omega^f, \\ \mathbf{u} = \mathbf{0} \quad \text{on } \Gamma, \\ \mathbf{u} = \Phi \mathbf{z} - (\Phi \mathbf{s}) \cdot \nabla \mathbf{u}_0 \quad \text{on } \Sigma, \\ -\mathbf{z} + r\mathbf{s} = \mathbf{g} \\ \\ M^{-1} \left[ (\mathbf{K} + \mathbf{B}^0) \mathbf{s} + \int_{\Sigma} \Phi^T \boldsymbol{\sigma}(\mathbf{u}, p) \mathbf{n} \right] + r\mathbf{z} = \mathbf{h}. \end{array} \right. \quad (1.4.30)$$

The underlying idea in the definition of operator  $\mathcal{T}$  comes from the fact that if  $(\lambda; \mathbf{u}, p, \mathbf{z}, \mathbf{s})$  is a spectral solution of (1.4.29), then  $\omega = \lambda + r$  is such that  $\omega \mathcal{T}(\mathbf{u}, \mathbf{z}, \mathbf{s}) = (\mathbf{u}, \mathbf{z}, \mathbf{s})$ , thus  $\omega \neq 0$  and  $(1/\omega; \mathbf{u}, \mathbf{z}, \mathbf{s})$  is an eigenpair of  $\mathcal{T}$ . Conversely, if  $\omega \neq 0$  is an eigenvalue of  $\mathcal{T}$  then  $1/\omega - r$  is an eigenvalue of (1.4.29).

We have shown that the operator  $\mathcal{T}$ , is well defined, linear and continuous. This is stated in the next result.

**Theorem 1.1** *For  $r > 3\|u_0\|_{1,\infty,\Omega^f}$  large enough, the problem (1.4.30) admits a unique solution  $(\mathbf{u}, p, \mathbf{s}) \in \mathbf{H}^1(\Omega^f) \times L_0^2(\Omega^f) \times \mathbb{C}^{n^s}$ . Moreover,*

$$|\mathbf{s}| + \|\mathbf{u}\|_{1,\Omega^f} + \|p\|_{0,\Omega^f} \leq C (\|\mathbf{f}\|_{0,\Omega^f} + |\mathbf{g}| + |\mathbf{h}|), \quad (1.4.31)$$

where  $C$  is a positive constant independent of  $(\mathbf{u}, p, \mathbf{s})$  and  $(\mathbf{f}, \mathbf{g}, \mathbf{h})$ .

The proof of this result is based on the vibrational decomposition  $(\mathbf{u}, p) = (\mathbf{u}_1, p_1) + (\mathbf{u}_2, p_2) + (\mathbf{u}_3, p_3)$ , where  $(\mathbf{u}_1, p_1)$  is solution of the pure fluid problem

$$\left\{ \begin{array}{l} \rho^f (\mathbf{u}_1 \cdot \nabla \mathbf{u}_0 + \mathbf{u}_0 \cdot \nabla \mathbf{u}_1) - 2\mu \operatorname{div} \boldsymbol{\epsilon}(\mathbf{u}_1) + \nabla p_1 + r\rho^f \mathbf{u}_1 = \rho^f \mathbf{f} \quad \text{in } \Omega^f, \\ \operatorname{div} \mathbf{u}_1 = 0 \quad \text{in } \Omega^f, \\ \mathbf{u}_1 = \mathbf{0} \quad \text{on } \Gamma, \\ \mathbf{u}_1 = -\Phi \mathbf{g} \quad \text{on } \Sigma, \end{array} \right.$$

$(\mathbf{u}_2, p_2)$  is solution of

$$\left\{ \begin{array}{l} \rho^f (\mathbf{u}_2 \cdot \nabla \mathbf{u}_0 + \mathbf{u}_0 \cdot \nabla \mathbf{u}_2) - 2\mu \operatorname{div} \boldsymbol{\epsilon}(\mathbf{u}_2) + \nabla p_2 + r\rho^f \mathbf{u}_2 = \mathbf{0} \quad \text{in } \Omega^f, \\ \operatorname{div} \mathbf{u}_2 = 0 \quad \text{in } \Omega^f, \\ \mathbf{u}_2 = 0 \quad \text{on } \Gamma, \\ \mathbf{u}_2 = -(\Phi \mathbf{s}) \cdot \nabla \mathbf{u}_0 \quad \text{on } \Sigma, \end{array} \right. \quad (1.4.32)$$

and  $(\mathbf{u}_3, p_3, \mathbf{s})$  is solution of

$$\left\{ \begin{array}{l} \rho^f (\mathbf{u}_3 \cdot \nabla \mathbf{u}_0 + \mathbf{u}_0 \cdot \nabla \mathbf{u}_3) - 2\mu \operatorname{div} \boldsymbol{\epsilon}(\mathbf{u}_3) + \nabla p_3 + r\rho^f \mathbf{u}_3 = \mathbf{0} \quad \text{in } \Omega^f, \\ \operatorname{div} \mathbf{u}_3 = 0 \quad \text{in } \Omega^f, \\ \mathbf{u}_3 = \mathbf{0} \quad \text{on } \Gamma, \\ \mathbf{u}_3 = r\Phi \mathbf{s} \quad \text{on } \Sigma, \\ \\ (\mathbf{K} + r^2 \mathbf{M} + \mathbf{B}^0) \mathbf{s} + \int_{\Sigma} \Phi^T \boldsymbol{\sigma}(\mathbf{u}_1, p_1) \mathbf{n} + \int_{\Sigma} \Phi^T \boldsymbol{\sigma}(\mathbf{u}_2, p_2) \mathbf{n} \\ + \int_{\Sigma} \Phi^T \boldsymbol{\sigma}(\mathbf{u}_3, p_3) \mathbf{n} = \mathbf{M}(\mathbf{h} + r\mathbf{g}). \end{array} \right. \quad (1.4.33)$$

For  $r > 0$  large enough we can invoke the classical theory for the Stokes problem (see, *e.g.*, [GR86]) to determine  $(\mathbf{u}_1, p_1)$  from  $\mathbf{f}$  and  $\mathbf{g}$ . Since, by hypothesis, the structural displacement is a superposition of a finite number of vibration modes, the fluid component  $(\mathbf{u}_2, p_2)$  can be eliminated in (1.4.33) via a load transfer operator  $\mathbf{L}(r) \in \mathbb{R}^{n^s \times n^s}$ , such that

$$\int_{\Sigma} \Phi^T \sigma(\mathbf{u}_2, p_2) \mathbf{n} = \mathbf{L}(r) \mathbf{s},$$

defined by

$$\mathbf{L}_{ij}(r) \stackrel{\text{def}}{=} \int_{\Sigma} (\sigma(\mathbf{w}_j, q_j) \mathbf{n}) \cdot \phi_i,$$

where the  $(\mathbf{w}_j, q_j)$  are the elementary solutions of (1.4.32), that is,

$$\left\{ \begin{array}{ll} \rho^f (\mathbf{w}_j \cdot \nabla \mathbf{u}_0 + \mathbf{u}_0 \cdot \nabla \mathbf{w}_j) - 2\mu \operatorname{div} \epsilon(\mathbf{w}_j) + \nabla q_j + r \rho^f \mathbf{w}_j = \mathbf{0} & \text{in } \Omega^f, \\ \operatorname{div} \mathbf{w}_j = 0 & \text{in } \Omega^f, \\ \mathbf{w}_j = \mathbf{0} & \text{on } \Gamma, \\ \mathbf{w}_j = -\phi_j \cdot \nabla \mathbf{u}_0 & \text{on } \Sigma. \end{array} \right.$$

Finally, for  $r > 0$  large enough, we can recover  $(\mathbf{u}_3, p_3, \mathbf{s})$  from (1.4.33), the estimate  $|\mathbf{L}(r)| = \mathcal{O}(1 + \sqrt{r} + r)$  and the  $r^2 \mathbf{M}$ -coercivity of the structure sub-problem.

**Remark 1.10** *The introduction of the load transfer operator  $\mathbf{L}(r)$  is a major ingredient in the proof of Theorem 1.1. This explains the assumption on the reduced behavior of the structure.*

Since  $\mathbf{H}^1(\Omega^f) \times \mathbb{C}^{n^s} \times \mathbb{C}^{n^s}$  is compactly embedded into  $\mathbf{L}^2(\Omega^f) \times \mathbb{C}^{n^s} \times \mathbb{C}^{n^s}$ , the continuity of  $\mathcal{T}$  leads to the compactness of  $\mathcal{T}$  as an operator from and into  $\mathbf{L}^2(\Omega^f) \times \mathbb{C}^{n^s} \times \mathbb{C}^{n^s}$ . Therefore the classical spectral theory for compact operators on Hilbert spaces (see, *e.g.*, [AG93]) yields the following characterization.

**Theorem 1.2** *The eigenvalues of (1.4.27) are, at most, a countable sequence of complex numbers, with finite multiplicity and which can only cluster at infinity.*

### Eigenfrequency localization

The eigenfrequencies of the spectral problem (1.4.27) can be localized by considering now the vibrational decomposition  $(\mathbf{u}, p) = (\mathbf{u}_1, p_1) + (\mathbf{u}_2, p_2)$ , where  $(\mathbf{u}_1, p_1)$  is solution of

$$\left\{ \begin{array}{ll} \rho^f (\mathbf{u}_1 \cdot \nabla \mathbf{u}_0 + \mathbf{u}_0 \cdot \nabla \mathbf{u}_1) - 2\mu \operatorname{div} \epsilon(\mathbf{u}_1) + \nabla p_1 + r \rho^f \mathbf{u}_1 = \mathbf{0} & \text{in } \Omega^f, \\ \operatorname{div} \mathbf{u}_1 = 0 & \text{in } \Omega^f, \\ \mathbf{u}_1 = \mathbf{0} & \text{on } \Gamma, \\ \mathbf{u}_1 = -(\Phi \mathbf{s}) \cdot \nabla \mathbf{u}_0 & \text{on } \Sigma, \end{array} \right.$$

and  $(\mathbf{u}_2, p_2, \mathbf{s})$  solves

$$\left\{ \begin{array}{ll} \rho^f (\mathbf{u}_2 \cdot \nabla \mathbf{u}_0 + \mathbf{u}_0 \cdot \nabla \mathbf{u}_2) - 2\mu \operatorname{div} \epsilon(\mathbf{u}_2) + \nabla p_2 + r \rho^f \mathbf{u}_2 = (\lambda + r) \rho^f (\mathbf{u}_1 + \mathbf{u}_2) & \text{in } \Omega^f, \\ \operatorname{div} \mathbf{u}_2 = 0 & \text{in } \Omega^f, \\ \mathbf{u}_2 = \mathbf{0} & \text{on } \Gamma, \\ \mathbf{u}_2 = -\lambda \Phi \mathbf{s} & \text{on } \Sigma, \\ \lambda^2 \mathbf{M} \mathbf{s} + (\mathbf{K} + \mathbf{B}^0 + \mathbf{L}(r)) \mathbf{s} = - \int_{\Sigma} \Phi^T \sigma(\mathbf{u}_2, p_2) \mathbf{n}. \end{array} \right.$$

This leads to the fundamental energy equality

$$\begin{aligned} 2\mu\|\boldsymbol{\epsilon}(\mathbf{u}_2)\|_{0,\Omega^f}^2 = & \lambda \left( \rho^f \|\mathbf{u}_2\|_{0,\Omega^f}^2 + |\lambda|^2 \mathbf{M} \mathbf{s} \cdot \bar{\mathbf{s}} \right) \\ & + (\mathbf{K} + \mathbf{B}^0 + \mathbf{L}(r)) \mathbf{s} \cdot (\bar{\lambda} \bar{\mathbf{s}}) + (\lambda + r) \rho(\mathbf{u}_1, \bar{\mathbf{u}}_2) \\ & - \rho^f ((\nabla \mathbf{u}_0) \mathbf{u}_2 + \mathbf{u}_0 \cdot \nabla \mathbf{u}_2, \bar{\mathbf{u}}_2). \end{aligned}$$

By taking, alternatively, the real and imaginary parts of this expression and after some manipulations we get the following result.

**Theorem 1.3** *The eigenvalues  $\lambda$  of (1.4.27) lie in the parabolic region (see Figure 1.4)*

$$(\operatorname{Im} \lambda)^2 \leq a \operatorname{Re} \lambda + b, \quad (1.4.34)$$

where  $a$  and  $b$  are two positive constants independent of  $\lambda$ .

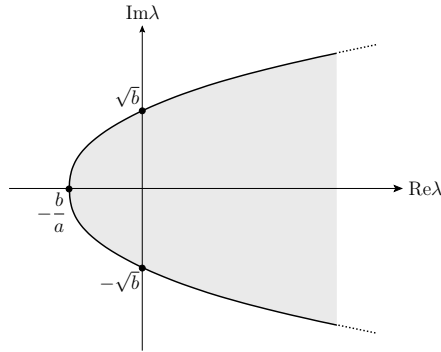


Figure 1.4: A parabolic region (in gray) in the complex plan containing the eigenfrequencies of the spectral problem (1.4.27).

**Remark 1.11** *Estimate (1.4.34) is a standard result in hydrodynamic stability theory [Geo85, Sat70]. Theorem 1.3 provides a generalization to the case of linear stability analysis in fluid-structure interaction, with a reduced structural behavior.*

Theorems 1.2 and 1.3 guarantee that

1. the eigenvalues cannot cluster at a leftmost eigenvalue. That is, there is at most a finite number of eigenvalues with negative real part,
2. the imaginary part of the leftmost eigenvalues remains bounded.

This implies that most of the eigenvalues of (1.4.27) have a positive real part and only a small number cross the imaginary axis. Therefore, to detect a stability change, we only need to compute the few eigenvalues with the smallest real parts, that is, the critical eigenfrequencies of the system. This is the topic of the next subsection.

### 1.4.2 Eigenvalues computation ([14], [47, Chap. 6, 7, 8])

After space discretization of problem (1.4.27) (using residual based stabilized finite elements, see §4.1) we obtain a generalized eigenvalue problem with the following block structure:

$$\underbrace{\begin{bmatrix} A_{\Pi} & A_{I\Sigma} & B_I & 0 & 0 \\ 0 & I & 0 & G^0 & G^1 \\ Q_I & Q_\Sigma & Q_p & 0 & 0 \\ 0 & 0 & 0 & -I & 0 \\ F_I & F_\Sigma & F_p & 0 & K + B^0 \end{bmatrix}}_{\mathbf{A}} \underbrace{\begin{bmatrix} u_I \\ u_\Sigma \\ p \\ z \\ s \end{bmatrix}}_{\mathbf{y}} = \lambda \underbrace{\begin{bmatrix} M_{\Pi} & M_{I\Sigma} & B_I & 0 & 0 \\ 0 & 0 & 0 & 0 & 0 \\ R_I & R_\Sigma & R_p & 0 & 0 \\ 0 & 0 & 0 & 0 & I \\ F_I & F_\Sigma & F_p & M & 0 \end{bmatrix}}_{\mathbf{B}} \begin{bmatrix} u_I \\ u_\Sigma \\ p \\ z \\ s \end{bmatrix} \quad (1.4.35)$$

The matrices  $\mathbf{A}$  and  $\mathbf{B}$  are real, sparse, non-symmetric and, in most of the applications, of large size. As noticed in §1.4.1, almost all the eigenvalues of (1.4.35) have positive real part and only a small number cross the imaginary axis. Therefore, to detect a stability change, the interest lies in computing a few eigenvalues with the smallest real parts. In what follows, we assume that (1.4.35) has  $m$  eigenvalues  $\{\lambda_i\}_{i=1}^m$ , that we suppose ordered in increasing order of their real parts,  $\text{Re}(\lambda_1) \leq \text{Re}(\lambda_2) \leq \dots \leq \text{Re}(\lambda_m)$ .

A complication arising in problem (1.4.35) is the singularity of matrix  $\mathbf{B}$ . This implies that (1.4.35) has “infinite” eigenvalues (see [Gar91, Ste73]), which are defined as the zero eigenvalues of the inverse problem

$$\mathbf{B}\mathbf{y} = \omega\mathbf{A}\mathbf{y}, \quad \omega = \frac{1}{\lambda}.$$

Although the infinite eigenvalues are not true eigenvalues of (1.4.35), in practice, they can introduce numerical difficulties (see, *e.g.*, [Gar91, CGS94, MS97, LS97]). When working in finite arithmetic, the matrix  $\mathbf{B}$  is often perturbed so that it may become “not-singular”. Eigenvalues with a very large module (and perhaps with negative real part) may appear which are, of course, irrelevant for the stability analysis.

Iterative methods for non symmetric problems, such as subspace iteration and Arnoldi, cannot be applied directly to the generalized eigenproblem (1.4.35). Before we must transform problem (1.4.35) in a standard problem of the form

$$\mathbf{T}\mathbf{y} = \theta\mathbf{y}. \quad (1.4.36)$$

The difficulty now is how to choose  $\mathbf{T}$ . It is well known that iterative methods quickly provide good approximations of well-separated eigenvalues (largest or smallest in magnitude). In general, these eigenvalues do not match with those of smallest real part. Thus  $\mathbf{T}$  must satisfy some *a priori* properties:

- matrix-vector products,  $\mathbf{T}\mathbf{z}$ , should be carried out efficiently;
- there is a known transformation between the solutions of (1.4.35) and (1.4.36);
- the eigenvalues with smallest real part of (1.4.35) are mapped to the eigenvalues of (1.4.36) which are easily approximated by the iterative method performed on (1.4.36).

The complication associated to the singularity of the matrix  $\mathbf{B}$  also restricts the choice of the transformation  $\mathbf{T}$ . We must use rational transformations, namely, it is necessary to invert problem (1.4.35). In this framework, standard choices when computing leftmost eigenvalues of problems like (1.4.35) are the shift-invert and the generalized Cayley transformations (see [LS97, DK98, DK99, LS01]).

**Remark 1.12** *By an appropriate selection of the shift (or pole)  $\alpha$  near the imaginary axis, the left-most eigenvalues of (1.4.35) can be mapped onto those of the shift-invert transformation  $(\mathbf{A} - \alpha\mathbf{B})^{-1}\mathbf{B}$  with largest magnitude. However, since  $\mathbf{A}$  and  $\mathbf{B}$  are real matrices, and in order to keep the computation in real arithmetic, we did not consider the use of complex shifts.*

Following [LS97], the leftmost eigenvalues of (1.4.35) have been approximated using an iterative algorithm combining the generalized Cayley transform and an Implicit Restarted Arnoldi Method (IRAM). For  $\alpha_1, \alpha_2 \in \mathbb{R}$  such that

$$\alpha_1 < \alpha_2, \quad \alpha_1 \neq \lambda_i \quad i = 1, \dots, m, \quad (1.4.37)$$

the generalized Cayley transform of problem (1.4.35) is defined as

$$\mathbf{T}_C(\alpha_1, \alpha_2) = (\mathbf{A} - \alpha_1\mathbf{B})^{-1}(\mathbf{A} - \alpha_2\mathbf{B}). \quad (1.4.38)$$

The relationship between the finite eigenvalues of (1.4.35) and those of  $\mathbf{T}_C(\alpha_1, \alpha_2)$  is given by the following result (see [Gar91]).

**Lemma 1.3** *Assume that (1.4.37) holds. The pair  $(\lambda, \mathbf{y})$  is an eigensolution of (1.4.35) if and only if  $(\theta, \mathbf{y})$  is an eigensolution of  $\mathbf{T}_C(\alpha_1, \alpha_2)$ , where*

$$\theta = c(\lambda) \stackrel{\text{def}}{=} \frac{\lambda - \alpha_2}{\lambda - \alpha_1}, \quad \lambda = c^{-1}(\theta) = \frac{\alpha_1\theta - \alpha_2}{\theta - 1}. \quad (1.4.39)$$

Here,  $c$  is a bijection of  $\mathbb{C} - \{\alpha_1\}$  in  $\mathbb{C} - \{1\}$ .

The main interest of the generalized Cayley transform lies in the properties of the bijection  $c$  and in the role of parameters  $\alpha_1$  and  $\alpha_2$  in this mapping. Roughly, the eigenvalues of (1.4.35) lying on the left of the straight line  $\text{Re}(\lambda) = (\alpha_1 + \alpha_2)/2$  in the complex plan, are mapped to extreme eigenvalues of  $\mathbf{T}_C(\alpha_1, \alpha_2)$ . More precisely, we have the following result (see [Gar91]):

**Lemma 1.4** *Let  $1 \leq k < m$  be such that  $\text{Re}(\lambda_k) < \text{Re}(\lambda_{k+1})$  and let  $\alpha_1, \alpha_2 \in \mathbb{R}$  such that (1.4.37) holds and*

$$\frac{1}{2}(\alpha_1 + \alpha_2) = \text{Re}(\lambda_{k+1}),$$

then

$$\begin{aligned} \theta_i &= c(\lambda_i) \notin B(0, 1), \quad i = 1, \dots, k, \\ \theta_i &= c(\lambda_i) \in B(0, 1), \quad i = k + 1, \dots, m, \end{aligned}$$

where  $B(0, 1)$  is the unit circle of the complex plane.

Thus,  $\alpha_1$  and  $\alpha_2$  are chosen in such a way that (see [Gar91, LS97]):

- the first unwanted eigenvalue,  $\theta_{k+1}$  (with  $k \geq 1$ ), is located in  $B(0, 1)$ ;
- the magnitude of  $\theta_1 = c(\lambda_1)$  is maximal.

In other words,  $\alpha_1$  and  $\alpha_2$  are chosen to maximize  $|\theta_1|$  under the constraints

$$\frac{\alpha_1 + \alpha_2}{2} = \text{Re}(\lambda_{k+1}), \quad \alpha_1 < \alpha_2.$$

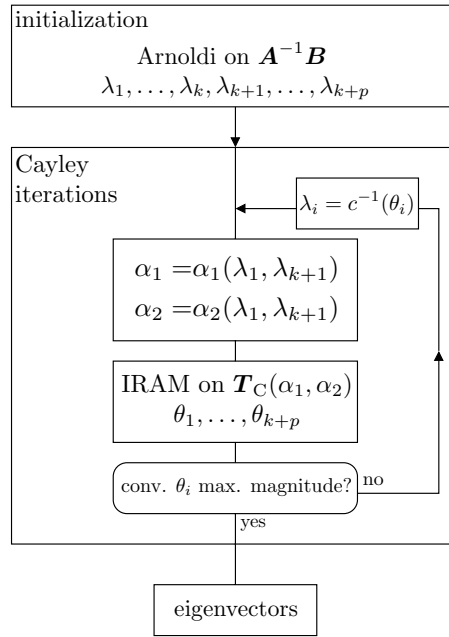


Figure 1.5: Sketch of the IRAM-Cayley iterative algorithm reported in [LS97].

The optimal values for  $\alpha_1$  and  $\alpha_2$  have been reported in [Gar91] and depend on the cases  $\lambda_1 \in \mathbb{R}$  and  $\lambda_1 = x_1 + iy_1$  ( $y_1 \neq 0$ ).

Figure 1.5 presents a sketch of the iterative algorithm used for the computation of the leftmost eigenvalues. Here,  $k$  stands for the number of sought eigenvalues and  $k+p$  ( $p > 0$ ) for the dimension of the Krylov subspace.

We conclude this section by briefly presenting (full details are given in [14] and [47, Chapter 8]) some numerical results obtained with the IRAM-Cayley algorithm (Figure 1.5) applied to (1.4.35). These numerical experiments illustrate the capabilities of the linearization-transpiration approach described in §1.3.1 to predict the linear stability of coupled fluid-structure systems.

### Rigid structure placed in a viscous flow at rest

As first example, we consider the eigenvalue problem (1.4.28) which describes the eigenmotions of a rigid structure immersed in a incompressible viscous fluid at rest. The fluid is contained in a two-dimensional cavity and the structure is assumed to be elastically mounted (with stiffness  $k > 0$ ), see Figure 1.6 (left).

Table 1.1 presents the 10 leftmost eigenvalues obtained with the IRAM-Cayley method, and Table 1.2 provides the eigenvalues reported in [CD95] (using a direct method). In both cases the critical damping is positive (*i.e.*, the system is linearly stable) and the number of complex eigenvalues does not exceeds 4 (as predicted by [CDP92]). Moreover, both spectra show a similar behavior when  $k$  varies. For illustration purposes, we have depicted in Figure 1.6 (center/right) the eigenvelocity and eigenpressure fields corresponding to  $\lambda_1 = 1.818 \times 10^{-2}$ .

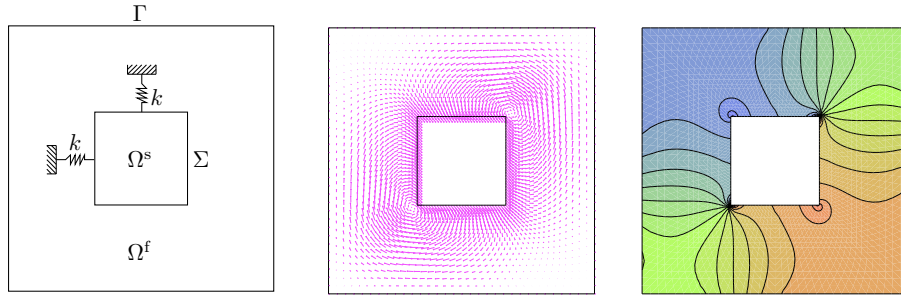


Figure 1.6: *Left*: test-case description. *Center/Right*: eigenvelocity and eigenpressure fields for  $\lambda_1 = 1.818 \times 10^{-2}$ .

$k = 0.01$	$k = 0.1$	$k = 1$	$k = 10$	$k = 100$
$1.810 \times 10^{-4}$	$1.811 \times 10^{-3}$	$1.818 \times 10^{-2}$	$1.894 \times 10^{-1}$	$2.061 + 1.696i$
$1.810 \times 10^{-4}$	$1.811 \times 10^{-3}$	$1.818 \times 10^{-2}$	$1.894 \times 10^{-1}$	$2.061 - 1.696i$
2.651	2.651	2.651	2.651	$2.061 + 1.696i$
3.870	3.869	3.855	3.707	$2.061 - 1.696i$
3.870	3.869	3.855	3.707	2.651
8.152	8.152	8.152	8.152	8.152
8.238	8.238	8.238	8.238	8.238
8.382	8.382	8.381	8.379	8.361
8.382	8.382	8.381	8.379	8.361
9.218	9.218	9.218	9.218	9.218

Table 1.1: The 10 leftmost eigenvalues obtained with the IRAM-Cayley algorithm.

$k = 0.01$	$k = 0.1$	$k = 1$	$k = 10$	$k = 100$
$1.868 \times 10^{-4}$	$1.869 \times 10^{-3}$	$1.876 \times 10^{-2}$	$1.960 \times 10^{-1}$	$2.067 + 1.752i$
$1.868 \times 10^{-4}$	$1.869 \times 10^{-3}$	$1.876 \times 10^{-2}$	$1.960 \times 10^{-1}$	$2.067 - 1.752i$
2.625	2.625	2.625	2.625	$2.067 + 1.752i$
3.863	3.862	3.847	3.696	$2.067 - 1.752i$
3.863	3.862	3.847	3.696	2.625
7.909	7.909	7.909	7.909	7.909
7.934	7.934	7.934	7.934	7.934
8.167	8.167	8.167	8.164	8.138
8.167	8.167	8.167	8.164	8.138
9.223	9.223	9.223	9.223	9.223

Table 1.2: The 10 leftmost eigenvalues reported in [CD95].

### Cantilever pipe conveying a fluid

We now consider the linear stability of a cantilever pipe conveying a fluid, see Figure 1.7. It is well known, see [Paï98, Ren98], that this fluid-structure system loses stability by flutter for high flow velocities.

The numerical results reported in Figure 1.8 show that the linearization-transpiration approach allows to reproduce the main stability predictions reported by Païdoussis [Paï98] and Renou

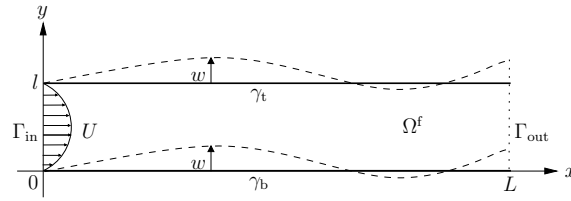


Figure 1.7: Two-dimensional representation of a cantilever pipe conveying a fluid.

[Ren98]. These results were obtained with the IRAM-Cayley iterative algorithm applied to the spectral problem (1.4.27) (with an outflow boundary condition). Note that for each value of the mean axial velocity,  $U$ , requires the computation of a new reference state  $(\mathbf{u}_0, p_0)$ .

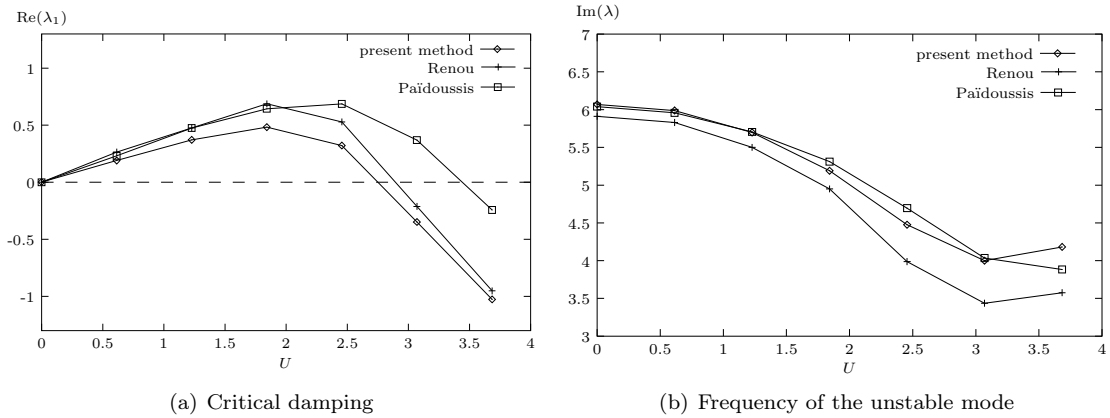


Figure 1.8: Real part of the left-most eigenvalue (critical damping) and frequency of the unstable mode *vs.* mean axial velocity of the flow (in m/s).

As in [Ren98], the motion of the pipe is described in terms of the first three modes of a cantilever beam (modeling the pipe walls). The stability predictions of [Pai98] are based on the usage of a simplified linear model of the system. In [Ren98], the analysis relies on the assumption that the interface fluid loads can be expressed in terms of added mass, added damping and added stiffness. These added matrices are usually computed in terms of the interface fluid load (over a fixed number of periods) associated to a forced sinusoidal oscillation of the structure (see also [PB01, WOOF78, WOOF80]). In [Ren98], this fluid load is computed by solving the incompressible Navier-Stokes equations with transpiration boundary conditions (which take into account the sinusoidal interface motion).

### Winds effects on a simplified bridge deck profile

We finally consider the aeroelastic flutter analysis of prismatic cylinders in torsional mode under the presence of a steady wing, see Figure 1.9.

Figure 1.10(a) presents the free oscillation experimental results reported in [WOOF80], for a rectangular cylinder of ratio 4. The ordinate is the amplitude of the limit cycle and the abscissa the dimensionless velocity  $\frac{U}{f_{\theta} D}$ , where  $U$ ,  $D$  and  $f_{\theta}$  stand, respectively, for the wind velocity, the

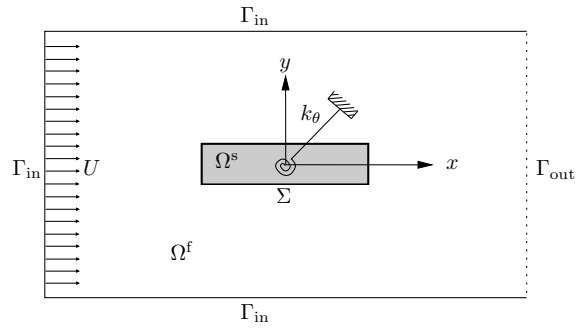


Figure 1.9: Test-case description: simplified bridge deck rectangular profile in torsional mode.

thickness and the natural frequency of the structure in torsional mode.

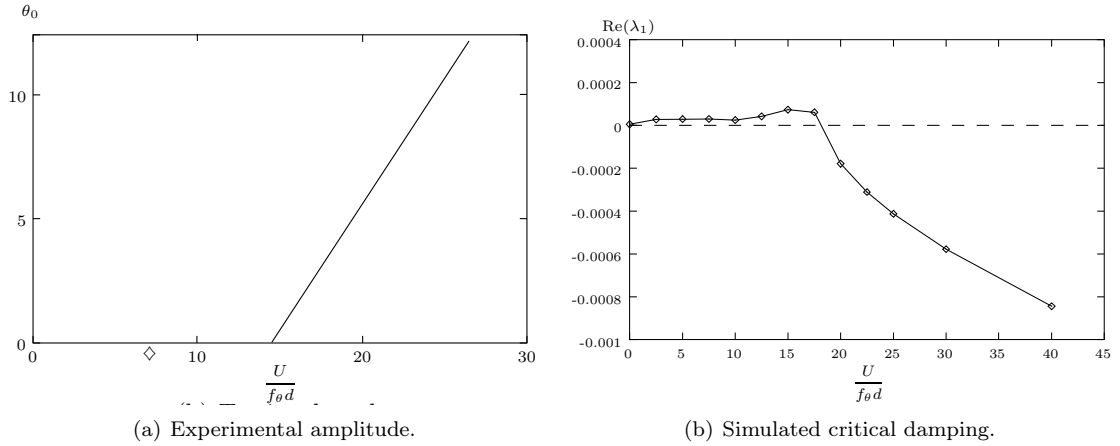


Figure 1.10: Experimental amplitude of the limit cycle (from [WOOF80]) and real part of the left-most eigenvalue (critical damping) *vs.* dimensionless velocity.

Figure 1.10(b) reports the numerically computed critical dampings as a function of the dimensionless velocity. When the velocity of the uniform flow  $U$  becomes large the critical damping,  $\text{Re}(\lambda_1)$ , takes negative values, indicating that torsional flutter might occur in the range 15–45 of dimensionless velocities. This is in agreement with the increase of amplitude shown in Figure 1.10(a).



## Chapter 2

# Algorithms for fluid-structure interaction

This chapter summarizes the research activity on the development of numerical methods for fluid-structure interaction, initiated at EPFL (Lausanne, Switzerland) in 2002 and pursued at INRIA since 2004.

### 2.1 Motivations

Computational Fluid-Structure Dynamics (CFSD) is of great importance in practically all engineering fields, from aeroelasticity to biomechanics (see, *e.g.*, [DGH82, MO95, Pip95, LTM01, MWR01, Tez01, GV03, WSKH04, BZ04, Hei04, COS05, FvdZG06, TS07, BC07, WRC<sup>+</sup>08, DSB<sup>+</sup>10]). The work summarized in this chapter stems from the numerical simulation of the (mechanical) interaction between the vessel wall and the blood flow in large arteries (see, *e.g.*, [Nob01, GV03, WSKH04, LK06, FVCJ<sup>+</sup>06, YLY07, KNE<sup>+</sup>08, KGF<sup>+</sup>09, FPQ09]).

The numerical simulation of this fluid-structure phenomenon raises many issues. Among them, the displacement of the wall cannot be supposed to be infinitesimal, geometrical nonlinearities are therefore present in the structure and the fluid has to be solved in a moving domain (ALE formalism). On the other hand, since the arteries are slender and the vessel and blood densities close, the coupling has to be tackled carefully in order to avoid numerical instabilities.

In large (or medium size) arteries, blood is commonly modeled as a homogeneous, viscous, Newtonian and incompressible fluid (see, *e.g.*, [Thi08, FPQ09]). Although the artery wall has a viscoelastic behavior (see, *e.g.*, [Fun93]), we limit the presentation to the case of a non-linear elastic solid. The coupling strategies presented below are, however, not restricted to this structural behavior. As mathematical model, we consider therefore the system of partial differential equations (1.2.9), which we repeat here for the sake of convenience: find the fluid domain displacement  $\mathbf{d}^f : \Omega^f \times \mathbb{R}^+ \rightarrow \mathbb{R}^d$ , the fluid velocity  $\hat{\mathbf{u}} : \Omega^f \times \mathbb{R}^+ \rightarrow \mathbb{R}^d$ , the fluid pressure  $\hat{p} : \Omega^f \times \mathbb{R}^+ \rightarrow \mathbb{R}$  and

the structure displacement  $\mathbf{d} : \Omega^s \times \mathbb{R}^+ \rightarrow \mathbb{R}^d$  such that

$$\begin{cases} \rho^f \partial_t \mathbf{u}|_{\mathcal{A}} + \rho^f (\mathbf{u} - \mathbf{w}) \cdot \nabla \mathbf{u} - \operatorname{div} \boldsymbol{\sigma}(\mathbf{u}, p) = \mathbf{0} & \text{in } \Omega^f(t), \\ \operatorname{div} \mathbf{u} = 0 & \text{in } \Omega^f(t), \\ \mathbf{u} = \mathbf{u}_{\text{in}} & \text{on } \Gamma^{\text{in}}, \\ \boldsymbol{\sigma}(\mathbf{u}, p) \mathbf{n} = -p_{\text{out}} \mathbf{n} & \text{on } \Gamma^{\text{out}}, \end{cases} \quad (2.1.1)$$

$$\begin{cases} \rho^s \partial_{tt} \mathbf{d} - \operatorname{div} (\boldsymbol{\Pi}(\mathbf{d})) = \mathbf{0} & \text{in } \Omega^s, \\ \mathbf{d} = \mathbf{0} & \text{on } \Gamma^{\text{d}}, \\ \boldsymbol{\Pi}(\mathbf{d}) \mathbf{n}^s = \mathbf{0} & \text{on } \Gamma^{\text{n}}, \end{cases} \quad (2.1.2)$$

$$\begin{cases} \mathbf{d}^f = \operatorname{Ext}(\mathbf{d}|_{\Sigma}), \quad \widehat{\mathbf{w}} = \partial_t \mathbf{d}^f & \text{in } \Omega^f, \\ \widehat{\mathbf{u}} = \partial_t \mathbf{d} & \text{on } \Sigma, \\ \boldsymbol{\Pi}(\mathbf{d}) \mathbf{n}^s = -J \widehat{\boldsymbol{\sigma}}(\mathbf{u}, p) \mathbf{F}^{-\text{T}} \mathbf{n} & \text{on } \Sigma, \end{cases} \quad (2.1.3)$$

with the initial conditions  $\mathbf{u}|_{t=0} = \mathbf{u}^0$ ,  $\mathbf{d}|_{t=0} = \mathbf{d}^0$  and  $\partial_t \mathbf{d}|_{t=0} = \dot{\mathbf{d}}^0$ . We refer to [Mad09] for a recent review on the mathematical analysis of this type of coupled problems. This chapter concerns the numerical resolution of (2.1.1)-(2.1.3).

In what follows,  $\tau > 0$  denotes a given time-step size and  $x^n$  an approximation of a given time-dependent field  $x$  at time  $t_n \stackrel{\text{def}}{=} n\tau$ , with  $n \in \mathbb{N}$ . Moreover,  $\partial_\tau x^{n+1} \stackrel{\text{def}}{=} (x^{n+1} - x^n)/\tau$  denotes the first order backward difference and  $x^{n+\frac{1}{2}} \stackrel{\text{def}}{=} (x^{n+1} + x^n)/2$  the mid-point value approximation. The time semi-discretizations of (2.1.1)-(2.1.3) exploit, in general, the heterogeneous structure of the coupled problem. That is, (2.1.1) and (2.1.2) are time semi-discretized by different time-marching schemes, tailored by their different mathematical properties. To fix the ideas, we consider an implicit scheme for the ALE Navier-Stokes equations (2.1.1),

$$\begin{cases} \rho^f \partial_\tau \mathbf{u}^{n+1}|_{\mathcal{A}} + \rho^f (\mathbf{u}^{n+1} - \mathbf{w}^{n+1}) \cdot \nabla \mathbf{u}^{n+1} - \operatorname{div} \boldsymbol{\sigma}(\mathbf{u}^{n+1}, p^{n+1}) = \mathbf{0} & \text{in } \Omega^{f,n+1}, \\ \operatorname{div} \mathbf{u}^{n+1} = 0 & \text{in } \Omega^{f,n+1}, \\ \mathbf{u}^{n+1} = \mathbf{u}_{\text{in}}(t_{n+1}) & \text{on } \Gamma^{\text{in}}, \\ \boldsymbol{\sigma}(\mathbf{u}^{n+1}, p^{n+1}) \mathbf{n} = p_{\text{out}}(t_{n+1}) \mathbf{n} & \text{on } \Gamma^{\text{out}}, \end{cases} \quad (2.1.4)$$

and a mid-point rule for the structural equation (2.1.2),

$$\begin{cases} \rho^s \partial_\tau \dot{\mathbf{d}}^{n+1} - \operatorname{div} \boldsymbol{\Pi}^{n+\frac{1}{2}} = \mathbf{0} & \text{in } \Omega^s, \\ \dot{\mathbf{d}}^{n+\frac{1}{2}} = \partial_\tau \mathbf{d}^{n+1} & \text{in } \Omega^s, \\ \mathbf{d}^{n+1} = \mathbf{0} & \text{on } \Gamma^{\text{d}}, \\ \boldsymbol{\Pi}^{n+\frac{1}{2}} \mathbf{n}^s = \mathbf{0} & \text{on } \Gamma^{\text{n}}, \end{cases} \quad (2.1.5)$$

with the notation  $\boldsymbol{\Pi}^{n+\frac{1}{2}} \stackrel{\text{def}}{=} \frac{1}{2}(\boldsymbol{\Pi}(\mathbf{d}^{n+1}) + \boldsymbol{\Pi}(\mathbf{d}^n))$ .

On the other side, the time semi-discretization of (2.1.3) defines the coupling strategy. The most basic coupling procedure is obtained by taking

$$\begin{cases} \mathbf{d}^{f,n+1} = \operatorname{Ext}(\mathbf{d}^n|_{\Sigma}), \quad \widehat{\mathbf{w}}^{n+1} = \partial_\tau \mathbf{d}^{f,n+1} & \text{in } \Omega^f, \quad \Omega^{f,n+1} = (\mathbf{I}_{\Omega^f} + \mathbf{d}^{f,n+1})(\Omega^f), \\ \widehat{\mathbf{u}}^{n+1} = \partial_\tau \mathbf{d}^n & \text{on } \Sigma, \\ \boldsymbol{\Pi}^{n+\frac{1}{2}} \mathbf{n}^s = -J^{n+1} \widehat{\boldsymbol{\sigma}}(\mathbf{u}^{n+1}, p^{n+1})(\mathbf{F}^{n+1})^{-\text{T}} \mathbf{n} & \text{on } \Sigma. \end{cases} \quad (2.1.6)$$

Hence, the explicit treatment of the interface motion in (2.1.6)<sub>1</sub> and (2.1.6)<sub>2</sub>, yields the scheme reported in Algorithm 2.1. In the aeroelastic literature, Algorithm 2.1 is known as *conventional serial staggered* scheme (see, *e.g.*, [Pip97, LF98, PF03, FvdZG06]). Note that Algorithm 2.1 is very appealing in terms of computational cost, since it allows a fully uncoupled (sequential) computation of  $\mathbf{d}^{f,n+1}$ ,  $(\mathbf{u}^{n+1}, p^{n+1})$  and  $\mathbf{d}^{n+1}$ .

---

**Algorithm 2.1** Explicit coupling (weakly or loosely coupled) scheme.

---

1. Update the fluid domain configuration (mesh) and velocities via (2.1.6)<sub>1</sub>;
  2. Advance in time the fluid by solving (2.1.4) with the Dirichlet condition (2.1.6)<sub>2</sub>;
  3. Advance in time the structure by solving (2.1.5) with the Neumann condition (2.1.6)<sub>3</sub>;
  4. Go to next time-step.
- 

*Explicit coupling* (weakly or loosely coupled) schemes are those for which (2.1.3)<sub>2</sub> or (2.1.3)<sub>3</sub> are explicitly treated. A spurious numerical power is therefore generated at the interface, which has to be controlled in order to guarantee stability. Algorithm 2.1 is an explicit coupling scheme, since the fluid and solid velocities do not match at the interface. Indeed, from (2.1.6), we have  $\widehat{\mathbf{u}}^{n+1} = \partial_\tau \mathbf{d}^n \neq \partial_\tau \mathbf{d}^{n+1}$  on  $\Sigma$ . Although explicit coupling algorithms are widely and successfully used in aeroelasticity (see, *e.g.*, [PB01, PF03, FP04, FvdZG06]), a number of numerical studies (see, *e.g.*, [MWR99, LTM01, RB01, Nob01, GV03]) have shown that Algorithm 2.1 is unstable under certain choices of the physical parameters. Typically, this happens when the fluid and solid densities are comparable or when the domain has a slender shape, irrespectively of the choice of the time-step size. Blood flows are a popular example of such a situation.

Theoretical explanations of this issue have been reported in [CGN05] (see also [FWR07]). In particular, the following instability condition is established in [CGN05] for a simplified framework:

$$\frac{\rho^s \epsilon}{\rho^f \lambda_{\text{add}}} < 1, \quad (2.1.7)$$

where  $\epsilon$  and  $\lambda_{\text{add}}$  are pure geometrical quantities. The former is related to the thickness of the structure, whereas the latter increases with the length of the domain (it is the largest eigenvalue of the so-called *added-mass* interface operator). Note that the left hand-side of (2.1.7) is a pure physical quantity, it measures the amount of *added-mass effect* in the system. In particular, since (2.1.7) is independent of  $\tau$ , reducing the time-step size does not cure the instabilities (as mentioned above).

*Implicit coupling* schemes are those that enforce exactly the transmission conditions (2.1.3) at each time level. The schemes that satisfy (2.1.3)<sub>2</sub> and (2.1.3)<sub>3</sub> exactly are also known as *strongly coupled*. The implicit coupling schemes are therefore strongly coupled. These schemes have been, for years, the unique way of circumventing the above mentioned numerical instabilities. Somehow, this explains why the development of efficient methods for the resolution of the coupled non-linear systems, arising in implicit coupling, has been (and still is) a very active field of research.

Some of these implicit coupling procedures are described in the next section. The rest of the chapter is devoted to the problem of avoiding strong coupling, without compromising stability. This issue is addressed from two different points of view: via the projection based *semi-implicit* coupling paradigm in §2.3, and through an appropriate weak treatment of the interface conditions at the (space) discrete level in §2.4.

## 2.2 Implicit coupling ([43], [17], [33])

As mentioned in the previous section, explicit coupling schemes may lead to numerical instabilities. These numerical instabilities have been traditionally circumvented by considering fully implicit time-discretizations of (2.1.1)-(2.1.3). For instance, by combining (2.1.4) and (2.1.5) with the following implicit treatment of (2.1.3):

$$\begin{cases} \mathbf{d}^{\text{f},n+1} = \text{Ext}(\mathbf{d}^{n+1}|_{\Sigma}), & \widehat{\mathbf{w}}^{n+1} = \partial_{\tau} \mathbf{d}^{\text{f},n+1} \quad \text{in } \Omega^{\text{f}}, & \Omega^{\text{f},n+1} = (\mathbf{I}_{\Omega^{\text{f}}} + \mathbf{d}^{\text{f},n+1})(\Omega^{\text{f}}), \\ \widehat{\mathbf{u}}^{n+1} = \partial_{\tau} \mathbf{d}^{n+1} \quad \text{on } \Sigma. \\ \mathbf{\Pi}^{n+\frac{1}{2}} \mathbf{n}^{\text{s}} = -J^{n+1} \widehat{\boldsymbol{\sigma}}(\mathbf{u}^{n+1}, \mathbf{p}^{n+1})(\mathbf{F}^{n+1})^{-\text{T}} \mathbf{n} \quad \text{on } \Sigma. \end{cases} \quad (2.2.8)$$

This yields the time-marching procedure summarized in Algorithm 2.2.

---

**Algorithm 2.2** Implicit coupling scheme.

---

1. Solve the coupled problem (2.1.4), (2.1.5) and (2.2.8);
  2. Go to next time-step.
- 

Note that Algorithm 2.2 is an implicit coupling (so, strongly coupled) scheme, since (2.1.3) is enforced exactly at each time-step. As a result, the scheme can be proved to satisfy a discrete counterpart of Lemma 1.1 and, therefore, is energy stable (under a *GCL* condition, see [Mou96, LTM01, LTH03] and [33]). The payoff of this enhanced stability is that the equations (2.1.4), (2.1.5) and (2.2.8) yield a highly nonlinear coupled system at each time-step. As a matter of fact, in addition to the common nonlinearities of the fluid and solid equations, implicit coupling induces geometrical nonlinearities within the fluid equations, due to the dependence of  $\Omega^{\text{f},n+1}$  on  $\mathbf{d}^{\text{f},n+1}$ .

The solution procedures for this coupled non-linear problem (and for coupled problems, in general) are commonly classified into two distinct categories: *monolithic* and *partitioned* (see, *e.g.*, [FPF01]). An *ad hoc* single solver whose purpose is to simultaneously solve (2.1.4)-(2.1.5) and (2.2.8) leads to a monolithic procedure (see, *e.g.*, [RB01, Tez01, Hei04, BZ04, HWD04, FVCJ<sup>+</sup>06, BCHZ08, BQQ08a, KGF<sup>+</sup>09, GKW10]). A solution method that couples independent fluid (2.1.4) and structure (2.1.5) solvers is termed a partitioned procedure (see, *e.g.*, [RVD00, MWR01, LTM01, MS02, GV03, DP06, LVSV06, DDFQ06, KW08, BNV08, JRLS08, DBV09, DSB<sup>+</sup>10]).

**Remark 2.1** *Needless to say that Algorithm 2.1 is a partitioned procedure.*

Monolithic methods are, by construction, less modular than partitioned approaches and do not allow the use of *legacy software*. Partitioned methods, on the contrary, facilitate the reuse of existing code. Moreover, because of their inherent modularity, new models and numerical schemes can be introduced while keeping everything else the same (see, *e.g.*, [WGR07, DdSGB08, AGPT09]). All these advantages come, however, with a price: computational efficiency over a monolithic approach is not necessarily guaranteed (see [HHB08, BQQ08a, KGF<sup>+</sup>09]).

### 2.2.1 Variational setting

In variational form, the non-linear coupled system (2.1.4), (2.1.5) and (2.2.8) can be formulated as the following monolithic problem (see, *e.g.*, [33]): for  $n \geq 0$ , find  $\mathbf{d}^{\text{f},n+1} \in \mathbf{H}_{\Gamma^{\text{in}} \cup \Gamma^{\text{out}}}^1(\Omega^{\text{f}})$ ,  $\widehat{\mathbf{u}}^{n+1} \in \mathbf{H}^1(\Omega^{\text{f}})$ ,  $\widehat{\mathbf{p}}^{n+1} \in L^2(\Omega^{\text{f}})$  and  $\mathbf{d}^{n+1} \in \mathbf{H}_{\Gamma^{\text{d}}}^1(\Omega^{\text{d}})$  with  $\mathbf{u}^{n+1}|_{\Gamma^{\text{in}}} = \mathbf{u}_{\text{in}}(t_{n+1})$ , satisfying

(2.2.8)<sub>1,2</sub> and such that

$$\begin{aligned} & \frac{\rho^f}{\tau} \left( \int_{\Omega^{f,n+1}} \mathbf{u}^{n+1} \cdot \mathbf{v}^f - \int_{\Omega^{f,n}} \mathbf{u}^n \cdot \mathbf{v}^f \right) + \rho^f \int_{\Omega^{f,n+1}} (\mathbf{u}^{n+1} - \mathbf{w}^{n+1}) \cdot \nabla \mathbf{u}^{n+1} \cdot \mathbf{v}^f \\ & - \rho^f \int_{\Omega^{f,n+1}} (\operatorname{div} \mathbf{w}^{n+1}) \mathbf{u} \cdot \mathbf{v}^f + \int_{\Omega^{f,n+1}} \boldsymbol{\sigma}(\mathbf{u}^{n+1}, p^{n+1}) : \nabla \mathbf{v}^f + \int_{\Omega^{f,n+1}} q \operatorname{div} \mathbf{u}^{n+1} \\ & + \frac{2\rho^s}{\tau^2} \int_{\Omega^s} (\mathbf{d}^{n+1} - \mathbf{d}^n - \tau \dot{\mathbf{d}}^n) \cdot \mathbf{v}^s + \int_{\Omega^s} \boldsymbol{\Pi}^{n+\frac{1}{2}} : \nabla \mathbf{v}^s \\ & = - \int_{\Gamma^{\text{out}}} p_{\text{out}}(t_{n+1}) \mathbf{v}^f \cdot \mathbf{n} \quad (2.2.9) \end{aligned}$$

for all  $(\widehat{\mathbf{v}}^f, \mathbf{v}^s, \widehat{q}) \in \mathbf{H}_{\Gamma^{\text{in}}}^1(\Omega^f) \times \mathbf{H}_{\Gamma^{\text{d}}}^1(\Omega^s) \times L^2(\Omega^f)$  with  $\widehat{\mathbf{v}}^f|_{\Sigma} = \mathbf{v}^s|_{\Sigma}$ .

Partitioned methods for the numerical solution of (2.2.9) typically stem from a domain-decomposition reformulation of this problem. Let  $\widehat{L}^f : \mathbf{H}^{\frac{1}{2}}(\Sigma) \rightarrow \mathbf{H}_{\Gamma^{\text{in}} \cup \Gamma^{\text{out}}}^1(\Omega^f)$  be a given continuous linear lift operator and consider the following splitting of the test functions space

$$\begin{aligned} \{(\widehat{\mathbf{v}}^f, \mathbf{v}^s) \in \mathbf{H}_{\Gamma^{\text{in}}}^1(\Omega^f) \times \mathbf{H}_{\Gamma^{\text{d}}}^1(\Omega^s) : \widehat{\mathbf{v}}^f|_{\Sigma} = \mathbf{v}^s|_{\Sigma}\} &= \{(\widehat{\mathbf{v}}^f, \mathbf{0}) : \widehat{\mathbf{v}}^f \in \mathbf{H}_{\Gamma^{\text{in}} \cup \Sigma}^1(\Omega^f)\} \\ &\oplus \{(\widehat{L}^f(\mathbf{v}^s|_{\Sigma}), \mathbf{v}^s) : \widehat{\mathbf{v}}^s \in \mathbf{H}_{\Gamma^{\text{d}}}^1(\Omega^s)\}. \end{aligned}$$

By applying this decomposition to (2.2.9) we recover the following equivalent formulation, involving two coupled subproblems:

$$\begin{cases} \mathcal{F}(\mathbf{d}^{f,n+1}, \widehat{\mathbf{u}}^{n+1}, \widehat{p}^{n+1}, \boldsymbol{\gamma}^{n+1}) = 0, \\ \mathcal{S}(\mathbf{d}^{n+1}, \boldsymbol{\mu}^{n+1}) = 0, \end{cases} \quad (2.2.10)$$

where  $\boldsymbol{\gamma}^{n+1} \stackrel{\text{def}}{=} \mathbf{d}^{n+1}|_{\Sigma}$  is the interface displacement and  $\boldsymbol{\mu}^{n+1} \stackrel{\text{def}}{=} \mathcal{R}^f(\mathbf{d}^{f,n+1}, \widehat{\mathbf{u}}^{n+1}, \widehat{p}^{n+1})$  the variationally consistent representation of the fluid stress at the interface (whose expression is given below). In short, equation (2.2.10)<sub>1</sub> ensure the fluid balance subjected to the interface displacement  $\boldsymbol{\gamma}^{n+1}$ , whereas (2.2.10)<sub>2</sub> ensure the solid balance subjected to the interface fluid stress  $\boldsymbol{\mu}^{n+1}$ .

The fluid operator

$$\mathcal{F} : \mathbf{H}_{\Gamma^{\text{in}} \cup \Gamma^{\text{out}}}^1(\Omega^f) \times \mathbf{H}^1(\Omega^f) \times L^2(\Omega^f) \times \mathbf{H}^{\frac{1}{2}}(\Sigma) \rightarrow (\mathbf{H}_{\Gamma^{\text{in}} \cup \Sigma}^1(\Omega^f) \times L^2(\Omega^f) \times \mathbf{L}^2(\Gamma^{\text{in}} \cup \Sigma) \times \mathbf{L}^2(\Omega^f))',$$

is defined as

$$\begin{aligned} \langle \mathcal{F}(\mathbf{d}^f, \widehat{\mathbf{u}}, \widehat{p}, \boldsymbol{\gamma}), (\widehat{\mathbf{v}}^f, \widehat{q}, \boldsymbol{\xi}, \boldsymbol{\zeta}) \rangle &\stackrel{\text{def}}{=} \frac{\rho^f}{\tau} \left( \int_{\Omega^f(\mathbf{d}^f)} \mathbf{u} \cdot \mathbf{v}^f - \int_{\Omega^{f,n}} \mathbf{u}^n \cdot \mathbf{v}^f \right) + \rho^f \int_{\Omega^f(\mathbf{d}^f)} (\mathbf{u} - \mathbf{w}(\mathbf{d}^f)) \cdot \nabla \mathbf{u} \cdot \mathbf{v}^f \\ & - \rho^f \int_{\Omega^f(\mathbf{d}^f)} (\operatorname{div} \mathbf{w}(\mathbf{d}^f)) \mathbf{u} \cdot \mathbf{v}^f + \int_{\Omega^f(\mathbf{d}^f)} \boldsymbol{\sigma}(\mathbf{u}, p) : \nabla \mathbf{v}^f \\ & + \int_{\Omega^f(\mathbf{d}^f)} q \operatorname{div} \mathbf{v}^f + \int_{\Gamma^{\text{out}}} p_{\text{out}}(t_{n+1}) \mathbf{v}^f \cdot \mathbf{n} + \int_{\Omega^f} (\mathbf{d}^f - \text{Ext}(\boldsymbol{\gamma})) \cdot \boldsymbol{\zeta} \\ & + \int_{\Sigma} (\widehat{\mathbf{u}} - \partial_{\tau} \boldsymbol{\gamma}) \cdot \boldsymbol{\xi} + \int_{\Gamma^{\text{in}}} (\mathbf{u} - \mathbf{u}_{\text{in}}(t_{n+1})) \cdot \boldsymbol{\xi} \end{aligned} \quad (2.2.11)$$

for all  $(\widehat{\mathbf{v}}^f, \widehat{q}, \boldsymbol{\xi}, \boldsymbol{\zeta}) \in \mathbf{H}_{\Gamma^{\text{in}} \cup \Sigma}^1(\Omega^f) \times L^2(\Omega^f) \times \mathbf{L}^2(\Gamma^{\text{in}} \cup \Sigma) \times \mathbf{L}^2(\Omega^f)$ . Here, we have used the notations  $\widehat{\mathbf{w}}(\mathbf{d}^f) \stackrel{\text{def}}{=} (\mathbf{d}^f - \mathbf{d}^{f,n})/\tau$ ,  $\partial_{\tau} \boldsymbol{\gamma} \stackrel{\text{def}}{=} (\boldsymbol{\gamma} - \boldsymbol{\gamma}^n)/\tau$  and  $\Omega^f(\mathbf{d}^f) \stackrel{\text{def}}{=} (\mathbf{I}_{\Omega^f} + \mathbf{d}^f)(\Omega^f)$ .

The interface fluid residual operator  $\mathcal{R}^f : \mathbf{H}^1(\Omega^f) \times \mathbf{H}^1(\Omega^f) \times L^2(\Omega^f) \rightarrow \mathbf{H}^{-\frac{1}{2}}(\Sigma)$  is then defined by

$$\langle \mathcal{R}^f(\mathbf{d}^f, \widehat{\mathbf{u}}, \widehat{p}), \boldsymbol{\lambda} \rangle \stackrel{\text{def}}{=} \langle \mathcal{F}(\mathbf{d}^f, \widehat{\mathbf{u}}, \widehat{p}, \boldsymbol{\gamma}), (\widehat{L}^f \boldsymbol{\lambda}, \mathbf{0}, \mathbf{0}, \mathbf{0}) \rangle \quad (2.2.12)$$

for all  $\boldsymbol{\lambda} \in \mathbf{H}^{\frac{1}{2}}(\Sigma)$ .

**Remark 2.2** Note that the test function  $\widehat{\mathbf{v}}^f$  in (2.2.11) vanishes on the boundary  $\Gamma^{\text{in}} \cup \Sigma$ , so that Dirichlet boundary conditions are strongly imposed. The last two terms of (2.2.11) are not included in practice in the variational formulation. They have been incorporated in the definition of the fluid operator in order to facilitate the presentation. The same observation applies to the third last term.

Similarly, the solid operator

$$\mathcal{S} : \mathbf{H}_{\Gamma^{\text{d}}}^1(\Omega^{\text{s}}) \times \mathbf{H}^{-\frac{1}{2}}(\Sigma) \rightarrow (\mathbf{H}_{\Gamma^{\text{d}}}^1(\Omega^{\text{s}}))',$$

is defined as

$$\langle \mathcal{S}(\mathbf{d}, \boldsymbol{\mu}), \mathbf{v}^{\text{s}} \rangle \stackrel{\text{def}}{=} \frac{2\rho^{\text{s}}}{\tau^2} \int_{\Omega^{\text{s}}} (\mathbf{d} - \mathbf{d}^{\text{n}} - \tau \dot{\mathbf{d}}^{\text{n}}) \cdot \mathbf{v}^{\text{s}} + \frac{1}{2} \int_{\Omega^{\text{s}}} (\boldsymbol{\Pi}(\mathbf{d}) + \boldsymbol{\Pi}(\mathbf{d}^{\text{n}})) : \nabla \mathbf{v}^{\text{s}} + \langle \boldsymbol{\mu}, \mathbf{v}^{\text{s}}|_{\Sigma} \rangle$$

for all  $\mathbf{v}^{\text{s}} \in \mathbf{H}_{\Gamma^{\text{d}}}^1(\Omega^{\text{s}})$ .

Finally, problem (2.2.10) can be reformulated as an interface problem in terms of the nonlinear fluid and solid Steklov-Poincaré operators (see [DDFQ06]). The fluid Steklov-Poincaré operator  $S^f : \mathbf{H}^{\frac{1}{2}}(\Sigma) \rightarrow \mathbf{H}^{-\frac{1}{2}}(\Sigma)$  (also called *Dirichlet-Neumann* map) is defined by

$$S^f(\boldsymbol{\gamma}) \stackrel{\text{def}}{=} \mathcal{R}^f(\mathbf{d}^f(\boldsymbol{\gamma}), \widehat{\mathbf{u}}(\boldsymbol{\gamma}), \widehat{p}(\boldsymbol{\gamma})) \quad \forall \boldsymbol{\gamma} \in \mathbf{H}^{\frac{1}{2}}(\Sigma), \quad (2.2.13)$$

where  $(\mathbf{d}^f(\boldsymbol{\gamma}), \widehat{\mathbf{u}}(\boldsymbol{\gamma}), \widehat{p}(\boldsymbol{\gamma}))$  is the solution of the Dirichlet fluid subproblem:

$$\mathcal{F}(\mathbf{d}^f(\boldsymbol{\gamma}), \widehat{\mathbf{u}}(\boldsymbol{\gamma}), \widehat{p}(\boldsymbol{\gamma}), \boldsymbol{\gamma}) = 0. \quad (2.2.14)$$

In other words,  $S^f(\boldsymbol{\gamma})$  gives the interface fluid stress associated to the displacement  $\boldsymbol{\gamma}$  of the interface. Analogously, the nonlinear solid inverse Steklov-Poincaré operator  $S^{\text{s}} : \mathbf{H}^{-\frac{1}{2}}(\Sigma) \rightarrow \mathbf{H}^{\frac{1}{2}}(\Sigma)$  (also called *Neumann-Dirichlet* map) is given by

$$S^{\text{s}}(\boldsymbol{\mu}) = \mathbf{d}(\boldsymbol{\mu})|_{\Sigma} \quad \forall \boldsymbol{\mu} \in \mathbf{H}^{-\frac{1}{2}}(\Sigma),$$

where  $\mathbf{d}(\boldsymbol{\mu})$  is the solution of the Neumann solid subproblem:

$$\mathcal{S}(\mathbf{d}(\boldsymbol{\mu}), \boldsymbol{\mu}) = 0.$$

From the above definitions, it follows that problem (2.2.10) (or, equivalently, (2.2.9)) is equivalent to the following interface problem: find  $\boldsymbol{\gamma}^{n+1} \in \mathbf{H}^{\frac{1}{2}}(\Sigma)$  such that

$$S^{\text{s}}(S^f(\boldsymbol{\gamma}^{n+1})) = \boldsymbol{\gamma}^{n+1}. \quad (2.2.15)$$

This equation is the so-called interface Dirichlet-Neumann formulation of (2.2.9). The composition of (2.2.16) with the inverse operator  $(S^{\text{s}})^{-1}$ , gives rise to the so-called Steklov-Poincaré equation (see [DDFQ06]):

$$(S^{\text{s}})^{-1}(\boldsymbol{\gamma}^{n+1}) - S^f(\boldsymbol{\gamma}^{n+1}) = 0. \quad (2.2.16)$$

**Remark 2.3** For the sake of conciseness, we have limited the presentation to the time semi-discrete problem (2.2.9). Nevertheless, the discussion also applies to the fully discrete case, for instance, after space discretization of (2.2.9) with finite elements.

## 2.2.2 Partitioned solution methods

These methods are generally based on the application of a particular nonlinear iterative method to the interface formulations (2.2.15) or (2.2.16). In this subsection we discuss some iterative procedures applied to (2.2.15). Some solution methods for the non-linear problem (2.2.16) are introduced in [DDFQ06]. Alternative partitioned procedures, based on Robin-Neumann transmission conditions, have been recently introduced in [BNV08, BNV09].

The formulation (2.2.15) reduces problem (2.2.10) to the determination of a fixed point of the *Dirichlet-Neumann* operator  $S^s \circ S^f$ . This motivates the use of fixed-point (*e.g.*, non-linear Richardson) based iterations, as shown in Algorithm 2.3 (see, *e.g.*, [MWR99, MWR01, LTM01, Nob01, Dep04, SHY06, KW08]), where  $\omega_k \in (0, 1]$  is a given relaxation parameter which is chosen in order to guarantee convergence. At the fully discrete level (*i.e.*, after discretization in space),

---

**Algorithm 2.3** Relaxed Dirichlet-Neumann fixed-point iterations.

---

1. Initialize  $\gamma_0$
2. For  $k \geq 0$  until convergence of  $\gamma_k$ 
  - (a) Solve fluid (including domain update):

$$\boldsymbol{\mu}_k = S^f(\boldsymbol{\gamma}_k);$$

- (b) Solve solid:

$$\tilde{\boldsymbol{\gamma}}_{k+1} = S^s(\boldsymbol{\mu}_k);$$

- (c) Relaxation:

$$\boldsymbol{\gamma}_{k+1} = \omega_k \tilde{\boldsymbol{\gamma}}_{k+1} + (1 - \omega_k) \boldsymbol{\gamma}_k.$$


---

an expression for this parameter (which significantly improves the convergence) is given by the following multi-dimensional Aitken's formula (see [MWR01, Dep04, KW08]):

$$\omega_k = \frac{(\boldsymbol{\gamma}_k - \boldsymbol{\gamma}_{k-1}) \cdot (\tilde{\boldsymbol{\gamma}}_{k+1} - \boldsymbol{\gamma}_k + \tilde{\boldsymbol{\gamma}}_k - \boldsymbol{\gamma}_{k-1})}{|\tilde{\boldsymbol{\gamma}}_{k+1} - \boldsymbol{\gamma}_k + \tilde{\boldsymbol{\gamma}}_k - \boldsymbol{\gamma}_{k-1}|}, \quad k \geq 1. \quad (2.2.17)$$

Algorithm 2.3 can be considered as the simplest way of solving implicit coupling in a partitioned fashion: existing fluid and solid solvers (possibly *black-box*) can be straightforwardly coupled, without significant modifications of the two solvers. The method, however, may suffer from a poor convergence behavior, which is dictated by the amount of added-mass effect in the system. Indeed, increased relaxation is required when the solid density decreases or the domain length increases, which can compromise efficiency in real applications. Theoretical explanations of this issue have been reported in [CGN05] using a simplified model (see also [LTM01, DHV08, JDP09, DAV10]). The limitations of Algorithm 2.3 have led to the development of new variants: for instance, based on the use of transpiration techniques [9], reduced order models [VLDV07], vector extrapolation [KW09], interface artificial compressibility [RVD00, JRLS08, DSB<sup>+</sup>10], and Robin-Neumann coupling [BNV08]. It is worth noticing that these last two variants achieve convergence without the need of relaxation and have a low sensitivity to the added-mass effect.

Alternatively, one can apply a Newton based method to (2.2.15), for a fast convergence towards the solution (see, *e.g.*, [GV03, GVF05, DBV09]). This yields Algorithm 2.4, which involves the

---

**Algorithm 2.4** Interface Dirichlet-Neumann Newton's method.

---

1. Initialize  $\gamma_0$
2. For  $k \geq 0$  until convergence of  $\gamma_k$ 
  - (a) Solve fluid (including domain update):

$$\boldsymbol{\mu}_k = S^f(\gamma_k);$$

- (b) Solve solid:

$$\tilde{\gamma}_{k+1} = S^s(\boldsymbol{\mu}_k);$$

- (c) Evaluate residual:

$$R(\gamma_k) = \tilde{\gamma}_{k+1} - \gamma_k;$$

- (d) Solve tangent problem:

$$D_\gamma R(\gamma_k) \delta \gamma_k = -R(\gamma_k); \quad (2.2.18)$$

- (e) Update rule:

$$\gamma_{k+1} = \gamma_k + \delta \gamma_k.$$


---

Jacobian  $D_\gamma R$  of the coupled operator

$$R(\gamma) \stackrel{\text{def}}{=} S^s(S^f(\gamma)) - \gamma. \quad (2.2.19)$$

In practice, the linearized fluid-structure problem (2.2.18) is solved using an operator-free (*Krylov*) iterative method, as GMRES, which only requires repeated evaluations of  $D_\gamma R(\gamma)$  against given interface displacements  $\boldsymbol{\lambda}$ . In other words, the Jacobian operator  $D_\gamma R(\gamma)$  is not explicitly needed.

Approximate evaluations of  $D_\gamma R(\gamma)\boldsymbol{\lambda}$  (or resolutions of (2.2.18)) lead to the so-called inexact (or quasi-) Newton methods (see, *e.g.*, [GV03, KW08, DBV09]). For instance, we can use as approximation the difference quotient

$$D_\gamma R(\gamma)\boldsymbol{\lambda} \approx \frac{1}{\epsilon} (R(\gamma + \epsilon\boldsymbol{\lambda}) - R(\gamma)), \quad (2.2.20)$$

with  $\epsilon > 0$  a given small enough parameter (see, *e.g.*, [BS94]). Note that this approach facilitates the use of black-box solvers (as Algorithm 2.3), since (2.2.20) only requires residual evaluations. Nevertheless, as noticed in [GV03, Remark 5.1] (see also [KW08]), such a strategy may lead to inefficient Newton iterations.

Using the chain rule, we have

$$D_\gamma R(\gamma)\boldsymbol{\lambda} = D_\mu S^s(S^f(\gamma)) D_\gamma S^f(\gamma)\boldsymbol{\lambda} - \boldsymbol{\lambda}, \quad (2.2.21)$$

so that the exact evaluation of  $D_\gamma R(\gamma)\boldsymbol{\lambda}$  can be split into the following three sequential steps:

- (i) Solve the linearized fluid subproblem:

$$\boldsymbol{\zeta} = D_\gamma S^f(\gamma)\boldsymbol{\lambda};$$

- (ii) Solve the linearized solid subproblem:

$$\boldsymbol{\eta} = D_\mu S^s(S^f(\gamma))\boldsymbol{\zeta}; \quad (2.2.22)$$

(iii) Update:  $D_\gamma R(\gamma)\boldsymbol{\lambda} = \boldsymbol{\eta} - \boldsymbol{\lambda}$ .

Steps (i) and (ii) require the linearized versions of the fluid and solid solvers. Note that step (ii) is standard in solid solvers. Step (i), on the contrary, is non-standard and usually not available in most fluid solvers. For this reason, this step is usually approximated (see, *e.g.*, [GV03, GVF05]).

We have proposed a procedure for the evaluation of  $D_\gamma R(\gamma)\boldsymbol{\lambda}$  based on shape-derivative calculus (see [SZ92, All07]). By derivation of (2.2.13) with respect to  $\gamma$  in the direction  $\boldsymbol{\lambda}$ , we have

$$\begin{aligned} \langle D_\gamma S^f(\gamma)\boldsymbol{\lambda}, \boldsymbol{\theta} \rangle &\stackrel{\text{def}}{=} - \langle D_{\mathbf{d}^f} \mathcal{F}(\mathbf{d}^f(\gamma), \widehat{\mathbf{u}}(\gamma), \widehat{p}(\gamma), \gamma) \delta \widehat{\mathbf{d}}^f, (\widehat{L}^f \boldsymbol{\theta}, \mathbf{0}, \mathbf{0}, \mathbf{0}) \rangle \\ &- \langle D_{(\widehat{\mathbf{u}}, \widehat{p}, \gamma)} \mathcal{F}(\mathbf{d}^f(\gamma), \widehat{\mathbf{u}}(\gamma), \widehat{p}(\gamma), \gamma) (\delta \widehat{\mathbf{u}}, \delta \widehat{p}, \boldsymbol{\lambda}), (\widehat{L}^f \boldsymbol{\theta}, \mathbf{0}, \mathbf{0}, \mathbf{0}) \rangle, \end{aligned} \quad (2.2.23)$$

for all  $\boldsymbol{\theta} \in \mathbf{H}^{\frac{1}{2}}(\Sigma)$  and with the notations  $\delta \widehat{\mathbf{d}}^f \stackrel{\text{def}}{=} D_\gamma \mathbf{d}^f(\gamma)\boldsymbol{\lambda}$ ,  $\delta \widehat{\mathbf{u}} \stackrel{\text{def}}{=} D_\gamma \widehat{\mathbf{u}}(\gamma)\boldsymbol{\lambda}$  and  $\delta \widehat{p} \stackrel{\text{def}}{=} D_\gamma \widehat{p}(\gamma)\boldsymbol{\lambda}$ . While the second derivative in the right hand-side of (2.2.23) is standard (*e.g.*, a classical Fréchet derivative), the cross-Jacobian  $D_{\mathbf{d}^f} \mathcal{F}$  requires shape-derivative calculus, since it involves the derivation with respect to  $\mathbf{d}^f$  of Eulerian integrals over  $\Omega(\mathbf{d}^f)$ . This yields the following expression (see [17] for details):

$$\begin{aligned} \langle D_{\mathbf{d}^f} \mathcal{F}(\mathbf{d}^f, \widehat{\mathbf{u}}, \widehat{p}, \gamma) \delta \widehat{\mathbf{d}}^f, (\widehat{\mathbf{v}}, \widehat{q}, \boldsymbol{\xi}, \boldsymbol{\zeta}) \rangle &= \frac{1}{\tau} \int_{\Omega(\mathbf{d}^f)} \rho^f (\text{div } \delta \mathbf{d}^f) \mathbf{u} \cdot \mathbf{v} + \int_{\Omega(\mathbf{d}^f)} \rho^f (\text{div } \delta \mathbf{d}^f) (\mathbf{u} - \mathbf{w}(\mathbf{d}^f)) \cdot \nabla \mathbf{u} \cdot \mathbf{v} \\ &- \int_{\Omega(\mathbf{d}^f)} \rho^f [\nabla \mathbf{u} \nabla \delta \mathbf{d}^f (\mathbf{u} - \mathbf{w}(\mathbf{d}^f))] \cdot \mathbf{v} - \frac{1}{\tau} \int_{\Omega(\mathbf{d}^f)} \rho^f \delta \mathbf{d}^f \cdot \nabla \mathbf{u} \cdot \mathbf{v} + \int_{\Omega(\mathbf{d}^f)} \boldsymbol{\sigma}(\mathbf{u}, p) [\mathbf{I} \text{div } \delta \mathbf{d}^f - (\nabla \delta \mathbf{d}^f)^T] : \nabla \mathbf{v} \\ &- \int_{\Omega(\mathbf{d}^f)} \mu [\nabla \mathbf{u} \nabla \delta \mathbf{d}^f + (\nabla \delta \mathbf{d}^f)^T (\nabla \mathbf{u})^T] : \nabla \mathbf{v} - \int_{\Omega(\mathbf{d}^f)} q \text{div} \{ \mathbf{u} [\mathbf{I} \text{div } \delta \mathbf{d}^f - (\nabla \delta \mathbf{d}^f)^T] \} + \int_{\Omega} \delta \widehat{\mathbf{d}}^f \cdot \boldsymbol{\zeta}, \end{aligned} \quad (2.2.24)$$

for all  $(\widehat{\mathbf{v}}, \widehat{q}, \boldsymbol{\xi}, \boldsymbol{\zeta}) \in \mathbf{H}_{\Gamma^{\text{in}} \cup \Sigma}^1(\Omega^f) \times L^2(\Omega^f) \times \mathbf{L}^2(\Gamma^{\text{in}} \cup \Sigma) \times \mathbf{L}^2(\Omega^f)$ . Note that the above terms (see also (see [DP06, BCHZ08]) are not standard in a fluid research code, which explains why these terms have been usually neglected, or approximated by finite differences (see, *e.g.*, [Tez01, MS02, Hei04]).

On the other hand,  $\delta \widehat{\mathbf{d}}^f$ ,  $\delta \widehat{\mathbf{u}}$  and  $\delta \widehat{p}$  can be obtained by implicit derivation of (2.2.14). This yields

$$\delta \widehat{\mathbf{d}}^f = D_\gamma \text{Ext}(\gamma)\boldsymbol{\lambda}, \quad (2.2.25)$$

and  $(\delta \widehat{\mathbf{u}}, \delta \widehat{p})$  solve the linearized fluid subproblem:

$$\begin{aligned} \langle D_{(\widehat{\mathbf{u}}, \widehat{p})} \mathcal{F}(\mathbf{d}^f(\gamma), \widehat{\mathbf{u}}(\gamma), \widehat{p}(\gamma), \gamma) (\delta \widehat{\mathbf{u}}, \delta \widehat{p}), (\widehat{\mathbf{v}}, \widehat{q}, \mathbf{0}, \mathbf{0}) \rangle \\ = - \langle D_{\mathbf{d}^f} \mathcal{F}(\mathbf{d}^f(\gamma), \widehat{\mathbf{u}}(\gamma), \widehat{p}(\gamma), \gamma) \delta \widehat{\mathbf{d}}^f, (\widehat{\mathbf{v}}, \widehat{q}, \mathbf{0}, \mathbf{0}) \rangle \end{aligned} \quad (2.2.26)$$

for all  $(\widehat{\mathbf{v}}, \widehat{q}) \in \mathbf{H}_{\Gamma^{\text{in}} \cup \Sigma}^1(\Omega^f) \times L^2(\Omega^f)$ , with the boundary conditions  $\delta \widehat{\mathbf{u}}|_{\Sigma} = \boldsymbol{\lambda}/\tau$ ,  $\delta \widehat{\mathbf{u}}|_{\Gamma^{\text{in}}} = \mathbf{0}$ .

In summary, for each interface displacement  $\boldsymbol{\lambda}$ , the sensitivity  $D_\gamma S_f(\gamma)\boldsymbol{\lambda}$  can be evaluated as follows:

- (i) Compute the fluid domain displacement sensitivity  $\delta \widehat{\mathbf{d}}^f$  from (2.2.25);
- (ii) Compute the fluid sensitivities  $(\delta \widehat{\mathbf{u}}, \delta \widehat{p})$  from (2.2.26) and (2.2.24);
- (iii) Evaluate  $D_\gamma S^f(\gamma)\boldsymbol{\lambda}$  from (2.2.23) and (2.2.24).

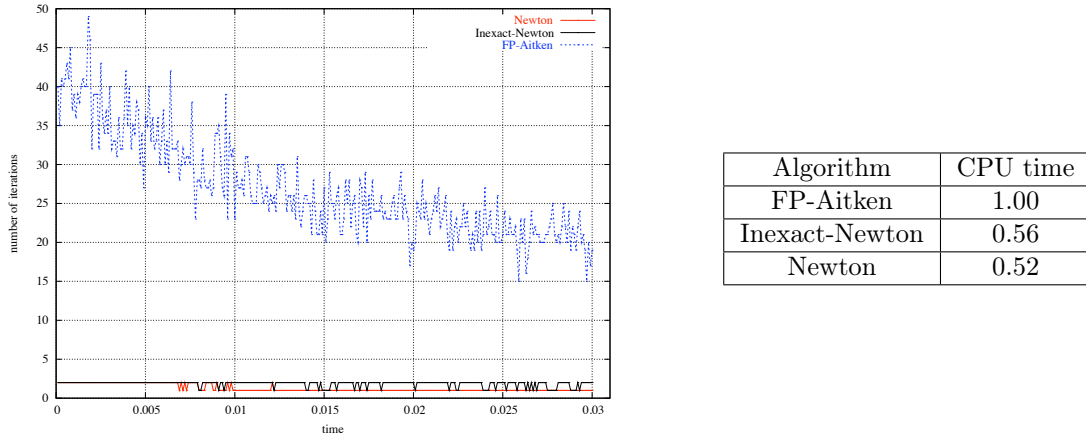


Figure 2.1: *Left*: number of non-linear iterations per time-step. *Right*: dimensionless elapsed CPU time ( $\tau = 10^{-4}$  s).

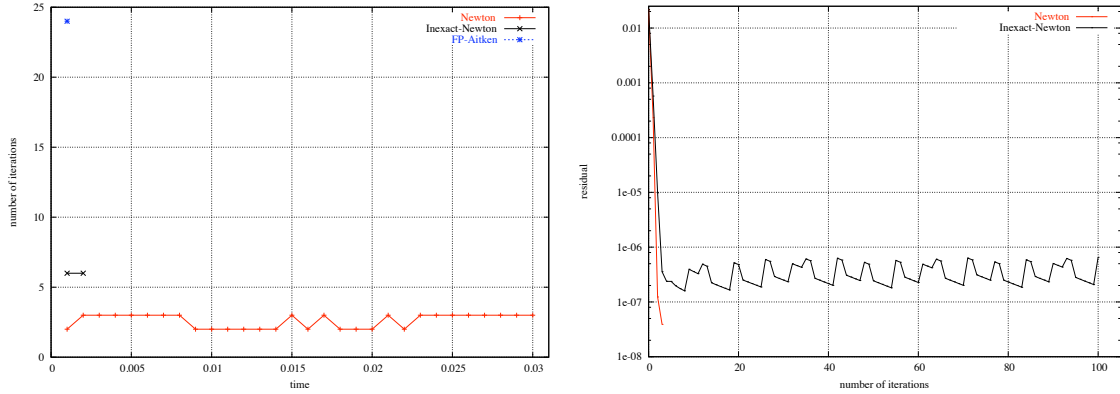


Figure 2.2: *Left*: number of non-linear iterations per time-step. *Right*: Newton residuals ( $\tau = 10^{-3}$  s).

**Remark 2.4** Note that each operator-free evaluation (2.2.21) (one per GMRES iteration in (2.2.18)) requires the resolution of the linearized fluid subproblem (2.2.26) and the linearized solid subproblem (2.2.22).

We conclude this subsection with a few numerical illustrations, involving the coupling of the ALE Navier-Stokes equations with the linear elasticity equations. The reported results correspond to the simulation of a pressure wave propagation in a compliant straight vessel (see [FGNQ01, GV03]). The following procedures are compared:

- FP-Aitken: Algorithm 2.3 with Aitken's dynamic relaxation (2.2.17);
- Newton: Algorithm 2.4 with exact Jacobian evaluation described above;
- Inexact-Newton: Algorithm 2.4 with the inexact Jacobian evaluation obtained by neglecting the cross-Jacobian  $D_{af}\mathcal{F}$  (shape terms) in (2.2.26) and (2.2.24).

Figure 2.1 (left) reports the number of iterations per time-step, performed by each procedure. The superior convergence behavior of both Newton algorithms is clearly visible. Figure 2.1 (right)

shows that both Newton algorithms are about 2 times faster than the fixed-point algorithm (see [17] for a detailed discussion). Note that the cost of each Newton iteration is higher than the cost of a fixed-point iteration (see Remark 2.4).

The impact of the exact Jacobian evaluations in Algorithm 2.4 can be highlighted by increasing the time-step size. Figure 2.2 (left), reports the number of iterations per time-step obtained with  $\tau = 10^{-3}$  s. The fixed-point and inexact-Newton algorithms fail to converge after two time steps (the allowed maximum number of iterations is reached) whereas the exact Newton method converges and requires a low number of iterations. Figure 2.2 (right) shows the evolution of the residual during the iteration process in both Newton algorithms at the third time step. While the exact Newton only requires 3 iterations to reach the convergence threshold, the inexact-Newton algorithm is unable to reduce the residual.

**Remark 2.5** *Numerical evidence shows that the convergence of the GMRES iterations involved in (2.2.18) is sensitive to the amount of added-mass effect in the system (see [BQQ08a]), whereas the number of Newton iterations is practically unaffected. The overall sensitivity is, however, remarkably lower than that of Algorithm 2.3 (see [BQQ08a, §6.1]). Note that, for linear fluid and solid solvers, Algorithms 2.3 and 2.4 can be viewed as, Dirichlet-Neumann preconditioned, Richardson and GMRES iterations, respectively. Hence, the superiority of Algorithms 2.4. At last, let us mention that the added-mass sensitivity of the GMRES iterations can be reduced by the use of Robin-Neumann preconditioners, as proposed in [BNV09].*

## 2.3 Semi-implicit coupling

A first approach to reduce the computational complexity of implicit coupling consists in treating the fluid domain geometry explicitly (see, *e.g.*, [Nob01, SS06, NV08, SM08]). This corresponds to the following *explicit-implicit* treatment of (2.1.3):

$$\mathbf{d}^{\text{f},n+1} = \text{Ext}(\mathbf{d}^n|_{\Sigma}), \quad \widehat{\mathbf{w}}^{n+1} = \partial_{\tau} \mathbf{d}^{\text{f},n+1} \quad \text{in } \Omega^{\text{f}}, \quad \Omega^{\text{f},n+1} = (\mathbf{I}_{\Omega^{\text{f}}} + \mathbf{d}^{\text{f},n+1})(\Omega^{\text{f}}), \quad (2.3.27)$$

$$\begin{cases} \widehat{\mathbf{u}}^{n+1} = \partial_{\tau} \mathbf{d}^{n+1} & \text{on } \Sigma, \\ \mathbf{\Pi}^{n+\frac{1}{2}} \mathbf{n}^{\text{s}} = -J^{n+1} \widehat{\boldsymbol{\sigma}}(\mathbf{u}^{n+1}, p^{n+1})(\mathbf{F}^{n+1})^{-\text{T}} \mathbf{n} & \text{on } \Sigma, \end{cases} \quad (2.3.28)$$

which, combined with (2.1.4) and (2.1.5), yields the time-marching scheme detailed in Algorithm 2.5. Although not fully implicit, this scheme is strongly coupled since the transmission conditions (2.1.3)<sub>2</sub> and (2.1.3)<sub>3</sub> are treated implicitly via (2.3.28). As a result, the stability of Algorithm 2.5 is not compromised by the amount of added-mass effect in the system (see [SS06, NV08, SM08]).

---

**Algorithm 2.5** Semi-implicit coupling scheme via explicit geometry treatment.

---

1. Update the fluid domain configuration (mesh) and velocities via (2.3.27);
  2. Solve the coupled problem (2.1.4), (2.1.5) and (2.3.28);
  3. Go to next time-step.
- 

At each time-step, Algorithm 2.5 involves the resolution of the non-linear system (2.1.4), (2.1.5) and (2.3.28). This coupled problem enters the abstract framework of the previous section (by simply removing the unknown  $\mathbf{d}^{\text{f},n+1}$  in (2.2.10)) and, therefore, can be solved by means of the partitioned procedures discussed therein. Note however that, due to the explicit treatment of

the fluid geometry, the corresponding fluid operator  $S^f$  does not involve the computation of the displacement  $\mathbf{d}^f$ . Hence, the shape terms, involved in the cross-derivative  $D_{\mathbf{d}^f}\mathcal{F}$ , are no longer needed for the exact evaluation of  $D_\gamma S^f$  in the tangent problem (2.2.18) of Algorithm 2.4.

### 2.3.1 Projection-based semi-implicit coupling ([11], [22])

As mentioned above, Algorithm 2.5 is still a strongly coupled scheme, in the sense that (2.1.3)<sub>2</sub> and (2.1.3)<sub>3</sub> are exactly enforced at each time-step. We have proposed a semi-implicit scheme that, without being strongly coupled, exhibits very good stability properties. Basically this scheme relies upon the three following ideas:

- the pressure-structure coupling is treated implicitly in order to avoid instabilities. This observation is motivated by the analysis reported in [CGN05], which shows that explicit pressure-structure coupling yields a scheme whose stability is dictated by the amount of added-mass effect in the system;
- the remaining terms of the fluid equations (dissipation, convection and geometrical nonlinearities) are explicitly coupled to the structure. This drastically reduces the cost of the coupling without compromising the overall stability of the scheme;
- this implicit-explicit coupling can be conveniently performed using a Chorin-Temam projection scheme (see, *e.g.*, [Tem68, Cho69, GMS06]) in the fluid. Indeed, at each time step we propose to couple implicitly the projection sub-step (carried out in a known fluid domain) with the structure, so accounting for the added-mass effect in an implicit way, while the ALE-advection-viscous sub-step is explicitly coupled.

The detailed steps of the proposed semi-implicit coupling scheme are given in Algorithm 2.6. Here, the scheme is presented in its (non-incremental) velocity-correction version and with a pressure-Darcy formulation of the projection step (see [GMS06, Section 4.1]).

**Remark 2.6** *Alternatively, the projection step (2.3.29) can be formulated as the pressure-Poisson problem:*

$$\left\{ \begin{array}{l} -\Delta p^{n+1} = -\frac{\rho^f}{\tau} \operatorname{div} \tilde{\mathbf{u}}^n \quad \text{in } \Omega^{f,n}, \\ \partial_{\mathbf{n}} p^{n+1} = -\rho^f \partial_t \mathbf{u}_{\text{in}}(t_{n+1}) \cdot \mathbf{n} \quad \text{on } \Gamma^{\text{in}}, \\ p^{n+1} = p_{\text{out}}(t_{n+1}) \quad \text{on } \Gamma^{\text{out}}, \\ \partial_{\mathbf{n}} p^{n+1} = -\frac{\rho^f}{\tau} (\partial_\tau \mathbf{d}^{n+1} - \tilde{\mathbf{u}}^n) \cdot \mathbf{n} \quad \text{on } \Sigma^n. \end{array} \right. \quad (2.3.33)$$

Moreover, the divergence free velocity unknown  $\mathbf{u}^{n+1}$  can then be eliminated in (2.3.32) via the relation

$$\frac{\rho^f}{\tau} \mathbf{u}^{n+1} = \frac{\rho^f}{\tau} \tilde{\mathbf{u}}^n - \nabla p^{n+1} \quad \text{in } \Omega^{f,n}.$$

Note that step 2 of Algorithm 2.6 is performed only once per time-step. Step 1 involves the resolution of a coupled problem ((2.3.29)-(2.3.30) or (2.3.33)-(2.3.30)) of reduced computational complexity (compared with step 1 of Algorithm 2.2 or with step 2 of Algorithm 2.5). This coupled problem can be solved, in a partitioned fashion, with simplified versions of the procedures discussed in §2.2. As a matter of fact, the main advantages of Algorithm 2.6 are its simplicity of implementation (specially compared to sophisticated Newton-like methods) and its efficiency compared to the solution procedures presented so far. Obviously, its main limitation is that it assumes the fluid to be solved with a projection-based scheme.

---

**Algorithm 2.6** Semi-implicit coupling projection scheme.

---

1. Implicit step (pressure-structure coupling):

- Fluid projection sub-step:

$$\left\{ \begin{array}{l} \frac{\rho^f}{\tau} (\mathbf{u}^{n+1} - \tilde{\mathbf{u}}^n) + \nabla p^{n+1} = \mathbf{0} \quad \text{in } \Omega^{f,n}, \\ \operatorname{div} \mathbf{u}^{n+1} = 0 \quad \text{in } \Omega^{f,n}, \\ \mathbf{u}^{n+1} \cdot \mathbf{n} = \mathbf{u}_{\text{in}}(t_{n+1}) \cdot \mathbf{n} \quad \text{on } \Gamma^{\text{in}}, \\ p^{n+1} = p_{\text{out}}(t_{n+1}) \quad \text{on } \Gamma^{\text{out}}, \\ \hat{\mathbf{u}}^{n+1} \cdot \mathbf{n} = \partial_\tau \mathbf{d}^{n+1} \cdot \mathbf{n} \quad \text{on } \Sigma. \end{array} \right. \quad (2.3.29)$$

- Solid:

$$\left\{ \begin{array}{l} \rho^s \partial_\tau \dot{\mathbf{d}}^{n+1} - \operatorname{div} \mathbf{\Pi}^{n+\frac{1}{2}} = \mathbf{0} \quad \text{in } \Omega^s, \\ \partial_\tau \mathbf{d}^{n+1} = \dot{\mathbf{d}}^{n+\frac{1}{2}} \quad \text{in } \Omega^s, \\ \mathbf{d}^{n+1} = \mathbf{0} \quad \text{on } \Gamma^{\text{d}}, \\ \mathbf{\Pi}^{n+\frac{1}{2}} \mathbf{n}^s = \mathbf{0} \quad \text{on } \Gamma^{\text{n}}, \\ \mathbf{\Pi}^{n+\frac{1}{2}} \mathbf{n}^s = -J^n \hat{\boldsymbol{\sigma}}(\tilde{\mathbf{u}}^n, p^{n+1}) (\mathbf{F}^n)^{-\text{T}} \mathbf{n} \quad \text{on } \Sigma. \end{array} \right. \quad (2.3.30)$$

2. Explicit step (viscous-structure coupling):

- Update fluid domain:

$$\mathbf{d}^{f,n+1} = \operatorname{Ext}(\mathbf{d}^n|_\Sigma), \quad \hat{\mathbf{w}}^{n+1} = \partial_\tau \mathbf{d}^{f,n+1} \quad \text{in } \Omega^f, \quad \Omega^{f,n+1} = (\mathbf{I}_{\Omega^f} + \mathbf{d}^{f,n+1})(\Omega^f). \quad (2.3.31)$$

- Fluid viscous sub-step:

$$\left\{ \begin{array}{l} \rho^f \frac{\tilde{\mathbf{u}}^{n+1} - \mathbf{u}^{n+1}}{\tau} \Big|_{\mathcal{A}} + \rho^f (\tilde{\mathbf{u}}^n - \mathbf{w}^{n+1}) \cdot \nabla \tilde{\mathbf{u}}^{n+1} - 2\mu \operatorname{div} \boldsymbol{\epsilon}(\tilde{\mathbf{u}}^{n+1}) = \mathbf{0} \quad \text{in } \Omega^{f,n+1}, \\ \tilde{\mathbf{u}}^{n+1} = \mathbf{u}_{\text{in}}(t_{n+1}) \quad \text{on } \Gamma^{\text{in}}, \\ 2\mu \boldsymbol{\epsilon}(\tilde{\mathbf{u}}^{n+1}) \mathbf{n}^f = \mathbf{0} \quad \text{on } \Gamma^{\text{out}}, \\ \hat{\mathbf{u}}^{n+1} = \partial_\tau \mathbf{d}^{n+1} \quad \text{on } \Sigma. \end{array} \right. \quad (2.3.32)$$

3. Go to next time-step.

---

**Remark 2.7** *The ideas presented here can be generalized to other fractional step schemes in the fluid. For instance, extensions in the framework of algebraic factorization methods have been reported in [QQ07, BQQ08b].*

Algorithm 2.6 is based on the following implicit-explicit time discretization of the coupling conditions (2.1.3):

$$\begin{cases} \mathbf{\Pi}^{n+\frac{1}{2}} \mathbf{n}^s = -J^n \widehat{\boldsymbol{\sigma}}(\widetilde{\mathbf{u}}^n, p^{n+1})(\mathbf{F}^n)^{-T} \mathbf{n} & \text{on } \Sigma, \\ \widehat{\mathbf{u}}^{n+1} \cdot \mathbf{n} = \partial_\tau \mathbf{d}^{n+1} \cdot \mathbf{n} & \text{on } \Sigma, \\ \mathbf{d}^{f,n+1} = \text{Ext}(\mathbf{d}^n|_\Sigma), \quad \widehat{\mathbf{w}}^{n+1} = \partial_\tau \mathbf{d}^{f,n+1} & \text{in } \Omega^f, \quad \Omega^{f,n+1} = (\mathbf{I}_{\Omega^f} + \mathbf{d}^{f,n+1})(\Omega^f), \\ \widehat{\mathbf{u}}^{n+1} = \partial_\tau \mathbf{d}^{n+1} & \text{on } \Sigma. \end{cases}$$

Note that (2.1.3)<sub>3</sub> is not exactly enforced at each time-step and, therefore, Algorithm 2.6 is not a strongly coupled scheme.

### Stability analysis (linear case)

The stability of Algorithm 2.6 has been analyzed in the framework of the following linear model problem, coupling the Stokes equations with a linear elastic solid model:

$$\begin{cases} \rho^f \partial_t \mathbf{u} - \mathbf{div} \boldsymbol{\sigma}(\mathbf{u}, p) = \mathbf{0} & \text{in } \Omega^f, \\ \mathbf{div} \mathbf{u} = 0 & \text{in } \Omega^f, \\ \mathbf{u} = \mathbf{u}_{\text{in}} & \text{on } \Gamma^{\text{in}}, \\ \boldsymbol{\sigma}(\mathbf{u}, p) \mathbf{n} = p_{\text{out}} \mathbf{n} & \text{on } \Gamma^{\text{out}}, \end{cases} \quad (2.3.34)$$

$$\begin{cases} \rho^s \partial_{tt} \mathbf{d} - \mathbf{div} \boldsymbol{\sigma}(\mathbf{d}) = \mathbf{0} & \text{in } \Omega^s, \\ \mathbf{d} = \mathbf{0} & \text{on } \Gamma^{\text{d}}, \\ \boldsymbol{\sigma}(\mathbf{d}) \mathbf{n}^s = \mathbf{0} & \text{on } \Gamma^n, \end{cases} \quad (2.3.35)$$

$$\begin{cases} \mathbf{u} = \partial_t \mathbf{d} & \text{on } \Sigma, \\ \boldsymbol{\sigma}(\mathbf{d}) \mathbf{n}^s = -\boldsymbol{\sigma}(\mathbf{u}, p) \mathbf{n} & \text{on } \Sigma. \end{cases} \quad (2.3.36)$$

Though simplified, the linear coupled problem (2.3.34)-(2.3.36) contains the key features of more complex fluid-structure problems involving an incompressible fluid, as regards the stability of the coupling schemes (see, *e.g.*, [CGN05]).

Since the analysis is carried out in the fully discrete case, we need to introduce some notation for the discretization in space. We define  $Q_h^f$  as an internal continuous Lagrange finite element approximation of  $L^2(\Omega^f)$ . Similarly,  $\mathbf{V}_h^f$  (resp.  $\mathbf{V}_{\omega,h}^f$ , with  $\omega \subset \partial\Omega^f$ , and  $\mathbf{V}_H^s$ ) is an internal continuous Lagrange finite element approximation of  $\mathbf{H}^1(\Omega^f)$  (resp.  $\mathbf{H}_\omega^1(\Omega^f)$  and  $\mathbf{H}_{\Gamma^{\text{d}}}^1(\Omega^s)$ ). Since the fluid and solid space discretizations do not necessarily match at the interface  $\Sigma$ , we introduce an interface matching operator  $\Pi_h : \mathbf{V}_H^s(\Sigma) \rightarrow \mathbf{V}_h^f(\Sigma)$ , where  $\mathbf{V}_H^s(\Sigma)$  (resp.  $\mathbf{V}_h^f(\Sigma)$ ) stands for the trace finite element space associated to  $\mathbf{V}_H^s$  (resp.  $\mathbf{V}_h^f$ ). The operator  $\Pi_h$  can be, for instance, the standard Lagrange interpolant (nodal-wise matching) or a projection based operator (see, *e.g.*, [FLLT98, GM98, AG10]).

The fully discretized problem writes as follows: for  $n \geq 0$ ,

1. Implicit step (pressure-structure coupling): find  $(\mathbf{u}_h^{n+1}, p_h^{n+1}, \mathbf{d}_H^{n+1}) \in \mathbf{V}_h^f \times Q_h^f \times \mathbf{V}_H^s$  such

that

$$\begin{cases} \mathbf{u}_h^{n+1} = \mathbf{u}_{\text{in}}(t_{n+1}), & \text{on } \Gamma^{\text{in}}, \\ \mathbf{u}_h^{n+1} = \Pi_h(\partial_\tau \mathbf{d}_H^{n+1}), & \text{on } \Sigma, \\ \frac{\rho^f}{\tau} \int_{\Omega^f} (\mathbf{u}_h^{n+1} - \tilde{\mathbf{u}}_h^n) \cdot \mathbf{v}_h^f - \int_{\Omega^f} p_h^{n+1} \operatorname{div} \mathbf{v}_h^f + \int_{\Omega^f} q_h \operatorname{div} \mathbf{u}_h^{n+1} \\ = - \int_{\Gamma^{\text{out}}} p_{\text{out}} \mathbf{v}_h^f \cdot \mathbf{n} \quad \forall (\mathbf{v}_h^f, q_h) \in \mathbf{V}_{\Sigma \cup \Gamma^{\text{in}}, h}^f \times Q_h^f, \end{cases} \quad (2.3.37)$$

$$\begin{cases} \frac{\rho^s}{\tau^2} \int_{\Omega^s} (\mathbf{d}_H^{n+1} - 2\mathbf{d}_H^n + \mathbf{d}_H^{n-1}) \cdot \mathbf{v}_H^s + a^s(\mathbf{d}_H^{n+1}, \mathbf{v}_H^s) = -\langle \mathcal{R}_\mu(\tilde{\mathbf{u}}_h^n), L_h(\mathbf{v}_H^s) \rangle \\ - \langle \mathcal{R}_p(\mathbf{u}_h^{n+1}, p_h^{n+1}), L_h(\mathbf{v}_H^s|_\Sigma) \rangle \quad \forall \mathbf{v}_H^s \in \mathbf{V}_H^s; \end{cases}$$

2. Explicit step (viscous-structure coupling): find  $\tilde{\mathbf{u}}_h^{n+1} \in \mathbf{V}_h^f$  such that

$$\begin{cases} \tilde{\mathbf{u}}_h^{n+1} = \mathbf{u}_{\text{in}}(t_{n+1}), & \text{on } \Gamma^{\text{in}}, \\ \tilde{\mathbf{u}}_h^{n+1} = \Pi_h(\partial_\tau \mathbf{d}_H^{n+1}), & \text{on } \Sigma, \\ \frac{\rho^f}{\tau} \int_{\Omega^f} (\tilde{\mathbf{u}}_h^{n+1} - \mathbf{u}_h^{n+1}) \cdot \tilde{\mathbf{v}}_h^f + 2\mu \int_{\Omega^f} \boldsymbol{\epsilon}(\tilde{\mathbf{u}}_h^{n+1}) : \boldsymbol{\epsilon}(\tilde{\mathbf{v}}_h^f) = 0 \quad \forall \tilde{\mathbf{v}}_h^f \in \mathbf{V}_{\Sigma \cup \Gamma^{\text{in}}, h}^f. \end{cases} \quad (2.3.38)$$

Here,  $a^s(\cdot, \cdot)$  stands for a general solid stiffness bilinear form and the fluid stress at the interface are given in terms of the (variationally consistent) residuals  $\mathcal{R}_\mu$  and  $\mathcal{R}_p$ , defined as

$$\begin{aligned} \langle \mathcal{R}_\mu(\tilde{\mathbf{u}}_h^{n+1}), \tilde{\mathbf{v}}_h^f \rangle &\stackrel{\text{def}}{=} \frac{\rho^f}{\tau} \int_{\Omega^f} (\tilde{\mathbf{u}}_h^{n+1} - \mathbf{u}_h^{n+1}) \cdot \tilde{\mathbf{v}}_h^f + 2\mu \int_{\Omega^f} \boldsymbol{\epsilon}(\tilde{\mathbf{u}}_h^{n+1}) : \boldsymbol{\epsilon}(\tilde{\mathbf{v}}_h^f), \\ \langle \mathcal{R}_p(\mathbf{u}_h^{n+1}, p_h^{n+1}), \mathbf{v}_h^f \rangle &\stackrel{\text{def}}{=} \frac{\rho^f}{\tau} \int_{\Omega^f} (\mathbf{u}_h^{n+1} - \tilde{\mathbf{u}}_h^n) \cdot \mathbf{v}_h^f - \int_{\Omega^f} p_h^{n+1} \operatorname{div} \mathbf{v}_h^f, \end{aligned}$$

and  $L_h : \mathbf{V}_H^s(\Sigma) \rightarrow \mathbf{V}_h^f$  stands for the standard discrete lifting operator, satisfying  $L_h(\mathbf{b}_H)|_\Sigma = \Pi_h(\mathbf{b}_H|_\Sigma)$  and  $L_h(\mathbf{b}_H)|_{\Gamma^{\text{in}} \cup \Gamma^{\text{out}}} = \mathbf{0}$  for all  $\mathbf{b}_H \in \mathbf{V}_H^s(\Sigma)$ .

**Remark 2.8** Note that, in (2.3.37), we impose  $\mathbf{u}_h^{n+1} = \Pi_h(\partial_\tau \mathbf{d}_H^{n+1})$  on  $\Sigma$  (instead of (2.3.29)<sub>5</sub>) which is also optimal in the framework of finite element approximations (see [Gue96]).

**Remark 2.9** We have considered here a simplified version of the coupling scheme given by Algorithm 2.6. The fluid domain being fixed, no ALE terms appear in the equations. Moreover, we assumed that the solid equations are discretized in time with a (non-conservative) leap-frog scheme. In spite of that, the main feature of the coupling scheme is preserved: the diffusion step is explicitly coupled with the structure. Without these simplifications, the stability analysis does not seem to be straightforward.

Let

$$E^n \stackrel{\text{def}}{=} \frac{\rho^f}{2} \|\mathbf{u}_h^n\|_{0, \Omega^f}^2 + \frac{\rho^s}{2} \|\partial_\tau \mathbf{d}_H^n\|_{0, \Omega^s}^2 + \frac{1}{2} a^s(\mathbf{d}_H^n, \mathbf{d}_H^n),$$

be the discrete energy of the system at time-step  $n$ . In what follows, the symbol  $\lesssim$  indicates an inequality up to a multiplicative constant independent of the discretization and physical parameters.

The following theorem provides the conditional stability of the coupling scheme (2.3.37)-(2.3.38).

**Theorem 2.1** *Assume that  $p_{\text{out}} = 0$ ,  $\mathbf{u}_{\text{in}} = \mathbf{0}$ ,  $\mathcal{R}_\mu(\tilde{\mathbf{u}}_h^0) = 0$  and that the interface matching operator  $\Pi_h : V_H^s(\Sigma) \rightarrow V_h^f(\Sigma)$  is  $L^2$ -stable. Then, under the condition*

$$\left( \rho^f \frac{h}{H^\alpha} + 2 \frac{\mu\tau}{hH^\alpha} \right) \lesssim \rho^s, \quad \text{with } \alpha \stackrel{\text{def}}{=} \begin{cases} 0, & \text{if } \overline{\Omega^s} = \Sigma, \\ 1, & \text{if } \overline{\Omega^s} \neq \Sigma, \end{cases} \quad (2.3.39)$$

there holds,

$$E^n + \mu \sum_{m=0}^{n-1} \tau \|\epsilon(\tilde{\mathbf{u}}_h^{m+1})\|_{0,\Omega^f}^2 \lesssim E^0$$

for  $n \geq 1$ .

Some observations are now in order:

- The assumption on the  $L^2$ -stability of the interface matching operator is satisfied by the standard finite element interpolation operator, for example, whenever the fluid interface triangulation is a sub-triangulation of the solid interface triangulation. This includes, in particular, the case of interface matching meshes. By construction, a mortar based matching operator also fulfills that assumption (see [BMP93]).
- The sufficient condition (2.3.39) can be satisfied by reducing the ratios  $h/H^\alpha$  and  $\tau/(hH^\alpha)$ . The later might be thought as a CFL-like condition. Note that this is a major advantage compared to the (in)stability condition (2.1.7) for the explicit-coupling scheme.
- In the case  $\overline{\Omega^s} = \Sigma$  (thin structure model), *i.e.*,  $\alpha = 0$ , condition (2.3.39) becomes independent of the solid mesh size  $H$ . In particular, we may set  $H = h$ , and stabilize the scheme by reducing  $h$  (and  $\tau$ ).
- In the case  $\overline{\Omega^s} \neq \Sigma$ , *i.e.*,  $\alpha = 1$ , the stability of the scheme can be ensured provided that the fluid mesh size  $h$  is small enough compared to the structure mesh size  $H$ . Numerical simulations performed in 2D and 3D, with  $h = H$ , showed however that this condition seems to be not necessary, when dealing with physiological parameters.

**Remark 2.10** *We refer to [AG10] for an a priori error analysis of (2.3.37)-(2.3.38) which ensures an overall  $O(\tau^{\frac{1}{2}} + h^k + H^m + h^l)$  convergence rate in the energy norm. Here,  $k, m$  are respectively the polynomial degrees of the fluid and solid discretizations and  $l$  depends on the choice of the matching operator  $\Pi_h$ .*

COUPLING	ALGORITHM	CPU time
Implicit	FP-Aitken	24.86
	Inexact-Newton	6.05
	Newton	4.77
Semi-Implicit	Newton	1

Table 2.1: Elapsed CPU time (dimensionless): straight cylinder, 50 time steps of length  $\tau = 2 \times 10^{-4}$  s.

We conclude this section with a few numerical illustrations, involving the coupling of the ALE Navier-Stokes equations with a non-linear shell model (based on MITC4 shell elements [CB03]).

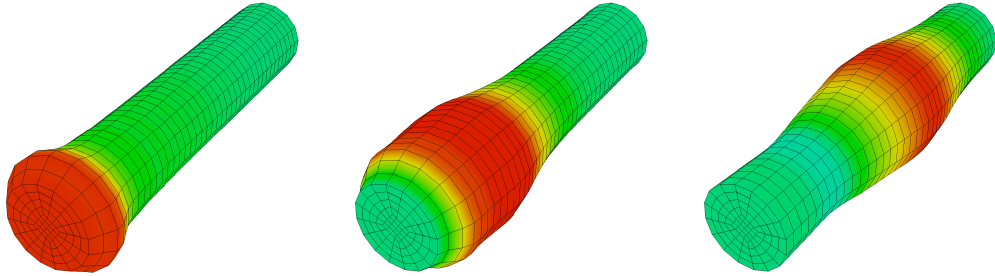


Figure 2.3: Pressure wave propagation in a straight vessel. Snapshots of the pressure at  $t = 1.8 \times 10^{-3}$ ,  $5.8 \times 10^{-3}$  and  $9.8 \times 10^{-3}$ .

COUPLING	CPU time
Implicit	9.3
Semi-Implicit	1.0

Table 2.2: Elapsed CPU time (dimensionless): blood flow in a idealized abdominal aortic aneurysm, 2 cardiac cycles (1000 time-steps of length  $\tau = 1.68 \times 10^{-3}$  s).

Table 2.1 shows a comparison of the elapsed CPU times (dimensionless) obtained in the simulation of a pressure wave propagation in a compliant straight vessel (see [FGNQ01, GV03]). Some snapshots of the pressure field are given in Figure 2.3. We can notice that the semi-implicit coupling is 4.7 times faster than the best implicit coupling. This performance rises much more when considering a more physiological situation. In Table 2.2 we have reported the the elapsed CPU times (dimensionless) obtained in the simulation of two cardiac cycles of blood flow in a idealized abdominal aortic aneurysm (see Figure 2.4 (left)) under physiological conditions (see [SSCL06]). The accuracy of the semi-implicit coupling scheme is highlighted in Figure 2.4 (right), in terms of the outflow rate.

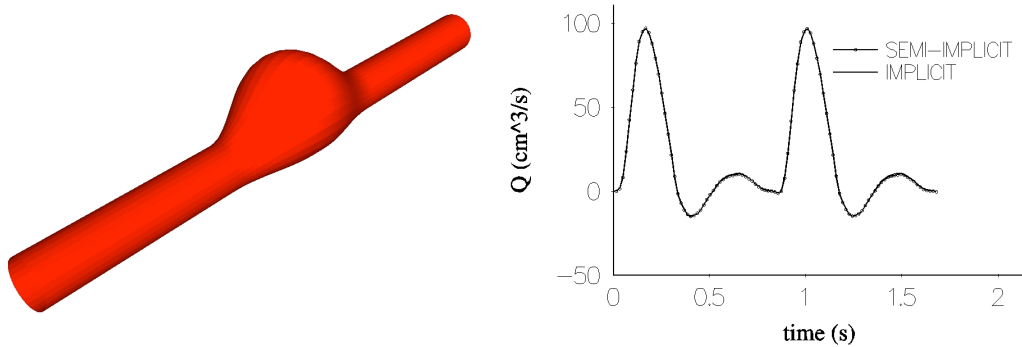


Figure 2.4: *Left*: idealized abdominal aortic aneurysm. *Right*: comparison of implicit and semi-implicit coupling schemes, outflow rate.

## 2.4 Nitsche's based interface treatment

The coupling schemes described in the previous sections treat the interface condition (2.1.3)<sub>2</sub> as a (strongly imposed) Dirichlet boundary condition in the fluid, and (2.1.3)<sub>3</sub> as a Neumann boundary condition in the solid, respectively. We shall see, in this section, that an appropriate weak treatment of these interface conditions, based on Nitsche's interface method [BHS03, Han05], benefits from:

- a specific treatment of the viscous contributions;
- further insights on the instability of explicit coupling (Algorithm 2.1).

These key features motivated the derivation of a *stabilized* explicit coupling scheme (§2.4.1) and of a new semi-implicit coupling scheme (§2.4.2), whose stability properties are independent of the added-mass effect.

### 2.4.1 Stabilized explicit coupling ([7], [20])

For the sake of simplicity and without loss of generality (see Remark 2.18 below), in this subsection we limit the presentation to the case of the linear coupled problem (2.3.34)-(2.3.36). We shall also make use of some of the notations introduced in §2.3.1 for the discretization in space.

#### Space semi-discretization: interface Nitsche's formulation

Originally, Nitsche's method [Nit71] is a technique for enforcing Dirichlet boundary conditions in a weak sense (instead of being built into the finite element space). The method has recently been generalized to other boundary conditions [JS09]. The extension of Nitsche's method to the approximation of elliptic and parabolic problems with discontinuous piecewise polynomials is known as *discontinuous Galerkin* (DG) method (see, *e.g.*, [Bak77, Whe78, Arn82, ABCM00]). In [BHS03], Nitsche's method was proposed for the approximation of an interface problem arising in the framework of domain decomposition with non-matching grids. Since then, it has then been extended to different multi-physics problems (see, *e.g.*, [BZ06, BH07], and [Han05] for a review). In the context of fluid-structure interaction, using implicit coupling, some results are given for vibration problems (acoustics) in [HH03] and for transient fluid-structure interaction problems with moving fluid domains in [HHS04].

A semi-discrete in space Nitsche's interface formulation of (2.3.34)-(2.3.36) can be formulated as follows: find  $(\mathbf{u}_h, p_h, \mathbf{d}_h, \dot{\mathbf{d}}_h) \in \mathbf{V}_h^f \times Q_h \times [\mathbf{V}_h^s]^2$ , with  $\mathbf{u}_h = \mathbf{u}_{\text{in}}$  on  $\Gamma^{\text{in}}$ , such that

$$\begin{aligned} A^f((\mathbf{u}_h, p_h), (\mathbf{v}_h^f, q_h)) + A^s((\mathbf{d}_h, \dot{\mathbf{d}}_h), (\mathbf{v}_h^s, \mathbf{r}_h)) \\ - \int_{\Sigma} \boldsymbol{\sigma}(\mathbf{u}_h, p_h) \mathbf{n} \cdot (\mathbf{v}_h^f - \mathbf{v}_h^s) - \int_{\Sigma} (\mathbf{u}_h - \partial_t \mathbf{d}_h) \cdot \boldsymbol{\sigma}(\mathbf{v}_h^f, -q_h) \mathbf{n} \\ + \frac{\gamma \mu}{h} \int_{\Sigma} (\mathbf{u}_h - \partial_t \mathbf{d}_h) \cdot (\mathbf{v}_h^f - \mathbf{v}_h^s) = - \int_{\Gamma^{\text{out}}} p_{\text{out}} \mathbf{v}_h^f \cdot \mathbf{n} \end{aligned} \quad (2.4.40)$$

for all  $(\mathbf{v}_h^f, q_h, \mathbf{v}_h^s, \mathbf{r}_h) \in \mathbf{V}_{\Gamma^{\text{in}}, h}^f \times Q_h \times [\mathbf{V}_h^s]^2$ . Here,  $\gamma > 0$  is a dimensionless penalty parameter (specified below), and the fluid and solid volume contributions are given by

$$\begin{aligned} A^f((\mathbf{u}_h, p_h), (\mathbf{v}_h^f, q_h)) &\stackrel{\text{def}}{=} \rho^f \int_{\Omega^f} \partial_t \mathbf{u}_h \cdot \mathbf{v}_h^f + 2\mu \int_{\Omega^f} \boldsymbol{\epsilon}(\mathbf{u}_h) : \boldsymbol{\epsilon}(\mathbf{v}_h^f) - \int_{\Omega^f} p_h \operatorname{div} \mathbf{v}_h^f + \int_{\Omega^f} q_h \operatorname{div} \mathbf{u}_h, \\ A^s((\mathbf{d}_h, \dot{\mathbf{d}}_h), (\mathbf{v}_h^s, \mathbf{r}_h)) &\stackrel{\text{def}}{=} \rho^s \int_{\Omega^s} \partial_t \dot{\mathbf{d}}_h \cdot \mathbf{v}_h^s + a^s(\mathbf{d}_h, \mathbf{v}_h^s) + \rho^s \int_{\Omega^f} (\dot{\mathbf{d}}_h - \partial_t \mathbf{d}_h) \cdot \mathbf{r}_h. \end{aligned}$$

**Remark 2.11** Note that, in (2.4.40),  $\mathbf{u}_h$  and  $\partial_t \mathbf{d}_h$  (and  $\mathbf{v}_h^f$  and  $\mathbf{v}_h^s$ ) do not necessarily match at the interface (interface DG formulation). The interface integrals involving the fluid stress  $\boldsymbol{\sigma}(\mathbf{u}_h, p_h) \mathbf{n}$  are computed face-wise, as broken integrals.

By taking alternatively  $(\mathbf{v}_h^f, q_h) = \mathbf{0}$  and  $\mathbf{v}_h^s = \mathbf{r}_h = \mathbf{0}$  in (2.4.40), this monolithic problem can be reformulated (in a partitioned fashion) in terms of two interface coupled problems:

- Solid subproblem: find  $(\mathbf{d}_h, \dot{\mathbf{d}}_h) \in [\mathbf{V}_h^s]^2$  such that

$$A^s((\mathbf{d}_h, \dot{\mathbf{d}}_h), (\mathbf{v}_h^s, \mathbf{r}_h)) + \frac{\gamma\mu}{h} \int_{\Sigma} \partial_t \mathbf{d}_h \cdot \mathbf{v}_h^s = \frac{\gamma\mu}{h} \int_{\Sigma} \mathbf{u}_h \cdot \mathbf{v}_h^s - \int_{\Sigma} \boldsymbol{\sigma}(\mathbf{u}_h, p_h) \mathbf{n} \cdot \mathbf{v}_h^s \quad (2.4.41)$$

for all  $(\mathbf{v}_h^s, \mathbf{r}_h) \in [\mathbf{V}_h^s]^2$ ;

- Fluid subproblem: find  $(\mathbf{u}_h, p_h) \in \mathbf{V}_h^f \times Q_h$ , with  $\mathbf{u}_h = \mathbf{u}_{\text{in}}$  on  $\Gamma^{\text{in}}$ , such that

$$\begin{aligned} A^f((\mathbf{u}_h, p_h), (\mathbf{v}_h^f, q_h)) - \int_{\Sigma} \boldsymbol{\sigma}(\mathbf{u}_h, p_h) \mathbf{n} \cdot \mathbf{v}_h^f - \int_{\Sigma} \mathbf{u}_h \cdot \boldsymbol{\sigma}(\mathbf{v}_h^f, -q_h) \mathbf{n} + \frac{\gamma\mu}{h} \int_{\Sigma} \mathbf{u}_h \cdot \mathbf{v}_h^f \\ = - \int_{\Sigma} \partial_t \mathbf{d}_h \cdot \boldsymbol{\sigma}(\mathbf{v}_h^f, -q_h) \mathbf{n} + \frac{\gamma\mu}{h} \int_{\Sigma} \partial_t \mathbf{d}_h \cdot \mathbf{v}_h - \int_{\Gamma^{\text{out}}} p_{\text{out}} \mathbf{v}_h^f \cdot \mathbf{n} \end{aligned} \quad (2.4.42)$$

for all  $(\mathbf{v}_h, q_h) \in \mathbf{V}_{\Gamma^{\text{in}}, h}^f \times Q_h$ .

### Time semi-discretization: implicit and explicit coupling

As in §2.1, we consider a first order backward difference discretization in the fluid and a mid-point rule for the structure. The fully discrete fluid and solid volume terms at time-step  $n$  are then given by

$$\begin{aligned} A_{\tau}^f((\mathbf{u}_h^{n+1}, p_h^{n+1}), (\mathbf{v}_h^f, q_h)) &\stackrel{\text{def}}{=} \rho^f \int_{\Omega^f} \partial_{\tau} \mathbf{u}_h^{n+1} \cdot \mathbf{v}_h^f + 2\mu \int_{\Omega^f} \boldsymbol{\epsilon}(\mathbf{u}_h^{n+1}) : \boldsymbol{\epsilon}(\mathbf{v}_h^f) - \int_{\Omega^f} p_h^{n+1} \text{div } \mathbf{v}_h^f \\ &\quad + \int_{\Omega^f} q_h \text{div } \mathbf{u}_h^{n+1}, \\ A_{\tau}^s((\mathbf{d}_h^{n+1}, \dot{\mathbf{d}}_h^{n+1}), (\mathbf{v}_h^s, \mathbf{r}_h)) &\stackrel{\text{def}}{=} \rho^s \int_{\Omega^s} \partial_{\tau} \dot{\mathbf{d}}_h^{n+1} \cdot \mathbf{v}_h^s + a^s(\mathbf{d}_h^{n+\frac{1}{2}}, \mathbf{v}_h^s) + \rho^s \int_{\Omega^s} (\dot{\mathbf{d}}_h^{n+\frac{1}{2}} - \partial_{\tau} \mathbf{d}_h^{n+1}) \cdot \mathbf{r}_h \end{aligned}$$

and (2.4.41)-(2.4.42) can be discretized in time as follows: for  $n \geq 0$ ,

- Solid subproblem: find  $(\mathbf{d}_h^{n+1}, \dot{\mathbf{d}}_h^{n+1}) \in [\mathbf{V}_h^s]^2$  such that

$$A_{\tau}^s((\mathbf{d}_h^{n+1}, \dot{\mathbf{d}}_h^{n+1}), (\mathbf{v}_h^s, \mathbf{r}_h)) + \frac{\gamma\mu}{h} \int_{\Sigma} \partial_{\tau} \mathbf{d}_h^{n+1} \cdot \mathbf{v}_h^s = \frac{\gamma\mu}{h} \int_{\Sigma} \mathbf{u}_h^* \cdot \mathbf{v}_h^s - \int_{\Sigma} \boldsymbol{\sigma}(\mathbf{u}_h^*, p_h^*) \mathbf{n} \cdot \mathbf{v}_h^s \quad (2.4.43)$$

for all  $(\mathbf{v}_h^s, \mathbf{r}_h) \in [\mathbf{V}_h^s]^2$ ;

- Fluid subproblem: find  $(\mathbf{u}_h^{n+1}, p_h^{n+1}) \in \mathbf{V}_h^f \times Q_h$ , with  $\mathbf{u}_h^{n+1} = \mathbf{u}_{\text{in}}(t_{n+1})$  on  $\Gamma^{\text{in}}$ , such that

$$\begin{aligned} A_{\tau}^f((\mathbf{u}_h^{n+1}, p_h^{n+1}), (\mathbf{v}_h^f, q_h)) - \int_{\Sigma} \boldsymbol{\sigma}(\mathbf{u}_h^*, p_h^*) \mathbf{n} \cdot \mathbf{v}_h^f - \int_{\Sigma} \mathbf{u}_h^{n+1} \cdot \boldsymbol{\sigma}(\mathbf{v}_h^f, -q_h) \mathbf{n} + \frac{\gamma\mu}{h} \int_{\Sigma} \mathbf{u}_h^{n+1} \cdot \mathbf{v}_h^f \\ = - \int_{\Sigma} \partial_{\tau} \mathbf{d}_h^{n+1} \cdot \boldsymbol{\sigma}(\mathbf{v}_h^f, -q_h) \mathbf{n} + \frac{\gamma\mu}{h} \int_{\Sigma} \partial_{\tau} \mathbf{d}_h^{n+1} \cdot \mathbf{v}_h^f - \int_{\Gamma^{\text{out}}} p_{\text{out}} \mathbf{v}_h^f \cdot \mathbf{n} \end{aligned} \quad (2.4.44)$$

for all  $(\mathbf{v}_h^f, q_h) \in \mathbf{V}_{\Gamma^{\text{in}}, h}^f \times Q_h$ .

If  $(\mathbf{u}_h^*, p_h^*) = (\mathbf{u}_h^{n+1}, p_h^{n+1})$ , the scheme (2.4.43)-(2.4.44) corresponds to an implicit coupling scheme. On the contrary, for  $(\mathbf{u}_h^*, p_h^*) = (\mathbf{u}_h^n, p_h^n)$  the coupling scheme is explicit (*i.e.*, loosely coupled).

Let  $E^n$  denote the total discrete energy of the system at the time level  $n$ , defined by

$$E^n \stackrel{\text{def}}{=} \frac{\rho_f}{2} \|\mathbf{u}_h^n\|_{0,\Omega_f}^2 + \frac{\rho_s}{2} \|\dot{\mathbf{d}}_h^n\|_{0,\Omega_s}^2 + \frac{1}{2} a^s(\mathbf{d}_h^n, \mathbf{d}_h^n).$$

The next result summarizes the energy based stability of the coupling schemes given by (2.4.43)-(2.4.44).

**Theorem 2.2** *Assume that the fluid-structure system is isolated (*i.e.*,  $\mathbf{u}_{\text{in}} = \mathbf{0}$  and  $p_{\text{out}} = 0$ ) and let  $(\mathbf{u}_h^{n+1}, p_h^{n+1}, \mathbf{d}_h^{n+1}, \dot{\mathbf{d}}_h^{n+1})$  be given by (2.4.43)-(2.4.44).*

- *Implicit coupling: For  $(\mathbf{u}_h^*, p_h^*) = (\mathbf{u}_h^{n+1}, p_h^{n+1})$ ,  $\gamma \geq 16C_{\text{TI}}$  and  $n \geq 1$ , there holds*

$$E^n + \mu \sum_{m=0}^{n-1} \tau \|\boldsymbol{\epsilon}(\mathbf{u}_h^{m+1})\|_{0,\Omega_f}^2 + \frac{\gamma\mu}{h} \sum_{m=0}^{n-1} \tau \|\mathbf{u}_h^{m+1} - \partial_\tau \mathbf{d}_h^{m+1}\|_{0,\Sigma}^2 \lesssim E^0;$$

- *Explicit coupling: For  $(\mathbf{u}_h^*, p_h^*) = (\mathbf{u}_h^n, p_h^n)$ ,  $\gamma \geq 256C_{\text{TI}}$  and  $n \geq 1$ , there holds*

$$\begin{aligned} E^n + \mu \sum_{m=0}^{n-1} \tau \|\boldsymbol{\epsilon}(\mathbf{u}_h^{m+1})\|_{0,\Omega_f}^2 + \frac{\gamma\mu}{h} \sum_{m=0}^{n-1} \tau \|\mathbf{u}_h^{m+1} - \partial_\tau \mathbf{d}_h^{m+1}\|_{0,\Sigma}^2 + \frac{\gamma\mu\tau}{h} \|\mathbf{u}_h^n\|_{0,\Sigma}^2 \\ \lesssim E^0 + \frac{\gamma\mu\tau}{h} \|\mathbf{u}_h^0\|_{0,\Sigma}^2 + \mu \|\boldsymbol{\epsilon}(\mathbf{u}_h^0)\|_{0,\Omega_f}^2 + \frac{h}{\gamma\mu} \sum_{m=0}^{n-1} \tau \|p_h^{m+1} - p_h^m\|_{0,\Sigma}^2. \end{aligned} \quad (2.4.45)$$

As expected implicit coupling is unconditionally stable. As regards explicit coupling, Theorem 2.2 shows that the Nitsche interface penalty and the viscous dissipation control the artificial interface viscous perturbation, generated by the explicit treatment of the coupling. Unfortunately, the artificial interface pressure contribution cannot be directly controlled by the discrete energy of the system  $E^n$ , since we not have control on the time pressure fluctuations at the interface. Somehow this illustrates the already mentioned infamous numerical instability featured by the explicit coupling scheme, when dealing with incompressible fluids (see §2.1 and [CGN05, FWR07]). Yet, the energy estimate (2.4.45) suggests that the scheme can be *stabilized* by the addition of perturbations giving enough control on the time pressure fluctuations at the interface.

**Remark 2.12** *The consistency term  $-\int_\Sigma \boldsymbol{\sigma}(\mathbf{u}_h^n, p_h^n) \mathbf{n} \cdot \mathbf{v}_h$  in (2.4.44) could also be evaluated at time level  $n+1$ , as originally proposed in [5]. However, in this case the artificial interface viscous perturbation can not be controlled by the viscous dissipation and the Nitsche's penalty term.*

**Remark 2.13** *The energy estimate (2.4.45) still remains valid if we neglect the viscous contribution of the (symmetrizing) term  $-\int_\Sigma (\mathbf{u}_h^{n+1} - \partial_\tau \mathbf{d}_h^{n+1}) \cdot \boldsymbol{\sigma}(\mathbf{v}_h^f, -q_h) \mathbf{n}$  in (2.4.44), giving the consistent term  $\int_\Sigma q_h (\mathbf{u}_h^{n+1} - \partial_\tau \mathbf{d}_h^{n+1}) \cdot \mathbf{n}$ . As a result, the explicit coupling scheme (and the mentioned variant) can be formally viewed as a space discrete counterpart of the following Robin-Robin based explicit treatment of (2.3.36):*

$$\left. \begin{aligned} \boldsymbol{\sigma}(\mathbf{d}^{n+\frac{1}{2}}) \mathbf{n}^s + \frac{\gamma\mu}{h} \partial_\tau \mathbf{d}^{n+1} &= \frac{\gamma\mu}{h} \mathbf{u}^n - \boldsymbol{\sigma}(\mathbf{u}^n, p^n) \mathbf{n} \\ \boldsymbol{\sigma}(\mathbf{u}^{n+1}, p^{n+1}) \mathbf{n} + \frac{\gamma\mu}{h} \mathbf{u}^{n+1} &= \frac{\gamma\mu}{h} \partial_\tau \mathbf{d}^{n+1} + \boldsymbol{\sigma}(\mathbf{u}^n, p^n) \mathbf{n} \end{aligned} \right\} \quad \text{on } \Sigma. \quad (2.4.46)$$

*We will come back to this observation in the works summarized in §2.4.2 and in §3.5.2.*

**Remark 2.14** Note that the scaling  $\gamma\mu/h$  of the so-called Robin parameter in (2.4.46) is provided by the Nitsche interface method. This choice differs from the Robin-Robin scaling proposed in [BNV08], based on simplified models and which aims at accelerating partitioned iterative solution methods within a fully implicit coupling framework. At last, it is worth mentioning that (2.4.46) also differs from recent Robin-Robin procedures proposed for time-dependent problems, in the framework of waveform relaxation methods (see, e.g., [GH07]).

### Stabilized explicit coupling

The spurious oscillations of the fluid pressure at the interface, arising in the energy estimate (2.4.45), can be controlled by the following weakly consistent penalty term:

$$S(p_h^{n+1}, q_h) \stackrel{\text{def}}{=} \frac{\gamma_0 h}{\gamma\mu} \int_{\Sigma} (p_h^{n+1} - p_h^n) q_h, \quad (2.4.47)$$

with  $\gamma_0 > 0$  a (dimensionless) parameter to be chosen sufficiently large (see Theorem 2.3). Hence we propose to add (2.4.47) to the fluid subproblem (2.4.44). The resulting stabilized explicit coupling scheme is given in Algorithm 2.7.

---

#### Algorithm 2.7 Stabilized explicit coupling.

---

1. Solid subproblem: find  $(\mathbf{d}_h^{n+1}, \dot{\mathbf{d}}_h^{n+1}) \in [\mathbf{V}_h^s]^2$  such that

$$A_{\tau}^s((\mathbf{d}_h^{n+1}, \dot{\mathbf{d}}_h^{n+1}), (\mathbf{v}_h^s, \mathbf{r}_h)) + \frac{\gamma\mu}{h} \int_{\Sigma} \partial_{\tau} \mathbf{d}_h^{n+1} \cdot \mathbf{v}_h^s = \frac{\gamma\mu}{h} \int_{\Sigma} \mathbf{u}_h^n \cdot \mathbf{v}_h^s - \int_{\Sigma} \boldsymbol{\sigma}(\mathbf{u}_h^n, p_h^n) \mathbf{n} \cdot \mathbf{v}_h^s$$

for all  $(\mathbf{v}_h^s, \mathbf{r}_h) \in [\mathbf{V}_h^s]^2$ ;

2. Fluid subproblem: find  $(\mathbf{u}_h^{n+1}, p_h^{n+1}) \in \mathbf{V}_h^f \times Q_h$ , with  $\mathbf{u}_h^{n+1} = \mathbf{u}_{\text{in}}(t_{n+1})$  on  $\Gamma^{\text{in}}$ , such that

$$\begin{aligned} & A_{\tau}^f((\mathbf{u}_h^{n+1}, p_h^{n+1}), (\mathbf{v}_h^f, q_h)) - \int_{\Sigma} \mathbf{u}_h^{n+1} \cdot \boldsymbol{\sigma}(\mathbf{v}_h^f, -q_h) \mathbf{n} + \frac{\gamma\mu}{h} \int_{\Sigma} \mathbf{u}_h^{n+1} \cdot \mathbf{v}_h^f + S(p_h^{n+1}, q_h) \\ &= \int_{\Sigma} \boldsymbol{\sigma}(\mathbf{u}_h^n, p_h^n) \mathbf{n} \cdot \mathbf{v}_h^f - \int_{\Sigma} \partial_{\tau} \mathbf{d}_h^{n+1} \cdot \boldsymbol{\sigma}(\mathbf{v}_h^f, -q_h) \mathbf{n} + \frac{\gamma\mu}{h} \int_{\Sigma} \partial_{\tau} \mathbf{d}_h^{n+1} \cdot \mathbf{v}_h^f - \int_{\Gamma^{\text{out}}} p_{\text{out}} \mathbf{v}_h^f \cdot \mathbf{n} \end{aligned}$$

$$\begin{aligned} & A_{\tau}^f((\mathbf{u}_h^{n+1}, p_h^{n+1}), (\mathbf{v}_h^f, q_h)) - \int_{\Sigma} \mathbf{u}_h^{n+1} \cdot \boldsymbol{\sigma}(\mathbf{v}_h^f, -q_h) \mathbf{n} + \frac{\gamma\mu}{h} \int_{\Sigma} \mathbf{u}_h^{n+1} \cdot \mathbf{v}_h^f + S(p_h^{n+1}, q_h) \\ &= \int_{\Sigma} \boldsymbol{\sigma}(\mathbf{u}_h^n, p_h^n) \mathbf{n} \cdot \mathbf{v}_h^f - \int_{\Sigma} \partial_{\tau} \mathbf{d}_h^{n+1} \cdot \boldsymbol{\sigma}(\mathbf{v}_h^f, -q_h) \mathbf{n} + \frac{\gamma\mu}{h} \int_{\Sigma} \partial_{\tau} \mathbf{d}_h^{n+1} \cdot \mathbf{v}_h^f - \int_{\Gamma^{\text{out}}} p_{\text{out}} \mathbf{v}_h^f \cdot \mathbf{n} \end{aligned}$$

for all  $(\mathbf{v}_h^f, q_h) \in \mathbf{V}_{\Gamma^{\text{in}}, h}^f \times Q_h$ .

3. Go to next time-step.
- 

The next theorem provides an energy estimate for the stabilized explicit coupling scheme (Algorithm 2.7).

**Theorem 2.3** Assume that the fluid-structure system is isolated (i.e.,  $\mathbf{u}_{\text{in}} = \mathbf{0}$  and  $p_{\text{out}} = 0$ ) and let  $(\mathbf{u}_h^{n+1}, p_h^{n+1}, \mathbf{d}_h^{n+1}, \dot{\mathbf{d}}_h^{n+1})$  be given by Algorithm 2.7. For  $\gamma \geq 256C_{\text{TI}}$ ,  $\gamma_0 \geq 8$  and  $n \geq 1$ , the

following energy estimate holds

$$\begin{aligned} E^n + \mu \sum_{m=0}^{n-1} \tau \|\boldsymbol{\epsilon}(\mathbf{u}_h^{m+1})\|_{0,\Omega_f}^2 + \frac{\gamma\mu}{h} \sum_{m=0}^{n-1} \tau \|\mathbf{u}_h^{m+1} - \partial_\tau \mathbf{d}_h^{m+1}\|_{0,\Sigma}^2 + \frac{\gamma\mu\tau}{h} \|\mathbf{u}_h^n\|_{0,\Sigma}^2 + \frac{\gamma_0 h \tau}{\gamma\mu} \|p_h^n\|_{0,\Sigma}^2 \\ \lesssim E^0 + \frac{\gamma\mu\tau}{h} \|\mathbf{u}_h^0\|_{0,\Sigma}^2 + \mu \|\boldsymbol{\epsilon}(\mathbf{u}_h^0)\|_{0,\Omega_f}^2 + \frac{\gamma_0 h \tau}{\gamma\mu} \|p_h^0\|_{0,\Sigma}^2. \end{aligned} \quad (2.4.48)$$

Therefore, Algorithm 2.7 is energy stable under the (hyperbolic-CFL like) condition

$$\tau = \mathcal{O}(h). \quad (2.4.49)$$

Two observations are now in order.

- According to Theorem 2.3, the stability of Algorithm 2.7 is independent of the added-mass effect: the fluid-solid density ratio  $\rho_f/\rho_s$  and the length of the domain do not come into play. This observation is confirmed by the numerical results reported in Figure 2.5, corresponding to the simulation of the pressure wave propagation in a two-dimensional straight channel. The numerical solution remains stable irrespectively of the amount of added-mass effect. Note that this is a major advantage compared to standard explicit-coupling schemes, whose (in)stability is dictated by these quantities, irrespectively of the discretization parameters (see the discussion in §2.1 and [CGN05, FWR07]).
- The proof of Theorem 2.3 is based, exclusively, on the dissipation due to the Nitsche coupling and the time pressure penalization term. As a result, the stability result is independent of the dissipative features of the fluid and solid time discretization schemes. This is a significant progress with respect to the stability result stated in Theorem 2.1, for the semi-implicit coupling scheme (2.3.37)-(2.3.38), whose proof depends on the dissipative properties of the solid time discretization scheme (see Remark 2.9). On the other hand, as regards the fluid time-discretization, one could use, for instance, a neutrally stable second order scheme.

**Remark 2.15** The discrete continuity equation in step 2 of Algorithm 2.7 is given by

$$\frac{\gamma_0 h \tau}{\gamma\mu} \int_{\Sigma} \partial_\tau p_h^{n+1} q_h + \int_{\Omega_f} q_h \operatorname{div} \mathbf{u}_h^{n+1} = \int_{\Sigma} (\mathbf{u}_h^{n+1} - \partial_\tau \mathbf{d}_h^{n+1}) \cdot \mathbf{n} q_h. \quad (2.4.50)$$

The right hand-side being a consistent term, we can interpret the stabilization term (2.4.47) as a weakly-consistent interface artificial compressibility. The proposed approach has therefore clear connections with the already mentioned interface artificial compressibility methods [RVD00, JRLS08, DSB<sup>+</sup>10] for solving implicit coupling in a partitioned fashion. In these iterative procedures, the compressibility term vanishes at convergence and the artificial compressibility parameter is chosen so as to optimize efficiency and not for consistency or stability purposes.

**Remark 2.16** From Remarks 2.13 and 2.15, we can conclude that the main ingredients in the stability of Algorithm 2.7 are:

- the Robin-Robin based explicit treatment of the interface coupling conditions (2.4.46);
- the interface artificial compressibility perturbation of the continuity equation (2.4.50).

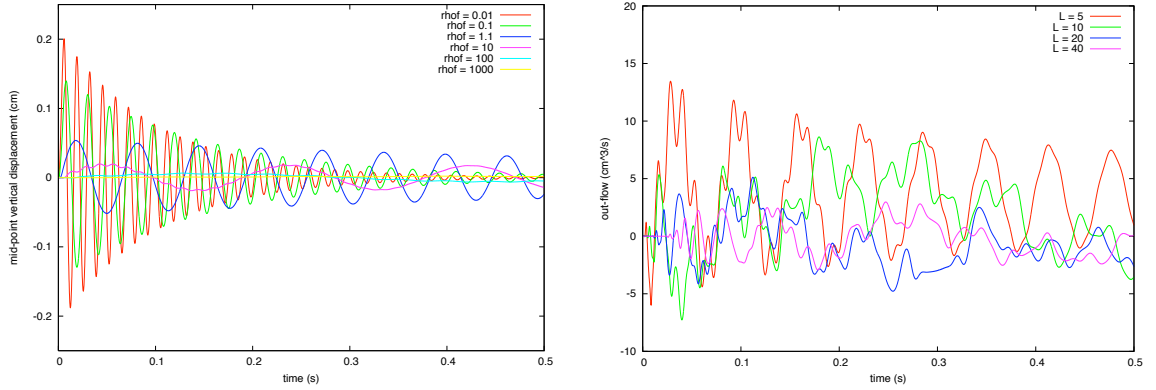


Figure 2.5: Stabilized explicit coupling (Algorithm 2.7). *Left*: interface mid-point  $y$ -displacement for different values of the fluid-solid density ratio  $\rho_f/\rho_s$ . *Right*: out-flow rate for different values of the vessel length  $L$ .

**Remark 2.17** *In the framework of a simplified structural behavior, given in terms of a  $(d - 1)$ -dimensional model (e.g., plates, shells or inertial-algebraic models), an alternative explicit coupling scheme has recently been reported in [GGC<sup>+</sup>09, GCC09] (see also [NV08, §4.1.1]). Since in this case  $\Sigma = \overline{\Omega^s}$ , the coupling condition (2.3.36) can be embedded into the fluid equations (as a Robin boundary condition) and, hence, treated implicitly through a specific (inertial/elastic) time-splitting of the solid equation.*

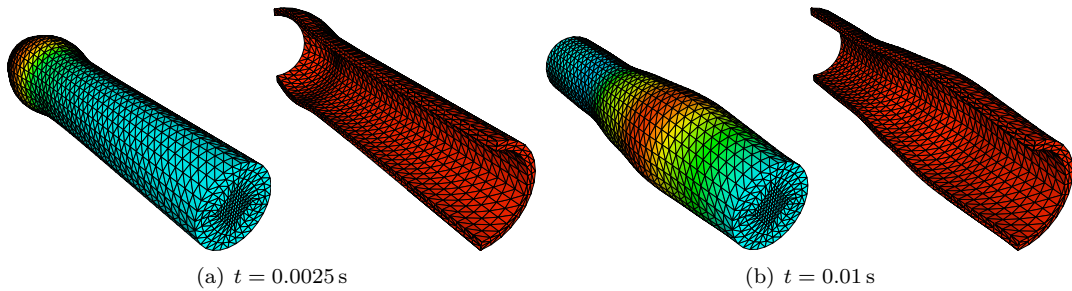


Figure 2.6: Stabilized explicit coupling without correction: snapshots of the pressure and solid deformation (exaggerated) at two time instants.

A formal error estimate for the stabilized explicit coupling scheme can be obtained from the energy estimate provided by Theorem 2.3. Let  $\boldsymbol{\theta}_h^n \stackrel{\text{def}}{=} \mathbf{u}_h^n - \pi_h \mathbf{u}(t_n)$ ,  $y_h^n \stackrel{\text{def}}{=} p_h^n - \pi_h p(t_n)$ ,  $\boldsymbol{\xi}_h^n \stackrel{\text{def}}{=} \mathbf{d}_h^n - \pi_h \mathbf{d}(t_n)$  and  $\dot{\boldsymbol{\xi}}_h^n \stackrel{\text{def}}{=} \dot{\mathbf{d}}_h^n - \pi_h \dot{\mathbf{d}}(t_n)$  be the discrete errors, where  $\pi_h$  denotes a suitable interpolation operator. We can derive the following error estimate

$$\mathcal{E}^n \lesssim \mathcal{E}^0 + r_1 + r_2, \quad (2.4.51)$$

---

**Algorithm 2.8** Stabilized explicit coupling with  $K \geq 0$  corrections.

---

1. Set  $\mathbf{u}_h^{n+1,0} \stackrel{\text{def}}{=} \mathbf{u}_h^n$  and  $p_h^{n+1,0} \stackrel{\text{def}}{=} p_h^n$ ;

2. Correction loop: for  $k = 0, \dots, K$  solve

(a) Solid subproblem: find  $(\mathbf{d}_h^{n+1,k+1}, \dot{\mathbf{d}}_h^{n+1,k+1}) \in [\mathbf{V}_h^s]^2$  such that

$$\begin{aligned} A_\tau^s((\mathbf{d}_h^{n+1,k+1}, \dot{\mathbf{d}}_h^{n+1,k+1}), (\mathbf{v}_h^s, \mathbf{r}_h)) + \frac{\gamma\mu}{h} \int_\Sigma \partial_\tau \mathbf{d}_h^{n+1,k+1} \cdot \mathbf{v}_h^s \\ = \frac{\gamma\mu}{h} \int_\Sigma \mathbf{u}_h^{n+1,k} \cdot \mathbf{v}_h^s - \int_\Sigma \boldsymbol{\sigma}(\mathbf{u}_h^{n+1,k}, p_h^{n+1,k}) \mathbf{n} \cdot \mathbf{v}_h^s \end{aligned}$$

for all  $(\mathbf{v}_h^s, \mathbf{r}_h) \in [\mathbf{V}_h^s]^2$ ;

(b) Fluid subproblem: find  $(\mathbf{u}_h^{n+1,k+1}, p_h^{n+1,k+1}) \in \mathbf{V}_h^f \times Q_h$ , with  $\mathbf{u}_h^{n+1,k+1} = \mathbf{u}_{\text{in}}(t_{n+1})$  on  $\Gamma^{\text{in}}$ , such that

$$\begin{aligned} A_\tau^f((\mathbf{u}_h^{n+1,k+1}, p_h^{n+1,k+1}), (\mathbf{v}_h^f, q_h)) - \int_\Sigma \mathbf{u}_h^{n+1,k+1} \cdot \boldsymbol{\sigma}(\mathbf{v}_h^f, -q_h) \mathbf{n} \\ + \frac{\gamma\mu}{h} \int_\Sigma \mathbf{u}_h^{n+1,k+1} \cdot \mathbf{v}_h^f + \frac{\gamma_0 h}{\gamma\mu} \int_\Sigma (p_h^{n+1,k+1} - p_h^{n+1,k}) q_h = \int_\Sigma \boldsymbol{\sigma}(\mathbf{u}_h^{n+1,k}, p_h^{n+1,k}) \mathbf{n} \cdot \mathbf{v}_h^f \\ - \int_\Sigma \partial_\tau \mathbf{d}_h^{n+1,k+1} \cdot \boldsymbol{\sigma}(\mathbf{v}_h^f, -q_h) \mathbf{n} + \frac{\gamma\mu}{h} \int_\Sigma \partial_\tau \dot{\mathbf{d}}_h^{n+1,k+1} \cdot \mathbf{v}_h^f - \int_{\Gamma^{\text{out}}} p_{\text{out}}(t_{n+1}) \mathbf{v}_h^f \cdot \mathbf{n} \end{aligned}$$

for all  $(\mathbf{v}_h^f, q_h) \in \mathbf{V}_h^f \times Q_h$ ;

3. Set  $\mathbf{u}_h^{n+1} \stackrel{\text{def}}{=} \mathbf{u}_h^{n+1,K+1}$ ,  $p_h^{n+1} \stackrel{\text{def}}{=} p_h^{n+1,K+1}$ ,  $\mathbf{d}_h^{n+1} \stackrel{\text{def}}{=} \mathbf{d}_h^{n+1,K+1}$  and  $\dot{\mathbf{d}}_h^{n+1} \stackrel{\text{def}}{=} \dot{\mathbf{d}}_h^{n+1,K+1}$ ;

4. Go to next time-step.

---

where

$$\begin{aligned} \mathcal{E}^n \stackrel{\text{def}}{=} \left( \frac{\rho^f}{2} \|\boldsymbol{\theta}_h^n\|_{0,\Omega^f}^2 + \frac{\rho^s}{2} \|\boldsymbol{\xi}_h^n\|_{0,\Omega^s}^2 + \frac{1}{2} a^s(\boldsymbol{\xi}_h^n, \boldsymbol{\xi}_h^n) + \mu \sum_{m=0}^{n-1} \tau \|\boldsymbol{\epsilon}(\boldsymbol{\theta}_h^{m+1})\|_{0,\Omega^f}^2 + \frac{\gamma\mu\tau}{h} \|\boldsymbol{\theta}_h^n\|_{0,\Sigma}^2 \right. \\ \left. + \frac{\gamma_0 h \tau}{\gamma\mu} \|y_h^n\|_{0,\Sigma}^2 + \frac{\gamma\mu\tau}{h} \sum_{m=0}^{n-1} \|\boldsymbol{\theta}_h^{m+1} - \partial_\tau \boldsymbol{\xi}_h^{m+1}\|_{0,\Sigma}^2 \right)^{\frac{1}{2}}. \end{aligned}$$

The terms on the right hand side of (2.4.51) consists of  $\mathcal{E}^0$ , which measures the error in the initial data,  $r_1$ , which consists of the terms related to the consistency of the fluid and solid discretizations, and  $r_2$ , which contains the explicit coupling consistency error and the weak-consistency introduced by the time penalty stabilization operator  $S$ . For the latter term we have

$$r_2 = \mathcal{O} \left( (\gamma\mu)^{\frac{1}{2}} \frac{\tau}{h^{\frac{1}{2}}} + \gamma\mu^{\frac{1}{2}} \frac{\tau}{h} + \frac{\gamma_0^{\frac{1}{2}}}{(\gamma\mu)^{\frac{1}{2}}} (h\tau)^{\frac{1}{2}} \right).$$

For a  $h$  fixed, the convergence order in time is imposed by the weak-consistency of the time penalty stabilization, which scales as  $\mathcal{O}(\tau^{\frac{1}{2}})$ . The other two terms scale as  $\mathcal{O}(\tau)$  but with a constant depends on  $1/h$ . Therefore, when refining both in  $\tau$  and in  $h$ , the stability condition (2.4.49) (*i.e.*,  $\tau = \mathcal{O}(h)$ )

is not enough to ensure convergence. We must take  $\tau = \mathcal{O}(h^2)$  in order to keep  $r_2 = \mathcal{O}(h)$ . Such a choice is optimal in the energy norm if piecewise affine approximations are used in space.

In practice, the method suffers from a deterioration of the accuracy, due to the weak consistency of the time penalty stabilization term, which rates as  $\mathcal{O}(\tau^{\frac{1}{2}})$  in a fixed mesh. We proposed to improve accuracy by performing one correction iteration (see, *e.g.*, [Ste78]). The stabilized explicit coupling scheme with  $K \geq 0$  corrections iterations is given in Algorithm 2.8. Note that, for  $K = 0$  (*i.e.*, without corrections) Algorithm 2.8 reduces to the original stabilized explicit coupling scheme (Algorithm 2.7). Conversely, for  $K \rightarrow \infty$  (*i.e.*, iterating until convergence) we recover the implicit coupling scheme (2.4.43)-(2.4.44),  $(\mathbf{u}_h^*, p_h^*) = (\mathbf{u}_h^{n+1}, p_h^{n+1})$ .

One of the main features of Algorithm 2.8 is that, after  $K \geq 0$  corrections, estimate (2.4.51) is expected to hold with (see, *e.g.*, [LLP02])

$$r_2 = \mathcal{O}\left(\frac{\tau^{K+1}}{h^{\frac{K+1}{2}}} + \frac{\tau^{K+1}}{h^{K+1}} + (h\tau)^{\frac{K+1}{2}}\right). \quad (2.4.52)$$

Therefore, one correction iteration (*i.e.*,  $K = 1$ ) is enough to retrieve first order time accuracy in a fixed mesh, since (2.4.52) yields  $r_2 = \mathcal{O}(\tau^2/h + \tau^2/h^2 + h\tau)$ . Note that, in this case, overall  $r_2 = \mathcal{O}(h)$  accuracy can be ensured under the (weakened) condition  $\tau = \mathcal{O}(h^{\frac{3}{2}})$ .

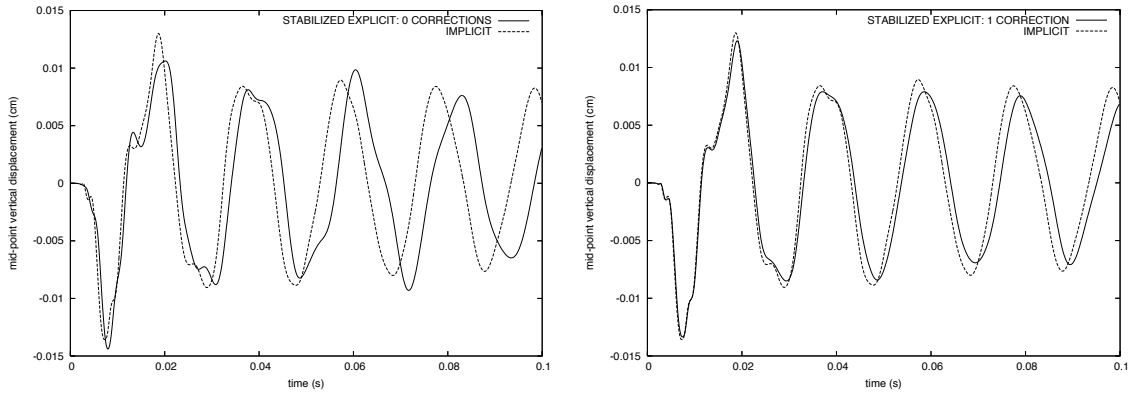


Figure 2.7: Interface mid-point  $y$ -displacement: stabilized explicit coupling (with and without correction) and implicit coupling (strongly enforced kinematic condition).

**Remark 2.18** *Algorithm 2.8 can be extended to the non-linear case (*i.e.*, to problem (2.1.1)-(2.1.3)) without major difficulty. Roughly, the idea consists in replacing steps 2 and 3 of Algorithm 2.1 by the non-linear counterparts of the fluid and solid correction steps in Algorithm 2.8. For the sake of conciseness, we skip the details and refer to [7, §5.5].*

We conclude this subsection with a few numerical illustrations in the framework of the already mentioned straight vessel benchmark (see §2.2). Some snapshots of the fluid pressure and solid deformation (half a section) obtained with the non-linear version of Algorithm 2.8 are reported in Figure 2.6. The impact of the correction iterations is highlighted in Figure 2.7, where we compare the results with those obtained with a fully implicit coupling scheme (Algorithm 2.2). Figure 2.7 (left) shows that, without correction, the stabilized explicit scheme is unable to accurately represent the solution provided by the implicit coupling scheme. Figure 2.7 (right) shows that one correction iteration is sufficient to recover all the local features of the implicit coupling solution (*i.e.*, we recover first order time accuracy).

### 2.4.2 Robin-based semi-implicit coupling ([1], [19])

The theoretical and numerical results summarized in §2.3 show that the projection semi-implicit coupling scheme drastically improves the stability properties of conventional explicit coupling and the efficiency of implicit coupling. In spite of that, the scheme has two flaws. From a theoretical point of view, a non-convervative solid time discretization (*i.e.*, with numerical dissipation) is required in the derivation of the energy stability estimate provided by Theorem 2.1 (see Remark 2.9). Secondly, though much less sensitive to the added-mass effect than explicit coupling, numerical evidence shows that the stability can be sensitive to changes in fluid-solid density ratio and other physical parameters (see the results reported in Figure 2.8 with the linear model (2.3.34)-(2.3.36)). As a matter of fact, the stability condition (2.3.39) provided by Theorem 2.1 depends on the solid

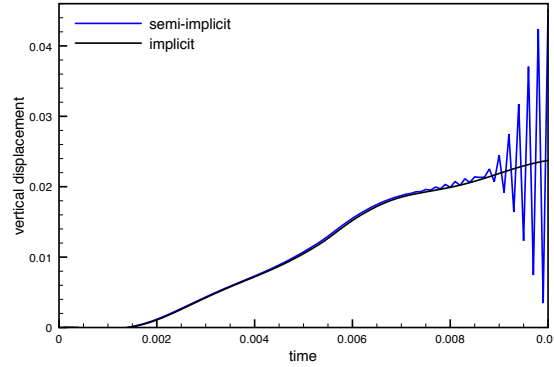


Figure 2.8: Comparison of implicit and semi-implicit coupling: interface mid-point vertical displacement ( $\rho^f = 1$ ,  $\rho^s = 1.2 \times 10^{-2}$ ,  $\mu = 10$ ).

and fluid densities. We have proposed an alternative semi-implicit coupling scheme that circumvents these two shortcomings. The key idea consists in treating the explicit part of the coupling in a full weak sense, by using a specific Robin-Robin coupling derived from Remark 2.13 (see also Remark 2.16).

Let us consider the original semi-implicit coupling scheme (2.3.37)-(2.3.38) applied to linear coupled problem (2.3.34)-(2.3.36). As we have already seen, this coupling scheme is based on the following implicit-explicit time discretization of (2.3.36):

$$\left. \begin{aligned} \mathbf{u}^{n+1} \cdot \mathbf{n} &= \partial_\tau \mathbf{d}^{n+1} \cdot \mathbf{n} \\ \boldsymbol{\sigma}(\mathbf{d}^{n+\frac{1}{2}}) \mathbf{n}^s &= -\boldsymbol{\sigma}(\tilde{\mathbf{u}}^n, p^{n+1}) \mathbf{n} \end{aligned} \right\} \text{ on } \Sigma, \quad (2.4.53)$$

$$\tilde{\mathbf{u}}^{n+1} = \partial_\tau \mathbf{d}^{n+1} \quad \text{on } \Sigma. \quad (2.4.54)$$

Note that, in (2.3.38), the kinematic interface conditions (2.4.53)<sub>1</sub> and (2.4.54) are both strongly imposed (*i.e.*, built in the finite element space). Instead, we now propose to treat the explicit part of the coupling (*i.e.*, the viscous-structure coupling) weakly, by using the following explicit

Robin-Robin treatment, derived from (2.4.46):

$$\left. \begin{aligned} \mathbf{u}^{n+1} \cdot \mathbf{n} &= \partial_\tau \mathbf{d}^{n+1} \cdot \mathbf{n} \\ \boldsymbol{\sigma}(\mathbf{d}^{n+\frac{1}{2}}) \mathbf{n}^s + \frac{\gamma^\mu}{h} \partial_\tau \mathbf{d}^{n+1} &= \frac{\gamma^\mu}{h} \tilde{\mathbf{u}}^n - \boldsymbol{\sigma}(\tilde{\mathbf{u}}^n, p^{n+1}) \mathbf{n} \end{aligned} \right\} \text{ on } \Sigma,$$

$$2\mu \boldsymbol{\epsilon}(\tilde{\mathbf{u}}^{n+1}) \mathbf{n} + \frac{\gamma^\mu}{h} \tilde{\mathbf{u}}^{n+1} = \frac{\gamma^\mu}{h} \partial_\tau \mathbf{d}^{n+1} + 2\mu \boldsymbol{\epsilon}(\tilde{\mathbf{u}}^n) \mathbf{n} \quad \text{on } \Sigma.$$

Note that, in contrast to (2.4.46), the pressure-structure coupling remains implicit and the kinematic interface condition (2.4.53)<sub>1</sub> is strongly enforced (as in the original semi-implicit coupling scheme).

The proposed Robin based semi-implicit coupling scheme, applied to the linear coupled problem (2.3.34)-(2.3.36), reads therefore as follows (compare with (2.3.37)-(2.3.38)): for  $n \geq 0$ ,

- Implicit step (pressure-solid coupling): find  $(\mathbf{u}_h^{n+1}, p_h^{n+1}, \mathbf{d}_H^{n+1}, \dot{\mathbf{d}}_H^{n+1}) \in \mathbf{V}_h^f \times Q_h^f \times [\mathbf{V}_H^s]^2$  such that

$$\left\{ \begin{aligned} \mathbf{u}_h^{n+1} &= \mathbf{u}_{\text{in}}(t_{n+1}) \quad \text{on } \Gamma^{\text{in}} \\ \mathbf{u}_h^{n+1} &= \Pi_h(\partial_\tau \mathbf{d}_H^{n+1}) \quad \text{on } \Sigma \\ \frac{\rho^f}{\tau} \int_{\Omega^f} (\mathbf{u}_h^{n+1} - \tilde{\mathbf{u}}_h^n) \cdot \mathbf{v}_h^f - \int_{\Omega^f} p_h^{n+1} \operatorname{div} \mathbf{v}_h^f + \int_{\Omega^f} q_h \operatorname{div} \mathbf{u}_h^{n+1} \\ &= - \int_{\Gamma^{\text{out}}} p_{\text{out}}(t_{n+1}) \mathbf{v}_h^f \cdot \mathbf{n} \quad \forall (\mathbf{v}_h^f, q_h) \in \mathbf{V}_{\Sigma \cup \Gamma^{\text{in}}, h}^f \times Q_h^f, \\ \frac{\rho^s}{\tau} \int_{\Omega^s} \partial_\tau \dot{\mathbf{d}}_H^{n+1} \cdot \mathbf{v}_H^s + a^s(\mathbf{d}_H^{n+\frac{1}{2}}, \mathbf{v}_H^s) + \rho^s \int_{\Omega^s} (\dot{\mathbf{d}}_H^{n+\frac{1}{2}} - \partial_\tau \mathbf{d}_H^{n+1}) \cdot \mathbf{r}_H \\ &+ \frac{\gamma^\mu}{h} \int_{\Sigma} \partial_\tau \mathbf{d}_H^{n+1} \cdot \mathbf{v}_H^s = \frac{\gamma^\mu}{h} \int_{\Sigma} \tilde{\mathbf{u}}_h^n \cdot \mathbf{v}_H^s - 2\mu \int_{\Sigma} \boldsymbol{\epsilon}(\tilde{\mathbf{u}}_h^n) \mathbf{n} \cdot \mathbf{v}_H^s \\ &- \langle \mathcal{R}_p(\mathbf{u}_h^{n+1}, p_h^{n+1}), L_h(\mathbf{v}_H^s |_{\Sigma}) \rangle \quad \forall (\mathbf{v}_H^s, \mathbf{r}_H) \in [\mathbf{V}_H^s]^2; \end{aligned} \right. \quad (2.4.55)$$

- Explicit step (viscous-solid coupling): find  $\tilde{\mathbf{u}}_h^{n+1} \in \mathbf{V}_h^f$  such that

$$\left\{ \begin{aligned} \tilde{\mathbf{u}}_h^{n+1} &= \mathbf{u}_{\text{in}}(t_{n+1}) \quad \text{on } \Gamma^{\text{in}}, \\ \frac{\rho^f}{\tau} \int_{\Omega^f} (\tilde{\mathbf{u}}_h^{n+1} - \mathbf{u}_h^{n+1}) \cdot \tilde{\mathbf{v}}_h^f + 2\mu \int_{\Omega^f} \boldsymbol{\epsilon}(\tilde{\mathbf{u}}_h^{n+1}) : \boldsymbol{\epsilon}(\tilde{\mathbf{v}}_h^f) + \frac{\gamma^\mu}{h} \int_{\Sigma} \tilde{\mathbf{u}}_h^{n+1} \cdot \tilde{\mathbf{v}}_h^f \\ &= \frac{\gamma^\mu}{h} \int_{\Sigma} \partial_\tau \mathbf{d}_H^{n+1} \cdot \tilde{\mathbf{v}}_h^f + 2\mu \int_{\Sigma} \boldsymbol{\epsilon}(\tilde{\mathbf{u}}_h^n) \mathbf{n} \cdot \tilde{\mathbf{v}}_h^f \quad \forall \tilde{\mathbf{v}}_h^f \in \mathbf{V}_{\Gamma^{\text{in}}, h}^f. \end{aligned} \right. \quad (2.4.56)$$

Note that in (2.4.55) we have considered a conservative time discretization for the structure.

Let us define the energy of the discrete coupled system, at time level  $n$ , as:

$$E^n = \frac{\rho^f}{2} \|\tilde{\mathbf{u}}_h^n\|_{0, \Omega^f}^2 + \frac{\rho^s}{2} \|\dot{\mathbf{d}}_H^n\|_{0, \Omega^s}^2 + \frac{1}{2} a^s(\mathbf{d}_H^n, \mathbf{d}_H^n).$$

The following result states the energy based stability of the Robin-based semi-implicit coupling scheme (2.4.55)-(2.4.56).

---

**Algorithm 2.9** Robin based semi-implicit coupling algorithm.

---

1. Explicit step: update fluid domain (mesh)

$$\begin{cases} \mathbf{d}_h^{f,n+1} = \text{Ext}_h(\mathbf{d}_H^n |_\Sigma), & \widehat{\mathbf{w}}_h^{n+1} = \partial_\tau \mathbf{d}_h^{f,n+1} \quad \text{in } \Omega^f, \\ \Omega^{f,n+1} = (\mathbf{I}_{\Omega^f} + \mathbf{d}_h^{f,n+1})(\Omega^f). \end{cases} \quad (2.4.57)$$

2. Implicit step (pressure-structure coupling):

- Fluid projection sub-step: find  $(\mathbf{u}_h^{n+1}, p_h^{n+1}) \in \mathbf{V}_h^f \times Q_h^f$  such that

$$\begin{cases} \mathbf{u}_h^{n+1} = \mathbf{u}_{\text{in}}(t_{n+1}) \quad \text{on } \Gamma^{\text{in}}, \\ \widehat{\mathbf{u}}_h^{n+1} = \Pi_h(\partial_\tau \mathbf{d}_H^{n+1}) \quad \text{on } \Sigma, \\ \frac{\rho^f}{\tau} \int_{\Omega^{f,n}} (\mathbf{u}_h^{n+1} - \widetilde{\mathbf{u}}_h^n) \cdot \mathbf{v}_h^f - \int_{\Omega^{f,n}} p_h^{n+1} \text{div } \mathbf{v}_h^f + \int_{\Omega^{f,n}} q_h \text{div } \mathbf{u}_h^{n+1} \\ = - \int_{\Gamma^{\text{out}}} p_{\text{out}}(t_{n+1}) \mathbf{v}_h^f \cdot \mathbf{n} \quad \forall (\widehat{\mathbf{v}}_h^f, q_h) \in \mathbf{V}_{\Sigma \cup \Gamma^{\text{in}},h}^f \times Q_h^f; \end{cases} \quad (2.4.58)$$

- Solid: find  $(\mathbf{d}_H^{n+1}, \dot{\mathbf{d}}_H^{n+1}) \in [\mathbf{V}_H^s]^2$  such that

$$\begin{cases} A_\tau^s(\mathbf{d}_H^{n+1}, \dot{\mathbf{d}}_H^{n+1}; \mathbf{v}_H^s, \mathbf{r}_H) + \frac{\gamma\mu}{h} \int_{\Sigma^{n+1}} \partial_\tau \mathbf{d}_H^{n+1} \cdot \mathbf{v}_H^s = \frac{\gamma\mu}{h} \int_{\Sigma^{n+1}} \widetilde{\mathbf{u}}_h^n \cdot \mathbf{v}_H^s \\ -2\mu \int_{\Sigma^{n+1}} \boldsymbol{\epsilon}(\widetilde{\mathbf{u}}_h^n) \mathbf{n} \cdot \mathbf{v}_H^s + \int_{\Sigma^{n+1}} p_h^{n+1} \mathbf{v}_H^s \cdot \mathbf{n} \quad \forall \mathbf{v}_H^s, \mathbf{r}_H \in [\mathbf{V}_H^s]^2; \end{cases} \quad (2.4.59)$$

3. Explicit step (viscous-structure coupling): find  $\widehat{\mathbf{u}}_h^{n+1} \in \mathbf{V}_h^f$  such that

$$\begin{cases} \widehat{\mathbf{u}}_h^{n+1} = \mathbf{u}_{\text{in}}(t_{n+1}) \quad \text{on } \Gamma^{\text{in}}, \\ \widetilde{A}_\tau^f(\widehat{\mathbf{u}}_h^{n+1}, \widetilde{\mathbf{v}}_h^f) + \frac{\gamma\mu}{h} \int_{\Sigma^{n+1}} \widehat{\mathbf{u}}_h^{n+1} \cdot \widetilde{\mathbf{v}}_h^f = \frac{\gamma\mu}{h} \int_{\Sigma^{n+1}} \partial_\tau \mathbf{d}_H^{n+1} \cdot \widetilde{\mathbf{v}}_h^f \\ + 2\mu \int_{\Sigma^{n+1}} \boldsymbol{\epsilon}(\widetilde{\mathbf{u}}_h^n) \mathbf{n} \cdot \widetilde{\mathbf{v}}_h^f \quad \forall \widetilde{\mathbf{v}}_h^f \in \mathbf{V}_{\Gamma^{\text{in}},h}^f; \end{cases} \quad (2.4.60)$$

4. Go to next time step.

---

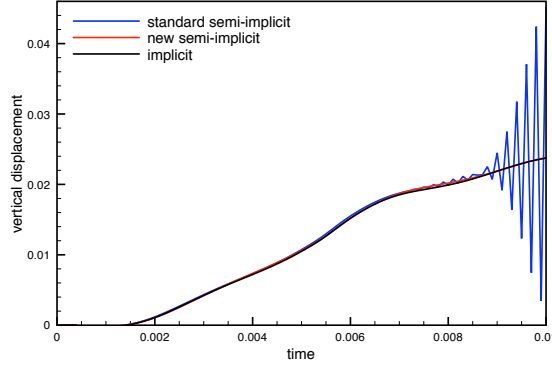


Figure 2.9: Comparison of the implicit, semi-implicit and Robin based semi-implicit coupling schemes: interface mid-point vertical displacement ( $\rho^f = 1$ ,  $\rho^s = 1.2 \times 10^{-2}$ ,  $\mu = 10$ ).

**Theorem 2.4** Let  $(\tilde{\mathbf{u}}_h^{n+1}, p_h^{n+1}, \mathbf{d}_h^{n+1}, \dot{\mathbf{d}}_h^{n+1})$  be given by (2.4.55)-(2.4.56) and assume that the system is isolated (i.e.,  $p_{\text{out}} = 0$  and  $\mathbf{u}_{\text{in}} = \mathbf{0}$ ). For  $\gamma \geq 4C_{\text{TI}}$  and  $n \geq 1$ , there holds

$$E^n + \mu \sum_{m=0}^{n-1} \tau \|\epsilon(\tilde{\mathbf{u}}_h^{m+1})\|_{0,\Omega^f}^2 + \frac{\gamma\mu}{h} \sum_{m=0}^{n-1} \tau \|\tilde{\mathbf{u}}_h^{m+1} - \partial_\tau \mathbf{d}_H^{m+1}\|_{0,\Sigma}^2 + \frac{\gamma\mu\tau}{h} \|\tilde{\mathbf{u}}_h^n\|_{0,\Sigma}^2 \lesssim E^0 + \mu\tau \|\epsilon(\tilde{\mathbf{u}}_h^0)\|_{0,\Omega^f}^2 + \frac{\gamma\mu\tau}{h} \|\tilde{\mathbf{u}}_h^0\|_{0,\Sigma}^2. \quad (2.4.61)$$

Therefore, the semi-implicit coupling scheme (2.4.55)-(2.4.56) is energy stable under the condition  $\tau = \mathcal{O}(h)$ .

Since the stability condition of Theorem 2.4 does not depend on the fluid-solid density ratio neither on the geometry of the domain, the semi-implicit coupling scheme (2.4.55)-(2.4.56) remains stable irrespectively of the added-mass effect. Moreover, thanks to the natural interface dissipation of the Robin-Robin coupling, a diffusive time marching in the structure is no longer needed to ensure stability. These observations are confirmed by the numerical results reported in Figure 2.9. The numerical instabilities shown in Figure 2.8, for the original semi-implicit coupling, are not present in the solution provided by the Robin based semi-implicit coupling scheme, which accurately predicts the results of the implicit coupling scheme.

**Remark 2.19** Theorem 2.4 follows by a combination of the arguments involved in the proofs of Theorems 2.1 and 2.2. Let us notice that, here, we do not need to stabilize pressure fluctuations, that is, to introduce the weakly consistent artificial compressibility at the interface (2.4.47). Indeed, due to the implicit treatment (2.4.55) of the pressure-solid coupling, no artificial interface pressure perturbations appears in the energy estimate (2.4.61).

**Remark 2.20** Theorem 2.4 can be extended to the case in which, instead of the pressure-Darcy formulation (2.4.55)<sub>1</sub>, we consider the pressure-Poisson formulation of the projection step (see Remark 2.6). We refer to [1, §4.3] for the details.

The non-linear counterpart of the semi-implicit coupling scheme (2.4.55)-(2.4.56) (namely, the Robin based counterpart of Algorithm 2.6) is detailed in Algorithm 2.9. Here,  $\text{Ext}_h$  stands for a

discrete version of the lifting operator Ext, the solid mass and stiffness contribution are given by

$$\begin{aligned} A_\tau^s(\mathbf{d}_H^{n+1}, \dot{\mathbf{d}}_H^{n+1}; \mathbf{v}_H^s, \mathbf{r}_H) &\stackrel{\text{def}}{=} \rho^s \int_{\Omega^s} \partial_\tau \dot{\mathbf{d}}_H^{n+1} \cdot \mathbf{v}_H^s + \frac{1}{2} \int_{\Omega^s} (\boldsymbol{\Pi}(\mathbf{d}_H^{n+1}) + \boldsymbol{\Pi}(\mathbf{d}_H^n)) : \nabla \mathbf{v}_H^s \\ &\quad + \rho^s \int_{\Omega^s} (\dot{\mathbf{d}}_H^{n+\frac{1}{2}} - \partial_\tau \mathbf{d}_H^{n+1}) \cdot \mathbf{r}_H, \end{aligned}$$

while, for the fluid

$$\begin{aligned} \tilde{A}_\tau^f(\tilde{\mathbf{u}}_h^{n+1}, \tilde{\mathbf{v}}_h^f) &\stackrel{\text{def}}{=} \frac{\rho^f}{\tau} \int_{\Omega^{f,n+1}} \tilde{\mathbf{u}}_h^{n+1} \cdot \tilde{\mathbf{v}}_h^f - \frac{\rho^f}{\tau} \int_{\Omega^{f,n}} \mathbf{u}_h^{n+1} \cdot \tilde{\mathbf{v}}_h^f + \frac{\rho^f}{2} \int_{\Omega^{f,n+1}} (\text{div } \tilde{\mathbf{u}}_h^n) \tilde{\mathbf{u}}_h^{n+1} \cdot \tilde{\mathbf{v}}_h^f \\ &\quad - \rho^f \int_{\Omega^{f,n+1}} (\text{div } \mathbf{w}_h^{n+1}) \tilde{\mathbf{u}}_h^{n+1} \cdot \tilde{\mathbf{v}}_h^f + \rho^f \int_{\Omega^{f,n+1}} (\tilde{\mathbf{u}}_h^n - \mathbf{w}_h^{n+1}) \cdot \nabla \tilde{\mathbf{u}}_h^{n+1} \cdot \tilde{\mathbf{v}}_h^f \\ &\quad + 2\mu \int_{\Omega^{f,n+1}} \boldsymbol{\epsilon}(\tilde{\mathbf{u}}_h^{n+1}) : \boldsymbol{\epsilon}(\tilde{\mathbf{v}}_h^f). \end{aligned}$$

We conclude this subsection with an illustration of the numerical results obtained with Algorithm 2.9 (pressure-Poisson version) and the physiological test case considered in §2.3. Figure 2.10 presents some snapshots of the wall deformation and the fluid velocity fields at two time instants. Figure 2.11 shows that, even in this complex case, both the original and the Robin based semi-implicit coupling schemes provide a prediction that compares well to the reference implicit solution.

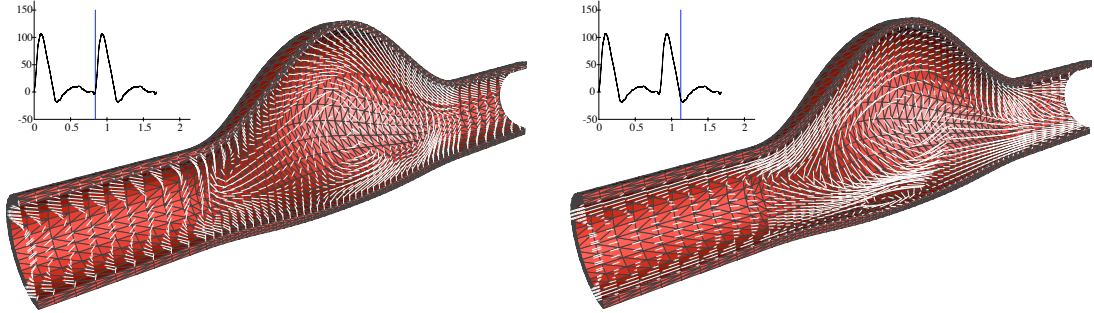


Figure 2.10: Robin based semi-implicit coupling: snapshots of the solid deformation and fluid velocity field at two different time instants.

## 2.5 Perspectives

The work summarized in this chapter was devoted to the approximation and numerical resolution of the mechanical interaction between a viscous incompressible fluid and an elastic structure, with a strong added-mass effect. In this framework, standard explicit (or loosely coupled) schemes are known to be unstable, irrespectively of the discretization parameters. In the context of implicit coupling, we have seen that the exact evaluation of the cross-derivative of the Jacobian (shape terms) leads to robust Newton iterations. Yet, these procedures remain computationally expensive in real applications.

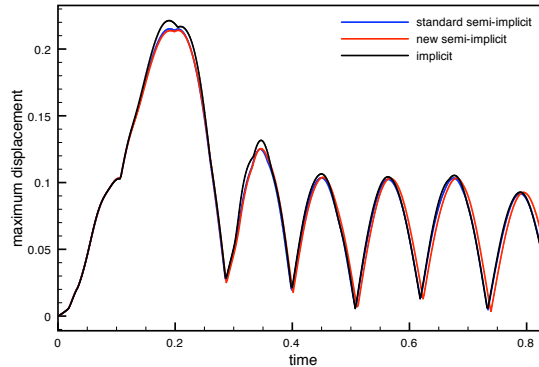


Figure 2.11: Comparison of the implicit, standard semi-implicit and Robin based semi-implicit coupling schemes: maximal displacement of the structure.

We have seen that implicit coupling can be avoided, without compromising stability, via the semi-implicit and the explicit coupling schemes described in §2.3 and §2.4, respectively. In particular, the explicit Robin-Robin treatment derived from the Nitsche treatment of the coupling yields added-mass free schemes. The price to pay is a perturbation of the truncation error, which enforces constraints on the rate of the discretization parameters (*e.g.*, parabolic-CFL). Let us emphasize, that for standard loosely coupled schemes, these constraints do not cure the instabilities!

Many aspects of the studies presented in this chapter are open to further investigations (some of them are in progress). In the context of the numerical analysis of the schemes, focus will be put on the convergence analysis in the linear case, for instance, in the spirit of [LTM00, AG10]. Further investigations shall address the generalization of the stability analysis to the non-linear case (see, *e.g.*, [LTH03] for implicit coupling). We will also investigate other explicit coupling schemes, motivated by the explicit Robin-Robin coupling (2.4.46):

- (i) stabilized explicit coupling with a residual based treatment of the fluid stresses at the interface (instead of face-wise, as in the interface Nitsche’s method);
- (ii) unstabilized explicit Robin-Robin coupling without consistency term  $\int_{\Sigma} (\mathbf{u}_h^{n+1} - \partial_{\tau} \mathbf{d}_h^{n+1}) \cdot \mathbf{n} q_h$ ;
- (iii) explicit Robin-Robin coupling with (pressure-Poisson) projection scheme.

The variants (i) and (iii) can be proved to be energy stable. In particular, it is worth noticing that the combination of the Robin-Robin splitting with the pressure-Poisson treatment of the projection step, in (iii), leads to a natural stabilization of the time pressure fluctuations. Numerical evidence suggests that also (ii) is energy stable, but the analysis does not seem to be straightforward.

Regarding the applications, we plan to incorporate some of the proposed procedures in the context of the simulation of the fluid-structure interaction phenomena in the heart (see [WSKH04]), using the reduced valves models recently proposed in [Ast10]. At last, in the context of inverse problems in blood flows, a PhD thesis co-guided with J.-F. Gergeau is ongoing. Some promising results, on the estimation of the mechanical properties of the vessel wall, have already been obtained using the filtering techniques recently developed in [CMLT09].



## Chapter 3

# Numerical simulation of electrocardiograms

This chapter summarizes some of the results of the PhD thesis of N. Zemzemi [Zem09], that I co-advised with J.F. Gerbeau (INRIA), during the period 2006–2009, in the framework of INRIA’s large-scale initiative action *CardioSense3D*<sup>1</sup>.

### 3.1 Motivations

Like skeletal muscles, the heart is electrically stimulated to contract. The electrocardiogram (ECG) is a noninvasive recording of heart’s electrical activity. It is obtained from a standard set of skin

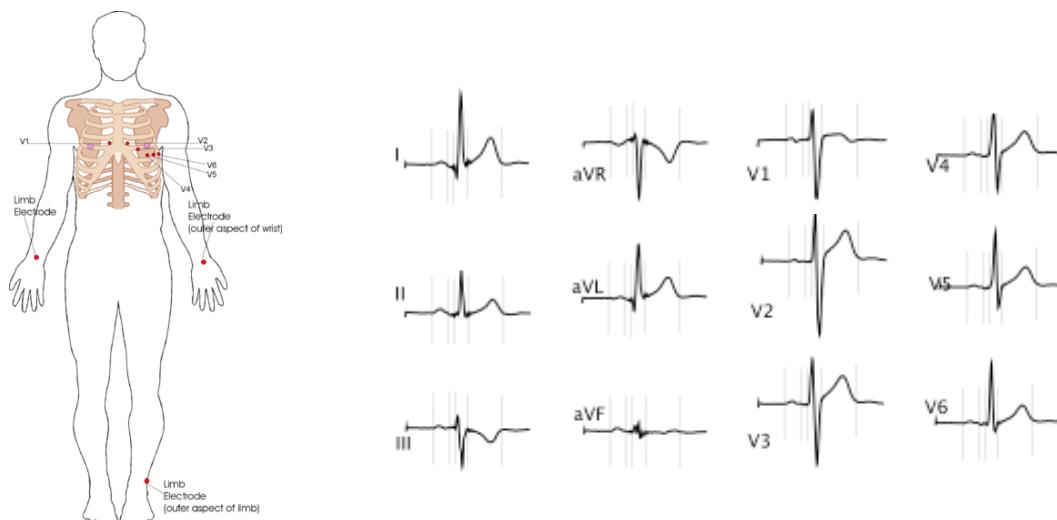


Figure 3.1: *Right*: ECG electrodes location (red dots). *Left*: measured normal 12-lead ECG (from: [www.wikipedia.org](http://www.wikipedia.org)): standard leads (I, II, III), augmented leads (aVR, aVL, aVF) and chest leads (V1, V2, ..., V6).

<sup>1</sup><http://www-sop.inria.fr/CardioSense3D>

electrodes (Figure 3.1 (left)) and presented to the physician as the *12-lead ECG*: that is, 12 graphs of the recorded voltage *vs.* time (Figure 3.1 (right)). Figure 3.2 illustrates the connection between the ECG deflections and the heart muscle electric state. The P-wave and the QRS-complex are, respectively, the result of the atrial and ventricular depolarizations, whereas the T-wave represents the repolarization of the ventricles (see, *e.g.*, [MP95]).

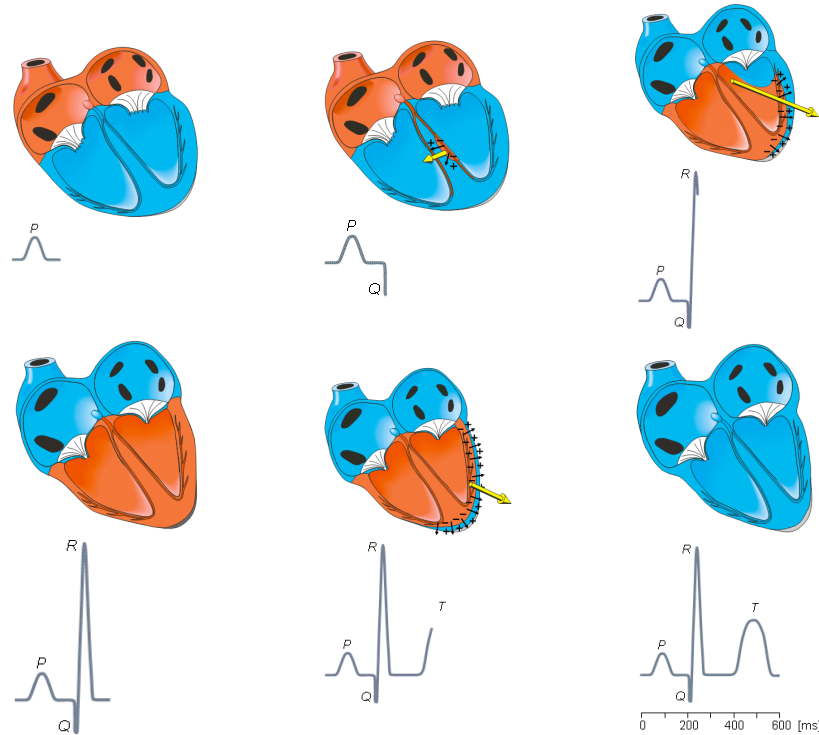


Figure 3.2: ECG deflections (P-wave, QRS-complex and T-wave) and heart muscle electric state: depolarized (red) and repolarized (blue). (From: [www.bem.fi](http://www.bem.fi), see also [MP95]).

The ECG can be considered as the most widely used clinical tool for the detection and the diagnosis of a broad range of cardiac conditions (see, *e.g.*, [Aeh06, Gol06]). In spite of that, the clinical meaning of some ECG findings is still not fully understood. Computer based simulations of the ECG, linking models of the electrical activity of the heart (in normal and pathological conditions) to the ECG signal, can therefore be a valuable tool for improving this knowledge. Such an ECG simulator can also be useful in building a virtual data base of pathological conditions, in order to test and train medical devices (see [39]). Moreover, being able to simulate realistic ECGs is a necessary step towards the development of patient-specific models from clinical ECG data.

Although many works have been devoted to the numerical simulation of cardiac electrophysiology (see, *e.g.*, [Sac04, PBC05, SLC<sup>+</sup>06] and the references therein), only a small number [Hui98, PDG03, LBG<sup>+</sup>03, KSW<sup>+</sup>07, TDP<sup>+</sup>04, PDV09] addresses the numerical simulation of ECGs using a whole-heart reaction-diffusion model. Among them, only a very few [PDG03, PDV09] provide meaningful simulations of the complete 12-lead ECG. These simulations rely on either a monodomain approximation or a heart-torso decoupling approximation and a multi-dipole cardiac source representation (see [LBG<sup>+</sup>03, Section 4.2.4] and [Gul88]).

This chapter concerns the numerical simulation of ECGs using a three-dimensional mathemati-

cal model fully based on partial/ordinary differential equations (PDE/ODE). The main ingredients of this model are standard: phenomenological cell dynamics, bidomain equations (for the heart) and a generalized Laplace equation (for the torso). They are briefly introduced in §3.2. A result on the existence of solution is presented in §3.3. Yet, in order to provide realistic ECG simulations, other critical modeling aspects have to be elucidated (*e.g.*, heart-torso transmission conditions, cell heterogeneity, His bundle modeling and tissue anisotropy). This is addressed in §3.4. Finally, some decoupled time discretization schemes for the bidomain and heart-torso systems are analyzed in §3.5.

## 3.2 Mathematical modeling

The mathematical modeling of the ECG is known as the *forward problem* of electrocardiography (see [LBG<sup>+</sup>03]). It relies on three main ingredients: a model for the electrical activity of the heart, a model for the torso (extracardiac regions) and some specific heart-torso coupling conditions.

### Isolated heart modeling

The bidomain equations, originally derived in [Tun78], are the most widely accepted mathematical model of the macroscopic electrical activity of the heart (see, *e.g.*, the monographs [SLC<sup>+</sup>06, PBC05]). This macroscopic model is based on the assumption that, at the cell scale, the cardiac tissue can be viewed as partitioned into two ohmic conducting media, separated by the cell membrane: intracellular, made of the cardiac cells, and extracellular which represents the space between them. After a homogenization process (see [NK93, PSCF05]), the intra- and extracellular domains are supposed to occupy the whole heart volume  $\Omega_H$  (this also applies to the cell membrane). Hence, the averaged intra- and extracellular densities of current,  $\mathbf{j}_i$  and  $\mathbf{j}_e$ , the conductivity tensors,  $\boldsymbol{\sigma}_i$  and  $\boldsymbol{\sigma}_e$ , and the electric potentials,  $u_i$  and  $u_e$ , are defined in the whole heart domain  $\Omega_H$ . The electrical charge conservation becomes

$$\operatorname{div}(\mathbf{j}_i + \mathbf{j}_e) = 0, \quad (3.2.1)$$

and the homogenized equation of the electrical activity of the cell membrane is given by

$$A_m (C_m \partial_t V_m + i_{\text{ion}}(V_m, w)) + \operatorname{div}(\mathbf{j}_i) = I_{\text{app}}, \quad (3.2.2)$$

complemented with the Ohm's laws

$$\mathbf{j}_i = -\boldsymbol{\sigma}_i \nabla u_i, \quad \mathbf{j}_e = -\boldsymbol{\sigma}_e \nabla u_e.$$

Here,  $V_m$  stands for the transmembrane potential, defined as  $V_m \stackrel{\text{def}}{=} u_i - u_e$ ,  $A_m$  is a constant representing the rate of membrane area per volume unit and  $C_m$  the membrane capacitance per area unit. The reaction term  $i_{\text{ion}}(V_m, w)$  represents the ionic current across the membrane and  $I_{\text{app}}$  a given applied current stimulus. In general, the ionic variable  $w$  (possibly vector valued) satisfies a system of ODE of the type:

$$\partial_t w + g(V_m, w) = 0. \quad (3.2.3)$$

The definition of the functions  $g$  and  $I_{\text{ion}}$  depends on the considered cell membrane ionic model (see [SLC<sup>+</sup>06, PBC05] and the references therein). According to their degree of complexity and realism, the ionic models typically fall into one of the following categories (see [PBC05, Chapter 3]): phenomenological (*e.g.*, [Fit61, NAY62, AP96, RM94, vCD80, FK98, MS03]) or physiological (*e.g.*, [BR77, LR91, LR94, NVKN98, DS05]).

To sum up, the system of equations modeling the electrical activity within the heart (in terms of  $V_m$  and  $u_e$ ) consists of a coupled system of ODE, (3.2.3), a nonlinear reaction-diffusion equation, (3.2.2), and an elliptic equation, (3.2.1):

$$\begin{cases} \partial_t w + g(V_m, w) = 0 & \text{in } \Omega_H \times (0, T), \\ \chi_m \partial_t V_m + I_{\text{ion}}(V_m, w) - \text{div}(\boldsymbol{\sigma}_i \nabla V_m) - \text{div}(\boldsymbol{\sigma}_i \nabla u_e) = I_{\text{app}} & \text{in } \Omega_H \times (0, T), \\ -\text{div}((\boldsymbol{\sigma}_i + \boldsymbol{\sigma}_e) \nabla u_e) - \text{div}(\boldsymbol{\sigma}_i \nabla V_m) = 0 & \text{in } \Omega_H \times (0, T), \end{cases} \quad (3.2.4)$$

with appropriate boundary

$$\begin{cases} \boldsymbol{\sigma}_i \nabla V_m \cdot \mathbf{n} + \boldsymbol{\sigma}_i \nabla u_e \cdot \mathbf{n} = 0 & \text{on } \Sigma \times (0, T), \\ \boldsymbol{\sigma}_e \nabla u_e \cdot \mathbf{n} = 0 & \text{on } \Sigma \times (0, T), \end{cases} \quad (3.2.5)$$

and initial conditions  $V_m|_{t=0} = V_m^0$  and  $w|_{t=0} = w^0$ . Here,  $(0, T)$  is the time interval of interest,  $\chi_m \stackrel{\text{def}}{=} A_m C_m$ ,  $I_{\text{ion}} \stackrel{\text{def}}{=} A_m i_{\text{ion}}$ , the vector  $\mathbf{n}$  stands for the outward unit normal to  $\Sigma \stackrel{\text{def}}{=} \partial\Omega_H$  and  $V_m^0, w^0$  are given initial data.

The boundary conditions (3.2.5)<sub>1,2</sub> state that the intra- and extracellular currents do not propagate outside the heart. While (3.2.5)<sub>1</sub> is a widely accepted condition (see, *e.g.*, [Tun78, KN94, PBC05, SLC<sup>+</sup>06]), the enforcement of (3.2.5)<sub>2</sub> is only justified under an isolated heart assumption (see [SLC<sup>+</sup>06, PBC05]). The coupled system of equations (3.2.4)-(3.2.5) is often known in the literature as *isolated bidomain* model (see [CFP04, CFPT05, SLC<sup>+</sup>06]).

**Remark 3.1** *The complexity of (3.2.4)-(3.2.5) can be reduced by using the so-called monodomain approximation:*

$$\begin{cases} \chi_m \partial_t V_m + I_{\text{ion}}(V_m, w) - \text{div}(\boldsymbol{\sigma} \nabla V_m) = I_{\text{app}} & \text{in } \Omega_H, \\ \boldsymbol{\sigma} \nabla V_m \cdot \mathbf{n} = 0 & \text{on } \Sigma, \end{cases} \quad (3.2.6)$$

where  $\boldsymbol{\sigma} \stackrel{\text{def}}{=} \boldsymbol{\sigma}_i(\boldsymbol{\sigma}_i + \boldsymbol{\sigma}_e)^{-1}\boldsymbol{\sigma}_e$  is the so called bulk conductivity tensor. Note that (3.2.6) decouples the computation of  $V_m$  from that of  $u_e$ . Under the isolating condition (3.2.5)<sub>2</sub>, problem (3.2.6) can be interpreted as the zeroth-order approximation of (3.2.4)<sub>2</sub> and (3.2.5)<sub>1</sub> with respect to a parameter  $\epsilon \in [0, 1]$  which measures the gap between the anisotropy ratios of the intra- and extracellular domains (see [CNLH04, CFPT05] for details). Although several simulation analyses (see, *e.g.*, [CNLH04, PDR<sup>+</sup>06]) suggest that the monodomain approximation may be adequate for some propagation studies in isolated hearts, it cannot be applied in all situations since it neglects the extracellular feedback into  $V_m$  (see, *e.g.*, [EGR00, CNLH04, PDR<sup>+</sup>06]).

## Coupling with the torso: ECG modeling

The myocardium is surrounded by a volume conductor,  $\Omega_T$ , that contains all the extramyocardial regions (see Figure 3.3). The torso volume is commonly modeled as a passive conductor (generalized Laplace equation). A perfect electric heart-torso coupling, across the interface  $\Sigma$ , is generally assumed (see, *e.g.*, [Tun78, KN94, PBC05, SLC<sup>+</sup>06]):

$$\begin{cases} u_e = u_T & \text{on } \Sigma, \\ \boldsymbol{\sigma}_e \nabla u_e \cdot \mathbf{n} = -\boldsymbol{\sigma}_T \nabla u_T \cdot \mathbf{n}_T & \text{on } \Sigma, \end{cases} \quad (3.2.7)$$

where  $\boldsymbol{\sigma}_T$  stands for the conductivity tensor of the torso tissue and  $\mathbf{n}_T$  for the outward unit normal to  $\partial\Omega_T$ .

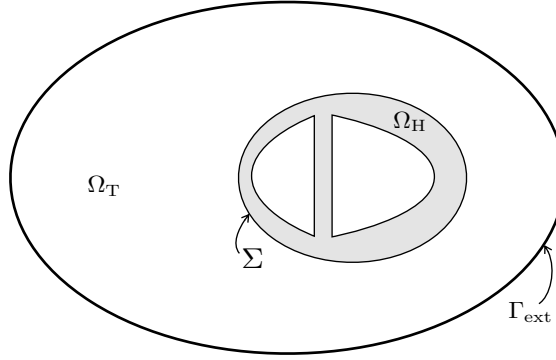


Figure 3.3: Two-dimensional geometrical description: heart domain  $\Omega_H$ , torso domain  $\Omega_T$  (extramycardial regions), heart-torso interface  $\Sigma$  and torso external boundary  $\Gamma_{\text{ext}}$ .

The resulting coupled system can be formulated in terms of  $V_m$ ,  $u_e$ ,  $w$  and the torso potential  $u_T$ , as follows (see, e.g., [SLC<sup>+</sup>06, PBC05]):

$$\left\{ \begin{array}{ll} \partial_t w + g(V_m, w) = 0, & \text{in } \Omega_H \times (0, T), \\ \chi_m \partial_t V_m + I_{\text{ion}}(V_m, w) - \text{div}(\sigma_i \nabla V_m) - \text{div}(\sigma_i \nabla u_e) = I_{\text{app}} & \text{in } \Omega_H \times (0, T), \\ -\text{div}((\sigma_i + \sigma_e) \nabla u_e) - \text{div}(\sigma_i \nabla V_m) = 0 & \text{in } \Omega_H \times (0, T), \\ -\text{div}(\sigma_T \nabla u_T) = 0 & \text{in } \Omega_T \times (0, T), \\ \sigma_T \nabla u_T \cdot \mathbf{n}_T = 0 & \text{on } \Gamma_{\text{ext}} \times (0, T), \\ \sigma_i \nabla V_m \cdot \mathbf{n} + \sigma_i \nabla u_e \cdot \mathbf{n} = 0 & \text{on } \Sigma \times (0, T), \\ u_T = u_e & \text{on } \Sigma \times (0, T), \\ \sigma_e \nabla u_e \cdot \mathbf{n} = -\sigma_T \nabla u_T \cdot \mathbf{n}_T & \text{on } \Sigma \times (0, T), \end{array} \right. \quad (3.2.8)$$

with the initial conditions  $V_m|_{t=0} = V_m^0$ ,  $w|_{t=0} = w^0$ . The boundary condition on  $\Gamma_{\text{ext}} \stackrel{\text{def}}{=} \partial\Omega_T \setminus \Sigma$  states that no current can flow from the external torso surface (see Figure 3.3).

The coupled system of equations (3.2.8) is often known in the literature as the *full bidomain* or *coupled bidomain* model (see, e.g., [CNLH04, SLC<sup>+</sup>06]). It can be considered as the state-of-the-art in the modeling of the ECG (see, e.g., [LBG<sup>+</sup>03, PBC05, SLC<sup>+</sup>06]).

**Remark 3.2** *A common approach to reduce the computational complexity of (3.2.8) consists in uncoupling the computation of  $(w, V_m, u_e)$  and  $u_T$ , by neglecting the electrical torso-to-heart feedback (see, e.g., [CNLH04, PDG03, LBG<sup>+</sup>03]). Thus, the coupling conditions (3.2.7) are replaced by*

$$\left\{ \begin{array}{ll} u_T = u_e & \text{on } \Sigma, \\ \sigma_e \nabla u_e \cdot \mathbf{n} = 0 & \text{on } \Sigma, \end{array} \right. \quad (3.2.9)$$

*which amounts to work with an isolated bidomain model.*

### 3.3 Mathematical analysis ([3])

Results on the existence and uniqueness of solution for the isolated bidomain system (3.2.4) have been reported in a number of works (see [CFS02, BK06, BCP09, Ven09]). However, none of these

works considers the analysis for the coupled heart-torso system (3.2.8). We have addressed the well-posedness analysis of this system for an abstract class of (two-variable) ionic models including:

- FitzHugh-Nagumo model [Fit61, NAY62]:

$$I_{\text{ion}}(v, w) = kv(v - a)(v - 1) + w, \quad g(v, w) = -\epsilon(\gamma v - w); \quad (3.3.10)$$

- Aliev-Panfilov model [AP96]:

$$I_{\text{ion}}(v, w) = kv(v - a)(v - 1) + vw, \quad g(v, w) = \epsilon(\gamma v(v - 1 - a) + w); \quad (3.3.11)$$

- Roger-McCulloch model [RM94]:

$$I_{\text{ion}}(v, w) = kv(v - a)(v - 1) + vw, \quad g(v, w) = -\epsilon(\gamma v - w); \quad (3.3.12)$$

- Mitchell-Schaeffer model [MS03]:

$$I_{\text{ion}}(v, w) = \frac{w}{\tau_{\text{in}}} v^2 (v - 1) - \frac{v}{\tau_{\text{out}}},$$

$$g(v, w) = \begin{cases} \frac{1 - w}{\tau_{\text{open}}} & \text{if } v \leq v_{\text{gate}}, \\ \frac{-w}{\tau_{\text{close}}} & \text{if } v > v_{\text{gate}}. \end{cases} \quad (3.3.13)$$

Here,  $0 < a < 1$ ,  $k$ ,  $\epsilon$ ,  $\gamma$ ,  $\tau_{\text{in}}$ ,  $\tau_{\text{out}}$ ,  $\tau_{\text{open}}$ ,  $\tau_{\text{close}}$  and  $0 < v_{\text{gate}} < 1$  are given positive constants.

The next theorem formally summarizes our main result.

**Theorem 3.1** *Let  $T > 0$ ,  $I_{\text{app}} \in L^2(\Omega_{\text{H}} \times (0, T))$ ,  $\sigma_{\text{i}}, \sigma_{\text{e}} \in \mathbf{L}^\infty(\Omega_{\text{H}})$  symmetric and uniformly definite positive,  $w_0 \in L^2(\Omega_{\text{H}})$  and  $v_0 \in H^1(\Omega_{\text{H}})$  be given data. Assume that  $I_{\text{ion}}$  and  $g$  are given by (3.3.10), (3.3.11), (3.3.12) or a regularized version of (3.3.13). Then, the heart-torso system (3.2.8) has a weak solution  $V_{\text{m}} \in L^\infty(0, T; H^1(\Omega_{\text{H}})) \cap H^1(0, T; L^2(\Omega_{\text{H}}))$ ,  $w \in H^1(0, T; L^2(\Omega_{\text{H}}))$  and  $u \in L^\infty(0, T; H^1(\Omega))$  with*

$$u \stackrel{\text{def}}{=} \begin{cases} u_{\text{e}} & \text{in } \Omega_{\text{H}}, \\ u_{\text{T}} & \text{in } \Omega_{\text{T}}, \end{cases}$$

and  $\Omega \stackrel{\text{def}}{=} \Omega_{\text{T}} \cup \overline{\Omega_{\text{H}}}$ . Moreover, for the FitzHugh-Nagumo model (3.3.10) the solution is unique.

The proof of Theorem 3.1 generalizes some of the arguments reported in [BK06, BCP09] to the case of the heart-torso coupling. The main idea consists in reformulating the bidomain system as a couple of degenerate reaction-diffusion equations and approximate the resulting heart-torso system by a suitably regularized problem in finite dimension, which is then analyzed through a Faedo-Galerkin/compactness procedure and a specific treatment of the non-linear terms. The heart-torso coupling is handled through an adequate definition of the Galerkin basis. To the best of our knowledge, the Mitchell-Schaeffer model has not yet been considered within a well-posedness study of the bidomain equations. Compared to models (3.3.10)-(3.3.12), this ionic model has a different structure that makes the existence proof slightly more involved. As we shall see in the next section, realistic ECG signals can be simulated via this ionic model.

### 3.4 Meaningful ECG simulations ([2, 18])

The aim of the work summarized in this section was twofold: first, provide realistic simulations of the 12-lead ECG based on (3.2.8); second, discuss through numerical simulations the impact of various modeling approximations (*e.g.*, uncoupling, monodomain, cell homogeneity, tissue anisotropy) and the sensitivity to the model parameters.

Our reference ECG mathematical model relies on (3.2.8) and the following additional modeling ingredients:

- the heart geometry only includes the ventricles (see Figure 3.4). Note that this simplification prevents us from computing the P-wave of the ECG (see Figure 3.2 (top-left));
- the torso geometry contains the lungs, bones and remaining extracardiac regions (see Figure 3.4);
- the fast conduction system (His bundle and Purkinje fibers) is modeled by initializing the activation with a (time-dependent) external volume current  $I_{\text{app}}$ , acting on a thin subendocardial layer of left and right ventricles. The propagation speed of this external stimulus is a parameter of the model (see [2] for details);
- the cardiac cell membrane dynamics are based on the Mitchell-Schaeffer ionic model (3.3.13);
- cells are heterogeneous in terms of action potential duration (APD), which transmurally varies within the left ventricle. In practice, this amounts to consider a parameter  $\tau_{\text{close}}$  in (3.3.13) which takes three different values in the ventricle (subendocardial, intracardial and subepicardial). This is important factor in the genesis of the normal ECG T-wave shape and polarity;
- the heart conductivities are anisotropic:

$$\boldsymbol{\sigma}_{i,e}(\mathbf{x}) \stackrel{\text{def}}{=} \sigma_{i,e}^t \mathbf{I} + (\sigma_{i,e}^l - \sigma_{i,e}^t) \mathbf{a}(\mathbf{x}) \otimes \mathbf{a}(\mathbf{x}),$$

where  $\mathbf{a}(\mathbf{x})$  is a unit vector parallel to the local fiber direction and  $\sigma_{i,e}^l$  and  $\sigma_{i,e}^t$  are, respectively, the conductivity coefficients in the intra- and extra-cellular media, measured along the fiber and transverse directions.

#### Numerical approximation

Problem (3.2.8) can be cast into weak form as follows: for  $t \in (0, T)$ , find  $w(\cdot, t) \in L^\infty(\Omega_{\text{H}})$ ,  $V_{\text{m}}(\cdot, t) \in H^1(\Omega_{\text{H}})$ ,  $u_{\text{e}}(\cdot, t) \in H^1(\Omega_{\text{H}}) \cap L_0^2(\Omega_{\text{H}})$  and  $u_{\text{T}}(\cdot, t) \in H^1(\Omega_{\text{T}})$  with  $u_{\text{e}}(\cdot, t) = u_{\text{T}}(\cdot, t)$  on  $\Sigma$ , such that

$$\begin{aligned} \int_{\Omega_{\text{H}}} (\partial_t w + g(V_{\text{m}}, w)) \xi &= 0, \\ \int_{\Omega_{\text{H}}} (\chi_{\text{m}} \partial_t V_{\text{m}} + I_{\text{ion}}(V_{\text{m}}, w)) \phi + \int_{\Omega_{\text{H}}} \boldsymbol{\sigma}_{\text{i}} \nabla(V_{\text{m}} + u_{\text{e}}) \cdot \nabla \phi &= \int_{\Omega_{\text{H}}} I_{\text{app}} \phi, \\ \int_{\Omega_{\text{H}}} (\boldsymbol{\sigma}_{\text{i}} + \boldsymbol{\sigma}_{\text{e}}) \nabla u_{\text{e}} \cdot \nabla \psi + \int_{\Omega_{\text{H}}} \boldsymbol{\sigma}_{\text{i}} \nabla V_{\text{m}} \cdot \nabla \psi + \int_{\Omega_{\text{T}}} \boldsymbol{\sigma}_{\text{T}} \nabla u_{\text{T}} \cdot \nabla \zeta &= 0 \end{aligned} \quad (3.4.14)$$

for all  $(\xi, \phi, \psi, \zeta) \in L^2(\Omega_{\text{H}}) \times H^1(\Omega_{\text{H}}) \times (H^1(\Omega_{\text{H}}) \cap L_0^2(\Omega_{\text{H}})) \times H^1(\Omega_{\text{T}})$  with  $\psi = \zeta$  on  $\Sigma$ . The weak formulation (3.4.14) is discretized in space using finite elements and in time using a semi-implicit scheme based on a backward difference formula (BDF).

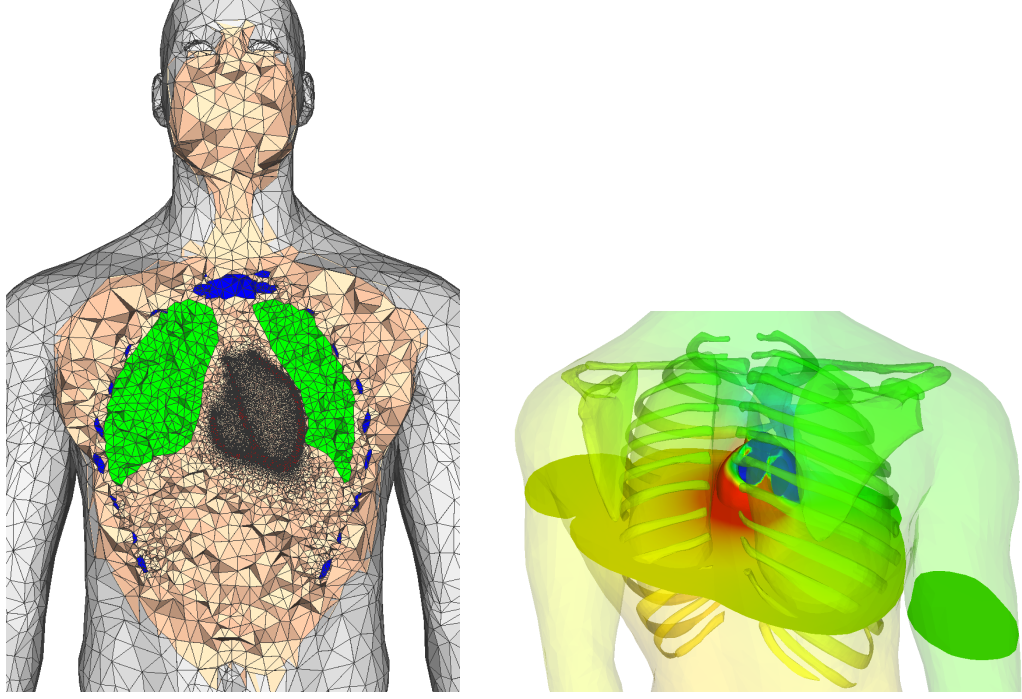


Figure 3.4: *Left*: cut view of the heart-torso computational mesh. Heart (red), lungs (green), bone (blue) and remaining tissue (apricot). *Right*: posterior view and cut plane of the torso and heart potentials at time  $t = 10$  ms.

Let  $N \in \mathbb{N}^*$  be a given integer and consider a uniform partition  $\{[t_n, t_{n+1}]\}_{0 \leq n \leq N-1}$ , with  $t_n \stackrel{\text{def}}{=} n\tau$ , of the time interval of interest  $(0, T)$ , with time-step size  $\tau \stackrel{\text{def}}{=} T/N$ . The notation  $\partial_\tau x^{n+1}$  represents a (first or second order) backward difference formula,  $\tilde{x}^{n+1}$  the corresponding explicit extrapolation (*i.e.*,  $x^n$  or  $2x^n - x^{n-1}$ ) and  $I_{\text{app}}^n \stackrel{\text{def}}{=} I_{\text{app}}(\cdot, t_n)$ . The space  $X_{H,h}$  (resp.  $X_{T,h}$ ) is the internal approximation of  $H^1(\Omega_H)$  (resp.  $H^1(\Omega_T)$ ) made of continuous piecewise affine functions. Moreover, we assume that the restrictions of  $X_{H,h}$  and  $X_{T,h}$  match at the interface  $\Sigma$ . The resulting fully discrete time advancing procedure reads as follows: For  $0 \leq n \leq N-1$ ,

1. Ionic state: find  $w^{n+1} \in X_{H,h}$  such that

$$\int_{\Omega_H} (\partial_\tau w^{n+1} + g(\tilde{V}_m^{n+1}, w^{n+1})) \xi = 0 \quad (3.4.15)$$

for all  $\xi \in X_{H,h}$ ;

2. Heart and torso potentials: find  $V_m^{n+1} \in X_{H,h}$ ,  $u_e^{n+1} \in X_{H,h} \cap L_0^2(\Omega_H)$  and  $u_T^{n+1} \in X_{T,h}$  with  $u_T^{n+1} = u_e^{n+1}$  on  $\Sigma$ , such that

$$\begin{aligned} \chi_m \int_{\Omega_H} \partial_\tau V_m^{n+1} \phi + \int_{\Omega_H} \sigma_i \nabla (V_m^{n+1} + u_e^{n+1}) \cdot \nabla \phi &= \int_{\Omega_H} (I_{\text{app}}^{n+1} - I_{\text{ion}}(\tilde{V}_m^{n+1}, w^{n+1})) \phi, \\ \int_{\Omega_H} (\sigma_i + \sigma_e) \nabla u_e^{n+1} \cdot \nabla \psi + \int_{\Omega_H} \sigma_i \nabla V_m^{n+1} \cdot \nabla \psi + \int_{\Omega_T} \sigma_T \nabla u_T^{n+1} \cdot \nabla \zeta &= 0, \end{aligned} \quad (3.4.16)$$

for all  $(\phi, \psi, \zeta) \in X_{H,h} \times (X_{H,h} \cap L_0^2(\Omega_H)) \times X_{T,h}$  with  $\psi = \zeta$  on  $\Sigma$ .

### Partitioned heart-torso coupling

At each time step, the linear problem (3.4.16) requires the coupled computation of the heart potentials  $(V_m^{n+1}, u_e^{n+1})$  and the torso potential  $u_T^{n+1}$ . This coupling can be solved monolithically, that is, after full assembling of the whole system matrix (see, *e.g.*, [LBG<sup>+</sup>03, Sections 4.6 and 4.5.1] and [SLMT02, SLC<sup>+</sup>06, BP02]), but this results in an increased number of unknowns with respect to the original bidomain system. Moreover, this procedure is less modular since the bidomain and torso equations cannot be solved independently. This shortcoming can be overcome using a partitioned iterative procedure based on domain decomposition (see, *e.g.*, [QV99, TW05]). In this study, the heart-torso coupling is solved, in a partitioned fashion, via relaxed Dirichlet-Neumann preconditioned Richardson iterations (as Algorithm 2.3 with (2.2.17)). A related approach is adopted in [BP02] (see also [LBG<sup>+</sup>03, PBC05]), using an integral formulation of the torso equation.

### Simulated ECG signals

Figure 3.5 shows some snapshots of the simulated body surface potentials. The corresponding 12-lead ECG signals are given in Figure 3.6. Despite some minor flaws, the comparison with Figure 3.1 (right) shows that the obtained numerical ECGs have the correct amplitudes, shapes and polarities, in all the twelve standard leads. To the best of our knowledge, this constitutes a breakthrough in the modeling of ECGs with partial differential equations.

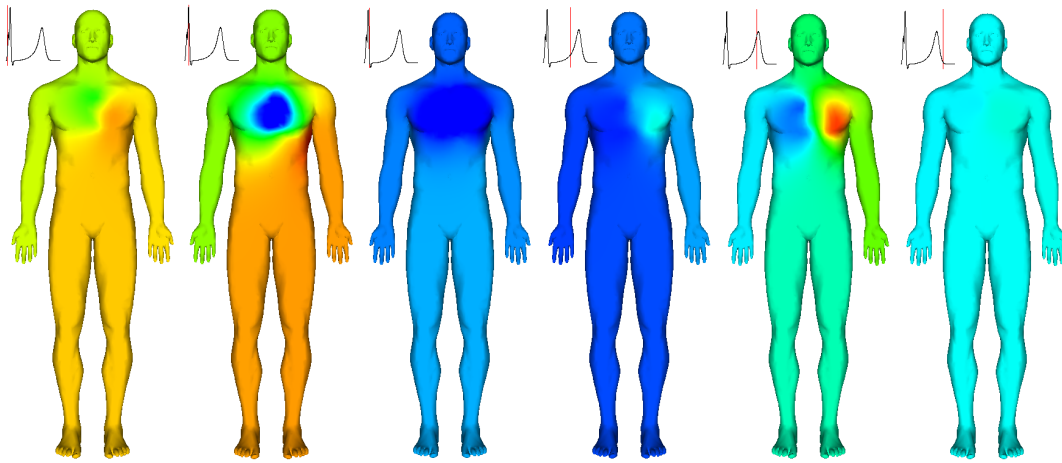


Figure 3.5: Snapshots of the body surface potentials at times  $t = 10, 32, 40$  ms (depolarization) and  $t = 200, 250$  and  $310$  ms (repolarization), from left to right.

**Remark 3.3** *It is worth mentioning that, for some pathological conditions (see [2] for details), our simulations have also provided ECG signals which satisfy the typical criteria used by medical doctors to detect the pathology, and this without any recalibration of the model parameters besides the natural modifications needed to model the disease. This shows, in particular, that our numerical model has some predictive features.*

**Remark 3.4** *We refer to [39, 36] for two examples of how the developed ECG simulator can be successfully used in different contexts and applications.*

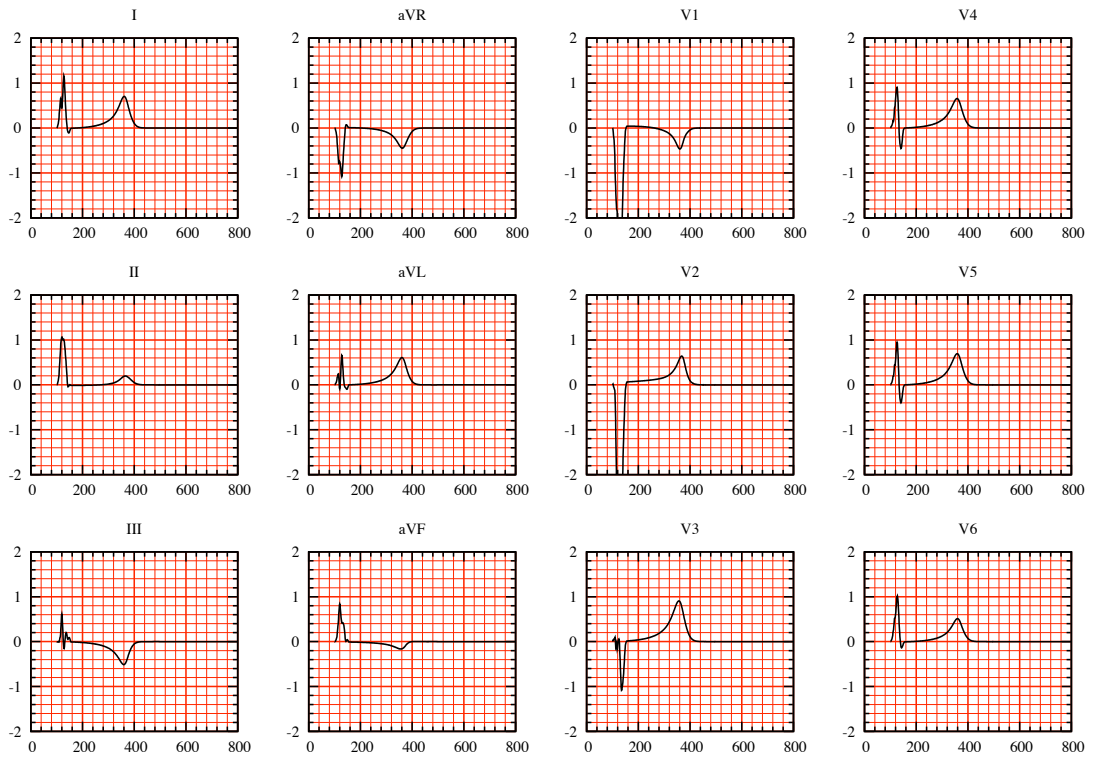


Figure 3.6: Simulated normal 12-lead ECG signals.

### Impact of some modeling assumptions

The ECG simulator has then been used to investigate numerically the impact of some modeling aspects. We have concluded that cell heterogeneity and tissue anisotropy are necessary modeling assumptions. For the considered cardiac conditions, the Mitchell-Schaeffer phenomenological ionic

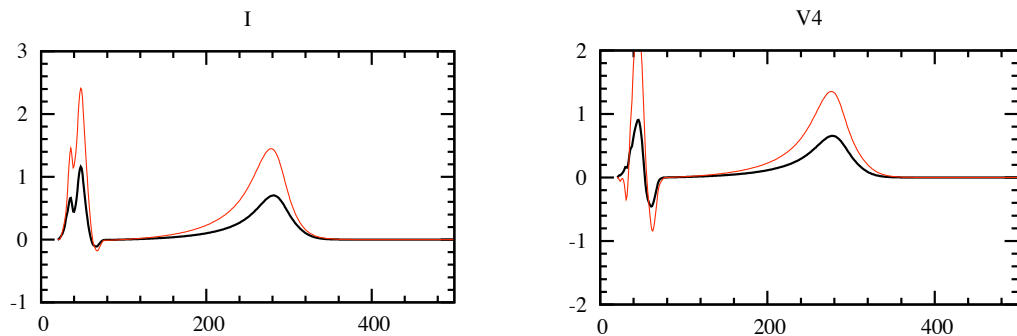


Figure 3.7: Simulated ECG signals (leads I and V4) obtained using heart-torso full coupling (black) and uncoupling (red).

model is enough. As regards the heart-torso uncoupling approximation (3.2.9), the comparison

reported in Figure 3.7 shows that heart-torso uncoupling compromises the accuracy of the ECG signals (notice the difference of amplitudes). Therefore uncoupling is not recommended in general.

The monodomain approximation (3.2.6) can be combined with the heart-torso uncoupling approximation (see, *e.g.* [Hui98, PDG03]). This yields a simplified mathematical model which allows a fully decoupled computation of  $V_m$ ,  $u_e$  and  $u_T$ . However, we have shown that without the uncoupling assumption (3.2.9) the monodomain approximation becomes

$$\begin{cases} \chi_m \partial_t V_m + I_{\text{ion}}(V_m, w) - \operatorname{div}(\boldsymbol{\sigma} \nabla V_m) = I_{\text{app}}, & \text{in } \Omega_H, \\ \boldsymbol{\sigma} \nabla V_m \cdot \mathbf{n} = -\mu \boldsymbol{\sigma}_e \nabla u_e \cdot \mathbf{n}, & \text{on } \Sigma, \end{cases} \quad (3.4.17)$$

where  $\mu \in (0, 1)$  is a dimensionless parameter related to the local conductivities (see also [CNLH04]). Note that, in (3.4.17), the unknowns  $V_m$  and  $u_e$  are still coupled. Therefore, under the full heart-torso coupling (3.2.7), the monodomain approximation does not reduce the computational complexity with respect to (3.2.8).

**Remark 3.5** *An alternative can be to neglect the boundary coupling in (3.4.17)<sub>2</sub> while keeping  $u_e$  and  $u_T$  fully coupled (see [PDV09]). In a pure propagation framework (i.e., without extracellular pacing) numerical experiments suggest that this approach can provide accurate ECG signals.*

## 3.5 Fully decoupled time marching schemes ([18])

In this section we introduce and analyze some time-marching schemes for the numerical approximation of the isolated bidomain model (§3.5.1) and the heart-torso system (§3.5.2). The particularity of these schemes is that they all allow an uncoupled computation of the involved fields (ionic state, transmembrane potential, extracellular and torso potentials).

In what follows, the quantity  $\partial_\tau x^n$  denotes the first order backward difference  $(x^n - x^{n-1})/\tau$ .

### 3.5.1 Isolated bidomain model

The isolated bidomain system (3.2.4)-(3.2.5) can be cast into weak form as follows: for  $t > 0$ , find  $w(\cdot, t) \in L^\infty(\Omega_H)$ ,  $V_m(\cdot, t) \in H^1(\Omega_H)$  and  $u_e(\cdot, t) \in H^1(\Omega_H) \cap L_0^2(\Omega_H)$ , such that

$$\begin{aligned} & \int_{\Omega_H} (\partial_t w + g(V_m, w)) \xi = 0, \\ & \int_{\Omega_H} (\chi_m \partial_t V_m + I_{\text{ion}}(V_m, w)) \phi + \int_{\Omega_H} \boldsymbol{\sigma}_i \nabla(V_m + u_e) \cdot \nabla \phi = \int_{\Omega_H} I_{\text{app}} \phi, \\ & \int_{\Omega_H} (\boldsymbol{\sigma}_i + \boldsymbol{\sigma}_e) \nabla u_e \cdot \nabla \psi + \int_{\Omega_H} \boldsymbol{\sigma}_i \nabla V_m \cdot \nabla \psi = 0 \end{aligned} \quad (3.5.18)$$

for all  $(\xi, \phi, \psi) \in L^2(\Omega_H) \times H^1(\Omega_H) \times (H^1(\Omega_H) \cap L_0^2(\Omega_H))$ .

The rapid dynamics of the ODE system (3.5.18)<sub>1</sub>, acting on the reaction terms (3.5.18)<sub>2</sub>, lead to the presence of a sharp propagating wavefront (see Figure 3.4 (right)), which often requires fine resolutions in space and in time. Fully implicit time-marching is, therefore, extremely difficult to perform since it involves the resolution of a large system of non-linear equations at each time step (see, *e.g.*, [HHLR94, BELB03, MC04]). Attempts to reduce this computational complexity (without compromising too much numerical stability) consist in introducing some sort of explicit treatment within the time-marching procedure. For instance, by considering semi-implicit (see, *e.g.*, §3.4 and [SLT01, LGT03, CFP04, ATP06, EB08]) or operator splitting (see, *e.g.*, [KB98, SLT05, VWdSP+08]) schemes. All these approaches uncouple the ODE system (ionic state and

non-linear reaction terms) from the electro-diffusive components (transmembrane and extracellular potentials). A few works [SLT01, LGT03, ATP06, VWdSP<sup>+</sup>08] considered (without analysis) a decoupled (*Gauss-Seidel* like) time-marching of the three fields.

We have shown that the Gauss-Seidel and the Jacobi electro-diffusive splittings do not compromise the stability of the resulting scheme. They simply alter the energy norm and the time-step restrictions are uniquely dictated by the semi-implicit treatment of the ODE system and the non-linear reaction terms. Let us consider the semi-discretization in time of (3.5.18) obtained by combining a first order semi-implicit treatment of the ionic current with an explicit (*Gauss-Seidel* or *Jacobi* like) treatment of the electro-diffusive coupling, as detailed in Algorithm 3.1.

---

**Algorithm 3.1** Decoupled time-marching for the bidomain equation.

---

1. Ionic state: find  $w^{n+1} \in L^\infty(\Omega_H)$  such that

$$\int_{\Omega_H} (\partial_\tau w^{n+1} + g(V_m^n, w^{n+1})) \xi = 0$$

for all  $\xi \in L^2(\Omega_H)$ ;

2. Transmembrane potential: find  $V_m^{n+1} \in H^1(\Omega_H)$  such that

$$\chi_m \int_{\Omega_H} \partial_\tau V_m^{n+1} \phi + \int_{\Omega_H} \sigma_i \nabla V_m^{n+1} \cdot \nabla \phi + \int_{\Omega_H} \sigma_i \nabla u_e^* \cdot \nabla \phi = \int_{\Omega_H} (I_{\text{app}}^{n+1} - I_{\text{ion}}(V_m^n, w^{n+1})) \phi$$

for all  $\phi \in H^1(\Omega_H)$ ;

3. Extracellular potential: find  $u_e^{n+1} \in H^1(\Omega_H) \cap L_0^2(\Omega_H)$ ,

$$\int_{\Omega_H} (\sigma_i + \sigma_e) \nabla u_e^{n+1} \cdot \nabla \psi + \int_{\Omega_H} \sigma_i \nabla V_m^* \cdot \nabla \psi = 0$$

for all  $\psi \in H^1(\Omega_H) \cap L_0^2(\Omega_H)$ ;

4. Go to next time-step.
- 

For  $(u_e^*, V_m^*) = (u_e^{n+1}, V_m^{n+1})$ , the unknown potentials  $V_m^{n+1}$  and  $u_e^{n+1}$  are implicitly coupled and, therefore, steps 2 and 3 of Algorithm 3.1 have to be performed simultaneously (as in §3.4). On the contrary, for  $(u_e^*, V_m^*) = (u_e^n, V_m^{n+1})$  or  $(u_e^*, V_m^*) = (u_e^n, V_m^n)$ , the electro-diffusive coupling becomes explicit and therefore these steps can be performed separately: either sequentially (*Gauss-Seidel*) or in parallel (*Jacobi*).

### Stability analysis

In order to facilitate the analysis we have made the following assumption (see [EB08, Section 3.2.2] and Remark 3.1 therein) on the structure of the non-linear terms:

$$\begin{aligned} I_{\text{ion}}(V_m, w) &\leq C_I (|V_m| + |w|), \\ g(V_m, w) &\leq C_g (|V_m| + |w|) \end{aligned} \tag{3.5.19}$$

for all  $V_m, w$ , and we set  $\alpha \stackrel{\text{def}}{=} 1 + 3C_I + C_g$  and  $\beta \stackrel{\text{def}}{=} C_I + 3C_g$ . In what follows, the symbol  $\lesssim$  indicates an inequality up to a multiplicative constant proportional to  $e^{T/(1-\tau \max\{\alpha, \beta\})}$ .

The next result states the energy based stability of Algorithm 3.1, in terms of  $u_e^*$  and  $V_m^*$ .

**Theorem 3.2** *Assume that (3.5.19) holds and let  $(w^n, V_m^n, u_e^n)$  be given by Algorithm 3.1. Then, under the condition*

$$\tau < \frac{1}{\max\{\alpha, \beta\}}, \quad (3.5.20)$$

there follows:

- For  $(u_e^*, V_m^*) = (u_e^{n+1}, V_m^{n+1})$ :

$$\begin{aligned} & \|w^n\|_{0,\Omega_H}^2 + \chi_m \|V_m^n\|_{0,\Omega_H}^2 + 2 \sum_{m=0}^{n-1} \tau \|\sigma_e^{\frac{1}{2}} \nabla u_e^{m+1}\|_{0,\Omega_H}^2 + 2 \sum_{m=0}^{n-1} \tau \|\sigma_i^{\frac{1}{2}} \nabla (V_m^{m+1} + u_e^{m+1})\|_{0,\Omega_H}^2 \\ & \lesssim \|w^0\|_{0,\Omega_H}^2 + \chi_m \|V_m^0\|_{0,\Omega_H}^2 + \sum_{m=0}^{n-1} \tau \|I_{\text{app}}^{m+1}\|_{0,\Omega_H}^2, \end{aligned}$$

with  $1 \leq n \leq N$ ;

- For  $(u_e^*, V_m^*) = (u_e^n, V_m^{n+1})$ :

$$\begin{aligned} & \|w^n\|_{0,\Omega_H}^2 + \chi_m \|V_m^n\|_{0,\Omega_H}^2 + \tau \|\sigma_i^{\frac{1}{2}} \nabla u_e^n\|_{0,\Omega_H}^2 \\ & + 2 \sum_{m=0}^{n-1} \tau \|\sigma_e^{\frac{1}{2}} \nabla u_e^{m+1}\|_{0,\Omega_H}^2 + \sum_{m=0}^{n-1} \tau \|\sigma_i^{\frac{1}{2}} \nabla (V_m^{m+1} + u_e^{m+1})\|_{0,\Omega_H}^2 \\ & \lesssim \|w^0\|_{0,\Omega_H}^2 + \chi_m \|V_m^0\|_{0,\Omega_H}^2 + \tau \|\sigma_i^{\frac{1}{2}} \nabla u_e^0\|_{0,\Omega_H}^2 + \sum_{m=0}^{n-1} \tau \|I_{\text{app}}^{m+1}\|_{0,\Omega_H}^2, \end{aligned}$$

with  $1 \leq n \leq N$ ;

- For  $(u_e^*, V_m^*) = (u_e^n, V_m^n)$ :

$$\begin{aligned} & \|w^n\|_{0,\Omega_H}^2 + \chi_m \|V_m^n\|_{0,\Omega_H}^2 + \tau \|\sigma_i^{\frac{1}{2}} \nabla u_e^n\|_{0,\Omega_H}^2 + \tau \|\sigma_i^{\frac{1}{2}} \nabla V_m^n\|_{0,\Omega_H}^2 + 2 \sum_{m=0}^{n-1} \tau \|\sigma_e^{\frac{1}{2}} \nabla u_e^{m+1}\|_{0,\Omega_H}^2 \\ & \lesssim \|w^0\|_{0,\Omega_H}^2 + \chi_m \|V_m^0\|_{0,\Omega_H}^2 + \tau \|\sigma_i^{\frac{1}{2}} \nabla V_m^0\|_{0,\Omega_H}^2 + \tau \|\sigma_i^{\frac{1}{2}} \nabla u_e^0\|_{0,\Omega_H}^2 + \sum_{m=0}^{n-1} \tau \|I_{\text{app}}^{m+1}\|_{0,\Omega_H}^2, \end{aligned}$$

with  $1 \leq n \leq N$ .

Theorem 3.2 shows that electro-diffusive Gauss-Seidel and Jacobi splittings are energy stable under condition (3.5.20), as for the unsplit case  $(u_e^*, V_m^*) = (u_e^{n+1}, V_m^{n+1})$  (analyzed in [EB08]), but with slightly altered energy norms. As a result, stability is not compromised.

**Remark 3.6** *The proof of Theorem 3.2 does not depend on the time discretization considered in steps 1 and 2 of Algorithm 3.1. Indeed, we do not make use of any numerical dissipation produced by the scheme, a part from that is directly provided by the splitting. Therefore, the backward Euler quotients,  $\partial_\tau w^{n+1}$  and  $\partial_\tau V_m^{n+1}$ , can be safely replaced by a second order backward difference formula, and perform one correction (see, e.g., [Ste78, SM00] and §2.4.1) to recover an overall second order accuracy.*

$\tau$ (ms)	Coupled	G-S	Jacobi
0.25	✓	✓	✓
0.50	✓	✓	✓
1.00	✓	✓	✓
1.25	✗	✗	✗
1.50	✗	✗	✗

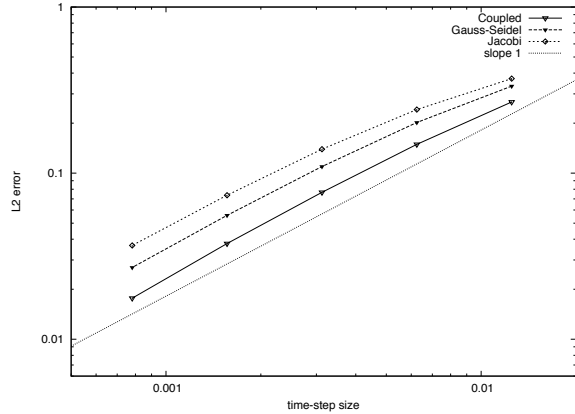


Figure 3.8: *Left*: stability sensitivity to time-step size (symbol ✗ indicates numerical instability). *Right*: time convergence history of the transmembrane potential error for the Coupled  $((u_e^*, V_m^*) = (u_e^{n+1}, V_m^{n+1}))$ , Gauss-Seidel  $((u_e^*, V_m^*) = (u_e^n, V_m^{n+1}))$  and Jacobi  $((u_e^*, V_m^*) = (u_e^n, V_m^n))$  bidomain time-marching schemes.

**Remark 3.7** *The above stability result can be adapted, with minor modifications, to the case  $((u_e^*, V_m^*) = (u_e^{n+1}, V_m^n))$ . The full Jacobi splitting, obtained after replacing  $I_{\text{ion}}(V_m^n, w^{n+1})$  by  $I_{\text{ion}}(V_m^n, w^n)$  in step 2 could, also be considered.*

We conclude this subsection with a few numerical illustrations. The results reported in Figure 3.8 (left) confirm that the electro-diffusive Gauss-Seidel and Jacobi splittings do not introduce additional constraints on the time step size  $\tau$ , as stated in Theorem 3.2. Figure 3.8 (right) shows that the Coupled, the Gauss-Seidel and the Jacobi time-marching schemes all provide the expected first order accuracy  $\mathcal{O}(\tau)$  in time. Note that, at a given time-step size, Gauss-Seidel is slightly more accurate than Jacobi and Coupled than Gauss-Seidel. This accuracy shifting could be related to the energy-norm weakening observed in the stability analysis.

### 3.5.2 Coupled heart-torso system

We have proposed a series of time-marching procedures for the heart-torso system (3.2.8), that allow a decoupled computation of the transmembrane, extracellular and torso potentials. The main idea consists in combining the bidomain splittings of the previous section, with a specific explicit Robin-Robin treatment of the heart-torso coupling conditions derived from §2.4. The proposed schemes are presented in Algorithm 3.2, with  $\gamma > 0$  is a dimensionless free parameter (fixed below) and where we have assumed that (without loss of generality)  $\sigma_{\text{T}}|_{\Sigma} = \sigma_{\text{T}}^{\text{t}} \mathbf{I}$ .

Note that the cardiac subproblem (steps 1–3) can be solved independently of the torso subproblem (step 4). In particular, the choices  $((u_e^*, V_m^*) = (u_e^n, V_m^{n+1}))$  or  $((u_e^*, V_m^*) = (u_e^n, V_m^n))$  lead to a fully decoupled computation of  $w^{n+1}$ ,  $V_m^{n+1}$ ,  $u_e^{n+1}$  and  $u_{\text{T}}^{n+1}$ . In other words, steps 1–4 are decoupled and can be performed sequentially.

**Remark 3.8** *The choices  $((u_e^*, V_m^*) = (u_e^n, V_m^{n+1}))$  or  $((u_e^*, V_m^*) = (u_e^n, V_m^n))$  in Algorithm 3.2 allow a fully decoupled computation of  $w^{n+1}$ ,  $V_m^{n+1}$ ,  $u_e^{n+1}$  and  $u_{\text{T}}^{n+1}$  without the need to resort to monodomain and uncoupling approximations (see §3.4).*

**Remark 3.9** *The interface coupling between steps 3 and 4 of Algorithm 3.2 corresponds to the*

following Robin-Robin based explicit time discretization of (3.2.7):

$$\begin{aligned} \sigma_e \nabla u_e^{n+1} \cdot \mathbf{n} + \frac{\gamma \sigma_T^t}{h} u_e^{n+1} &= -\sigma_T \nabla u_T^n \cdot \mathbf{n}_T + \frac{\gamma \sigma_T^t}{h} u_T^n, & \text{on } \Sigma, \\ \sigma_T \nabla u_T^{n+1} \cdot \mathbf{n}_T + \frac{\gamma \sigma_T^t}{h} u_T^{n+1} &= \sigma_T \nabla u_T^n \cdot \mathbf{n}_T + \frac{\gamma \sigma_T^t}{h} u_e^{n+1}, & \text{on } \Sigma, \end{aligned} \quad (3.5.21)$$

derived from §2.4. Note that, since the (quasi-static) time discretization of (3.2.8)<sub>3,4</sub> does not generate numerical dissipation in time, a naive Dirichlet-Neumann explicit coupling, obtained by enforcing

$$\begin{cases} u_T^{n+1} = u_e^n, & \text{on } \Sigma, \\ \sigma_e \nabla u_e^{n+1} \cdot \mathbf{n} = -\sigma_T \nabla u_T^{n+1} \cdot \mathbf{n}_T, & \text{on } \Sigma, \end{cases}$$

might lead to numerical instability.

---

**Algorithm 3.2** Decoupled time-marching for the heart-torso system.

---

1. Ionic state: find  $w^{n+1} \in X_{H,h}$  such that

$$\int_{\Omega_H} (\partial_\tau w^{n+1} + g(V_m^n, w^{n+1})) \xi = 0$$

for all  $\xi \in X_{H,h}$ ;

2. Transmembrane potential: find  $V_m^{n+1} \in X_{H,h}$  such that

$$\begin{aligned} \chi_m \int_{\Omega_H} \partial_\tau V_m^{n+1} \phi + \int_{\Omega_H} \sigma_i \nabla V_m^{n+1} \cdot \nabla \phi + \int_{\Omega_H} \sigma_i \nabla u_e^* \cdot \nabla \phi \\ = \int_{\Omega_H} (I_{\text{app}}^{n+1} - I_{\text{ion}}(V_m^n, w^{n+1})) \phi \end{aligned}$$

for all  $\phi \in X_{H,h}$ ;

3. Extracellular potential: find  $u_e^{n+1} \in X_{H,h}$  such that

$$\begin{aligned} \int_{\Omega_H} (\sigma_i + \sigma_e) \nabla u_e^{n+1} \cdot \nabla \psi + \int_{\Omega_H} \sigma_i \nabla V_m^* \cdot \nabla \psi + \frac{\gamma \sigma_T^t}{h} \int_{\Sigma} u_e^{n+1} \psi \\ = - \int_{\Sigma} \sigma_T \nabla u_T^n \cdot \mathbf{n}_T \psi + \frac{\gamma \sigma_T^t}{h} \int_{\Sigma} u_T^n \psi \end{aligned}$$

for all  $\psi \in X_{H,h}$ ;

4. Torso potential: find  $u_T^{n+1} \in X_{T,h}$

$$\int_{\Omega_T} \sigma_T \nabla u_T^{n+1} \cdot \nabla \zeta + \frac{\gamma \sigma_T^t}{h} \int_{\Sigma} u_T^{n+1} \zeta = \int_{\Sigma} \sigma_T \nabla u_T^n \cdot \mathbf{n}_T \zeta + \frac{\gamma \sigma_T^t}{h} \int_{\Sigma} u_e^{n+1} \zeta$$

for all  $\zeta \in X_{T,h}$ ;

5. Go to next time-step.
-

The next result states the energy based stability of Algorithm 3.2. There,  $E_{\text{H}}^0(u_e^*, V_m^*)$  (resp.  $E_{\text{H}}^n(u_e^*, V_m^*)$ ) denotes the discrete bidomain energy arising in the stability estimates provided by Theorem 3.2. For instance, in the case  $(u_e^*, V_m^*) = (u_e^n, V_m^n)$ , we have

$$\begin{aligned} E_{\text{H}}^0(u_e^*, V_m^*) &\stackrel{\text{def}}{=} \|w^0\|_{0,\Omega_{\text{H}}}^2 + \chi_m \|V_m^0\|_{0,\Omega_{\text{H}}}^2 + \tau \|\sigma_i^{\frac{1}{2}} \nabla V_m^0\|_{0,\Omega_{\text{H}}}^2 + \tau \|\sigma_i^{\frac{1}{2}} \nabla u_e^0\|_{0,\Omega_{\text{H}}}^2, \\ E_{\text{H}}^n(u_e^*, V_m^*) &\stackrel{\text{def}}{=} \|w^n\|_{0,\Omega_{\text{H}}}^2 + \chi_m \|V_m^n\|_{0,\Omega_{\text{H}}}^2 + \tau \|\sigma_i^{\frac{1}{2}} \nabla u_e^n\|_{0,\Omega_{\text{H}}}^2 + \tau \|\sigma_i^{\frac{1}{2}} \nabla V_m^n\|_{0,\Omega_{\text{H}}}^2 \\ &\quad + 2 \sum_{m=0}^{n-1} \tau \|\sigma_e^{\frac{1}{2}} \nabla u_e^{m+1}\|_{0,\Omega_{\text{H}}}^2, \end{aligned}$$

and similarly for the rest.

**Theorem 3.3** *Assume that the hypotheses of Theorem 3.2 hold and let  $(w^n, V_m^n, u_e^n, u_{\text{T}}^n)$  be given by Algorithm 3.2. Then, for  $\gamma \geq 2C_{\text{ti}}$  and  $1 \leq n \leq N$  the following estimate holds*

$$\begin{aligned} E_{\text{H}}^n(u_e^*, V_m^*) + \tau \frac{\gamma \sigma_{\text{T}}^{\text{t}}}{h} \|u_{\text{T}}^n\|_{0,\Sigma}^2 + \sum_{m=0}^{n-1} \tau \|\sigma_{\text{T}}^{\frac{1}{2}} \nabla u_{\text{T}}^{m+1}\|_{0,\Omega_{\text{T}}}^2 + \frac{\gamma \sigma_{\text{T}}^{\text{t}}}{h} \sum_{m=0}^{n-1} \tau \|u_{\text{T}}^{m+1} - u_e^{m+1}\|_{0,\Sigma}^2 \\ \lesssim E_{\text{H}}^0(u_e^*, V_m^*) + \tau \frac{\gamma \sigma_{\text{T}}^{\text{t}}}{h} \|u_{\text{T}}^0\|_{0,\Sigma}^2 + \tau \|\sigma_{\text{T}}^{\frac{1}{2}} \nabla u_{\text{T}}^0\|_{0,\Omega_{\text{T}}}^2 + \sum_{m=0}^{n-1} \tau \|I_{\text{app}}^{m+1}\|_{0,\Omega_{\text{H}}}^2. \end{aligned}$$

Therefore, the explicit heart-torso coupling Algorithm 3.2 is energy stable under the condition  $\tau = \mathcal{O}(h)$ .

**Remark 3.10** *The proof of the above result does not make use of any numerical dissipation apart from that directly provided by the explicit Robin-Robin splitting (3.5.21). Note that this is particularly well adapted to the heart-torso coupling (3.2.8), since the quasi-static elliptic equations (3.2.8)<sub>3,4</sub> do not generate numerical dissipation in time.*

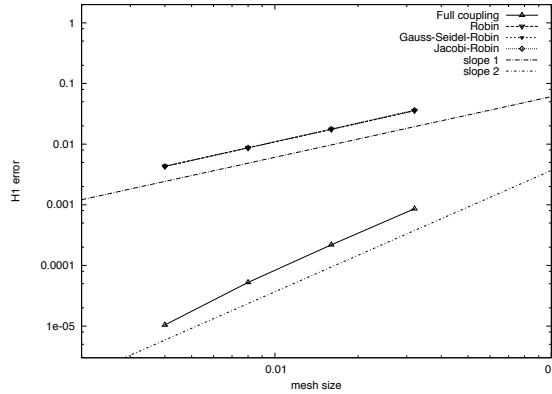


Figure 3.9: Convergence history of the torso potential error for the full coupling ((3.4.15)-(3.4.16)), Robin  $((u_e^*, V_m^*) = (u_e^{n+1}, V_m^{n+1}))$ , Gauss-Seidel-Robin  $((u_e^*, V_m^*) = (u_e^n, V_m^{n+1}))$  and Jacobi-Robin  $((u_e^*, V_m^*) = (u_e^n, V_m^n))$  with  $\tau = \mathcal{O}(h^2)$ .

We conclude this subsection with a few numerical illustrations on the accuracy of Algorithm 3.2. Figure 3.9 shows that the superior stability properties and computational cost reduction

featured by the proposed Robin heart-torso decoupling schemes come with a price: a condition  $\tau = \mathcal{O}(h^2)$  is required to guarantee an overall  $\mathcal{O}(h)$  convergence rate. Indeed, the penalty  $1/h$  involved in the explicit Robin treatment introduces a non-standard coupling between the space and time discretizations, which has a consistency of  $\mathcal{O}(\tau/h)$  (see §2.4.1).

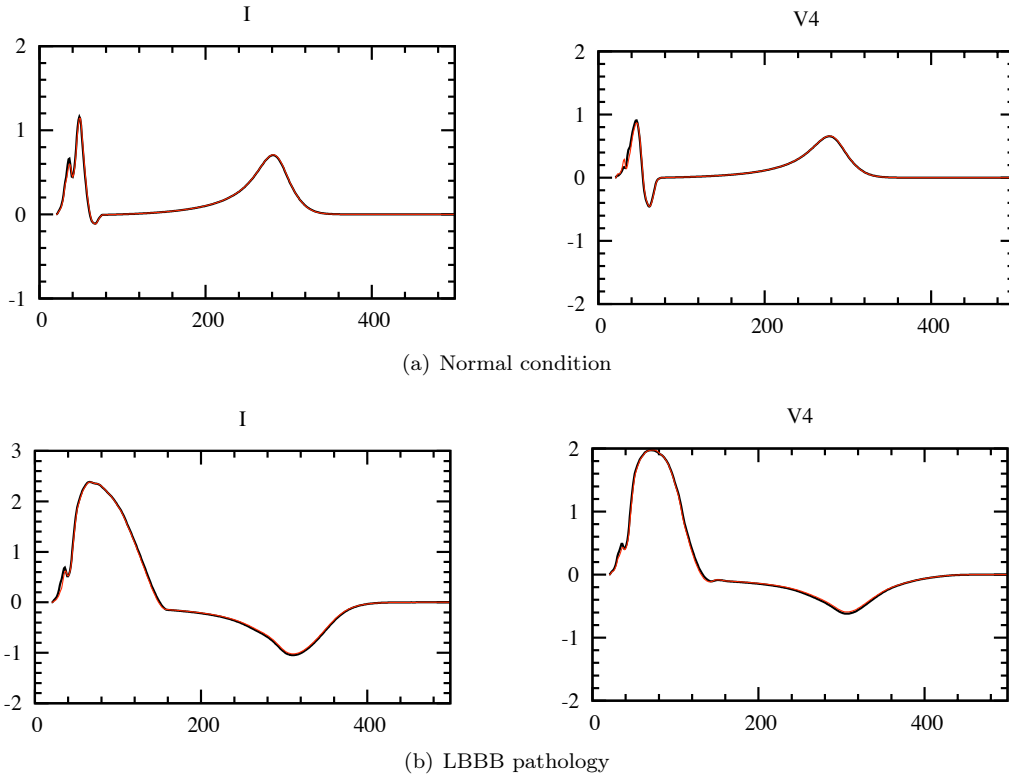


Figure 3.10: Simulated ECG signals (leads I and V4) obtained using heart-torso full coupling (black) and the Jacobi-Robin scheme (red).

In spite of that, Figure 3.10 shows that the proposed Robin splittings are able to provide accurate 12-lead ECG signals, both for a healthy and a pathological condition. Note that this is a major advantage with respect to the conventional heart-torso uncoupling approximation, which (for a similar computational cost) provides inaccurate ECG signals (see Figure 3.7). Somehow the discretization error introduced by the Robin heart-torso decoupling is negligible with respect to the modeling error involved in the heart-torso uncoupling approximation.

### 3.6 Perspectives

Many aspects of these works can be improved and may lead to future extensions. In the context of ECG modeling, our numerical signals were obtained with a mathematical model that completely neglects the mechanical feedback into the electrical model (see, *e.g.*, [LTS96, NSH05]). We think it would be worth highlighting, for instance, the impact of the myocardium motion on the shape of the ECG. The atria were also not considered in our simulations and the His bundle and the Purkinje fibers were roughly modeled via a parametrized stimulation wave. Clearly, there

is room for improvements on these aspects. Further investigations could also be oriented to the determination of the main factors involved in the shape and polarity of the T-wave in the 12-lead ECG, for instance, in the spirit of the recent study [CFPST09]. Regarding the mathematical well-posedness of the heart-torso problem, the uniqueness issues and the consideration of more complex ionic models certainly call for further investigations.

The decoupled time-marching schemes introduced in this work are limited to discretizations yielding overall first order accuracy in time. The generalization of the proposed analysis to higher order extrapolations might not be straightforward (unless correction iterations are allowed). Therefore, further numerical investigations would definitely help to clarify this issue and could be the topic of future work. As regards the discretization in space, some preliminary results on mesh adaptation are given in [Zem09, Appendix 9.9]. Further investigations could also address the feasibility of an ECG-based goal-oriented mesh adaptation.

At last, future investigations will also concern the inverse problem of electrocardiography and optimization related problems. A preliminary study on the optimal pacemaker lead positioning, based on our ECG simulator, has been recently reported in [DEA07].

## Chapter 4

# Stabilized finite element methods for transient problems

The work summarized in this chapter is the result of a long collaboration with E. Burman (University of Sussex, UK), initiated in 2003 at EPFL (Lausanne, Switzerland) and pursued later thanks to the Visiting Professors program of INRIA Paris-Rocquencourt and, more recently, the French-British PHC Alliance program (British Council and French Embassy in London).

### 4.1 Motivations

The main motivation of this work stems from the simulation of incompressible viscous flows (involved in Chapters 1 and 2), driven by the transient Navier-Stokes equations

$$\begin{cases} \partial_t \mathbf{u} + \mathbf{u} \cdot \nabla \mathbf{u} - \nu \Delta \mathbf{u} + \nabla p = \mathbf{f} & \text{in } \Omega \times (0, T), \\ \operatorname{div} \mathbf{u} = 0 & \text{in } \Omega \times (0, T), \end{cases} \quad (4.1.1)$$

which describe the evolution, during the time interval  $(0, T)$ , of the velocity  $\mathbf{u}$  and the pressure  $p$  in a given control volume  $\Omega$ . The constant  $\nu$  stands for the kinematic viscosity of the fluid and  $\mathbf{f}$  is a given source field.

A natural approach to approximate numerically (4.1.1) is the method of lines: first, semi-discretize in space with a finite element method (FEM) and, then, apply an  $\mathcal{A}$ -stable scheme to discretize in time (see, *e.g.*, [HR90]). Regardless of the time dependence and of the non-linearity treatment, it is well known that the standard Galerkin FEM applied to (4.1.1) loses stability in the following cases:

- dominating advection ( $0 < \nu \ll \|\mathbf{u}\|_{L^\infty(\Omega)}$ );
- use of equal order velocity and pressure approximations (which is of practical use).

The first situation leads to spurious oscillations in the velocity approximations. The second violates the so-called discrete *inf-sup* condition (see, *e.g.*, [GR86]), leading to instabilities in the pressure. These problems are usually overcome with the use of *stabilized* finite element methods, where suitable (consistent) terms are added to the standard Galerkin formulation in order to enhance stability without compromising accuracy.

A favored approach is to stabilize both the velocity and the pressure by combining the Streamline-Upwind/Petrov-Galerkin (SUPG) [BH82] and the Pressure-Stabilized/Petrov-Galerkin (PSPG)

[HFB86] methods. Stability is hence enhanced by adding to the Galerkin formulation an element-wise weighted residual. Other related methods, involving alternative residual testings, are the Galerkin-Least-Square (GLS) method [FF92] and the Algebraic-Subgrid-Scale (ASGS) method [Cod01, CPGB07]. Because of their structure, these methods are usually termed as (element-wise) *residual based stabilizations*. The SUPG/PSPG method owes its success to its unified treatment of the velocity and pressure instabilities. It allows for *a priori* error estimates that are uniform on the viscosity coefficient (see, *e.g.*, [HS90, TV96]) and has been used extensively with good results.

In spite of that, residual based stabilizations have some undesirable features (see [GLOS05, BBJL07]). The stabilization introduces artificial non-symmetric terms and non-physical pressure-velocity couplings. Moreover, the analysis of the extensions of these methods to the transient case is not yet completely understood (unless one resorts to space-time finite element formulations [HS90, Tez92]). As a matter of fact, the combination of these methods with standard time-stepping procedures is known to lead to numerical instabilities when the time-step size is small (see, *e.g.*, [BGS04, BGL07]). In [CPGB07], these instabilities were cured by including time-dependent sub-grid scales in the ASGS method. We refer also to [Bur10a], for recent analysis of the SUPG method applied to a scalar transient transport problem.

To overcome these disadvantages, alternative stabilization techniques have been reported in the literature. For instance, the orthogonal sub-scales method [Cod00], the subgrid viscosity method [Gue99], the local projection method [BB01, BB06] and the continuous interior penalty (CIP) method [BH04, BH06]. The price to pay for these symmetric stabilization techniques is the larger stencil of the corresponding stiffness matrix due to projection computations or gradient jumps involved in the stabilization operator.

The extension of the CIP method to the Oseen problem and the time dependent Navier-Stokes equations is summarized in §4.3 and §4.4, respectively. A priori error bounds uniform on the viscosity coefficient are provided for arbitrary equal-order velocity/pressure approximations. We then present an abstract error analysis for symmetric stabilization methods, applied to the transient Stokes equations in §4.5, and to the transient reaction-advection-diffusion equation in §4.6. For Stokes we show, in particular, that the small time-step stability can be removed by a suitable choice of the initial velocity approximation. For reaction-advection-diffusion we address the problem of the perturbation of the stencil via an explicit treatment of the stabilization (see also [CB00]).

## 4.2 Preliminaries

We will consider the Sobolev spaces  $W^{m,q}(\Omega)$ , with norm  $\|\cdot\|_{m,q,\Omega}$ ,  $m \geq 0$  and  $q \geq 1$ . In particular, we have  $L^q(\Omega) = W^{0,q}(\Omega)$ . We use the standard notation  $H^m(\Omega) \stackrel{\text{def}}{=} W^{m,2}(\Omega)$ . The norm of  $H^m(\Omega)$  is denoted by  $\|\cdot\|_{m,\Omega}$  and its semi-norm by  $|\cdot|_{m,\Omega}$ . The space of  $L^2(\Omega)$  solenoidal (*i.e.*, divergence free) functions is denoted by  $\mathbf{H}_0(\text{div}; \Omega)$ . The norm in  $L^2(\Omega)$  is denoted by  $\|\cdot\|_{0,\Omega}$  and its inner-product by  $(\cdot, \cdot)$ . The closed subspaces  $H_0^1(\Omega)$ , consisting of functions in  $H^1(\Omega)$  with zero trace on  $\partial\Omega$ , and  $L_0^2(\Omega)$ , consisting of function in  $L^2(\Omega)$  with zero mean in  $\Omega$ , will also be used. The vector counterpart of a scalar space will be denoted by a bold character.

In what follows,  $\{\mathcal{T}_h\}_{0 < h \leq 1}$  denotes a family of shape regular triangulations of a domain  $\Omega$  in  $\mathbb{R}^d$  ( $d = 2$  or  $3$ ) with polyhedral boundary  $\Gamma \stackrel{\text{def}}{=} \partial\Omega$  and outward pointing normal  $\mathbf{n}$ . In order to simplify the presentation, and without loss of generality, we assume that the triangulations  $\mathcal{T}_h$  are quasi-uniform. The elements of  $\mathcal{T}_h$  will be denoted by  $K$ . To each element we associate an outward unit normal  $\mathbf{n}_K$ . The faces of the triangulation will be denoted  $F$ ,  $\mathcal{F}(K)$  stands for the set of faces in the boundary of  $K \in \mathcal{T}_h$  and  $\mathcal{F}_{\text{in}}(K)$  for the set of inner faces in the boundary of  $K$ , *i.e.*, such that  $\text{int}(F) \cap \Gamma = \emptyset$ . For each triangulation  $\mathcal{T}_h$ , the subscript  $h \in (0, 1]$  refers to the

level of refinement of the triangulation, which is defined by

$$h \stackrel{\text{def}}{=} \max_{K \in \mathcal{T}_h} h_K, \quad h_K \stackrel{\text{def}}{=} \max_{F \subset \mathcal{F}(K)} h_F,$$

with  $h_F$  the diameter of the face  $F$ . For a general function  $v : \Omega \rightarrow \mathbb{R}$  (possibly vector valued), the jump across the boundary of the simplex  $K \in \mathcal{T}_h$  is denoted by

$$[[v]] \stackrel{\text{def}}{=} v_K^- - v_K^+,$$

with

$$v_K^\pm(\mathbf{x}) \stackrel{\text{def}}{=} \lim_{\epsilon \rightarrow 0^\pm} v(\mathbf{x} + \epsilon \mathbf{n}_K), \quad \forall \mathbf{x} \in \bigcup_{F \in \mathcal{F}_{\text{in}}(K)} \text{int}(F)$$

and the jump of the normal derivative by

$$[[\partial_{\mathbf{n}_K} v]] \stackrel{\text{def}}{=} \mathbf{n}_K \cdot [(\nabla v)_K^- - (\nabla v)_K^+].$$

We shall also consider the notation

$$\langle u, v \rangle_\Gamma \stackrel{\text{def}}{=} \sum_{\substack{K \in \mathcal{T}_h \\ K \cap \Gamma \neq \emptyset}} \int_{\partial K \cap \Gamma} uv.$$

We let  $V_h$  (resp.  $V_h^{\text{disc}}$ ) denote the standard finite element space of continuous (resp. discontinuous), piecewise polynomial functions of degree  $k \geq 1$ . We also define the discrete spaces  $\mathbf{V}_h \stackrel{\text{def}}{=} [V_h]^d$ ,  $\mathbf{V}_h^{\text{disc}} \stackrel{\text{def}}{=} [V_h^{\text{disc}}]^d$  and  $Q_h \stackrel{\text{def}}{=} V_h \cap L_0^2(\Omega)$ . For a given integer  $N \geq 2$ , we consider a uniform partition of the time interval of interest  $(0, T)$  with time-step size  $\tau \stackrel{\text{def}}{=} T/N$ . For a given time dependent function  $x$ , we denote by  $x^n$  and approximation of  $x(t_n)$  and by

$$\partial_\tau x^n \stackrel{\text{def}}{=} \frac{1}{\tau} (x^n - x^{n-1}), \quad \bar{\partial}_\tau x^n \stackrel{\text{def}}{=} \frac{1}{\tau} \left( \frac{3}{2} x^n - 2x^{n-1} + \frac{1}{2} x^{n-2} \right),$$

the first and second order backward differences. The symbol  $\lesssim$  indicates an inequality up to a multiplicative constant independent of the discretization and physical parameters. Note, in particular, that the constant is independent of  $T$ .

Finally, Dirichlet boundary conditions will be enforced in a weak sense (this simplifies the analysis), using Nitsche's method [Nit71].

### 4.3 CIP stabilized FEM for the Oseen's equations ([8])

Let us consider the following Oseen problem with reaction: Find the velocity  $\mathbf{u} : \Omega \rightarrow \mathbb{R}^d$  and the pressure  $p : \Omega \rightarrow \mathbb{R}$  such that

$$\begin{cases} \sigma \mathbf{u} + \boldsymbol{\beta} \cdot \nabla \mathbf{u} - \nu \Delta \mathbf{u} + \nabla p = \mathbf{f} & \text{in } \Omega, \\ \text{div } \mathbf{u} = 0 & \text{in } \Omega, \\ \mathbf{u} = \mathbf{0} & \text{on } \Gamma, \end{cases} \quad (4.3.2)$$

with  $\boldsymbol{\beta}$  a given solenoidal velocity field,  $\mathbf{f}$  the source term, and  $\sigma, \nu$  positive constants. We assume that  $\boldsymbol{\beta} \in \mathbf{W}^{1,\infty}(\Omega) \cap \mathbf{H}_0(\text{div}; \Omega)$  and  $\mathbf{f} \in \mathbf{L}^2(\Omega)$ . The weak formulation of problem (4.3.2) then reads:

$$\begin{cases} \text{Find } (\mathbf{u}, p) \in \mathbf{H}_0^1(\Omega) \times L_0^2(\Omega) \text{ such that} \\ a(\mathbf{u}, \mathbf{v}) + b(p, \mathbf{v}) - b(q, \mathbf{u}) = (\mathbf{f}, \mathbf{v}) \quad \forall (\mathbf{v}, q) \in \mathbf{H}_0^1(\Omega) \times L_0^2(\Omega), \end{cases} \quad (4.3.3)$$



The discrete formulation (4.3.6) overcomes the inconveniences of the standard residual-based stabilizations mentioned in §4.1, without the need of projection computations or hierarchical meshes [Gue99, Cod00, BB01, BB06]. This comes however with a price: the jump terms lead to a non-standard stiffness matrix pattern, with a bandwidth which doubles in 2D and triples in 3D. This issue will be (partially) addressed in §4.6, within the framework of transient problems.

The jump terms  $j_{\mathbf{u}}$  and  $j_p$  serve three purposes:

1. the first sum in  $j_{\mathbf{u}}$  stabilizes convection;
2. the second sum in  $j_{\mathbf{u}}$  gives additional control on the incompressibility constraint and is necessary to recover  $\nu$ -uniform error estimates;
3. term  $j_p$  makes the discretization globally *inf-sup* stable.

Note that the velocity parameter  $\omega_K(\boldsymbol{\beta}, h)$  is independent of the viscosity coefficient. On the contrary, the pressure parameter  $\omega_K(\boldsymbol{\beta}, h, \nu)$  scales as  $h^2/\|\boldsymbol{\beta}\|_{0,\infty,K}$  when the local Reynolds number  $\text{Re}_K$  is large, and as  $h^3/\nu$  when it is small. In the analysis summarized below we only require the (dimensionless) stabilization parameter  $\gamma$  to be positive. The optimal choice of this parameter (which depends on the polynomial order  $k$ ) can be inferred from a *hp*-analysis, as shown in [BE07] (see also [BBJL07]).

Assuming sufficient regularity of the exact solution, the above formulation is strongly consistent. More generally, we have the following result.

**Lemma 4.1** *Let  $(\mathbf{u}, p) \in \mathbf{H}^{\frac{3}{2}+\varepsilon}(\Omega) \times L_0^2(\Omega)$  (for an  $\varepsilon > 0$ ) be solution of (4.3.2) and  $(\mathbf{u}_h, p_h) \in \mathbf{V}_h \times Q_h$  be solution of (4.3.6). Then*

$$a_h(\mathbf{u} - \mathbf{u}_h, \mathbf{v}_h) + b_h(p - p_h, \mathbf{v}_h) - b_h(q_h, \mathbf{u} - \mathbf{u}_h) + j_{\mathbf{u}}(\mathbf{u} - \mathbf{u}_h, \mathbf{v}_h) = j_p(p_h, q_h)$$

for all  $(\mathbf{v}_h, q_h) \in \mathbf{V}_h \times Q_h$ . Moreover, for  $(\mathbf{u}, p) \in \mathbf{H}^r(\Omega) \times H^s(\Omega)$  with  $r \geq 2$  and  $s \geq 1$ , we have the consistency estimate

$$\begin{aligned} j_{\mathbf{u}}(\mathbf{u} - \pi_h \mathbf{u}, \mathbf{u} - \pi_h \mathbf{u})^{\frac{1}{2}} &\lesssim \max \{ \|\boldsymbol{\beta}\|_{0,\infty,\Omega} h, \nu \}^{\frac{1}{2}} h^{r_{\mathbf{u}}-1} \|\mathbf{u}\|_{r,\Omega}, \\ j_p(\pi_h p, \pi_h p)^{\frac{1}{2}} &\lesssim \max_{K \in \mathcal{T}_h} \min \{ \|\boldsymbol{\beta}\|_{0,\infty,K}^{-1}, h_K/\nu \}^{\frac{1}{2}} h^{s_p-\frac{1}{2}} \|p\|_{s,\Omega}, \end{aligned} \quad (4.3.9)$$

where  $\pi_h$  stands for the  $L^2$ -projection onto the discrete spaces,  $r_{\mathbf{u}} \stackrel{\text{def}}{=} \min\{k+1, r\}$  and  $s_p \stackrel{\text{def}}{=} \min\{k+1, s\}$ .

## Stability and well-posedness

The enhanced stability of the CIP method is based on the following approximation estimate for the discrete gradients (see [BH04, Bur05]):

$$\inf_{\mathbf{z}_h \in \mathbf{V}_h} \|h^{\frac{1}{2}}(\nabla v_h - \mathbf{z}_h)\|_{0,\Omega}^2 \lesssim \sum_{K \in \mathcal{T}_h} \sum_{F \in \mathcal{F}_{\text{in}}(K)} h^2 \int_F \|[\partial_{\mathbf{n}_K} v_h]\|^2 \quad (4.3.10)$$

for all  $v_h \in V_h$ . In other words, the gradient jumps over inner-faces provide control on the part of the gradient which is orthogonal to the finite element space. Somehow, this indicates that the stabilization acts only on the scales which are not resolved by the spatial discretization. Similar ideas are at the origin of the methods proposed in [Gue99, Cod00, BB01, BB06] involving hierarchical meshes and/or projection computations.

Estimate (4.3.10) was established in [BH04, Bur05] for the case of affine approximations ( $k = 1$ ). We have extended this result to all the polynomial degrees, by proving the following general *quasi-interpolation* error estimate for  $k \geq 1$ :

**Lemma 4.2** *There exists an operator  $\pi_h^* : \mathbf{V}_h^{\text{disc}} \rightarrow \mathbf{V}_h$  such that*

$$\|h^{\frac{1}{2}}(\nabla v_h - \pi_h^*(\nabla v_h))\|_{0,\Omega}^2 \lesssim \sum_{K \in \mathcal{T}_h} \sum_{F \in \mathcal{F}_{\text{in}}(K)} h^2 \int_F \|\llbracket \partial_{\mathbf{n}_K} v_h \rrbracket\|^2$$

for all  $v_h \in V_h$ .

This estimate shows that the jump terms (4.3.7) provide the key control on the pressure gradient and on the stream-derivative and divergence, necessary to enhance stability. In particular, a first consequence of this result is the following *modified* inf-sup condition, which provides the stability of the discrete pressures.

**Lemma 4.3** *For all  $q_h \in Q_h$  there holds*

$$\|q_h\|_{0,\Omega} \lesssim \sup_{\mathbf{v}_h \in \mathbf{V}_h} \frac{|b_h(q_h, \mathbf{v}_h)|}{\|\mathbf{v}_h\|_{1,\Omega}} + \max\{\|\boldsymbol{\beta}\|_{0,\infty,\Omega} h, \nu\}^{\frac{1}{2}} j_p(q_h, q_h)^{\frac{1}{2}}. \quad (4.3.11)$$

On the other hand, the least-square control on the jump of the divergence makes the left-hand side of (4.3.6) coercive (for  $\gamma_{\text{bc}} > 0$  large enough) with respect to the following enhanced semi-norm (is only a norm for the velocity):

$$\begin{aligned} \|(\mathbf{v}_h, q_h)\|_h^2 &\stackrel{\text{def}}{=} \|\sigma^{\frac{1}{2}} \mathbf{v}_h\|_{0,\Omega}^2 + \|\nu^{\frac{1}{2}} \nabla \mathbf{v}_h\|_{0,\Omega}^2 + j_{\mathbf{u}}(\mathbf{v}_h, \mathbf{v}_h) + j_p(q_h, q_h) + \|(|\boldsymbol{\beta}|h)^{\frac{1}{2}} \text{div } \mathbf{v}_h\|_{0,\Omega}^2 \\ &\quad + \|\mathbf{v}\|_{h,\Gamma}^2, \end{aligned} \quad (4.3.12)$$

where  $\|\cdot\|_{h,\Gamma}$  denotes the norm contribution from the weak-treatment of the boundary conditions (omitted for brevity). Note the enhanced control on the divergence constraint provided by the coercivity norm  $\|\cdot\|_h$  in the high local Reynolds regime.

The well-posedness of the discrete formulation (4.3.6) follows from the  $\|\cdot\|_h$ -coercivity and the inf-sup estimate provided by Lemma 4.3.

## Error estimates

We have shown that the gradient jump stabilization (4.3.7) with the scaling (4.3.8) allows to derive *a priori* error estimates which are uniform in the viscosity coefficient  $\nu$ . These estimates are (quasi-) optimal in the high local Reynolds regime, provided the solution is smooth  $(\mathbf{u}, p) \in \mathbf{H}^{k+1}(\Omega) \times H^{k+1}(\Omega)$ , and in the low local Reynolds regime, under standard regularity assumptions. The convergence results are summarized in the following theorem.

**Theorem 4.1** *Let  $(\mathbf{u}, p) \in \mathbf{H}^r(\Omega) \times H^s(\Omega)$  with  $r \geq 2$  and  $s \geq 1$ , be the solution of (4.3.2) and  $(\mathbf{u}_h, p_h) \in \mathbf{V}_h \times Q_h$  be the solution of (4.3.6). There holds*

$$\begin{aligned} \|(\mathbf{u} - \mathbf{u}_h, p_h)\|_h &\lesssim C_1 h^{r_{\mathbf{u}}-1} \|\mathbf{u}\|_{r,\Omega} + C_2 h^{s_p-\frac{1}{2}} \|p\|_{s,\Omega}, \\ \|p - p_h\|_{0,\Omega} &\lesssim C_3 \left( C_1 h^{r_{\mathbf{u}}-1} \|\mathbf{u}\|_{r,\Omega} + C_2 h^{s_p-\frac{1}{2}} \|p\|_{s,\Omega} \right), \end{aligned}$$

with

$$\begin{aligned} C_1 &\stackrel{\text{def}}{=} \sigma^{\frac{1}{2}} h + \max\{\|\boldsymbol{\beta}\|_{0,\infty,\Omega} h, \nu\}^{\frac{1}{2}} + \sigma^{-\frac{1}{2}} |\boldsymbol{\beta}|_{1,\infty,\Omega} h, \\ C_2 &\stackrel{\text{def}}{=} \max_{K \in \mathcal{T}_h} \min\{\|\boldsymbol{\beta}\|_{0,\infty,K}^{-1}, h_K/\nu\}^{\frac{1}{2}}, \\ C_3 &\stackrel{\text{def}}{=} C_L \sigma^{\frac{1}{2}} + \max\{\|\boldsymbol{\beta}\|_{0,\infty,\Omega} h, \nu\}^{\frac{1}{2}} + \sigma^{-\frac{1}{2}} \|\boldsymbol{\beta}\|_{0,\infty,\Omega}^{\frac{1}{2}}, \end{aligned}$$

and where  $C_L$  is a constant (scaling as a length) depending only on  $\Omega$ .

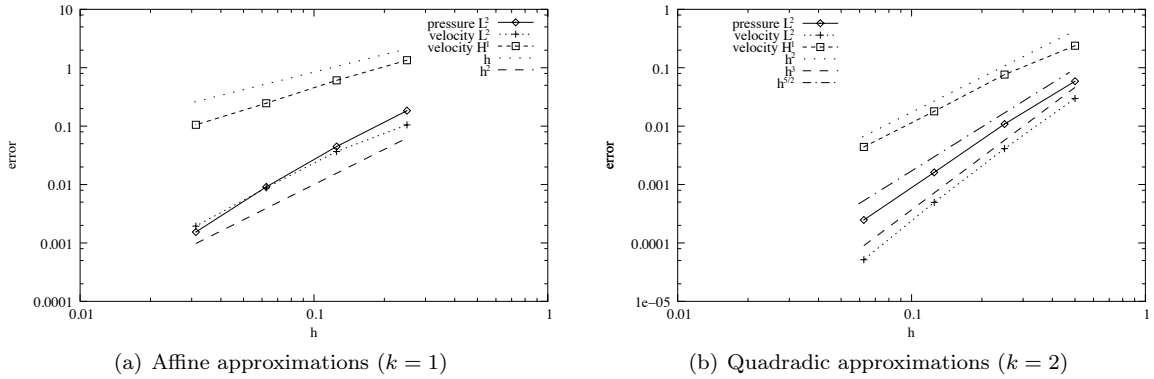


Figure 4.1: Convergence history of the velocity and the pressure approximations for a smooth solution.

This result shows that by adding the  $L^2$ -coercivity ( $\sigma > 0$ ), we can use the stabilization  $j_{\mathbf{u}}$  to control the convective term and the incompressibility constraint without the need to resort to the  $\nu$ -weighted  $H^1$ -coercivity. This leads to a  $\nu$ -uniform estimate for  $\|(\mathbf{u} - \mathbf{u}_h, p_h)\|_h$ , showing that the stabilization handles the numerical instability present in the standard Galerkin method.

**Remark 4.1** *Note that, in the time dependent case, the  $L^2$ -coercivity can always be obtained by change of variables or handled via Gronwall's lemma (see, e.g., §4.4).*

When the local Reynolds number is high and the solution is regular, for instance  $r = s = k + 1$ , we enjoy the standard (quasi-) optimal  $\mathcal{O}(h^{k+\frac{1}{2}})$  convergence order for the velocity and the pressure in the  $L^2$ -norm. For less regular pressures, for instance  $r = k + 1$  and  $s = k$ , and when the local Reynolds number is low we get an optimal  $\mathcal{O}(h^k)$  estimate in the energy norm for the velocity and in the  $L^2$ -norm for the pressure. However, a sub-optimal  $\mathcal{O}(h^{k-\frac{1}{2}})$  rate is obtained when the local Reynolds number is high. This sub-optimality comes from the consistency rate of the pressure jumps (4.3.9), but also from the coupling between the convective and incompressibility effects in the high local Reynolds number regime. Indeed, to control the divergence constraint while maintaining the estimates  $\nu$ -uniform, we need to replace the  $\nu$ -weighted  $H^1$ -coercivity by the  $h$ -weighted  $\mathbf{H}(\text{div})$ -coercivity (hence an  $h^{\frac{1}{2}}$  is lost).

Finally, for illustration purposes, we have reported in Figure 4.1 the convergence results obtained with (4.3.6) for the approximation of a smooth solution of (4.3), with  $\sigma = 1$ ,  $\|\boldsymbol{\beta}\|_{0,\infty,\Omega} \approx 3$  and  $\nu = 10^{-4}$ . The obtained convergences rate are in agreement with those predicted by Theorem 4.1.

## 4.4 CIP stabilized FEM for the transient Navier-Stokes equations ([5])

We consider now the problem of solving, for  $\mathbf{u} : \Omega \times (0, T) \rightarrow \mathbb{R}^d$  and  $p : \Omega \times (0, T) \rightarrow \mathbb{R}$ , the time-dependent Navier-Stokes equations

$$\left\{ \begin{array}{ll} \partial_t \mathbf{u} + \mathbf{u} \cdot \nabla \mathbf{u} - \nu \Delta \mathbf{u} + \nabla p = \mathbf{f} & \text{in } \Omega \times (0, T), \\ \operatorname{div} \mathbf{u} = 0 & \text{in } \Omega \times (0, T), \\ \mathbf{u} = \mathbf{0} & \text{on } \Gamma \times (0, T), \\ \mathbf{u}|_{t=0} = \mathbf{u}_0 & \text{in } \Omega, \end{array} \right. \quad (4.4.13)$$

which describe the motion of a viscous incompressible fluid confined in  $\Omega$ . Here,  $\mathbf{f} : \Omega \times (0, T) \rightarrow \mathbb{R}^d$  stands for a given source term and  $\mathbf{u}_0 : \Omega \rightarrow \mathbb{R}^d$  for the initial velocity. We assume that, at least,  $\mathbf{f} \in \mathbf{L}^\infty(0, T; L^2(\Omega))$  and  $\mathbf{u}_0 \in \mathbf{L}^2(\Omega)$ . We refer to [Lio96, Chapter 3] for a review of some known results on the existence and regularity of solutions for problem (4.4.13). For sufficiently regular functions  $\mathbf{u}$  and  $p$ , problem (4.4.13) holds if, and only if,

$$\left\{ \begin{array}{ll} (\partial_t \mathbf{u}, \mathbf{v}) + c(\mathbf{u}; \mathbf{u}, \mathbf{v}) + a(\mathbf{u}, \mathbf{v}) + b(p, \mathbf{v}) = (\mathbf{f}, \mathbf{v}) & \text{in } (0, T), \\ b(q, \mathbf{u}) = 0 & \text{in } (0, T), \\ \mathbf{u}(0) = \mathbf{u}_0 & \text{in } \Omega, \end{array} \right. \quad (4.4.14)$$

for all  $(\mathbf{v}, q) \in \mathbf{H}_0^1(\Omega)^d \times L_0^2(\Omega)$ , where  $c(\mathbf{w}; \mathbf{u}, \mathbf{v}) \stackrel{\text{def}}{=} (\mathbf{w} \cdot \nabla \mathbf{u}, \mathbf{v})$  and  $a(\cdot, \cdot)$  and  $b(\cdot, \cdot)$  are defined as in §4.3.

There exists a quite vast literature on finite element approximations of (4.4.14) providing error estimates valid in the low local Reynolds number regime (*i.e.*, not uniform in  $\nu$ ). Let us cite, for instance, the series of papers [HR82, HR86, HR88, HR90] and the references [BR85, BMMR97, GQ98, Cod02, He03]. Nevertheless, to the best of our knowledge,  $\nu$ -uniform convergence analyses have been only performed in [JS86, HS90], using space-time finite elements and a SUPG/PSPG-like stabilization (with a velocity-vorticity formulation in [JS86] and the velocity-pressure formulation in [HS90]). We have extended the CIP stabilized method and the analysis of the previous section (§4.3) to the non-linear time-dependent problem (4.4.13). For the sake of simplicity, we assumed the fluid velocity to be dimensionless and that the mean fluid velocity equals one (the local Reynolds number is then given by  $h/\nu$ ). The analysis was restricted to the high local Reynolds number regime  $\nu < h$ .

Problem (4.4.13) is semi-discretized in space using the following stabilized finite element formulation, with weakly imposed boundary conditions:

$$\left\{ \begin{array}{l} \text{For all } t \in (0, T), \text{ find } (\mathbf{u}_h(t), p_h(t)) \in \mathbf{V}_h \times Q_h \text{ such that} \\ (\partial_t \mathbf{u}_h, \mathbf{v}_h) + (A + J)[\mathbf{u}_h; (\mathbf{u}_h, p_h), (\mathbf{v}_h, q_h)] = (\mathbf{f}, \mathbf{v}_h) \quad \forall (\mathbf{v}_h, q_h) \in \mathbf{V}_h \times Q_h, \\ \mathbf{u}_h(0) = \mathbf{u}_{0,h}, \end{array} \right. \quad (4.4.15)$$

where  $\mathbf{u}_{0,h}$  is a suitable approximation of  $\mathbf{u}_0$  in  $\mathbf{V}_h$  and with the notations

$$A[\mathbf{w}_h; (\mathbf{u}_h, p_h), (\mathbf{v}_h, q_h)] \stackrel{\text{def}}{=} a_h(\mathbf{u}_h, \mathbf{v}_h) + c_h(\mathbf{w}_h; \mathbf{u}_h, \mathbf{v}_h) + b_h(p_h, \mathbf{v}_h) - b_h(q_h, \mathbf{u}_h),$$

with

$$\begin{aligned}
a_h(\mathbf{u}_h, \mathbf{v}_h) &\stackrel{\text{def}}{=} a(\mathbf{u}_h, \mathbf{v}_h) - \langle \nu \partial_{\mathbf{n}} \mathbf{u}_h, \mathbf{v}_h \rangle_{\Gamma} - \langle \mathbf{u}_h, \nu \partial_{\mathbf{n}} \mathbf{v}_h \rangle_{\Gamma} + \frac{\gamma_{bc} \mathcal{V}}{h} \langle \mathbf{u}_h, \mathbf{v}_h \rangle_{\Gamma} \\
&\quad + \gamma_{bc} \langle \mathbf{u}_h \cdot \mathbf{n}, \mathbf{v}_h \cdot \mathbf{n} \rangle_{\Gamma}, \\
b_h(p_h, \mathbf{v}_h) &\stackrel{\text{def}}{=} b(p_h, \mathbf{v}_h) + \langle p_h, \mathbf{v}_h \cdot \mathbf{n} \rangle_{\Gamma}, \\
c_h(\mathbf{w}_h; \mathbf{u}_h, \mathbf{v}_h) &\stackrel{\text{def}}{=} c(\mathbf{w}_h; \mathbf{u}_h, \mathbf{v}_h) + \frac{1}{2} ((\operatorname{div} \mathbf{w}_h) \mathbf{u}_h, \mathbf{v}_h) - \frac{1}{2} \langle \mathbf{w}_h \cdot \mathbf{n} \mathbf{u}_h, \mathbf{v}_h \rangle_{\Gamma}, \\
J[(\mathbf{u}_h, p_h), (\mathbf{v}_h, q_h)] &\stackrel{\text{def}}{=} j_{\mathbf{u}}(\mathbf{w}_h; \mathbf{u}_h, \mathbf{v}_h) + j_p(p_h, q_h).
\end{aligned}$$

Here the jump terms  $j_{\mathbf{u}}$  and  $j_p$  are given

$$\begin{aligned}
j_{\mathbf{u}}(\mathbf{w}_h; \mathbf{u}_h, \mathbf{v}_h) &\stackrel{\text{def}}{=} \gamma \sum_{K \in \mathcal{T}_h} h_K^2 (1 + \|\mathbf{w}_h\|_{0, \infty, K}^2) \sum_{F \in \mathcal{F}_{\text{in}}(K)} \int_F \llbracket \partial_{\mathbf{n}_K} \mathbf{u}_h \rrbracket \cdot \llbracket \partial_{\mathbf{n}_K} \mathbf{v}_h \rrbracket, \\
j_p(p_h, q_h) &\stackrel{\text{def}}{=} \sum_{K \in \mathcal{T}_h} h_K^2 \sum_{F \in \mathcal{F}_{\text{in}}(K)} \int_F \llbracket \partial_{\mathbf{n}_K} p_h \rrbracket \llbracket \partial_{\mathbf{n}_K} q_h \rrbracket.
\end{aligned}$$

Note that these expressions are essentially the same than in the previous section. As in [Tem68], an artificial term is added in  $c$  that ensures stability while remaining strongly consistent (since  $\operatorname{div} \mathbf{u} = 0$ ).

**Remark 4.2** *Fully discrete approximations of (4.4.13) can be obtained by simply discretizing (4.4.15) in time using any standard  $\mathcal{A}$ -stable scheme. The numerical analysis of the resulting schemes, for two simplified linear versions of (4.4.13), will be summarized in §4.5 and §4.6 below. Like the pure Galerkin discretization of (4.4.13), here the space and the time discretization commute. Note that this feature is only trivial for stabilized methods that are not residual-based (i.e., that do not involve the residual of the equation).*

The *a priori* convergence analysis summarized here is inspired by the one reported in [HS90], but our results using the CIP stabilization are sharper. In fact, to control the convective velocity, which is only weakly divergence free, special non-linear stabilization terms are introduced in [HS90], leading to a more complex formulation with stronger regularity assumptions on the exact solution. In our case, the fact that the stabilization of the velocities is decoupled from the stabilization of the pressure, allows us to prove convergence using essentially the stabilization terms of the linear case and under similar regularity assumptions (see §4.3). Moreover, we prove convergence for all polynomial orders  $k \geq 1$ , whereas in [HS90] the analysis is restricted to piecewise linear approximations in space and in time.

For the velocity error analysis we assume the following regularity on the solution

$$\begin{aligned}
\mathbf{u} &\in \mathbf{L}^{\infty}(0, T; W^{1, \infty}(\Omega)) \cap \mathbf{H}^1(0, T; L^2(\Omega)) \cap \mathbf{L}^{\infty}(0, T; H^{k+1}(\Omega)), \\
p &\in L^2(0, T; H^{k+1}(\Omega)), \quad \mathbf{u}_0 \in \mathbf{H}^{k+1}(\Omega) \cap \mathbf{H}_0^1(\Omega) \cap \mathbf{H}_0(\operatorname{div}; \Omega),
\end{aligned} \tag{4.4.16}$$

and for the pressure error estimates

$$\mathbf{u} \in \mathbf{H}^1(0, T; H^{k+1}(\Omega)), \quad p \in L^2(0, T; H^{k+1}(\Omega)) \cap H^1(0, T; H^1(\Omega)). \tag{4.4.17}$$

Moreover, we make use of the following Ritz-projection operator (based on a Stokes-like problem): for  $\mathbf{u} \in \mathbf{H}^{\frac{3}{2}+\epsilon}(\Omega) \cap \mathbf{H}_0^1(\Omega) \cap \mathbf{H}_0(\operatorname{div}; \Omega)$ , we denote by  $(P_h \mathbf{u}, R_h \mathbf{u}) \in \mathbf{V}_h \times Q_h$  the unique solution of

$$\begin{cases} (P_h \mathbf{u}, \mathbf{v}_h) + a_h(P_h \mathbf{u}, \mathbf{v}_h) + b_h(R_h \mathbf{u}, \mathbf{v}_h) = (\mathbf{u}, \mathbf{v}_h) + a_h(\mathbf{u}, \mathbf{v}_h), \\ -b_h(q_h, P_h \mathbf{u}) + j_p(R_h \mathbf{u}, q_h) = 0, \end{cases} \tag{4.4.18}$$

for all  $(\mathbf{v}_h, q_h) \in \mathbf{V}_h \times Q_h$ . The approximation properties of  $P_h$  are a direct consequence of the analysis summarized in §4.3.

The following well-posedness result follows from Lemma 4.3 and the Cauchy-Lipschitz theorem.

**Lemma 4.4** *The discrete problem (4.4.15) with  $\mathbf{u}_{0,h} = P_h \mathbf{u}_0$  has a unique solution  $(\mathbf{u}_h, p_h) \in C^1(0, T; \mathbf{V}_h) \times C^0(0, T; Q_h)$ .*

Our main convergence result is summarized in the next theorem, with the coercivity triple-norm (for  $\gamma_{bc} > 0$  large enough) defined by

$$\|(\mathbf{v}_h, q_h)\|_{\mathbf{w}_h}^2 \stackrel{\text{def}}{=} \|\nu^{\frac{1}{2}} \nabla \mathbf{v}_h\|_{0,\Omega}^2 + j_{\mathbf{u}}(\mathbf{w}_h, \mathbf{v}_h, \mathbf{v}_h) + j_p(q_h, q_h) + \|h^{\frac{1}{2}} \operatorname{div} \mathbf{v}_h\|_{0,\Omega}^2 + \|\mathbf{v}\|_{h,\Gamma}^2.$$

**Theorem 4.2** *Let  $\mathbf{u}_{0,h} = P_h \mathbf{u}_0$  and assume that (4.4.16) holds. Then, for  $\gamma > 0$  large enough, we have*

$$\begin{aligned} \|\mathbf{u} - \mathbf{u}_h\|_{L^\infty(0,T;L^2(\Omega))} &\lesssim C_{\mathbf{u},p,T} h^{k+\frac{1}{2}}, \\ \left( \int_0^T \|(\mathbf{u} - \mathbf{u}_h, p - p_h)\|_{\mathbf{w}_h}^2 \right)^{\frac{1}{2}} &\lesssim C_{\mathbf{u},p,T} h^{k+\frac{1}{2}}, \\ \|p - p_h\|_{L^2(0,T;L^2(\Omega))} &\lesssim C_{\mathbf{u},p,T} h^k + \|\partial_t(\mathbf{u} - \mathbf{u}_h)\|_{L^2(0,T;V'(\Omega))}, \\ \|\nabla(p - p_h)\|_{L^2(0,T;L^2(\Omega))} &\lesssim C_{\mathbf{u},p,T} h^{k-\frac{1}{2}} + h^k \|p\|_{L^2(0,T;H^{k+1}(\Omega))} \\ &\quad + \|\partial_t(\mathbf{u} - \mathbf{u}_h)\|_{L^2(0,T;L^2(\Omega))}, \end{aligned}$$

with  $C_{\mathbf{u},p,T} > 0$  independent of  $\nu$  and  $h$ , but depending on

$$e^{T\|\mathbf{u}\|_{L^\infty(0,T;W^{1,\infty}(\Omega))}}, \quad \|\mathbf{u}\|_{L^2(0,T;H^{k+1}(\Omega))}, \quad \|p\|_{L^2(0,T;H^{k+1}(\Omega))}, \quad \|\mathbf{u}\|_{L^\infty(0,T;W^{1,\infty}(\Omega))},$$

and  $V'(\Omega)$  standing for the dual of  $H^1(\Omega)$ . In particular,  $\|\mathbf{u}_h\|_{L^\infty(\Omega \times (0,T))}$  is bounded irrespectively of  $h$ .

The proof of this result uses the arguments of the steady linear case (see §4.3) and a discrete commutator property (see, e.g., [Ber99, JSH90]) to handle the non-linear terms.

From the optimal velocity convergence rate  $\mathcal{O}(h^{k+\frac{1}{2}})$  provided by Theorem 4.2, one would expect a similar rate for the pressure (as in Theorem 4.1 with  $r = s = k + 1$ ). However, since in (4.4.15) the discrete convective velocity  $\mathbf{u}_h$  is not divergence free (contrarily to  $\beta$  in (4.3.6)), we have to pay a loss of  $h^{\frac{1}{2}}$  in the  $L^2$ -estimate of the pressure with an inverse inequality. The reason for this is that we do not have stability of  $\nabla \mathbf{u}_h$  in  $L^\infty(\Omega \times (0, T))$ . Nevertheless, as shown by Theorem 4.2, we can bound the error in the gradients of the pressure, leading to an estimate which is close to optimal and which uses the  $L^2$ -norm of the error in the time derivative.

To close the problem of convergence of the pressure approximations we need an estimate of the error in the time derivative of the error. It seems difficult to obtain an estimate of the time derivative of the velocities in the dual norm. Instead, we have proved the following bound in the  $L^2$ -norm, that requires minimum assumptions on the pressure regularity, but that makes the second pressure estimate in Theorem 4.2 quasi-optimal for piecewise linear approximations (only a factor  $h^{\frac{1}{2}}$  is lost).

**Theorem 4.3** *Under the assumptions of Theorem 4.2 and if, in addition, the regularity (4.4.17) holds, we have*

$$\|\partial_t(\mathbf{u} - \mathbf{u}_h)\|_{L^2(0,T;L^2(\Omega))} \lesssim C_{\mathbf{u},p,T} h^{k-\frac{1}{2}} + h^{\frac{2k+1}{4}} \|p\|_{H^1(0,T;H^1(\Omega))}^{\frac{1}{2}}. \quad (4.4.19)$$

For polynomial orders  $k \geq 2$  the estimate (4.4.19) is suboptimal (due to the non-consistency of the projection (4.4.18), see Remark 4.3 in §4.5). This estimate can be improved assuming more pressure regularity, typically  $p \in C^1(0, T; H^{k+1}(\Omega))$  (see Theorem 4.5). It is questionable, however, whether such a regularity can be justified for the Navier-Stokes equations (see the discussion in [HR82]).

Finally, for illustration purposes, we have reported in Figure 4.2 some snapshots of the flow past a cylinder obtained by discretizing (4.4.15) with a BDF2 scheme. The geometrical and physical data (Reynolds number of 100) are from [HS90], we used the same time-step size and a coarser space mesh. These results compare well with those reported in [HS90], in particular we obtain a similar value 0.159 for the Strouhal number.

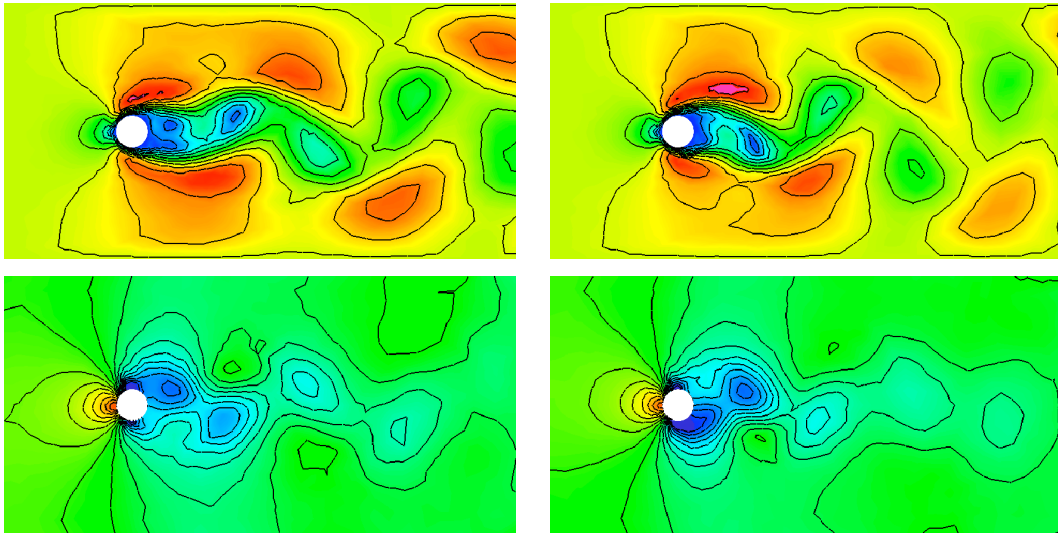


Figure 4.2: Flow past a cylinder (Reynolds 100): cup-plane snapshots of the velocity (top) and pressure (bottom) at two different time instants.

In the next sections (§4.5 and §4.6) we consider the discretization in time of two simplified versions of (4.4.13). We introduce a general abstract stabilization framework that allows us to consider a fairly large class of symmetric stabilization techniques (including CIP).

## 4.5 Transient Stokes equations (14)

We consider the problem of solving, for  $\mathbf{u} : \Omega \times (0, T) \rightarrow \mathbb{R}^d$  and  $p : \Omega \times (0, T) \rightarrow \mathbb{R}$ , the following time-dependent Stokes problem:

$$\begin{cases} \partial_t \mathbf{u} - \nu \Delta \mathbf{u} + \nabla p = \mathbf{f} & \text{in } \Omega \times (0, T), \\ \operatorname{div} \mathbf{u} = 0 & \text{in } \Omega \times (0, T), \\ \mathbf{u} = \mathbf{0} & \text{on } \Gamma \times (0, T), \\ \mathbf{u}(\cdot, 0) = \mathbf{u}_0 & \text{in } \Omega. \end{cases} \quad (4.5.20)$$

This problem can be formulated in weak form as follows: For all  $t > 0$ , find  $(\mathbf{u}(t), p(t)) \in \mathbf{H}_0^1(\Omega) \times L_0^2(\Omega)$  such that

$$\begin{cases} (\partial_t \mathbf{u}, \mathbf{v}) + a(\mathbf{u}, \mathbf{v}) + b(p, \mathbf{v}) - b(q, \mathbf{u}) = (\mathbf{f}, \mathbf{v}) & \text{in } (0, T), \\ \mathbf{u}(\cdot, 0) = \mathbf{u}_0 & \text{in } \Omega \end{cases} \quad (4.5.21)$$

for all  $(\mathbf{v}, q) \in \mathbf{H}_0^1(\Omega) \times L_0^2(\Omega)$ , with where  $a(\mathbf{u}, \mathbf{v}) \stackrel{\text{def}}{=} (\nu \nabla \mathbf{u}, \nabla \mathbf{v})$  and  $b(p, \mathbf{v}) \stackrel{\text{def}}{=} -(p, \operatorname{div} \mathbf{v})$ . The well-posedness of (4.5.21) follows by standard arguments (see, *e.g.*, [EG04]).

For methods of standard pressure stabilized Petrov–Galerkin (PSPG) or Galerkin least squares (GLS) type, the analysis of time-discretization schemes is a difficult issue, unless a space-time approach is applied. Indeed, for standard finite difference type time discretizations, the finite difference term must be included in the stabilization operator to ensure consistency (see, *e.g.*, [BH82, FF92]). It has been shown in [BGL07] that, even for first order backward difference (BDF1) schemes, this perturbs the stability when the time-step size is small, unless a condition

$$h^2 \lesssim \tau, \quad (4.5.22)$$

between the space mesh size  $h$  and the time-step size  $\tau$  is verified (see also [27]). For higher order schemes, such as Crank–Nicholson or second order backward differencing, the strongly consistent scheme appears to be unstable (see, *e.g.*, [BC09]). Similar initial time-step instabilities were observed in [CPGB07] for the algebraic (static) subscale stabilization (ASGS) scheme applied to the Navier–Stokes equations, and they were cured by including time dependent subscales.

The aim of the work summarized here was to show that, for a large class of symmetric pressure stabilization methods, stability and convergence of velocities and pressures can be obtained without conditions on the space- and time-discretization parameters, provided the initial data are chosen in terms of a specific (method-dependent) Ritz-projection (see, *e.g.*, [Sur83, Tho06]) onto a space of discretely divergence-free functions. *Discretely divergence-free* has to be interpreted in the sense of the stabilized method. If, on the other hand, the initial data is chosen as some interpolant that does not conserve the discrete divergence-free character, a condition  $h^{2k} \lesssim \tau$  has to be respected in order to avoid pressure oscillations in the transient solution for small times.

### Space semi-discretization: symmetric pressure stabilization

Let us consider the following (pressure stabilized) finite element space semi-discretization of (4.5.21), with weakly imposed boundary conditions:

$$\begin{cases} \text{For all } t \in (0, T), \text{ find } (\mathbf{u}_h(t), p_h(t)) \in \mathbf{V}_h \times Q_h \text{ such that} \\ (\partial_t \mathbf{u}_h, \mathbf{v}_h) + a_h(\mathbf{u}_h, \mathbf{v}_h) + b_h(p_h, \mathbf{v}_h) - b_h(q_h, \mathbf{u}_h) + j(p_h, q_h) = (\mathbf{f}, \mathbf{v}_h) \\ \forall (\mathbf{v}_h, q_h) \in \mathbf{V}_h \times Q_h, \\ \mathbf{u}_h(0) = \mathbf{u}_h^0, \end{cases} \quad (4.5.23)$$

with  $\mathbf{u}_h^0$  a suitable approximation of  $\mathbf{u}_0$  in  $\mathbf{V}_h$  and

$$\begin{aligned} a_h(\mathbf{u}_h, \mathbf{v}_h) &\stackrel{\text{def}}{=} a(\mathbf{u}_h, \mathbf{v}_h) - \langle \nu \partial_n \mathbf{u}_h, \mathbf{v}_h \rangle_\Gamma - \langle \mathbf{u}_h, \nu \partial_n \mathbf{v}_h \rangle_\Gamma + \frac{\gamma_{bc} \nu}{h} \langle \mathbf{u}_h, \mathbf{v}_h \rangle_\Gamma, \\ b_h(p_h, \mathbf{v}_h) &\stackrel{\text{def}}{=} b(p_h, \mathbf{v}_h) + \langle p_h, \mathbf{v}_h \cdot \mathbf{n} \rangle_\Gamma. \end{aligned}$$

We assume that the pressure stabilization operator  $j : Q_h \times Q_h \rightarrow \mathbb{R}$  satisfies the following abstract properties:

(A1) Symmetry:

$$j(p_h, q_h) = j(q_h, p_h) \quad \forall p_h, q_h \in Q_h;$$

(A2) continuity:

$$|j(p_h, q_h)| \leq j(p_h, p_h)^{\frac{1}{2}} j(q_h, q_h)^{\frac{1}{2}} \lesssim \nu^{-1} \|p_h\|_{0,\Omega} \|q_h\|_{0,\Omega} \quad \forall p_h, q_h \in Q_h;$$

(A3) weak consistency:

$$j(\Pi_h q, \Pi_h q)^{\frac{1}{2}} \lesssim \frac{h^{s_p}}{\nu^{\frac{1}{2}}} \|q\|_{s_p, \Omega} \quad \forall q \in H^s(\Omega),$$

with  $s \geq 1$  and  $s_p \stackrel{\text{def}}{=} \min\{s, \tilde{k}, k+1\}$ ,  $\tilde{k} \geq 1$  denoting the order of weak consistency of the stabilization operator, and  $\Pi_h : L^2(\Omega) \rightarrow Q_h$  a given projection operator such that

$$\|q - \Pi_h q\|_{0,\Omega} \lesssim h^{k+1} \|q\|_{k+1,\Omega} \quad \forall q \in H^{k+1}(\Omega);$$

(A4) *generalized Fortin operator*: there exists a projection operator  $\mathcal{I}_h : \mathbf{H}_0^1(\Omega) \rightarrow \mathbf{V}_h$  such that

$$\begin{aligned} |b_h(q_h, \mathbf{v} - \mathcal{I}_h \mathbf{v})| &\lesssim \nu^{\frac{1}{2}} j(q_h, q_h)^{\frac{1}{2}} (\|h^{-1}(\mathbf{v} - \mathcal{I}_h \mathbf{v})\|_{0,\Omega} + \|\nabla(\mathbf{v} - \mathcal{I}_h \mathbf{v})\|_{0,\Omega}), \\ \|\mathbf{v} - \mathcal{I}_h \mathbf{v}\|_{0,\Omega} + h \|\nabla(\mathbf{v} - \mathcal{I}_h \mathbf{v})\|_{0,\Omega} &\lesssim h^{r_u} \|\mathbf{v}\|_{r_u, \Omega} \end{aligned}$$

for all  $\mathbf{v} \in \mathbf{H}^r(\Omega)$ ,  $(q_h, \mathbf{v}_h) \in Q_h \times \mathbf{V}_h$  and with  $r_u \stackrel{\text{def}}{=} \min\{r, k+1\}$ ,  $r \geq 2$ .

We have shown that the pressure stabilized finite element methods introduced in [BP84, CB97, BB01, DB04, BH06] enter the above abstract framework (see [4, §3.1.1] for the details).

The major consequence of (A4) is the following result (similar to Lemma 4.3 with  $\beta = \mathbf{0}$ ) which ensures the stability of the discrete pressures in (4.5.23).

**Lemma 4.5** *There holds*

$$\|q_h\|_{0,\Omega} \lesssim \sup_{\mathbf{v}_h \in \mathbf{V}_h} \frac{|b_h(q_h, \mathbf{v}_h)|}{\|\mathbf{v}_h\|_{1,\Omega}} + \nu^{\frac{1}{2}} j(q_h, q_h)^{\frac{1}{2}} \quad \forall q_h \in Q_h.$$

For the stability and convergence analysis below we need to redefine the triple-norm (4.3.12) as follows (basically we take  $\beta = \mathbf{0}$  and replace  $j_p$  by  $j$ ):

$$\|(\mathbf{v}_h, q_h)\|_h^2 \stackrel{\text{def}}{=} \|\nu^{\frac{1}{2}} \nabla \mathbf{v}_h\|_{0,\Omega}^2 + \frac{\gamma_{bc\nu}}{h} \|\mathbf{v}_h\|_{0,\Gamma}^2 + j(q_h, q_h).$$

As for the transient Navier-Stokes problem in §4.4, it is also crucial here to introduce a Ritz-projection operator  $(P_h, R_h) : \mathbf{H}^2(\Omega) \times H^1(\Omega) \rightarrow \mathbf{V}_h \times Q_h$ , but with a slightly different structure since in (4.5.23) we can expect the pressure to be more regular. For  $(\mathbf{u}, p) \in \mathbf{H}^2(\Omega) \times H^1(\Omega)$ , the projection  $(P_h(\mathbf{u}, p), R_h(\mathbf{u}, p)) \in \mathbf{V}_h \times Q_h$  is defined as the unique solution of

$$\begin{cases} a_h(P_h(\mathbf{u}, p), \mathbf{v}_h) + b_h(R_h(\mathbf{u}, p), \mathbf{v}_h) = a_h(\mathbf{u}, \mathbf{v}_h) + b_h(p, \mathbf{v}_h), \\ -b_h(q_h, P_h(\mathbf{u}, p)) + j(R_h(\mathbf{u}, p), q_h) = 0 \end{cases} \quad (4.5.24)$$

for all  $(\mathbf{v}_h, q_h) \in \mathbf{V}_h \times Q_h$ . Assumptions (A1)-(A4) ensure that  $(P_h, R_h)$  is well-defined and that it has the necessary stability and approximation properties.

**Remark 4.3** *Note that the projection (4.5.24) is “pressure consistent”, in the sense that  $R_h(\mathbf{u}, p)$  approximates  $p$ . On the contrary, this is not the case for the projection (4.4.18) introduced in §4.4, that is,  $R_h \mathbf{u}$  is not an approximation of  $p$ .*

## Time discretization

We consider the following fully discrete approximation of (4.5.21), by discretizing (4.5.23) in time using the backward-Euler (BDF1) scheme:

$$\left\{ \begin{array}{l} \text{For } 0 \leq n \leq N-1, \text{ find } (\mathbf{u}_h^{n+1}, p_h^{n+1}) \in \mathbf{V}_h \times Q_h \text{ such that} \\ (\partial_\tau \mathbf{u}_h^{n+1}, \mathbf{v}_h) + a_h(\mathbf{u}_h^{n+1}, \mathbf{v}_h) + b_h(p_h^{n+1}, \mathbf{v}_h) - b_h(q_h, \mathbf{u}_h^{n+1}) + j(p_h^{n+1}, q_h) \\ = (\mathbf{f}^{n+1}, \mathbf{v}_h) \quad \forall (\mathbf{v}_h, q_h) \in \mathbf{V}_h \times Q_h. \end{array} \right. \quad (4.5.25)$$

The next result summarizes the stability properties of the discrete scheme (4.5.25) and, in particular, highlights the impact of the initial velocity approximation  $\mathbf{u}_h^0$  on the stability of the pressure.

**Theorem 4.4** *Let  $\mathbf{u}_h^0$  be a given  $L^2$ -stable approximation of  $\mathbf{u}_0$  in  $\mathbf{V}_h$ . Then, for  $1 \leq n \leq N$ ,*

$$\begin{aligned} \|\mathbf{u}_h^n\|_{0,\Omega}^2 + \sum_{m=0}^{n-1} \tau \|\mathbf{u}_h^{m+1}, p_h^{m+1}\|_h^2 &\lesssim \|\mathbf{u}_0\|_{0,\Omega}^2 + \frac{1}{\nu} \sum_{m=0}^{n-1} \tau \|\mathbf{f}^{m+1}\|_{0,\Omega}^2, \\ \sum_{m=0}^{n-1} \tau \|p_h^{m+1}\|_{0,\Omega}^2 &\lesssim \sum_{m=0}^{n-1} \tau \left( \nu \|\mathbf{u}_h^{m+1}, p_h^{m+1}\|_h^2 + \|\mathbf{f}^{m+1}\|_{0,\Omega}^2 + \|\partial_\tau \mathbf{u}_h^{m+1}\|_{0,\Omega}^2 \right). \end{aligned}$$

Moreover, if  $\mathbf{u}_0 \in \mathbf{H}^1(\Omega)$  and  $\mathbf{u}_h^0 = P_h(\mathbf{u}_0, 0)$ , then, for  $1 \leq n \leq N$ ,

$$\sum_{m=0}^{n-1} \tau \|p_h^{m+1}\|_{0,\Omega}^2 \lesssim \|\nabla \mathbf{u}_0\|_{0,\Omega}^2 + \sum_{m=0}^{n-1} \tau \left( \nu \|\mathbf{u}_h^{m+1}, p_h^{m+1}\|_h^2 + \|\mathbf{f}^{m+1}\|_{0,\Omega}^2 \right).$$

On the other hand, if  $\mathbf{u}_0 \in \mathbf{H}^r(\Omega) \cap \mathbf{H}_0^1(\Omega) \cap \mathbf{H}_0(\text{div}; \Omega)$ ,  $r \geq 2$ , and  $\mathbf{u}_h^0 = \mathcal{I}_h \mathbf{u}_0$ , and

$$h^{2(r-u-1)} \lesssim \tau, \quad (4.5.26)$$

then, for  $1 \leq n \leq N$ ,

$$\sum_{m=0}^{n-1} \tau \|p_h^{m+1}\|_{0,\Omega}^2 \lesssim \nu \|\nabla \mathbf{u}_0\|_{0,\Omega}^2 + \|\mathbf{u}_0\|_{r,\Omega}^2 + \sum_{m=0}^{n-1} \tau \left( \nu \|\mathbf{u}_h^{m+1}, p_h^{m+1}\|_h^2 + \|\mathbf{f}^{m+1}\|_{0,\Omega}^2 \right).$$

Theorem 4.4 states the unconditional stability of (4.5.25) provided the initial velocity approximation  $\mathbf{u}_h^0$  is given in terms of the Ritz-projection operator (4.5.24). In the general case, that is, whenever  $\mathbf{u}_h^0$  does not satisfy a discrete divergence-free condition (as  $\mathbf{u}_h^1$  does), only a conditional stability can be guaranteed. As a matter of fact, from the stability condition (4.5.26), pressure instabilities are expected for very small time-step sizes. Note that, for piecewise affine approximations ( $k = 1$ ) and regular enough initial data  $r \geq 2$ , the stability condition (4.5.26) is similar to (4.5.22) introduced in [BGL07] for residual based stabilizations. It is worth emphasizing that, although the stability conditions (4.5.22) and (4.5.26) are similar, their natures are different. Actually, the instabilities anticipated by Theorem 4.4 are related to the discrete divergence-free character of the initial velocity approximation, but not to the structure of the pressure stabilization  $j(\cdot, \cdot)$ .

Based on the stability estimates of Theorem 4.4, we have proved the following optimal error estimates for the velocity and the pressure.

**Theorem 4.5** *Assume that  $\mathbf{u} \in \mathbf{H}^1(0, T; H^r(\Omega)) \cap \mathbf{H}^2(0, T; L^2(\Omega))$  and  $p \in C^0((0, T]; H^s(\Omega))$  with  $r \geq 2$ ,  $s \geq 1$ , and let  $\mathbf{u}_h^0 = P_h(\mathbf{u}_0, 0)$ . Then, for  $1 \leq n \leq N$ ,*

$$\begin{aligned} \|\mathbf{u}_h^n - \mathbf{u}(t_n)\|_{0,\Omega} &\lesssim c_1 h^{r_{\mathbf{u}}-1} + c_2 h^{s_p} + c_3 \tau, \\ \left( \sum_{m=0}^{n-1} \tau \|(\mathbf{u}_h^{m+1} - \mathbf{u}(t_{m+1}), p_h^{m+1})\|_h^2 \right)^{\frac{1}{2}} &\lesssim c_1 h^{r_{\mathbf{u}}-1} + c_2 h^{s_p} + c_3 \tau, \\ \left( \sum_{m=0}^{n-1} \tau \|p_h^{m+1} - p(t_{m+1})\|_{0,\Omega}^2 \right)^{\frac{1}{2}} &\lesssim C_4 h^{s_p} + \nu^{\frac{1}{2}} (c_1 h^{r_{\mathbf{u}}-1} + c_2 h^{s_p} + c_3 \tau) \\ &\quad + \left( \sum_{m=0}^{n-1} \tau \|\partial_\tau \mathbf{u}_h^{m+1} - \partial_t \mathbf{u}(t_{m+1})\|_{0,\Omega}^2 \right)^{\frac{1}{2}}, \end{aligned}$$

with

$$\begin{aligned} c_1 &\stackrel{\text{def}}{=} h \left( (1 + \nu) \|\mathbf{u}\|_{C^0([0, T]; H^{r_{\mathbf{u}}}(\Omega))} + \nu^{-\frac{1}{2}} \|\partial_t \mathbf{u}\|_{L^2(0, T; H^{r_{\mathbf{u}}}(\Omega))} \right) \\ &\quad + (\nu T)^{\frac{1}{2}} \|\mathbf{u}\|_{C^0((0, T]; H^{r_{\mathbf{u}}}(\Omega))}, \\ c_2 &\stackrel{\text{def}}{=} \nu^{-\frac{1}{2}} T^{\frac{1}{2}} \|p\|_{C^0((0, T]; H^{s_p}(\Omega))}, \\ c_3 &\stackrel{\text{def}}{=} \nu^{-\frac{1}{2}} \|\partial_{tt} \mathbf{u}\|_{L^2(0, T; L^2(\Omega))}, \\ c_4 &\stackrel{\text{def}}{=} T^{\frac{1}{2}} \|p\|_{C^0((0, T]; H^{s_p}(\Omega))}. \end{aligned}$$

If, in addition,  $\mathbf{u} \in \mathbf{C}^1(0, T; H^r(\Omega))$ ,  $p \in C^1([0, T]; H^s(\Omega))$  and  $\mathbf{u}_0 \in \mathbf{H}_0^1(\Omega) \cap \mathbf{H}_0(\text{div}; \Omega)$ , we have

$$\left( \sum_{m=0}^{n-1} \tau \|\partial_\tau \mathbf{u}_h^{m+1} - \partial_t \mathbf{u}(t_{m+1})\|_{0,\Omega}^2 \right)^{\frac{1}{2}} \lesssim c_5 h^{r_{\mathbf{u}}} + c_6 h^{s_p} + c_7 \tau$$

for  $1 \leq n \leq N$ , where

$$\begin{aligned} c_5 &\stackrel{\text{def}}{=} \|\partial_t \mathbf{u}\|_{L^2(0, T; H^{r_{\mathbf{u}}}(\Omega))} + \nu^{\frac{1}{2}} T^{\frac{1}{2}} \|\partial_t \mathbf{u}\|_{C^0((0, T]; H^{r_{\mathbf{u}}}(\Omega))}, \\ c_6 &\stackrel{\text{def}}{=} \nu^{-\frac{1}{2}} \|p(0)\|_{s_p, \Omega} + h \nu^{-\frac{1}{2}} T^{\frac{1}{2}} \|\partial_t p\|_{C^0((0, T]; H^{s_p}(\Omega))}, \\ c_7 &\stackrel{\text{def}}{=} \|\partial_{tt} \mathbf{u}\|_{L^2(0, T; L^2(\Omega))}. \end{aligned}$$

Similar stability and convergence estimates can be derived if, instead of BDF1, we consider alternative  $\mathcal{A}$ -stable time discretizations like BDF2 or Crank-Nicholson (see [4, §4.2] for the details).

**Remark 4.4** *The above abstract framework can be adapted, with minor modifications, to cover the case of mixed interpolations (with possibly discontinuous pressures). In particular, the low-order method which consists of using piecewise affine continuous velocities, elementwise constant pressures and a stabilization based on the pressure jump over element faces (see, e.g., [HFB86]) is covered by the analysis. Moreover, in the case in which  $\mathbf{V}_h/Q_h$  is an inf-sup stable pair, we can take  $j(\cdot, \cdot) = 0$  in (4.5.23), as usual. This choice is compatible with assumptions (A1)-(A4), so that the above results still apply. In particular, the relation (4.3.11) becomes the standard inf-sup condition between  $\mathbf{V}_h$  and  $Q_h$ .*

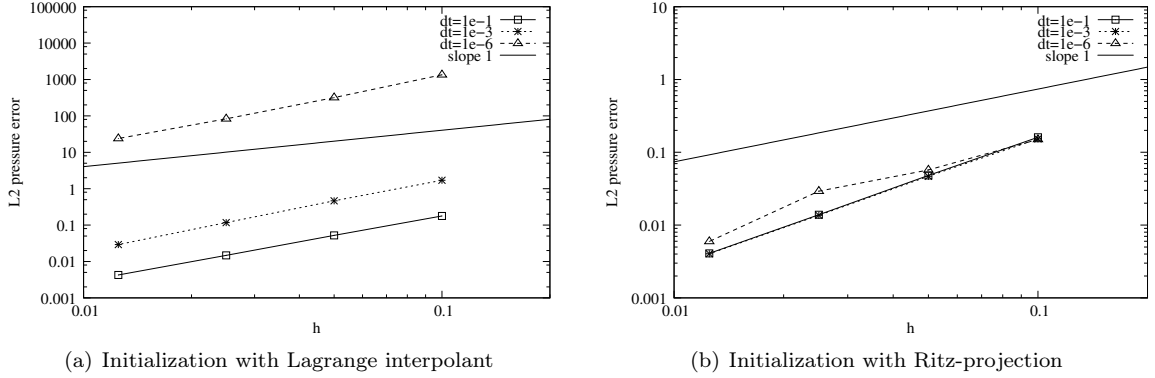


Figure 4.3: Impact of the initial velocity approximation: BDF1 scheme and CIP stabilized piecewise affine finite elements ( $k = 1$ ).

We conclude this section with a numerical illustration that highlights some of the above theoretical results. Figure 4.3 presents the convergence history (in space) of the pressure error, at the first time-step, using  $\mathbb{P}_1/\mathbb{P}_1$  finite elements ( $k = 1$ ) for different time-step sizes. The pressure instability for small time-steps is illustrated in Figure 4.3(a), where the initial velocity approximation is given in terms of the Lagrange interpolant. Indeed, we can observe that the pressure error has the right convergence rate in space, but it grows when the time-step size is decreased. On the other hand, as shown in Figure 4.3(b), the instability is eliminated when the initial velocity approximation is provided in terms of the Ritz-projection (4.5.24).

## 4.6 Transient reaction-advection-diffusion equation ([6])

We consider the problem of solving for  $u : \Omega \times (0, T) \rightarrow \mathbb{R}$ :

$$\begin{cases} \partial_t u + \sigma u + \boldsymbol{\beta} \cdot \nabla u - \nu \Delta u = f & \text{in } \Omega \times (0, T), \\ u = 0 & \text{on } \Gamma \times (0, T), \\ u(\cdot, 0) = u_0 & \text{in } \Omega. \end{cases} \quad (4.6.27)$$

where  $\boldsymbol{\beta}$  is a given, Lipschitz continuous, velocity field satisfying  $\operatorname{div} \boldsymbol{\beta} = 0$  (and that may depend on  $t$ ),  $f$  is a source function,  $u_0$  the initial data and  $\sigma \geq 0$  and  $\nu > 0$  are given bounded functions. In weak form, problem (4.6.27) read as follows:

$$\begin{cases} \text{For all } t \in (0, T), \text{ find } u(t) \in H_0^1(\Omega) \text{ such that} \\ (\partial_t u, v) + a(u, v) = (f, v) \quad \forall v \in H_0^1(\Omega), \\ u(0) = u_0. \end{cases} \quad (4.6.28)$$

with

$$a(u, v) \stackrel{\text{def}}{=} (\sigma u + \boldsymbol{\beta} \cdot \nabla u, v) + (\nu \nabla u, \nabla v).$$

**Remark 4.5** *The results below are also valid for  $\nu = 0$  (hyperbolic regime). In this case, the boundary conditions of (4.6.27) and the functional spaces in (4.6.28) have to be modified accordingly. In particular, we only impose  $u = 0$  on the inflow boundary  $\Gamma_{\text{in}} \stackrel{\text{def}}{=} \{\mathbf{x} \in \Gamma : (\boldsymbol{\beta} \cdot \mathbf{n})(\mathbf{x}) < 0\}$ .*

### Space semi-discretization: symmetric stabilization

Let us consider the following general stabilized finite element semi-discretization of (4.6.28):

$$\begin{cases} \text{For all } t \in (0, T), \text{ find } u_h(t) \in V_h \text{ such that} \\ (\partial_t u_h, v_h) + a_h(u_h, v_h) + s(u_h, v_h) = (f, v_h) \quad \forall v_h \in V_h, \\ (u_h(0), v_h) = (u_0, v_h) \quad \forall v_h \in V_h, \end{cases} \quad (4.6.29)$$

where  $s(\cdot, \cdot)$  represents an abstract symmetric stabilization operator (whose properties will be specified later on) and

$$a_h(u_h, v_h) \stackrel{\text{def}}{=} a(u_h, v_h) - \langle \nu \partial_{\mathbf{n}} u_h, v_h \rangle_{\Gamma} - \langle u_h, \nu \partial_{\mathbf{n}} v_h \rangle_{\Gamma} + \frac{\gamma_{\text{bc}} \nu}{h} \langle u_h, v_h \rangle_{\Gamma} - \langle \boldsymbol{\beta} \cdot \mathbf{n} u_h, v_h \rangle_{\Gamma_{\text{in}}}.$$

As pointed in §4.3, symmetric stabilization methods [Gue99, Cod00, BH04, BB04] have several advantages compared to the SUPG method, mainly thanks to the fact that the stabilizing term does not couple to all the terms of the residual and is therefore independent of both time derivatives, source terms and higher derivatives. In practice, however, these advantages come with a price: the size of the system matrix increases and/or degrees of freedoms must be added. In other words, the matrix pattern corresponding to  $s(\cdot, \cdot)$  does not necessarily coincide with that of the standard Galerkin method. This is a consequence of the fact that the symmetric stabilizations control small scale fluctuations rather than forcing the local residual to be small.

One of the aims of the work presented in this section is to show that, for certain time discretizations of (4.6.29), we can perform a fully explicit treatment of the stabilization term, and hence deal with a linear system with a matrix having a standard Galerkin matrix pattern.

**Remark 4.6** *For the semi-implicit treatment of the stabilization, we refer to [CB00] and [6].*

For the stability and convergence analysis below, we introduce the following norm

$$\|v_h\|_h^2 \stackrel{\text{def}}{=} \|\sigma^{\frac{1}{2}} v_h\|_{0,\Omega}^2 + \|\nu^{\frac{1}{2}} \nabla v_h\|_{0,\Omega}^2 + s(v_h, v_h) + \|(\gamma_{\text{bc}} \nu / h)^{\frac{1}{2}} v_h\|_{0,\Gamma}^2 + \| |\boldsymbol{\beta} \cdot \mathbf{n}|^{\frac{1}{2}} v_h \|_{0,\Gamma}^2.$$

The analysis is valid for a general class of symmetric stabilization operators  $s(\cdot, \cdot)$  satisfying the following assumptions:

(A1) Symmetry and positivity:

$$s(u_h, v_h) = s(v_h, u_h), \quad s(v_h, v_h) \geq 0 \quad \forall u_h, v_h \in V_h;$$

(A2) coercivity:

$$\|v_h\|_h^2 \leq a_h(v_h, v_h) + s(v_h, v_h) \quad (4.6.30)$$

for all  $v_h \in V_h$  and for a given  $\gamma_{\text{bc}}$  sufficiently large;

(A3) Cauchy-Schwarz and continuity:

$$s(u_h, v_h) \leq s(u_h, u_h)^{\frac{1}{2}} s(v_h, v_h)^{\frac{1}{2}} \lesssim \gamma |\boldsymbol{\beta}|_{\infty} h^{-1} \|u_h\|_{0,\Omega} \|v_h\|_{0,\Omega} \quad \forall u_h, v_h \in V_h$$

and where the parameter  $\gamma$  is a dimensionless stabilization parameter (typically chosen in the range  $(0, 1]$ ).

(A4) projection and consistency: there exists a projection  $\pi_h : L^2(\Omega) \rightarrow V_h$  such that

$$\|\nabla \pi_h u\|_{0,\Omega} \lesssim \|\nabla u\|_{0,\Omega} \quad \forall u \in H^1(\Omega) \quad (4.6.31)$$

and

$$\begin{aligned} |a_h(v - \pi_h v, v_h)| &\lesssim h^k (|\boldsymbol{\beta}|_\infty^{\frac{1}{2}} h^{\frac{1}{2}} + |\sigma|_\infty^{\frac{1}{2}} h + |\nu|_\infty^{\frac{1}{2}}) \|v\|_{k+1,\Omega} \|v_h\|_h \\ &\quad + h^{k+1} |\boldsymbol{\beta}|_{1,\infty,\Omega} \|v\|_{k+1,\Omega} \|v_h\|_{0,\Omega}, \end{aligned} \quad (4.6.32)$$

$$|s(\pi_h v, v_h)| \lesssim h^{k+\frac{1}{2}} |\boldsymbol{\beta}|_\infty^{\frac{1}{2}} \|v\|_{k+1,\Omega} \|v_h\|_h$$

for all  $v_h \in V_h$ ,  $v \in H^{k+1}(\Omega)$  and with the notations  $|\boldsymbol{\beta}|_\infty \stackrel{\text{def}}{=} \|\boldsymbol{\beta}\|_{0,\infty,\Omega}$ ,  $|\sigma|_\infty \stackrel{\text{def}}{=} \|\sigma\|_{0,\infty,\Omega}$  and  $|\nu|_\infty \stackrel{\text{def}}{=} \|\nu\|_{0,\infty,\Omega}$ .

One can readily verify that the Orthogonal-Subscale (OSS) method [Cod00], the continuous interior penalty (CIP) method [BH04] and the local-projection stabilization (LPS) method [BB04] enter the above framework (see [6, §4] for the details).

### First-order time-stepping

Let us consider the following backward-Euler (BDF1) time discretizations of (4.6.28):

$$\begin{cases} \text{For } 0 \leq n \leq N-1, \text{ find } u_h^{n+1} \in V_h \text{ such that} \\ (\partial_\tau u_h^{n+1}, v_h) + a_h(u_h^{n+1}, v_h) + s(u_h^{n+1}, v_h) = (f^{n+1}, v_h) \quad \forall v_h \in V_h, \\ u_h^0 = \pi_h u_0, \end{cases} \quad (4.6.33)$$

with  $\lambda \in \{0, 1\}$ . For  $\lambda = 1$  (extended matrix pattern), (4.6.33) reduces to the standard BDF1 time-discretization of (4.6.29). For  $\lambda = 0$ , the stabilization term is explicitly treated and, therefore, the left-hand side of (4.6.33) yields (at each time level) a *stiffness* matrix with the same structure as the standard Galerkin method.

The next theorem states the stability properties of the fully discrete formulations (4.6.33). In particular, it shows that for  $\lambda = 0$  (explicit stabilization treatment) the scheme is stable under a standard CFL condition (independent of the diffusion parameter  $\nu$ ).

**Theorem 4.6** *Assume that one of the following two conditions holds:*

- *Extended matrix pattern,  $\lambda = 1$ ;*
- *standard Galerkin matrix pattern,  $\lambda = 0$ , and*

$$\gamma \tau |\boldsymbol{\beta}|_\infty \lesssim h. \quad (4.6.34)$$

*Then, there holds*

$$\|u_h^n\|_{0,\Omega}^2 + \sum_{m=0}^{n-1} \|u_h^{m+1} - u_h^m\|_{0,\Omega}^2 + \sum_{m=0}^{n-1} \tau \|u_h^{m+1}\|_h^2 \lesssim T \sum_{m=0}^{n-1} \tau \|f^{m+1}\|_{0,\Omega}^2 + \|u_h^0\|_{0,\Omega}^2$$

for  $1 \leq n \leq N$ .

The proof for  $\lambda = 1$  follows by standard arguments (see, *e.g.*, [Tho06]) using assumption (A2). In the case  $\lambda = 0$  the idea consists in controlling the defect  $-s(\mathbf{u}_h^{n+1} - \mathbf{u}_h^n, \mathbf{u}_h^{n+1} - \mathbf{u}_h^n)$  via the natural numerical dissipation  $\|\mathbf{u}_h^{n+1} - \mathbf{u}_h^n\|_{0,\Omega}^2$  provided by BDF1 time marching, using (4.6.34) and assumption (A3).

From the assumptions on the stabilization operator and the stability result of Theorem 4.6 we can derive the following optimal *a priori* error estimate.

**Theorem 4.7** *Assume that the hypotheses of Theorem 4.6 are satisfied and let  $e_h^n \stackrel{\text{def}}{=} \pi_h u(t_n) - u_h^n$  be the discrete part of the error. Then, there holds*

$$\|e_h^n\|_{0,\Omega} + \left( \sum_{m=0}^{n-1} \tau \|e_h^{m+1}\|_h^2 \right)^{\frac{1}{2}} \lesssim c_1 h^k + c_2 \tau$$

for  $1 \leq n \leq N$  and with the notations

$$c_1 \stackrel{\text{def}}{=} (|\beta|_{\infty}^{\frac{1}{2}} h^{\frac{1}{2}} + T^{\frac{1}{2}} |\beta|_{1,\infty,\Omega} h + |\sigma|_{\infty}^{\frac{1}{2}} h + |\nu|_{\infty}^{\frac{1}{2}}) T^{\frac{1}{2}} \|u\|_{C^0([0,T];H^{k+1}(\Omega))},$$

$$c_2 \stackrel{\text{def}}{=} T^{\frac{1}{2}} \|\partial_{tt} u\|_{L^2(0,T;L^2(\Omega))}.$$

Note that the above estimate is uniform in  $\nu$  and that the error may grow as  $T^{\frac{1}{2}}$  due to the lack of parabolic smoothing.

## Second-order time-stepping

Finally, let us consider the following BDF2 time discretizations of (4.6.28):

$$\begin{cases} \text{For } 1 \leq n \leq N-1, \text{ find } u_h^{n+1} \in V_h \text{ such that:} \\ (\bar{\partial}_\tau u_h^{n+1}, v_h) + a_h(u_h^{n+1}, v_h) + s(\tilde{u}_h^{n+\lambda}, v_h) = (f^{n+1}, v_h) \quad \forall v_h \in V_h, \end{cases} \quad (4.6.35)$$

with  $\lambda \in \{0, 1\}$ ,  $u_h^0 = \pi_h u_0$  and  $u_h^1$  obtained by performing one time-step of (4.6.33). Moreover, we have considered the notations  $\tilde{u}_h^{n+1} \stackrel{\text{def}}{=} u_h^{n+1}$  and  $\tilde{u}_h^n \stackrel{\text{def}}{=} 2u_h^n - u_h^{n-1}$  (second order extrapolation).

For  $\lambda = 1$  (extended matrix pattern), the scheme (4.6.35) is nothing but to the standard implicit BDF2 time-discretization of (4.6.29). For  $\lambda = 0$ , the scheme (4.6.35) involves an algebraic system with the same structure as the standard Galerkin method.

By adapting the arguments used in the proof of Theorem 4.6 for the BDF1 scheme, we can derive the following stability result for the fully discrete formulations (4.6.35).

**Theorem 4.8** *Assume that one of the following two conditions holds:*

- *Full matrix pattern,  $\lambda = 1$ ;*
- *standard Galerkin matrix pattern,  $\lambda = 0$ , and*

$$\gamma \tau |\beta|_{\infty} \lesssim h. \quad (4.6.36)$$

Then, there holds

$$\|u_h^n\|_{0,\Omega}^2 + \sum_{m=1}^{n-1} \|u_h^{m+1} - \tilde{u}_h^m\|_{0,\Omega}^2 + \sum_{m=1}^{n-1} \tau \|u_h^{m+1}\|_h^2 \lesssim T \sum_{m=1}^{n-1} \tau \|f^{m+1}\|_{0,\Omega}^2 + \|u_h^0\|_{0,\Omega}^2 + \|u_h^1\|_{0,\Omega}^2$$

for all  $2 \leq n \leq N$ . The bound for  $\|u_h^1\|_{0,\Omega}$  being provided by Theorem 4.6.

The next theorem states an optimal *a priori* error estimate for the fully discrete formulations (4.6.35).

**Theorem 4.9** *Let the hypotheses of Theorem 4.8 be satisfied and let  $e_h^n \stackrel{\text{def}}{=} \pi_h u(t_n) - u_h^n$ . Then, there holds*

$$\|e_h^n\|_{0,\Omega} + \left( \sum_{m=1}^{n-1} \tau \|e_h^{m+1}\|_h^2 \right)^{\frac{1}{2}} \lesssim c_1 h^k + c_2 \tau^2 + \|e_h^1\|_{0,\Omega}$$

for  $2 \leq n \leq N$ , with  $c_1$  given as in Theorem 4.7,  $c_2 \stackrel{\text{def}}{=} T^{\frac{1}{2}} \|\partial_{ttt} u\|_{L^2(0,T;L^2(\Omega))}$  and  $\|e_h^1\|_{0,\Omega}$  is the error induced by the BDF1 initialization.

Note that, from Theorem 4.7 with  $T = \tau$ , we have  $\|e_h^1\|_{0,\Omega} \lesssim c_1 h^k + \tau^2 \|\partial_{tt} u\|_{L^\infty(0,\tau;L^2(\Omega))}$ . Therefore, for sufficiently regular solutions, the BDF1 initialization does not perturb the overall convergence rate expected for the BDF2 scheme.

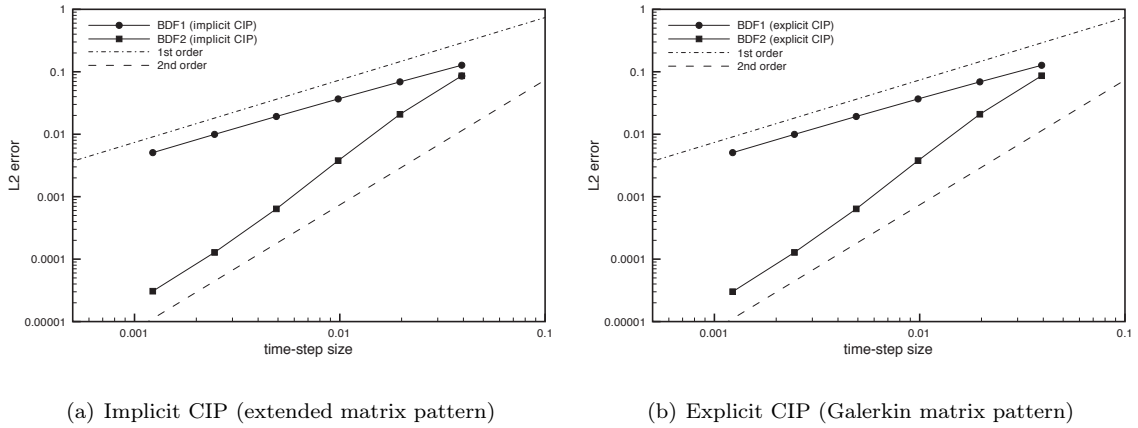


Figure 4.4: Convergence history of the Backward-Euler (BDF1) and BDF2 schemes with implicit ( $\lambda = 1$ ) and explicit ( $\lambda = 0$ ) treatment of the CIP stabilization.

For illustration purposes, Figure 4.4 presents the convergence histories (in time), obtained with the above BDF1 and BDF2 schemes and the CIP method, for the approximation of the solution of a pure transport problem ( $\sigma = 0$ ,  $\nu = 0$  and  $|\beta|_\infty \approx 1$ ). Optimal convergence in the  $L^2$ -norm was obtained for all the variants, which is in agreement with the results of Theorems 4.7 and 4.9. A comparison of Figures 4.4(a) and 4.4(b) shows that the explicit variant is as accurate as the implicit one, both for the BDF1 and BDF2 schemes.

**Remark 4.7** *Instead of BDF1 or BDF2, we can also consider a Crank-Nicolson time discretization of (4.6.29). Unconditional stability and optimal convergence are then obtained for  $\lambda = 1$  with minor modifications (see [6]). It is worth noting that this seems not to be the case for finite element stabilizations involving the residual of the PDE, like GLS, in which the time derivative included in the residual perturbs the stability of the traditional Crank-Nicolson scheme (see [LW95]). For  $\lambda = 0$ , the arguments can also be adapted to cope with the lack of numerical dissipation, so that stability and convergence still follow under the CFL condition (see [Bur10b]).*

## 4.7 Perspectives

The work summarized in this chapter shows that symmetrically stabilized finite element methods are well adapted to the approximation of time dependent problems. In particular, space and time

discretization commute and can be combined with any type of time-marching scheme. We therefore think it is interesting to pursue our investigations on that direction.

A natural question that arises from §4.6 is the investigation of whether the stabilization and the advection terms can be explicitly treated simultaneously. This is of fundamental importance, since the corresponding solution procedure would be purely based on the solution of symmetric algebraic systems with a standard Galerkin pattern (in the spirit of the method of characteristics [Pir82, DR82]). We have already obtained some preliminary results on this issue, using Runge-Kutta (RK) time discretizations. Let us consider, for instance, the following two-stage explicit RK2 discretization of (4.6.29):

$$\left\{ \begin{array}{l} \text{For } 1 \leq n \leq N-1, \text{ find } u_h^{n+1} \in V_h \text{ such that:} \\ \frac{1}{\tau}(w_h^n - u_h^n, v_h) = (f^n, v_h) - a_h(u_h^n, v_h) - s(u_h^n, v_h), \\ \frac{1}{\tau}(u_h^{n+1} - u_h^n, v_h) = (f^{n+\frac{1}{2}}, v_h) - \frac{1}{2}a_h(u_h^n + w_h^n, v_h) - \frac{1}{2}s(u_h^n + w_h^n, v_h) \\ \text{for all } v_h \in V_h. \end{array} \right.$$

For a pure transport problem (*i.e.*, (4.6.27) with  $\sigma = \nu = 0$ ), we can show that the above scheme is stable and optimally convergent under CFL-like conditions (see [26]). The next step will be to consider the case of a non vanishing diffusion ( $\nu > 0$ ) and the treatment of the incompressibility constraint. The ultimate goal is to extend this kind of approaches to the transient Navier-Stokes equations.



# Bibliography

- [ABCM00] D.N. Arnold, F. Brezzi, B. Cockburn, and D. Marini. Discontinuous Galerkin methods for elliptic problems. In *Discontinuous Galerkin methods (Newport, RI, 1999)*, volume 11 of *Lect. Notes Comput. Sci. Eng.*, pages 89–101. Springer, 2000.
- [Aeh06] B. Aehlert. *ECGs Made Easy*. Mosby Jems, Elsevier, third edition, 2006.
- [AG93] N.I. Akhiezer and I.M. Glazman. *Theory of linear operators in Hilbert space*. Dover Publications, 1993.
- [AG10] M. Astorino and C. Grandmont. Convergence analysis of a projection semi-implicit coupling scheme for fluid-structure interaction problems. *Numer. Math.*, 116:721–767, 2010.
- [AGPT09] M. Astorino, J.-F. Gerbeau, O. Pantz, and K.-F. Traoré. Fluid-structure interaction and multi-body contact: application to aortic valves. *Comput. Methods Appl. Mech. Engrg.*, 198(45-46):3603–3612, 2009.
- [All07] G. Allaire. *Conception optimale de structures*, volume 58 of *Mathématiques & Applications*. Springer, 2007.
- [AP96] R.R. Aliev and A.V. Panfilov. A simple two-variable model of cardiac excitation. *Chaos, Solitons & Fractals*, 3(7):293–301, 1996.
- [Arn82] D.N. Arnold. An interior penalty finite element method with discontinuous elements. *SIAM J. Numer. Anal.*, 19(4):742–760, 1982.
- [Ast10] M. Astorino. *Interaction fluide-structure dans le système cardiovasculaire. Analyse numérique et simulation*. PhD thesis, Université Paris VI, France, 2010.
- [ATP06] T.M. Austin, M.L. Trew, and A.J. Pullan. Solving the cardiac bidomain equations for discontinuous conductivities. *IEEE Trans. Biomed. Eng.*, 53(7):1265–72, 2006.
- [Bak77] G.A. Baker. Finite element methods for elliptic equations using nonconforming elements. *Math. Comp.*, 31(137):45–59, 1977.
- [BB01] R. Becker and M. Braack. A finite element pressure gradient stabilization for the Stokes equations based on local projections. *Calcolo*, 38(4):173–199, 2001.
- [BB04] R. Becker and M. Braack. A two-level stabilization scheme for the Navier-Stokes equations. In *Numerical mathematics and advanced applications*, pages 123–130. Springer, 2004.

- [BB06] M. Braack and E. Burman. Local projection stabilization for the Oseen problem and its interpretation as a variational multiscale method. *SIAM J. Numer. Anal.*, 43(6):2544–2566 (electronic), 2006.
- [BBJL07] M. Braack, E. Burman, V. John, and G. Lube. Stabilized finite element methods for the generalized Oseen problem. *Comput. Methods Appl. Mech. Engrg.*, 196(4-6):853–866, 2007.
- [BC07] S. Badia and R. Codina. On some fluid-structure iterative algorithms using pressure segregation methods. Application to aeroelasticity. *Internat. J. Numer. Methods Engrg.*, 72(1):46–71, 2007.
- [BC09] S. Badia and R. Codina. On a multiscale approach to the transient Stokes problem: dynamic subscales and anisotropic space-time discretization. *Appl. Math. Comput.*, 207(2):415–433, 2009.
- [BCHZ08] Y. Bazilevs, V.M. Calo, T.J.R. Hughes, and Y. Zhang. Isogeometric fluid-structure interaction: theory, algorithms, and computations. *Comput. Mech.*, 43(1):3–37, 2008.
- [BCP09] Y. Bourgault, Y. Coudière, and C. Pierre. Existence and uniqueness of the solution for the bidomain model used in cardiac electrophysiology. *Nonlinear Anal. Real World Appl.*, 10(1):458–482, 2009.
- [BE07] E. Burman and A. Ern. Continuous interior penalty *hp*-finite element methods for advection and advection-diffusion equations. *Math. Comp.*, 76(259):1119–1140, 2007.
- [BELB03] Y. Bourgault, M. Ethier, and V.G. Le Blanc. Simulation of electrophysiological waves with an unstructured finite element method. *M2AN Math. Model. Numer. Anal.*, 37(4):649–661, 2003.
- [Ber99] S. Bertoluzza. The discrete commutator property of approximation spaces. *C. R. Acad. Sci. Paris Sér. I Math.*, 329(12):1097–1102, 1999.
- [BGL07] P.B. Bochev, M.D. Gunzburger, and R.B. Lehoucq. On stabilized finite element methods for the Stokes problem in the small time step limit. *Internat. J. Numer. Methods Fluids*, 53(4):573–597, 2007.
- [BGS04] P.B. Bochev, M.D. Gunzburger, and J.N. Shadid. On inf-sup stabilized finite element methods for transient problems. *Comput. Methods Appl. Mech. Engrg.*, 193(15-16):1471–1489, 2004.
- [BH82] A.N. Brooks and T.J.R. Hughes. Streamline upwind/Petrov-Galerkin formulations for convection dominated flows with particular emphasis on the incompressible Navier-Stokes equations. *Comput. Methods Appl. Mech. Engrg.*, 32(1-3):199–259, 1982.
- [BH04] E. Burman and P. Hansbo. Edge stabilization for Galerkin approximations of convection-diffusion-reaction problems. *Comput. Methods Appl. Mech. Engrg.*, 193(15-16):1437–1453, 2004.
- [BH06] E. Burman and P. Hansbo. Edge stabilization for the generalized Stokes problem: a continuous interior penalty method. *Comput. Methods Appl. Mech. Engrg.*, 195(19-22):2393–2410, 2006.

- [BH07] E. Burman and P. Hansbo. A unified stabilized method for Stokes' and Darcy's equations. *J. Comput. Appl. Math.*, 198:35–51, 2007.
- [BHS03] R. Becker, P. Hansbo, and R. Stenberg. A finite element method for domain decomposition with non-matching grids. *M2AN Math. Model. Numer. Anal.*, 37(2):209–225, 2003.
- [BK06] M. Bendahmane and K.H. Karlsen. Analysis of a class of degenerate reaction-diffusion systems and the bidomain model of cardiac tissue. *Netw. Heterog. Media*, 1(1):185–218 (electronic), 2006.
- [BMMR97] K. Boukir, Y. Maday, B. Métivet, and E. Razafindrakoto. A high-order characteristics/finite element method for the incompressible Navier-Stokes equations. *Internat. J. Numer. Methods Fluids*, 25(12):1421–1454, 1997.
- [BMP93] C. Bernardi, Y. Maday, and A. T. Patera. Domain decomposition by the mortar element method. In *Asymptotic and numerical methods for partial differential equations with critical parameters (Beaune, 1992)*, volume 384 of *NATO Adv. Sci. Inst. Ser. C Math. Phys. Sci.*, pages 269–286. Kluwer Acad. Publ., Dordrecht, 1993.
- [BNV08] S. Badia, F. Nobile, and C. Vergara. Fluid-structure partitioned procedures based on Robin transmission conditions. *J. Comp. Phys.*, 227:7027–7051, 2008.
- [BNV09] S. Badia, F. Nobile, and C. Vergara. Robin-Robin preconditioned Krylov methods for fluid-structure interaction problems. *Comput. Methods Appl. Mech. Engrg.*, 198(33-36):2768–2784, 2009.
- [BP84] F. Brezzi and J. Pitkäranta. On the stabilization of finite element approximations of the Stokes equations. In *Efficient solutions of elliptic systems (Kiel, 1984)*, volume 10 of *Notes Numer. Fluid Mech.*, pages 11–19. Vieweg, 1984.
- [BP02] M. Buist and A. Pullan. Torso coupling techniques for the forward problem of electrocardiography. *Ann. Biomed. Eng.*, 30(10):1299–1312, 2002.
- [BQQ08a] S. Badia, A. Quaini, and A. Quarteroni. Modular vs. non-modular preconditioners for fluid-structure systems with large added-mass effect. *Comput. Methods Appl. Mech. Engrg.*, 197(49-50):4216–4232, 2008.
- [BQQ08b] S. Badia, A. Quaini, and A. Quarteroni. Splitting methods based on algebraic factorization for fluid-structure interaction. *SIAM J. Sci. Comput.*, 30(4):1778–1805, 2008.
- [BR77] G. Beeler and H. Reuter. Reconstruction of the action potential of ventricular myocardial fibres. *J. Physiol. (Lond.)*, 268:177—210, 1977.
- [BR85] C. Bernardi and G. Raugel. A conforming finite element method for the time-dependent Navier-Stokes equations. *SIAM J. Numer. Anal.*, 22(3):455–473, 1985.
- [BS91] K.Y. Billiah and R.H. Scanlan. Resonance, Tacoma Narrows bridge failure, and undergraduate physics textbooks. *Am. J. Phys.*, 59(2):118–124, 1991.
- [BS94] P. N. Brown and Y. Saad. Convergence theory of nonlinear Newton-Krylov algorithms. *SIAM J. Optim.*, 4(2):297–330, 1994.

- [Bur05] E. Burman. A unified analysis for conforming and nonconforming stabilized finite element methods using interior penalty. *SIAM J. Numer. Anal.*, 43(5):2012–2033, 2005.
- [Bur10a] E. Burman. Consistent SUPG-method for transient transport problems: Stability and convergence. *Comput. Methods Appl. Mech. Engrg.*, 199(17-20):1114–1123, 2010.
- [Bur10b] E. Burman. Crank-Nicolson finite element methods with symmetric stabilization for optimal control problems subject to transient advection-diffusion equations. Submitted, 2010.
- [BZ04] K.J. Bathe and H. Zhang. Finite element developments for general fluid flows with structural interactions. *Int. J. Num. Meth. Engrg.*, 2004.
- [BZ06] E. Burman and P. Zunino. A domain decomposition method based on interior penalties for advection–diffusion–reaction problems. *Siam Jour. Num. Anal.*, 44:1612–1638, 2006.
- [CB97] R. Codina and J. Blasco. A finite element formulation for the Stokes problem allowing equal velocity-pressure interpolation. *Comput. Methods Appl. Mech. Engrg.*, 143(3-4):373–391, 1997.
- [CB00] R. Codina and J. Blasco. Stabilized finite element method for the transient Navier-Stokes equations based on a pressure gradient projection. *Comput. Methods Appl. Mech. Engrg.*, 182(3-4):277–300, 2000.
- [CB03] D. Chapelle and K.J. Bathe. *The Finite Element Analysis of Shells - Fundamentals*. Springer, 2003.
- [CCC<sup>+</sup>04] R. Clark, D. Cox, H.C. Jr. Curtiss, J.W. Edwards, K.C. Hall, D.A. Peters, R.H. Scanlan, E. Simiu, F. Sisto, T.W. Strganac, and E.H. Dowell. *A modern course in aeroelasticity*. Kluwer, 2004.
- [CD95] C. Conca and M. Durán. A numerical study of a spectral problem in solid-fluid type structures. *Numer. Methods Partial Differential Equations*, 11(4):423–444, 1995.
- [CDP92] C. Conca, M. Durán, and J. Planchard. A quadratic eigenvalue problem involving Stokes equations. *Comput. Methods Appl. Mech. Engrg.*, 100(3):295–313, 1992.
- [CFP04] P. Colli Franzone and L.F. Pavarino. A parallel solver for reaction-diffusion systems in computational electrocardiology. *Math. Models Methods Appl. Sci.*, 14(6):883–911, 2004.
- [CFPST09] P. Colli Franzone, L.F. Pavarino, S. Scacchi, and B. Taccardi. Effects of anisotropy and transmural heterogeneity on the T-wave polarity of simulated electrograms. In N. Ayache, H. Delingette, and M. Sermesant, editors, *Functional Imaging and Modeling of the Heart*, volume 5528 of *Lecture Notes in Computer Science*, pages 513–523. Springer, 2009.
- [CFPT05] P. Colli Franzone, L.F. Pavarino, and B. Taccardi. Simulating patterns of excitation, repolarization and action potential duration with cardiac bidomain and monodomain models. *Math. Biosci.*, 197(1):35–66, 2005.

- [CFS02] P. Colli Franzone and G. Savaré. Degenerate evolution systems modeling the cardiac electric field at micro- and macroscopic level. In *Evolution equations, semigroups and functional analysis (Milano, 2000)*, volume 50 of *Progr. Nonlinear Differential Equations Appl.*, pages 49–78. Birkhäuser, Basel, 2002.
- [CGN05] P. Causin, J.-F. Gerbeau, and F. Nobile. Added-mass effect in the design of partitioned algorithms for fluid-structure problems. *Comput. Methods Appl. Mech. Engrg.*, 194(42–44):4506–4527, 2005.
- [CGS94] K.A. Cliffe, T.J. Garratt, and A. Spence. Eigenvalues of block matrices arising from problems in fluid mechanics. *SIAM J. Matrix Anal. Appl.*, 15(4):1310–1318, 1994.
- [CH00] W.S. Clark and K.C. Hall. A time-linearized Navier-Stokes analysis of stall flutter. *J. Turbomach.*, 122:467–476, 2000.
- [Cho69] A.J. Chorin. On the convergence of discrete approximations to the Navier-Stokes equations. *Math. Comp.*, 23:341–353, 1969.
- [Cia88] P.G. Ciarlet. *Mathematical elasticity. Vol. I*, volume 20 of *Studies in Mathematics and its Applications*. North-Holland, 1988.
- [CMLT09] D. Chapelle, P. Moireau, and P. Le Tallec. Robust filtering for joint state-parameter estimation in distributed mechanical systems. *Discrete Contin. Dyn. Syst.*, 23(1-2):65–84, 2009.
- [CNLH04] J. Clements, J. Nenonen, P.K.J. Li, and B.M. Horacek. Activation dynamics in anisotropic cardiac tissue via decoupling. *Ann. Biomed. Eng.*, 32(7):984–990, 2004.
- [Cod00] R. Codina. Stabilization of incompressibility and convection through orthogonal subscales in finite element methods. *Comput. Methods Appl. Mech. Engrg.*, 190(13-14):1579–1599, 2000.
- [Cod01] R. Codina. A stabilized finite element method for generalized stationary incompressible flows. *Comput. Methods Appl. Mech. Engrg.*, 190(20-21):2681–2706, 2001.
- [Cod02] R. Codina. Stabilized finite element approximation of transient incompressible flows using orthogonal subscales. *Comput. Methods Appl. Mech. Engrg.*, 191(39-40):4295–4321, 2002.
- [COS05] Y. Cheng, H. Oertel, and T. Schenkel. Fluid-structure coupled CFD simulation of the left ventricular flow during filling phase. *Ann. Biomed. Eng.*, 33(5):567–576, 2005.
- [CPGB07] R. Codina, J. Principe, O. Guasch, and S. Badia. Time dependent subscales in the stabilized finite element approximation of incompressible flow problems. *Comput. Methods Appl. Mech. Engrg.*, 196(21-24):2413–2430, 2007.
- [CPTV94] C. Conca, J. Planchard, B. Thomas, and M. Vanninatanh. *Problèmes mathématiques en couplage fluide-structure*. Eyrolles, 1994.
- [DAV10] J. Degroote, S. Annerel, and J. Vierendeels. Stability analysis of Gauss-Seidel iterations in a partitioned simulation of fluid-structure interaction. *Comp. & Struct.*, 88(5-6):263–271, 2010.
- [DB04] C.R. Dohrmann and P.B. Bochev. A stabilized finite element method for the Stokes problem based on polynomial pressure projections. *Internat. J. Numer. Methods Fluids*, 46(2):183–201, 2004.

- [DBV09] J. Degroote, K.-J. Bathe, and J. Vierendeels. Performance of a new partitioned procedure versus a monolithic procedure in fluid-structure interaction. *Comp. & Struct.*, 87(11-12):793–801, 2009.
- [DD76] J. Douglas, Jr. and T. Dupont. Interior penalty procedures for elliptic and parabolic Galerkin methods. In *Computing methods in applied sciences (Second Internat. Sympos., Versailles, 1975)*, pages 207–216. Lecture Notes in Phys., Vol. 58. Springer, 1976.
- [DDFQ06] S. Deparis, M. Discacciati, G. Fourestey, and A. Quarteroni. Fluid-structure algorithms based on Steklov-Poincaré operators. *Comput. Methods Appl. Mech. Engrg.*, 195(41-43):5797–5812, 2006.
- [DdSGB08] N. Diniz dos Santos, J.-F. Gerbeau, and J.-F. Bourgat. A partitioned fluid-structure algorithm for elastic thin valves with contact. *Comput. Methods Appl. Mech. Engrg.*, 197(19-20):1750–1761, 2008.
- [DEA07] L. Dumas and L. El Alaoui. How genetic algorithms can improve a pacemaker efficiency. In *GECCO '07: Proceedings of the 2007 GECCO conference companion on Genetic and evolutionary computation*, pages 2681–2686, New York, NY, USA, 2007. ACM.
- [Deb96] C. Debiez. *Approximation et linéarisation d'écoulements aérodynamiques instationnaires*. PhD thesis, Université de Nice Sophia-Antipolis, France, 1996.
- [Dep04] S. Deparis. *Numerical Analysis of Axisymmetric Flows and Methods for Fluid-Structure Interaction Arising in Blood Flow Simulation*. PhD thesis, EPFL, Switzerland, 2004.
- [DGH82] J. Donéa, S. Giuliani, and J. P. Halleux. An arbitrary Lagrangian-Eulerian finite element method for transient dynamic fluid-structure interactions. *Comp. Meth. Appl. Mech. Engrg.*, pages 689–723, 1982.
- [DHV08] P. Degroote, J. Bruggeman, R. Haelterman, and J. Vierendeels. Stability of a coupling technique for partitioned solvers in FSI applications. *Comp. & Struct.*, 86(23-24):2224–2234, 2008.
- [DK98] Y. Ding and M. Kawahara. Linear stability of incompressible flow using a mixed finite element method. *J. Comput. Phys.*, 139(2):243–273, 1998.
- [DK99] Y. Ding and M. Kawahara. Three-dimensional linear stability analysis of incompressible viscous flows using the finite element method. *Internat. J. Numer. Methods Fluids*, 31(2):451–479, 1999.
- [DP06] W. Dettmer and D. Perić. A computational framework for fluid-rigid body interaction: finite element formulation and applications. *Comput. Methods Appl. Mech. Engrg.*, 195(13-16):1633–1666, 2006.
- [DR82] J. Douglas, Jr. and T.F. Russell. Numerical methods for convection-dominated diffusion problems based on combining the method of characteristics with finite element or finite difference procedures. *SIAM J. Numer. Anal.*, 19(5):871–885, 1982.
- [DS05] K. Djabella and M. Sorine. Differential model of the excitation-contraction coupling in a cardiac cell for multicycle simulations. In *EMBECC'05*, volume 11, pages 4185–4190, Prague, 2005.

- [DSB<sup>+</sup>10] J. Degroote, A. Swillens, P. Bruggeman, R. Haelterman, P. Segers, and J. Vierendeels. Simulation of fluid-structure interaction with the interface artificial compressibility method. *Int. J. Numer. Meth. Biomed. Engng.*, 26(3-4):276–289, 2010.
- [EB08] M. Ethier and Y. Bourgault. Semi-implicit time-discretization schemes for the bidomain model. *SIAM J. Numer. Anal.*, 46(5):2443–2468, 2008.
- [EG04] A. Ern and J.-L. Guermond. *Theory and practice of finite elements*, volume 159 of *Applied Mathematical Sciences*. Springer, 2004.
- [EGR00] I.R. Efimov, R.A. Gray, and B.J. Roth. Virtual electrodes and deexcitation: new insights into fibrillation induction and defibrillation. *J. Cardiovasc. Electrophysiol.*, 11(3):339–353, 2000.
- [Fan01] T. Fanion. *Étude de la simulation numérique des phénomènes d’aéroélasticité dynamique. Application au problème du flottement des avions*. PhD thesis, Université de Paris IX, France, 2001.
- [FF92] L.P. Franca and S.L. Frey. Stabilized finite element methods. II. The incompressible Navier-Stokes equations. *Comput. Methods Appl. Mech. Engrg.*, 99(2-3):209–233, 1992.
- [FGNQ01] L. Formaggia, J.-F. Gerbeau, F. Nobile, and A. Quarteroni. On the coupling of 3D and 1D Navier-Stokes equations for flow problems in compliant vessels. *Comp. Meth. Appl. Mech. Engrg.*, 191(6-7):561–582, 2001.
- [Fit61] R. Fitzhugh. Impulses and physiological states in theoretical models of nerve membrane. *Biophys. J.*, 1:445–465, 1961.
- [FK98] F. Fenton and A. Karma. Vortex dynamics in three-dimensional continuous myocardium with fiber rotation: Filament instability and fibrillation. *Chaos*, 8(1):20–47, 1998.
- [FLLT98] C. Farhat, M. Lesoinne, and P. Le Tallec. Load and motion transfer algorithms for fluid/structure interaction problems with non-matching discrete interfaces: Momentum and energy conservation, optimal discretization and application to aeroelasticity. *Comput. Methods Appl. Mech. Engrg.*, 157:95–114, 1998.
- [FP04] G. Fourestey and S. Piperno. A second-order time-accurate ALE Lagrange-Galerkin method applied to wind engineering and control of bridge profiles. *Comput. Methods Appl. Mech. Engrg.*, 193(39-41):4117–4137, 2004.
- [FPF01] C.A. Felippa, K.C. Park, and C. Farhat. Partitioned analysis of coupled mechanical systems. *Comput. Methods Appl. Mech. Engrg.*, 190(24-25):3247–3270, 2001.
- [FPQ09] L. Formaggia, K. Perktold, and A. Quarteroni. Basic mathematical models and motivations. In *Cardiovascular mathematics*, volume 1 of *MS&A. Model. Simul. Appl.*, pages 47–75. Springer, 2009.
- [Fun93] Y.C. Fung. *Biomechanics, Mechanical properties of living tissues*. Springer, 1993.
- [FVCJ<sup>+</sup>06] C.A. Figueroa, I.E. Vignon-Clementel, K.E. Jansen, T.J.R. Hughes, and C.A. Taylor. A coupled momentum method for modeling blood flow in three-dimensional deformable arteries. *Comput. Methods Appl. Mech. Engrg.*, 195(41-43):5685–5706, 2006.

- [FvdZG06] C. Farhat, K. van der Zee, and Ph. Geuzaine. Provably second-order time-accurate loosely-coupled solution algorithms for transient nonlinear aeroelasticity. *Comput. Methods Appl. Mech. Engrg.*, 195(17–18):1973–2001, 2006.
- [FWR07] C. Förster, W.A. Wall, and E. Ramm. Artificial added mass instabilities in sequential staggered coupling of nonlinear structures and incompressible viscous flows. *Comput. Methods Appl. Mech. Engrg.*, 196(7):1278–1293, 2007.
- [Gar91] T.J. Garrat. *The numerical detection of Hopf bifurcations in large systems arising in fluids mechanics*. PhD thesis, University of Bath, UK, 1991.
- [Geo85] A. Georgescu. *Hydrodynamic stability theory*. Martinus Nijhoff, Dordrecht, 1985.
- [GGC<sup>+</sup>09] G. Guidoboni, R. Glowinski, N. Cavallini, S. Canic, and S. Lapin. A kinematically coupled time-splitting scheme for fluid-structure interaction in blood flow. *Appl. Math. Lett.*, 22(5):684–688, 2009.
- [GGCC09] G. Guidoboni, R. Glowinski, N. Cavallini, and S. Canic. Stable loosely-coupled-type algorithm for fluid-structure interaction in blood flow. *J. Comp. Phys.*, 228(18):6916–6937, 2009.
- [GH07] M.J. Gander and L. Halpern. Optimized Schwarz waveform relaxation methods for advection reaction diffusion problems. *SIAM J. Numer. Anal.*, 45(2):666–697, 2007.
- [GKW10] M.W. Gee, U. Küttler, and W. Wall. Truly monolithic algebraic multigrid for fluid-structure interaction. *Int. J. Numer. Meth. Engrg.*, 2010. To appear.
- [GLOS05] T. Gelhard, G. Lube, M.A. Olshanskii, and J.-H. Starcke. Stabilized finite element schemes with LBB-stable elements for incompressible flows. *J. Comput. Appl. Math.*, 177(2):243–267, 2005.
- [GM98] C. Grandmont and Y. Maday. Nonconforming grids for the simulation of fluid-structure interaction. In *Domain decomposition methods, 10 (Boulder, CO, 1997)*, volume 218 of *Contemp. Math.*, pages 262–270. Amer. Math. Soc., Providence, RI, 1998.
- [GMS06] J. L. Guermond, P. Mineev, and J. Shen. An overview of projection methods for incompressible flows. *Comput. Methods Appl. Mech. Engrg.*, 195(44-47):6011–6045, 2006.
- [Gol06] A.L. Goldberger. *Clinical Electrocardiography: A Simplified Approach*. Mosby-Elsevier, 7th edition, 2006.
- [GQ98] J.-L. Guermond and L. Quartapelle. On stability and convergence of projection methods based on pressure Poisson equation. *Internat. J. Numer. Methods Fluids*, 26(9):1039–1053, 1998.
- [GR86] V. Girault and P.-A. Raviart. *Finite element methods for Navier-Stokes equations*. Springer, 1986.
- [Gue96] J.-L. Guermond. Some implementation of projection methods for Navier-Stokes equations. *M2AN Math. Model. Numer. Anal.*, 30:637–667, 1996.
- [Gue99] J.L. Guermond. Stabilization of Galerkin approximations of transport equations by subgrid modeling. *M2AN Math. Model. Numer. Anal.*, 33(6):1293–1316, 1999.

- [Gul88] R.M. Gulrajani. Models of the electrical activity of the heart and computer simulation of the electrocardiogram. *Crit. Rev. Biomed. Eng.*, 16(1):1–6, 1988.
- [Gur81] M.E. Gurtin. *An introduction to continuum mechanics*, volume 158 of *Mathematics in Science and Engineering*. Academic Press Inc., 1981.
- [GV03] J.-F. Gerbeau and M. Vidrascu. A quasi-Newton algorithm based on a reduced model for fluid-structure interactions problems in blood flows. *Math. Model. Num. Anal.*, 37(4):631–648, 2003.
- [GVF05] J.-F. Gerbeau, M. Vidrascu, and P. Frey. Fluid-structure interaction in blood flows on geometries based on medical imaging. *Comp. & Struct.*, 83(2-3):155–165, 2005.
- [Han05] P. Hansbo. Nitsche’s method for interface problems in computational mechanics. *GAMM-Mitt.*, 28(2):183–206, 2005.
- [HC89] K.C. Hall and E.F. Crawley. Calculation of unsteady flows in turbomachinery using the linearized Euler equations. *AIAA*, 27(6):777–787, 1989.
- [HC93] K.C. Hall and W.S. Clark. Linearized euler predictions of unsteady aerodynamic loads in cascades. *AIAA*, 31(3):540–550, 1993.
- [He03] Y. He. A fully discrete stabilized finite-element method for the time-dependent Navier-Stokes problem. *IMA J. Numer. Anal.*, 23(4):665–691, 2003.
- [Hei04] M. Heil. An efficient solver for the fully coupled solution of large-displacement fluid-structure interaction problems. *Comput. Methods Appl. Mech. Engrg.*, 193(1-2):1–23, 2004.
- [HFB86] T.J.R. Hughes, L.P. Franca, and M. Balestra. A new finite element formulation for computational fluid dynamics. V. Circumventing the Babuška-Brezzi condition: a stable Petrov-Galerkin formulation of the Stokes problem accommodating equal-order interpolations. *Comput. Methods Appl. Mech. Engrg.*, 59(1):85–99, 1986.
- [HH03] P. Hansbo and J. Hermansson. Nitsche’s method for coupling non-matching meshes in fluid-structure vibration problems. *Computational Mechanics*, 32(1–2):134–139, 2003.
- [HHB08] M. Heil, A.L. Hazel, and J. Boyle. Solvers for large-displacement fluid-structure interaction problems: Segregated vs. monolithic approaches. *Comp. Mech.*, 43:91–101, 2008.
- [HHLR94] N. Hooke, C.S. Henriquez, P. Lanzkron, and D. Rose. Linear algebraic transformations of the bidomain equations: implications for numerical methods. *Math. Biosci.*, 120(2):127–145, 1994.
- [HHS04] P. Hansbo, J. Hermansson, and T. Svedberg. Nitsche’s method combined with space-time finite elements for ALE fluid-structure interaction problems. *Comput. Methods Appl. Mech. Engrg.*, 193:4195–4206, 2004.
- [HR82] J.G. Heywood and R. Rannacher. Finite element approximation of the nonstationary Navier-Stokes problem. I. Regularity of solutions and second-order error estimates for spatial discretization. *SIAM J. Numer. Anal.*, 19(2):275–311, 1982.

- [HR86] J.G. Heywood and R. Rannacher. Finite element approximation of the nonstationary Navier-Stokes problem. II. Stability of solutions and error estimates uniform in time. *SIAM J. Numer. Anal.*, 23(4):750–777, 1986.
- [HR88] J.G. Heywood and R. Rannacher. Finite element approximation of the nonstationary Navier-Stokes problem. III. Smoothing property and higher order error estimates for spatial discretization. *SIAM J. Numer. Anal.*, 25(3):489–512, 1988.
- [HR90] J.G. Heywood and R. Rannacher. Finite-element approximation of the nonstationary Navier-Stokes problem. IV. Error analysis for second-order time discretization. *SIAM J. Numer. Anal.*, 27(2):353–384, 1990.
- [HS90] P. Hansbo and A. Szepessy. A velocity-pressure streamline diffusion finite element method for the incompressible Navier-Stokes equations. *Comput. Methods Appl. Mech. Engrg.*, 84(2):175–192, 1990.
- [Hui98] G. Huiskamp. Simulation of depolarization in a membrane-equations-based model of the anisotropic ventricle. *IEEE Trans. Biomed. Eng.*, 50(7):847–855, 1998.
- [HWD04] B. Hübner, E. Walhorn, and D. Dinkle. A monolithic approach to fluid-structure interaction using space-time finite elements. *Comp. Meth. Appl. Mech. Engrg.*, 193:2087–2104, 2004.
- [JDP09] M.M. Joosten, W.G. Dettmer, and D. Perić. Analysis of the block Gauss-Seidel solution procedure for a strongly coupled model problem with reference to fluid-structure interaction. *Internat. J. Numer. Methods Engrg.*, 78(7):757–778, 2009.
- [JRLS08] E. Järvinen, P. Råback, M. Lyly, and J.-P. Salenius. A method for partitioned fluid-structure interaction computation of flow in arteries. *Medical Engineering & Physics*, 30(7):917–923, 2008.
- [JS86] C. Johnson and J. Saranen. Streamline diffusion methods for the incompressible Euler and Navier-Stokes equations. *Math. Comp.*, 47(175):1–18, 1986.
- [JS09] M. Juntunen and R. Stenberg. Nitsche’s method for general boundary conditions. *Math. Comp.*, 78(267):1353–1374, 2009.
- [JSH90] C. Johnson, A. Szepessy, and P. Hansbo. On the convergence of shock-capturing streamline diffusion finite element methods for hyperbolic conservation laws. *Math. Comp.*, 54(189):107–129, 1990.
- [KB98] J. P. Keener and K. Bogar. A numerical method for the solution of the bidomain equations in cardiac tissue. *Chaos*, 8(1):234–241, 1998.
- [KGF<sup>+</sup>09] U. Küttler, M.W. Gee, C. Förster, A. Comerford, and W.A. Wall. Coupling strategies for biomedical fluid-structure interaction problems. *Int. J. Numer. Meth. Biomed. Engrg.*, 26(3-4):305–321, 2009.
- [KN94] W. Krassowska and J.C. Neu. Effective boundary conditions for syncytial tissues. *IEEE Trans. Biomed. Eng.*, 41(2):143–150, 1994.
- [KNE<sup>+</sup>08] S.A. Kock, J.V. Nygaard, N. Eldrup, E.-T. Fründ, A. Klaerke, W.P. Paaske, E. Falk, and W. Yong Kim. Mechanical stresses in carotid plaques using mri-based fluid-structure interaction models. *J. Biomech.*, 41(8):1651–1658, 2008.

- [KSW<sup>+</sup>07] D.U.J Keller, G. Seemann, D.L. Weiss, D. Farina, J. Zehelein, and O. Dössel. Computer based modeling of the congenital long-qt 2 syndrome in the visible man torso: From genes to ECG. In *Proceedings of the 29th Annual International Conference of the IEEE EMBS*, pages 1410–1413, 2007.
- [KW08] U. Küttler and W.A. Wall. Fixed-point fluid-structure interaction solvers with dynamic relaxation. *Comp. Mech.*, 43(1):61–72, 2008.
- [KW09] U. Küttler and W.A. Wall. Vector extrapolation for strong coupling fluid-structure interaction solvers. *J. App. Mech.*, 76(2):021205, 2009.
- [LBG<sup>+</sup>03] G. T. Lines, M. L. Buist, P. Grottum, A. J. Pullan, J. Sundnes, and A. Tveito. Mathematical models and numerical methods for the forward problem in cardiac electrophysiology. *Comput. Visual. Sci.*, 5(4):215–239, 2003.
- [LF98] M. Lesoinne and C. Farhat. Higher-order subiteration-free staggered algorithm for nonlinear transient aeroelastic problems. *AIAA Journal*, 36(9):1754–1757, 1998.
- [LGT03] G.T. Lines, P. Grøttum, and A. Tveito. Modeling the electrical activity of the heart: a bidomain model of the ventricles embedded in a torso. *Comput. Vis. Sci.*, 5(4):195–213, 2003.
- [Lig58] M.J. Lighthill. On displacement thickness. *J. Fluid Mech.*, 4:383–392, 1958.
- [Lio96] P.-L. Lions. *Mathematical topics in fluid mechanics. Vol. 1: Incompressible models*, volume 3 of *Oxford Lecture Series in Mathematics and its Applications*. The Clarendon Press Oxford University Press, 1996.
- [LK06] Z. Li and C. Kleinstreuer. Computational analysis of type II endoleaks in a stented abdominal aortic aneurysm model. *J. Biomech.*, 39(14):2573–2582, 2006.
- [LLP02] W. Layton, H. K. Lee, and J. Peterson. A defect-correction method for the incompressible Navier-Stokes equations. *Appl. Math. Comput.*, 129(1):1–19, 2002.
- [LR91] C.H. Luo and Y. Rudy. A model of the ventricular cardiac action potential. depolarisation, repolarisation, and their interaction. *Circ. Res.*, 68(6):1501–1526, 1991.
- [LR94] C. Luo and Y. Rudy. A dynamic model of the cardiac ventricular action potential. i. simulations of ionic currents and concentration changes. *Circ. Res.*, 74(6):1071–1096, 1994.
- [LS97] R.B. Lehoucq and J.A. Scott. Implicitly restarted Arnoldi methods and eigenvalues of the discretized Navier-Stokes equations. Technical Report 2712J, Sandia National Laboratories, 1997.
- [LS01] R.B. Lehoucq and A.G. Salinger. Large-scale eigenvalue calculations for stability analysis of steady flows on massively parallel computers. *Internat. J. Numer. Methods Fluids*, 36(3):309–327, 2001.
- [LSHF01] M. Lesoinne, M. Sarkis, U. Hetmaniuk, and C. Farhat. A linearized method for the frequency analysis of three-dimensional fluid/structure interaction problems in all flow regimes. *Comput. Methods Appl. Mech. Engrg.*, 190:3121–3146, 2001.
- [LT94] P. Le Tallec. Numerical methods for nonlinear three-dimensional elasticity. In *Handbook of numerical analysis, Vol. III*, pages 465–622. North-Holland, 1994.

- [LTH03] P. Le Tallec and P. Hauret. Energy conservation in fluid structure interactions. In *Numerical methods for scientific computing. Variational problems and applications*, pages 94–107. Internat. Center Numer. Methods Eng. (CIMNE), Barcelona, 2003.
- [LTM00] P. Le Tallec and S. Mani. Numerical analysis of a linearised fluid-structure interaction problem. *Numer. Math.*, 87(2):317–354, 2000.
- [LTM01] P. Le Tallec and J. Mouro. Fluid structure interaction with large structural displacements. *Comput. Meth. Appl. Mech. Engrg.*, 190:3039–3067, 2001.
- [LTS96] M.J. Lab, P. Taggart, and F. Sachs. Mechano-electric feedback. *Cardiovasc. Res.*, 32:1–2, 1996.
- [LVSV06] L. Lanoye, J. Vierendeels, P. Segers, and P. Verdonck. Vascular fluid-structure-interaction using Fluent and Abaqus software. *J. Biomech.*, 39(Supplement 1):S440–S440, 2006.
- [LW95] G. Lube and D. Weiss. Stabilized finite element methods for singularly perturbed parabolic problems. *Appl. Numer. Math.*, 17(4):431–459, 1995.
- [Mad09] Y. Maday. Analysis of coupled models for fluid-structure interaction of internal flows. In *Cardiovascular mathematics*, volume 1 of *MS&A. Model. Simul. Appl.*, pages 279–306. Springer, 2009.
- [MC04] M. Murillo and X.-C. Cai. A fully implicit parallel algorithm for simulating the non-linear electrical activity of the heart. *Numer. Linear Algebra Appl.*, 11(2-3):261–277, 2004.
- [Med99] G. Medic. *Étude mathématique des modèles aux tensions de Reynolds et simulation numérique d'écoulements turbulents sur parois fixes et mobiles*. PhD thesis, Université de Paris VI, France, 1999.
- [MGS95] L. Morino, M. Gennaretti, and S.F. Shen. Lighthill transpiration velocity revisited: an exact formulation. *Meccanica*, 30(2):127–137, 1995.
- [MMS98] G. Medic, B. Mohammadi, and M. Stanciu. Prediction and aeroelastic simulation of turbulent flows in civil engineering applications. In *Proceedings of ECCOMAS'98*, pages 1062–1068. John Wiley & Sons, 1998.
- [MO95] H. Morand and R. Ohayon. *Fluid-Structure Interaction: Applied Numerical Methods*. John Wiley & Sons, 1995.
- [Mor97] G. Mortchéléwicz. Application of linearized Euler equations to flutter. In *85th AGARD SMP meeting*, Aalborg, Danemark, 1997.
- [Mou96] J. Mouro. *Interactions fluide structure en grands déplacements. Résolution numérique et application aux composants hydrauliques automobiles*. PhD thesis, Ecole Polytechnique, France, 1996.
- [Mou02] M. Moubachir. *Contrôle des phénomènes d'interaction fluide-structure, application à la stabilité aéroélastique*. PhD thesis, Ecole Nationale des Ponts et Chaussées, France, 2002.
- [MP95] J. Malmivuo and R. Plonsey. Bioelectromagnetism. Principles and applications of bioelectric and biomagnetic fields. *Oxford University Press, New York*, 1995.

- [MS97] K. Meerbergen and A. Spence. Implicitly restarted Arnoldi with purification for the shift-invert transformation. *Math. Comp.*, 66(218):667–689, 1997.
- [MS02] H.G. Matthies and J. Steindorf. Partitioned but strongly coupled iteration schemes for nonlinear fluid-structure interaction. *Comp. & Struct.*, 80(27-30):1991–1999, 2002.
- [MS03] C.C. Mitchell and D.G. Schaeffer. A two-current model for the dynamics of cardiac membrane. *Bulletin Math. Bio.*, 65:767–793, 2003.
- [MW01] D.P. Mok and W.A. Wall. Partitioned analysis schemes for the transient interaction of incompressible flows and nonlinear flexible structures. In W.A. Wall, K.U. Bletzinger, and K. Schweizerhof, editors, *Trends in computational structural mechanics*, Barcelona, 2001. CIMNE.
- [MWR99] D.P. Mok, W.A. Wall, and E. Ramm. Partitioned analysis approach for the transient, coupled response of viscous fluids and flexible structures. In W. Wunderlich, editor, *Proceedings of the European Conference on Computational Mechanics. ECCM'99*, TU Munich, 1999.
- [MWR01] D.P. Mok, W.A. Wall, and E. Ramm. Accelerated iterative substructuring schemes for instationary fluid-structure interaction. In Bathe. K.J., editor, *Computational Fluid and Solid Mechanics*, pages 1325–1328. Elsevier, 2001.
- [MZ06] M. Moubachir and J.-P. Zolésio. *Moving shape analysis and control*, volume 277 of *Pure and Applied Mathematics*. Chapman & Hall/CRC, 2006.
- [NAY62] J. Nagumo, S. Arimoto, and S. Yoshizawa. An active pulse transmission line simulating nerve axon. *Proceedings of the IRE*, 50(10):2061–2070, 1962.
- [NH92] T. Nomura and T.J.R. Hughes. An arbitrary Lagrangian-Eulerian finite element method for interaction of fluid and rigid body. *Comput. Methods Appl. Mech. Eng.*, 95(1):115–138, 1992.
- [Nit71] J. Nitsche. Über ein Variationsprinzip zur Lösung von Dirichlet-Problemen bei Verwendung von Teilräumen, die keinen Randbedingungen unterworfen sind. *Abh. Math. Sem. Univ. Hamburg*, 36:9–15, 1971.
- [NK93] J.C. Neu and W. Krassowska. Homogenization of syncytial tissues. *Crit. Rev. Biomed. Eng.*, 21(2):137–199, 1993.
- [Nob01] F. Nobile. *Numerical approximation of fluid-structure interaction problems with application to haemodynamics*. PhD thesis, EPFL, Switzerland, 2001.
- [NSH05] D. Nickerson, N.P. Smith, and P. Hunter. New developments in a strongly coupled cardiac electromechanical model. *Europace*, 7 Suppl 2:118–127, 2005.
- [NV08] F. Nobile and C. Vergara. An effective fluid-structure interaction formulation for vascular dynamics by generalized Robin conditions. *SIAM J. Sci. Comput.*, 30(2):731–763, 2008.
- [NVKN98] D. Noble, A. Varghese, P. Kohl, and P. Noble. Improved guinea-pig ventricular cell model incorporating a diadic space,  $ikr$  and  $iks$ , and length- and tension-dependent processes. *Can. J. Cardiol.*, 14(1):123–134, 1998.

- [Paï98] M.P. Païdoussis. *Fluid-structure interactions: slender structures and axial flow*, volume 1. Academic Press, 1998.
- [PB01] S. Piperno and P.E. Bournet. Numerical simulations of wind effects on flexible civil engineering structures. *Rev. Eur. Élé. Finis*, 8(5–6):659–687, 2001.
- [PBC05] A.J. Pullan, M.L. Buist, and L.K. Cheng. *Mathematically modelling the electrical activity of the heart: From cell to body surface and back again*. World Scientific Publishing Co. Pte. Ltd., Hackensack, NJ, 2005.
- [PDG03] M. Potse, B. Dubé, and M. Gulrajani. ECG simulations with realistic human membrane, heart, and torso models. In *Proceedings of the 25th Annual International Conference of the IEEE EMBS*, pages 70–73, 2003.
- [PDR<sup>+</sup>06] M. Potse, B. Dube, J. Richer, A. Vinet, and R. M. Gulrajani. A comparison of monodomain and bidomain reaction-diffusion models for action potential propagation in the human heart. *IEEE Trans. Biomed. Eng.*, 53(12):2425–2435, 2006.
- [PDV09] M. Potse, B. Dubé, and A. Vinet. Cardiac anisotropy in boundary-element models for the electrocardiogram. *Med. Biol. Eng. Comput.*, 47:719–729, 2009.
- [PF03] S. Piperno and C. Farhat. Design of efficient partitioned procedures for the transient solution of aeroelastic problems. In *Fluid-structure interaction*, Innov. Tech. Ser., pages 23–49. Kogan Page Sci., 2003.
- [Pip95] S. Piperno. *Simulation numérique de phénomènes d’interaction fluide-structure*. PhD thesis, Ecole Nationale des Ponts et Chaussées, France, 1995.
- [Pip97] S. Piperno. Explicit/implicit fluid/structure staggered procedures with a structural predictor and fluid subcycling for 2D inviscid aeroelastic simulations. *Internat. J. Numer. Methods Fluids*, 25(10):1207–1226, 1997.
- [Pir82] O. Pironneau. On the transport-diffusion algorithm and its applications to the Navier-Stokes equations. *Numer. Math.*, 38(3):309–332, 1981/82.
- [PSCF05] M. Pennacchio, G. Savaré, and P. Colli Franzone. Multiscale modeling for the bioelectric activity of the heart. *SIAM Journal on Mathematical Analysis*, 37(4):1333–1370, 2005.
- [PT93] J. Planchard and B. Thomas. On the dynamical stability of cylinders placed in cross-flow. *J. Fluid & Structures*, 7:321–339, 1993.
- [QQ07] A. Quaini and A. Quarteroni. A semi-implicit approach for fluid-structure interaction based on an algebraic fractional step method. *Math. Models Methods Appl. Sci.*, 17(6):957–983, 2007.
- [QV99] A. Quarteroni and A. Valli. *Domain decomposition methods for partial differential equations*. Numerical Mathematics and Scientific Computation. The Clarendon Press Oxford University Press, 1999.
- [RB01] S. Rugonyi and K.J. Bathe. On finite element analysis of fluid flows coupled with structural interaction. *CMES - Comp. Modeling Eng. Sci.*, 2(2):195–212, 2001.
- [Ren98] J.Y. Renou. *Une méthode eulérienne pour le calcul de forces fluide-élastiques*. PhD thesis, Université de Paris VI, France, 1998.

- [RH93] P. Raj and B. Harris. Using surface transpiration with an Euler method for cost-effective aerodynamic analysis. In *AIAA 24th Applied Aerodynamics Conference*, number 93-3506, Monterey, Canada, 1993.
- [RM94] J.M. Roger and A.D. McCulloch. A collocation-Galerkin finite element model of cardiac action potential propagation. *IEEE Trans. Biomed. Engr.*, 41(8):743–757, 1994.
- [RVD00] K. Riemsdagh, J. Vierendeels, and E. Dick. An efficient coupling procedure for flexible wall fluid-structure interaction. In *ECCOMAS 2000*, Barcelona, 2000.
- [Sac04] F.B. Sachse. *Computational Cardiology: Modeling of Anatomy, Electrophysiology, and Mechanics*. Springer, 2004.
- [Sat70] D.H. Sattinger. The mathematical problem of hydrodynamic stability. *J. Math. Mech.*, 19(9):797–817, 1970.
- [SHY06] M. Schäfer, M. Heck, and S. Yigit. An implicit partitioned method for the numerical simulation of fluid-structure interaction. In *Fluid-structure interaction*, volume 53 of *Lect. Notes Comput. Sci. Eng.*, pages 171–194. Springer, 2006.
- [SLC<sup>+</sup>06] J. Sundnes, G.T. Lines, X. Cai, B.F. Nielsen, K.-A. Mardal, and A. Tveito. *Computing the electrical activity in the heart*. Springer, 2006.
- [SLMT02] J. Sundnes, G.T. Lines, K.A. Mardal, and A. Tveito. Multigrid block preconditioning for a coupled system of partial differential equations modeling the electrical activity in the heart. *Comput. Methods Biomech. Biomed. Engin.*, 5(6):397–409, 2002.
- [SLT01] J. Sundnes, G.T. Lines, and A. Tveito. Efficient solution of ordinary differential equations modeling electrical activity in cardiac cells. *Math. Biosci.*, 172(2):55–72, 2001.
- [SLT05] J. Sundnes, G.T. Lines, and A. Tveito. An operator splitting method for solving the bidomain equations coupled to a volume conductor model for the torso. *Math. Biosci.*, 194(2):233–248, 2005.
- [SM00] N. Skouibine, K. Trayanova and P. Moore. A numerically efficient model for simulation of defibrillation in an active bidomain sheet of myocardium. *Math. Biosci.*, 166(1):85–100, 2000.
- [SM08] S. Sy and C.M. Murea. A stable time advancing scheme for solving fluid-structure interaction problem at small structural displacements. *Comput. Methods Appl. Mech. Engrg.*, 198(2):210–222, 2008.
- [SS96] E. Simiu and R.H. Scanlan. *Wind effects on structures. Fundamentals and Applications to Design*. John Wiley & Sons, 1996.
- [SS06] E. W. Swim and P. Seshaiyer. A nonconforming finite element method for fluid-structure interaction problems. *Comput. Methods Appl. Mech. Engrg.*, 195(17-18):2088–2099, 2006.
- [SSCL06] A.-V. Salsac, S.R. Sparks, J.M. Chomaz, and J.C. Lasheras. Evolution of the wall shear stresses during the progressive enlargement of symmetric abdominal aortic aneurysms. *J. Fluid Mech.*, 550:19–51, 2006.

- [ST71] R.H. Scanlan and J.J. Tomko. Airfoil and bridge deck flutter derivatives. *J. Eng. Mech.*, 97:1717–1737, 1971.
- [Ste73] G.V. Stewart. *Introduction to matrix computations*. Academic Press, 1973.
- [Ste78] H.J. Stetter. The defect correction principle and discretization methods. *Numer. Math.*, 29:425–443, 1978.
- [Sur83] M. Suri. *Mixed variational principles for time-dependent problems*. PhD thesis, Carnegie-Mellon University, 1983.
- [SZ92] J. Sokolowski and J.-P. Zolésio. *Introduction to shape optimization*, volume 16 of *Springer Series in Computational Mathematics*. Springer, 1992.
- [TDP<sup>+</sup>04] M.-C. Trudel, B. Dubé, M. Potse, R.M. Gulrajani, and L.J. Leon. Simulation of qrst integral maps with a membrane-based computer heart model employing parallel processing. *IEEE Trans. Biomed. Eng.*, 51(8):1319–1329, 2004.
- [Tem68] R. Temam. Une méthode d’approximation de la solution des équations de Navier-Stokes. *Bull. Soc. Math. France*, 96:115–152, 1968.
- [Tez92] T.E. Tezduyar. Stabilized finite element formulations for incompressible flow computations. In *Advances in applied mechanics, Vol. 28*, volume 28 of *Adv. Appl. Mech.*, pages 1–44. Academic Press, Boston, MA, 1992.
- [Tez01] T.E. Tezduyar. Finite element methods for fluid dynamics with moving boundaries and interfaces. *Arch. Comput. Methods Engrg.*, 8:83–130, 2001.
- [Thi08] M. Thiriet. *Biology and Mechanics of Blood Flows. Part II: Mechanics and Medical Aspects*. CRM Series in Mathematical Physics. Springer, 2008.
- [Tho06] V. Thomée. *Galerkin finite element methods for parabolic problems*, volume 25 of *Springer Series in Computational Mathematics*. Springer, Berlin, second edition, 2006.
- [TS07] T.E. Tezduyar and S. Sathe. Modelling of fluid-structure interactions with the space-time finite elements: solution techniques. *Internat. J. Numer. Methods Fluids*, 54(6-8):855–900, 2007.
- [Tun78] L. Tung. *A bi-domain model for describing ischemic myocardial D-C potentials*. PhD thesis, MIT, USA, 1978.
- [TV96] L. Tobiska and R. Verfürth. Analysis of a streamline diffusion finite element method for the Stokes and Navier-Stokes equations. *SIAM J. Numer. Anal.*, 33(1):107–127, 1996.
- [TW05] A. Toselli and O. Widlund. *Domain decomposition methods—algorithms and theory*, volume 34 of *Springer Series in Computational Mathematics*. Springer, Berlin, 2005.
- [vCD80] F.H. van Capelle and D. Durrer. Computer simulation of arrhythmias in a network of coupled excitable elements. *Circ. Res.*, 47:453–466, 1980.
- [Ven09] M. Veneroni. Reaction-diffusion systems for the macroscopic bidomain model of the cardiac electric field. *Nonlinear Anal. Real World Appl.*, 10(2):849–868, 2009.

- [VLDV07] J. Vierendeels, Lanoye. L., J. Degroote, and P. Verdonck. Implicit coupling of partitioned fluid-structure interaction problems with reduced order models. *Comp. & Struct.*, 85(11-14):970–976, 2007.
- [VWdSP<sup>+</sup>08] E.J. Vigmond, R. Weber dos Santos, A.J. Prassl, M Deo, and G. Plank. Solvers for the cardiac bidomain equations. *Progr. Biophys. Molec. Biol.*, 96(1–3):3–18, 2008.
- [WGR07] W.A. Wall, S. Genkinger, and E. Ramm. A strong coupling partitioned approach for fluid-structure interaction with free surfaces. *Comput. & Fluids*, 36(1):169–183, 2007.
- [Whe78] M.F. Wheeler. An elliptic collocation-finite element method with interior penalties. *SIAM J. Numer. Anal.*, 15(1):152–161, 1978.
- [WOOF78] K. Washizu, A. Ohya, Y. Otsuki, and K. Fujii. Aeroelastic instability of rectangular cylinders in a heaving mode. *J. Sound Vib.*, 59(2):195–210, 1978.
- [WOOF80] K. Washizu, A. Ohya, Y. Otsuki, and K. Fujii. Aeroelastic instability of rectangular cylinders in a torsional mode due to a transverse wind. *J. Sound Vib.*, 72(4):507–521, 1980.
- [WRC<sup>+</sup>08] L. Wiechert, T. Rabczuk, A. Comerford, R. Metzke, and W.A. Wall. Towards stresses and strains in the respiratory system. In *Mathematical and numerical modelling of the human lung*, volume 23 of *ESAIM Proc.*, pages 98–113. EDP Sci., 2008.
- [WSKH04] H. Watanabe, S. Sugiura, H. Kafuku, and T. Hisada. Multiphysics simulation of left ventricular filling dynamics using fluid-structure interaction finite element method. *Biophysical Journal*, 87(3):2074–2085, 2004.
- [YLY07] X.L. Yang, Y. Liu, and J.M. Yang. Fluid-structure interaction in a pulmonary arterial bifurcation. *J. Biomech.*, 40(12):2694–2699, 2007.
- [Zem09] N. Zemzemi. *Étude théorique et numérique de l'activité électrique du cœur: Applications aux électrocardiogrammes*. PhD thesis, Université Paris XI, 2009. <http://tel.archives-ouvertes.fr/tel-00470375/en/>.